

**Impact of Stress and Equilibration Time on the Petrophysical
Properties of Tight Gas Sandstones**

Ibrahim Ali Almakrami

Submitted in accordance with the requirements for the degree of
Doctor of Philosophy

The University of Leeds
School of Earth and Environment

September, 2017

Intellectual Property and Publication Statements

The candidate confirms that the work submitted is his/her own and that appropriate credit has been given where reference has been made to the work of others.

This copy has been supplied on the understanding that it is copyright material and that no quotation from the thesis may be published without proper acknowledgement.

Acknowledgements

First, I would like to thank Pro. Quentin Fisher for providing the samples and access to the data base and all the resources needed to complete my research in addition to his continuous guidance, valuable discussions and comments throughout my PhD research. A special mention for Dr. Carlos Grattoni for all the guidance and support during the experimental work conducted in the Wolfson laboratory in addition to the valuable feedback and discussions during my research. Thanks also go to Phil Guise and Samuel Allshorn for the support in the Wolfson laboratory.

Thanks to my dear friend Saleh Alqahtani for all the discussions and coffee breaks.

I express my gratitude to my sponsor Saudi Aramco (Exploration Organization - Upstream Venture Department, Speciality Development Program and Educational Partnerships Department) for giving me the opportunity to pursue my PhD. Special thanks go to Mrs Aggie Cooper in Saudi Aramco office in London for all the support.

Above all, I'm grateful to my wife and my two daughters whose love, energy and enthusiasm support me throughout my research work and in all aspects of life. I'm also so thankful to my parents for their love, continuous prayers and encouragement. Thanks to my brothers and sisters for their prayers and support during my PhD.

Abstract

Petrophysical properties (permeability, ultrasonic velocity and electrical properties) of tight gas sandstones are found to be more stress dependent at ambient conditions than at in-situ stresses. Analyses of the petrophysical properties measured at wide ranges of net stresses coupled with scanning electron microscopy (SEM) images indicate the presence of microfractures formed during or after drilling might play a major role on the stress dependency of the properties. Yet, the stress dependencies of the properties diminish as the net stress increases. This could be explained by partial or complete closure of the microfractures. Drawdown experiments were conducted to further analyse the stress dependency of permeability at reservoir conditions and to mimic the gas production from a tight gas sandstone reservoir. Results showed all the petrophysical properties were less stress dependent at higher net stress (>3000 psi) which was consistent with the theory of the microfracture closure. Drawdown tests (5000-7000 psi net stress) showed the least stress dependent of permeability.

Net stress is often defined as the difference between the confining pressure (P_{con}) and the pore pressure (P_p) with the assumption that changes in pore pressure and confining pressure have an equal effect on the permeability. The introduction of an effective stress coefficient χ into the simple net stress ($P_{con} - \chi P_p$) provides better understanding and quantitative analyses of which pressure has more effect on the gas permeability. This was investigated by measuring the gas permeability under 12 different combinations of confining stress and pore pressure. Biot's coefficients that are dependent on the elastic properties of the samples were calculated and correlated with the determined coefficient χ . The determined effective stress coefficients for permeability were less than unity indicating less effect of the change in the pore pressure compared to the change of the confining stress.

Comparison between capillary pressure data obtained from porous plate and vapour desorption methods using air-brine system and capillary pressure obtained from mercury injection (MICP) technique has shown discrepancies. Several factors identified as the key causes of the discrepancies are the equilibration time required

for the porous plate and vapour desorption, the impact of injecting mercury on the delicate clay in the samples, the conversion factor of MICP to air-brine capillary pressure. The impact of stress on MICP measurements were analysed by conducting MICP under stress using a custom-built equipment. Results indicated capillary pressure was stress dependent similar to the other petrophysical properties. Also, permeabilities estimated from MICP models showed a better correlation with permeabilities measured at stresses equivalent to the displacement pressures of the samples, which confirmed the effect of stress on MICP measurements of the tight sandstones.

Table of Contents

Acknowledgements	iii
Abstract.....	iv
Table of Contents.....	vi
List of Tables.....	xii
List of Figures.....	xiv
1 Introduction	1
1.1 Background	5
1.1.1 Porosity	5
1.1.2 Permeability	6
1.1.3 Saturation.....	9
1.1.4 Capillary pressure.....	10
1.1.5 Depositional controls on porosity and permeability	12
1.1.6 Diagenetic controls on porosity and permeability	17
1.1.6.1 Mechanical compaction	17
1.1.6.2 Chemical processes	18
1.1.7 What are tight gas sandstones?.....	22
1.1.8 Effect of stress on petrophysical properties	24
1.2 Objectives.....	25
1.3 Thesis outline	26
2 Data and Methodology.....	28
2.1 Introduction	28
2.2 Samples analysed	28
2.3 Sample preparation.....	28
2.4 Bulk Density.....	29
2.5 Helium porosimetry	30
2.5.1 Helium pycnometer	30
2.5.2 Pycnometer calibration.....	31
2.5.3 Porosity calculation	32
2.5.4 Stress-corrected porosity.....	32
2.6 Permeability determination.....	33
2.6.1 Gas pulse decay permeameter	33

2.6.2	Klinkenberg permeability correction	34
2.6.3	Drawdown experiments.....	35
2.7	X-Ray Diffraction (XRD)	36
2.8	Scanning Electron Microscopy (SEM).....	36
2.9	Ultrasonic velocities	37
2.10	Reservoir simulated brine preparation and properties	37
2.10.1	Brine preparation	37
2.10.2	Brine resistivity.....	38
2.10.3	Brine density	38
2.10.4	Brine viscosity.....	38
2.10.5	Brine Compressibility	39
2.11	Saturating Samples with brine	39
2.12	Liquid pulse decay permeameter.....	40
2.13	Electrical resistivity under stress.....	41
2.14	Nuclear magnetic resonance	42
2.14.1	NMR measurements	43
2.15	Capillary pressure measurements	45
2.15.1	Air-brine capillary pressure tests	45
2.15.1.1	Porous plate	45
2.15.1.2	Vapour desorption	47
2.15.2	Mercury injection capillary pressure	48
2.15.2.1	Mercury injection capillary pressure.....	48
2.15.2.2	Mercury injection porosimetry under confining stress (PUCS)	51
3	Routine Core Analysis Results	53
3.1	Introduction	53
3.2	Methodology.....	53
3.3	Results	54
3.3.1	Porosity	54
3.3.2	Permeability	56
3.3.3	Porosity permeability relationship.....	58
3.3.4	Brine permeability.....	59
3.3.5	Quantitative mineralogy	60
3.3.6	SEM analysis.....	62
3.3.7	Mercury injection capillary pressure data with SEM images.....	71

3.4	Discussion.....	101
3.4.1	Controls on k_g/k_b ratios	101
3.4.2	Controls on porosity and permeability of sandstones.....	102
3.4.2.1	Grain size and sorting.....	102
3.4.2.2	Presence of microfractures	106
3.4.2.3	Confining stress	107
3.4.2.4	Clay type	108
3.5	Conclusion	109
4	Stress-Dependent Permeability, Ultrasonic Velocity and Electrical Properties of Tight Gas Sandstones.....	111
4.1	Introduction	111
4.1.1	Background	113
4.1.1.1	Electrical properties	113
4.1.1.2	Ultrasonic velocity.....	118
4.1.1.3	Controls on the stress dependency of properties	120
4.2	Materials and methods.....	122
4.2.1	Porosity	122
4.2.2	Permeability measurements and Klinkenberg correction	122
4.2.3	Drawdown experiments.....	122
4.2.4	Equilibration time.....	123
4.3	Results	124
4.3.1	Porosity	124
4.3.2	Gas permeability	124
4.3.2.1	Equilibration time prior to permeability measurement	131
4.3.2.2	Klinkenberg correction.....	131
4.3.3	Pore size distribution	133
4.3.4	Ultrasonic velocities	134
4.3.5	Electrical properties under stress	137
4.4	Discussion.....	141
4.4.1	Controls on stress dependency of permeability	141
4.4.2	Controls on electrical properties	143
4.4.3	Controls on the stress dependency of electrical properties.....	145
4.4.4	Implication in calculating GOIP	146
4.4.5	Controls on velocities.....	147
4.4.6	Controls on the stress dependency of velocities.....	148

4.4.7	Relationship between the stress dependencies of different properties.....	149
4.4.7.1	Relationship between stress dependencies of electrical properties and permeability.....	150
4.4.7.2	Relationship between stress dependencies of electrical properties and ultrasonic velocity.....	151
4.4.7.3	Relationship between stress dependencies of permeability and ultrasonic velocity.....	152
4.4.8	Implications of gas slippage and stress dependency of permeability on production strategies	153
4.5	Conclusions	154
5	Effective Stress Law for Permeability of Tight Gas Sandstones.....	156
5.1	Introduction	156
5.1.1	Background	158
5.2	Methodology.....	161
5.2.1	Samples	161
5.2.2	Quantitative X-ray diffraction	161
5.2.3	Porosity and density measurement.....	162
5.2.4	Gas pulse decay permeameter	162
5.2.4.1	Loading and unloading cycles.....	162
5.2.5	Biot coefficients from elastic properties.....	165
5.3	Results:.....	166
5.3.1	Quantitative XRD.....	166
5.3.2	Porosity with bulk density and ultrasonic velocity	166
5.3.3	Gas permeability under stress	167
5.3.4	Elastic properties and Biot's coefficients.....	173
5.4	Discussion.....	174
5.4.1	Comparison with previous studies.....	174
5.4.2	Models for effective stress coefficient	176
5.4.2.1	Clay shell model.....	176
5.4.2.2	Clay particle model.....	178
5.4.3	Biot coefficient and the elastic static and dynamic moduli.....	180
5.4.4	Impact of equilibration time	182
5.4.5	Impact of microfractures	184
5.4.6	Implications for gas production	185
5.4.7	Gas slippage effect.....	188

5.5	Conclusions	189
6	Effects of Stress and Equilibration Time on Capillary Pressure Measurements and Permeability Predictions from MICP Models for Tight Gas Sandstones.....	192
6.1	Introduction	192
6.1.1	Reservoir scale capillary pressure	193
6.1.2	Sample scale capillary pressure	194
6.1.3	Capillary pressure.....	195
6.1.4	MICP and permeability prediction models	198
6.2	Methodology.....	204
6.2.1	Air-brine capillary pressure tests	205
6.2.2	Mercury injection capillary pressure	205
6.2.3	Estimating permeability from MICP measurements	205
6.2.4	Nuclear magnetic resonance measurements	205
6.3	Results	205
6.3.1	Porous plate and vapour desorption	205
6.3.1.1	Capillary pressure drainage curves from porous plate and vapour desorption	205
6.3.1.2	Water saturation vs. equilibration time in porous plate	206
6.3.1.3	Water saturation vs. equilibration time in vapour desorption	207
6.3.2	NMR 210	
6.3.3	Mercury injection capillary pressure	211
6.3.4	Mercury injection capillary pressure under stress	213
6.3.5	Permeability predicted from models using standard MICP.....	215
6.3.6	Comparison of mercury injection capillary pressure to porous plate and vapour desorption composite capillary pressure.....	216
6.3.6.1	Porous plate capillary pressure against MICP converted to air-brine system.....	217
6.3.6.2	Vapour desorption capillary pressure compared to MICP converted to air-brine system	218
6.3.6.3	Composite porous plate-vapour desorption capillary pressure compared to MICP converted to air-brine system.....	220
6.4	Discussion.....	224

6.4.1	Causes for the discrepancies between capillary pressure obtained from air-brine system and from mercury injection.....	224
6.4.1.1	Equilibration time for air-brine system capillary pressure.....	224
6.4.1.2	Irreducible water saturation	225
6.4.1.3	Impact of mercury injection on microstructures	226
6.4.1.4	Conversion of mercury injection data to air-brine system	227
6.4.2	Nuclear magnetic resonance analyses.....	228
6.4.3	Impact of stress on mercury injection capillary pressure.....	229
6.4.1	Permeability predicted from stressed MICP data.....	230
6.4.2	Implications for water saturations estimation	231
6.5	Conclusions	232
7	Conclusions and recommendations.....	235
7.1	Conclusions	235
7.1.1	Controls on porosity and permeability	235
7.1.2	Stress dependency of petrophysical properties	236
7.1.3	Effective stress law for permeability.....	237
7.1.4	Effect of stress and equilibration time on capillary pressure measurement.....	239
7.2	Implications	240
7.3	Recommendations for further work.....	240
	References.....	242

List of Tables

Table 2-1: Properties of the simulated brine.....	38
Table 2-2: Relative humidity RH percentage with equivalent capillary pressure determined with different salt types.	48
Table 3-1: Routine helium ambient porosity in percentage with $\pm 0.2\%$ error and brine permeability k_w at 1500 psi and gas permeability k_g at 500, 1500 and 5000 psi all within $\pm 10\%$ uncertainty, and k_g/k_w ratio at 1500 psi for the samples of the three suites. Grain size is shown as very fine (VF), lower fine (LF), upper fine (UF) and medium (M). Grain sorting is shown as very well sorted (VW), well sorted (W), moderately sorted (M).....	56
Table 3-2: Mineralogy (%) of all samples obtained using quantitative x-ray diffraction technique (QXRD).....	61
Table 4-1: Gas permeability measurements under a fixed confining stress and varying pore pressure in drawdown tests.....	123
Table 4-2: Corrected helium permeability (mD) under a range of confining stresses (psi) with different pore pressures (psi) with maximum net stress of 3300 psi for group-A samples.....	125
Table 4-3: Corrected helium permeability (mD) under a drawdown measurements with confining stress of 10000 psi with pore pressure in the range 5000-7300 psi for group-A samples.....	126
Table 4-4: Determined slippage factor b (psi) for all samples under 3500 psi confining stress with varying mean pore pressures (1000, 700 and 400 psi).....	132
Table 4-5: Ultrasonic P-wave velocity (m/s) measurements under a range of confining stresses 1000, 2000, 3000, 4000 and 5000 psi with the ratio of P-wave to S-wave (V_p/V_s) at 1000 and 5000 psi for group-A samples. ..	136
Table 4-6: Calculated electrical resistivity measurements (ohm-m) for the five representative samples in group A under a range of stress 1500, 3000 and 5000 psi. All measurements were corrected to 25° C.....	138
Table 4-7: Formation resistivity factor (FRF) determined at 1500 psi and porosity (fraction) stress-corrected at 1500 psi and calculated cementation exponent (m) for all samples in group A.	140
Table 4-8: Water saturation S_w calculated from Archie formula using different values of m at different porosities.....	146
Table 4-9: Calculated volume of gas in billion cubic feet based on base case of $m=2$ and $\pm 20\%$ of the value of m at different porosities. Relative differences show error in percentage of using different m values with larger error at lower porosity.	147

Table 5-1: An example of loading and unloading cycles performed for sample TS7-4 with permeability (mD) measured at each net stress (psi).....	163
Table 5-2: Total of 12 points at which gas permeability was measured under different combinations of pore pressures and confining stresses for each sample.	165
Table 5-3: Elastic modulus of minerals used to calculate the composite bulk modulus of the minerals forming the rock (from Mavko et al., 2009).	166
Table 5-4: Measured porosity and bulk density at ambient condition with ultrasonic velocity V_p and V_s (m/s) measured at 1000 and 5000 psi confining stress for group-B samples. *TS 5-5 was broken prior to measuring the ultrasonic velocity.	167
Table 5-5: Permeability measurements (10% uncertainty) under a fixed pore pressure of 2000 psi and increasing confining stress 3000 to 6000 psi (that is 1000 to 4000 psi simple net stress) for group-B samples.....	167
Table 5-6: Values of the determined effective stress coefficients for permeability χ of group-B samples with the correlation coefficients of the power law models.	171
Table 5-7: Measured helium permeability in (mD) for all the samples in group-B under a fixed confining stress of 10,000 psi and varying pore pressure 7000-4000 psi.....	172
Table 5-8: Dry bulk modulus K_b at 1000 and 5000 psi calculated from density and velocity data, and calculated minerals bulk modulus K_s. Biot coefficients determined for the group-B samples at 1000 and 5000 psi from the calculated K_b and K_s.....	173
Table 5-9: Bulk modulus (GPa) for quartz and the total clay present in each sample and the clay to quartz stiffness ratio for the samples in group B.	174
Table 5-10: Equilibration times with relative error in (%) for gas permeability k_g (mD) measured at different net stresses (psi) for the five samples in group B.....	184
Table 6-1: Water saturation (%) and equilibration time (days) for the group-C samples at the three different pressures 35, 75 and 130 psi used in the porous plate method.	207
Table 6-2: Displacement and threshold pressures (psi) obtained from the mercury injection technique for group-C samples.	212

List of Figures

Figure 1-1: Resource triangle for natural gas (from Holditch, 2013).....	1
Figure 1-2: Prediction of unconventional gas resources to be the dominant source of natural gas in US with tight gas contributing approximately 20% (from EIA, 2016).	2
Figure 1-3: Apparatus used by Darcy for determining permeability by flowing water through a vertical pack of sand inside an iron cylinder (from Hubert, 1953).....	7
Figure 1-4: Diagram for the definition of permeability based on Darcy's law (from McPhee et al., 2015).	7
Figure 1-5: Diagram showing the drainage process that is the displacement capillary pressure for hydrocarbon as it migrates into the reservoir and displaces the initial water in the reservoir (from Schowalter, 1979).....	12
Figure 1-6: Capillary pressure curves for different sandstone samples with different clay types plotted as mercury pressure against Pore Volume (PV) occupied by mercury (%) (from Newsham, 1977).	12
Figure 1-7: Porosity of different packing systems of uniform spheres (left) 47.6% for a cubic system and (right) 26% for a rhombohedral system (modified from Glover, 2016).	13
Figure 1-8: Degrees of roundness and sphericity of grains based on the erosional processes during transport and deposition (from Pettijhon et al., 1987).	13
Figure 1-9: Erosional processes which sediments go through during transport and deposition that affect the geometry and smoothness of the grains (from Nichols, 2009).	14
Figure 1-10: Diagram showing the impact of grain sorting that is sand to clay ratios on porosity with minimum porosity of 24% for a mixture of 60% sand and 40% clay (from Revil et al., 2002)	15
Figure 1-11: Effect of grain size (left) and grain sorting (right) on porosity and permeability based on the numerical modeling (from Cade et al., 1994).....	16
Figure 1-12: Cross plot of porosity and permeability at in-situ showing the effect of the different facies on the properties in Lower Silurian Sandstones in the Appalachian Basin (from Castle and Byrnes, 2005).	16
Figure 1-13: Semi-log plot of permeability (log scale) against porosity (linear scale) showing the relationship between porosity and permeability for different lithologies (from Glover, 2016).	17

Figure 1-14: Sketch showing impact of mechanical compaction on rearranging sand grains and crushing shale particles affecting the porosity and permeability (from Revil et al., 2002).....	18
Figure 1-15: Classification of clay types based on their position in sandstones (from Neasham, 1977).....	20
Figure 1-16: Porosity vs. air permeability for several sandstone samples with different types of clay (from Neasham, 1977).....	21
Figure 1-17: Relationships of porosity and permeability of clean sandstones (clay-free) and sandstones with different clay types (from Wilson, 1982).....	21
Figure 1-18: Water-sensitivity of the Spiney sandstone, Moray Firth Basin, showing the reduction in permeability based on the change in the salinity of the brine (from Lever and Dawe, 1987).....	22
Figure 1-19: Pore throat size comparison between conventional sandstones and tight sandstones (modified from Nelson, 2009).	23
Figure 2-1: A schematic of the helium pycnometer used to determine the grain volume based on the gas expansion method (from Glover, 2016).	30
Figure 2-2: Left: A picture of the CoreLab PDP 200 redesigned in the Wolfson laboratory. Right: a schematic diagram of the pulse-decay permeameter (PDP) for gas permeability measurements under stress (from Wolfson laboratory website).....	34
Figure 2-3: An example of estimating Klinkenberg-corrected permeability (mD) for TS2-5 by plotting permeability (mD) against the reciprocal of mean pore pressures (1/psi). Permeability measurements were within 10% error (based on Klinkenberg, 1941).....	35
Figure 2-4: Brine permeability determined from pressure as a function of time modelled using CYDAR software that uses Newton-Raphson algorithm.	41
Figure 2-5: NMR T_2 relaxation time distribution (ms) with a $T_{2\text{cutoff}}$ value subdividing the fluids into non-movable (bulk volume irreducible BVI and clay bound water) and movable free fluid (free fluid index FFI) (from Coates et al., 1999).	43
Figure 2-6: NMR amplitude signal decay against time in millisecond with measured raw data points and a fitting curve (from Coates et al., 1999).....	44
Figure 2-7: NMR T_2 distribution against incremental porosity (left y-axis) and cumulative porosity (right y-axis) in percentage, with the $T_{2\text{cutoff}}$ determined at the intersection of the BVI cumulative porosity with the 100% saturated porosity (from Coates et al., 1999).	45
Figure 2-8: Porous plate chamber showing a core plug on top of a porous diaphragm used for capillary pressure measurements (from McPhee et al., 2015).	46

Figure 2-9: A schematic of the mercury injection porosimetry (from Glover, 2016).....	50
Figure 2-10: A nomogram to determine the conversion factor from mercury-air to air-water system at laboratory conditions (from Schowalter, 1979).....	51
Figure 3-1: Histogram showing the porosity frequency in all the 29 analysed samples. The porosity values were rounded to the nearest whole number.	54
Figure 3-2: Histogram showing the range of the gas permeability measured at 500 psi stress ($\pm 10\%$ uncertainty). The permeability value in x-axis is the upper limit for the bin range.....	57
Figure 3-3: Histogram showing the range of the gas permeability measured at 1500 psi stress $\pm 10\%$ uncertainty. The permeability value in x-axis is the upper limit for the bin range.....	57
Figure 3-4: Histogram showing the range of the gas permeability measured at 5000 psi stress $\pm 10\%$ uncertainty. The permeability value in x-axis is the upper limit for the bin range.....	57
Figure 3-5: Plot of ambient porosity (fraction) with $\pm 0.2\%$ uncertainty vs. measured gas permeability (k_g) at 500 psi with $\pm 10\%$ uncertainty for all samples fitted with an exponential relationship having a correlation coefficient of 0.64.....	58
Figure 3-6: Plot of porosity (fraction) stress-corrected at 5000 psi with $\pm 1\%$ uncertainty vs. gas permeability (k_g) measured at 5000 psi net stress with $\pm 10\%$ uncertainty for all samples fitted with a power law relationship with a correlation coefficient of 0.75.	59
Figure 3-7: Plot of brine permeability (k_w) against the gas permeability (k_g) both measured under 1500 psi net stress and within $\pm 10\%$ uncertainty. A power law relationship exists with a correlation coefficient of 0.91.....	60
Figure 3-8: Ternary plot showing the major mineral composition of the samples in all three groups (group A, B and C).	61
Figure 3-9: SEM image for sample TS2-1 showing clay (illite) (red arrows) blocking and bridging the pores and pore throats between quartz grains (Qtz) and contributing in the formation of microporosity formation (yellow).	62
Figure 3-10: SEM images for TS2-4. Left: Abundance of microcracks and grain boundaries cracks (red). Right: microcrystalline quartz (blue) and calcite cement (yellow).....	63
Figure 3-11: SEM images showing the microcracks (red) resulting from the change in stress state in sample TS2-7.	64
Figure 3-12: SEM image showing the microfractures (red) with the poorly sorted grains and the abundance of microporosity (blue) in sample TS2-3.....	64

Figure 3-13: SEM images showing the poorly sorted grains which are compacted and cemented with the presence of micro-cracks (red) in sample TS2-9.....	65
Figure 3-14: SEM image showing the micro-scale heterogeneity of the sample TS3-1 with micro-pores (yellow) and clasts (red).	65
Figure 3-15: SEM image showing a micro-pore space filled with chlorite and illite coating the right surface of the pore in sample TS2-4.	66
Figure 3-16: SEM image showing quartz overgrowth (red) and kaolinite filling the pore space (blue) in sample TS5-2.	67
Figure 3-17: SEM image showing kaolinite filling the pore space (red) in sample TS5-5.....	67
Figure 3-18: SEM image of sample TS7-5 with microcracks (red arrows) that are few microns to sub microns in width, and clay lining the pore (yellow arrow).....	68
Figure 3-19: SEM image showing the presence of illite filling the pore space (red) of sample TS7-5 (left). SEM image showing hairy grain coating hairy illite (red) in sample TS1-55 (right).	68
Figure 3-20: SEM image showing grain coating illite (red) and pore filling chlorite (blue) in sample TS1-305.....	69
Figure 3-21: SEM image showing quartz overgrowth (red) in sample TS4-4 (left). SEM image showing the presence of chlorite filling and lining the pores (red) in sample TS4-11 (right).	69
Figure 3-22: SEM image showing pore filling kaolinite (blue) and dolomite (red) in sample TS1-25.	70
Figure 3-23: SEM image showing pore filling kaolinite in sample TS2-25.....	70
Figure 3-24: SEM image showing pore filling kaolinite (red) with the presence of dolomite (blue) in sample TS3-47.....	71
Figure 3-25: A montage showing the mercury injection data that is mercury saturation, capillary pressure, pore size distribution, SEM image and the porosity and permeability for sample TS2-1. See caption of Figure 3-5 for porosity and permeability uncertainties in plotted values.	72
Figure 3-26: A montage showing the mercury injection data that is mercury saturation, capillary pressure, pore size distribution, SEM image and the porosity and permeability for sample TS2-2. See caption of Figure 3-5 for porosity and permeability uncertainties in plotted values.	73
Figure 3-27: A montage showing the mercury injection data that is mercury saturation, capillary pressure, pore size distribution, SEM image and the porosity and permeability for sample TS2-3. See caption of Figure 3-5 for porosity and permeability uncertainties in plotted values.	74

Figure 3-28: A montage showing the mercury injection data that is mercury saturation, capillary pressure, pore size distribution, SEM image and the porosity and permeability for sample TS2-4. See caption of Figure 3-5 for porosity and permeability uncertainties in plotted values.	75
Figure 3-29: A montage showing the mercury injection data that is mercury saturation, capillary pressure, pore size distribution, SEM image and the porosity and permeability for sample TS2-5. See caption of Figure 3-5 for porosity and permeability uncertainties in plotted values.	76
Figure 3-30: A montage showing the mercury injection data that is mercury saturation, capillary pressure, pore size distribution, SEM image and the porosity and permeability for sample TS2-6. See caption of Figure 3-5 for porosity and permeability uncertainties in plotted values.	77
Figure 3-31: A montage showing the mercury injection data that is mercury saturation, capillary pressure, pore size distribution, SEM image and the porosity and permeability for sample TS2-7. See caption of Figure 3-5 for porosity and permeability uncertainties in plotted values.	78
Figure 3-32: A montage showing the mercury injection data that is mercury saturation, capillary pressure, pore size distribution, SEM image and the porosity and permeability for sample TS2-8. See caption of Figure 3-5 for porosity and permeability uncertainties in plotted values.	79
Figure 3-33: A montage showing the mercury injection data that is mercury saturation, capillary pressure, pore size distribution, SEM image and the porosity and permeability for sample TS2-9. See caption of Figure 3-5 for porosity and permeability uncertainties in plotted values.	80
Figure 3-34: A montage showing the mercury injection data that is mercury saturation, capillary pressure, pore size distribution, SEM image and the porosity and permeability for sample TS2-10. See caption of Figure 3-5 for porosity and permeability uncertainties in plotted values.	81
Figure 3-35: A montage showing the mercury injection data that is mercury saturation, capillary pressure, pore size distribution, SEM image and the porosity and permeability for sample TS3-1. See caption of Figure 3-5 for porosity and permeability uncertainties in plotted values.	82
Figure 3-36: A montage showing the mercury injection data that is mercury saturation, capillary pressure, pore size distribution, SEM image and the porosity and permeability for sample TS3-2. See caption of Figure 3-5 for porosity and permeability uncertainties in plotted values.	83

Figure 3-37: A montage showing the mercury injection data that is mercury saturation, capillary pressure, pore size distribution, SEM image and the porosity and permeability for sample TS3-3. See caption of Figure 3-5 for porosity and permeability uncertainties in plotted values.	84
Figure 3-38: A montage showing the mercury injection data that is mercury saturation, capillary pressure, pore size distribution, SEM image and the porosity and permeability for sample TS3-4. See caption of Figure 3-5 for porosity and permeability uncertainties in plotted values.	85
Figure 3-39: A montage showing the mercury injection data that is mercury saturation, capillary pressure, pore size distribution, SEM image and the porosity and permeability for sample TS3-5. See caption of Figure 3-5 for porosity and permeability uncertainties in plotted values.	86
Figure 3-40: A montage showing the mercury injection data that is mercury saturation, capillary pressure, pore size distribution, SEM image and the porosity and permeability for sample TS5-2. See caption of Figure 3-5 for porosity and permeability uncertainties in plotted values.	87
Figure 3-41: A montage showing the mercury injection data that is mercury saturation, capillary pressure, pore size distribution, SEM image and the porosity and permeability for sample TS5-5. See caption of Figure 3-5 for porosity and permeability uncertainties in plotted values.	88
Figure 3-42: A montage showing the mercury injection data that is mercury saturation, capillary pressure, pore size distribution, SEM image and the porosity and permeability for sample TS7-1. See caption of Figure 3-5 for porosity and permeability uncertainties in plotted values.	89
Figure 3-43: A montage showing the mercury injection data that is mercury saturation, capillary pressure, pore size distribution, SEM image and the porosity and permeability for sample TS7-4. See caption of Figure 3-5 for porosity and permeability uncertainties in plotted values.	90
Figure 3-44: A montage showing the mercury injection data that is mercury saturation, capillary pressure, pore size distribution, SEM image and the porosity and permeability for sample TS7-5. See caption of Figure 3-5 for porosity and permeability uncertainties in plotted values.	91
Figure 3-45: A montage showing the mercury injection data that is mercury saturation, capillary pressure, pore size distribution, SEM image and the porosity and permeability for sample TS1-55. See caption of Figure 3-5 for porosity and permeability uncertainties in plotted values.	92

Figure 3-46: A montage showing the mercury injection data that is mercury saturation, capillary pressure, pore size distribution, SEM image and the porosity and permeability for sample TS1-197. See caption of Figure 3-5 for porosity and permeability uncertainties in plotted values. 93

Figure 3-47: A montage showing the mercury injection data that is mercury saturation, capillary pressure, pore size distribution, SEM image and the porosity and permeability for sample TS1-305. See caption of Figure 3-5 for porosity and permeability uncertainties in plotted values. 94

Figure 3-48: A montage showing the mercury injection data that is mercury saturation, capillary pressure, pore size distribution, SEM image and the porosity and permeability for sample TS4-4. See caption of Figure 3-5 for porosity and permeability uncertainties in plotted values. 95

Figure 3-49: A montage showing the mercury injection data that is mercury saturation, capillary pressure, pore size distribution, SEM image and the porosity and permeability for sample TS4-11. See caption of Figure 3-5 for porosity and permeability uncertainties in plotted values. 96

Figure 3-50: A montage showing the mercury injection data that is mercury saturation, capillary pressure, pore size distribution, SEM image and the porosity and permeability for sample TS5-11. See caption of Figure 3-5 for porosity and permeability uncertainties in plotted values. 97

Figure 3-51: A montage showing the mercury injection data that is mercury saturation, capillary pressure, pore size distribution, SEM image and the porosity and permeability for sample TS1-25. See caption of Figure 3-5 for porosity and permeability uncertainties in plotted values. 98

Figure 3-52: A montage showing the mercury injection data that is mercury saturation, capillary pressure, pore size distribution, SEM image and the porosity and permeability for sample TS2-25. See caption of Figure 3-5 for porosity and permeability uncertainties in plotted values. 99

Figure 3-53: A montage showing the mercury injection data that is mercury saturation, capillary pressure, pore size distribution, SEM image and the porosity and permeability for sample TS3-47. See caption of Figure 3-5 for porosity and permeability uncertainties in plotted values. 100

Figure 3-54: Cross plot of brine permeability (k_w) and absolute gas permeability (k_∞) for tight sandstone samples showing lower brine permeability for all the samples (from Jones and Owen, 1980)..... 102

Figure 3-55: Porosity-permeability plot with colour coding for grain size. See caption of Table 3-1 for grain size definitions. No clear correlation exists between the grain size and the position of samples on porosity-permeability. See caption of Figure 3-5 for porosity and permeability uncertainties in plotted values..... 104

Figure 3-56: Porosity-permeability plot with colour coding for grain sorting. See caption of Table 3-1 for grain sorting definitions. No relationship found between the grain sorting and the position of the samples in the porosity-permeability cross plot. See caption of Figure 3-5 for porosity and permeability uncertainties in plotted values..... 104

Figure 3-57: Mercury injection capillary pressure showing the monomodal for sample TS5-11 indicating the homogeneous pore system from the well sorted grains (blue) and the bimodal curve for TS1-25 indicating heterogeneous pore system resulting from the poorly sorted grains (red)..... 105

Figure 3-58: Pore size distribution derived from MICP showing narrower pore size distribution for sample TS1-305 indicating the homogenous pore system as a result from the well sorted grains (blue) and the broader pore size distribution curve for TS1-197 indicating heterogeneous pore system resulting from the poorly sorted grains (red)..... 106

Figure 3-59: Left: Plot of gas permeability measured at 500 psi net stress against permeability measured at 5000 psi with 1:1 correlation (blue line). Right: Porosity measured at ambient against porosity determined at 5000 psi with 1:1 correlation (blue line). See caption of Figure 3-5 for porosity and permeability uncertainties in plotted values. 108

Figure 3-60: Plot of porosity-permeability with different types of clay present in the samples as indicated by the colours (Red = grain coating illite, Purple = low clay samples and Brown = pore filling clay). See caption of Figure 3-5 for porosity and permeability uncertainties in plotted values. 109

Figure 4-1: A schematic of the Pickett plot used to determine the cementation exponent m as the slop of the porosity vs formation resistivity in log-log scale (from Pickett, 1966). 114

Figure 4-2: Relationship between the cementation exponent (m) and porosity (fraction) based on the Shell formula suggesting that m increases as the porosity decreases (from Neustaedter, 1968). 115

Figure 4-3: Cross plot of the in-situ Archie exponent (m) against in-situ porosity (%) in semi-log graph showing correlation using reduced major axis RMA (red) and linear regression analysis LRA (black) for Mesaverde tight gas sandstones (from Cluff et al., 2009). 116

Figure 4-4: Large errors in water saturation calculation as a result of using wrong values of the cementation exponent m in Archie's law (from Watfa and Nurmi, 1987).	117
Figure 4-5: Effect of the pore geometry (i.e. fractures) in increasing the electrical efficiency of tight rocks despite their low porosity (from Herrick and Kennedy, 1993).	118
Figure 4-6: A schematic demonstrating the higher contribution to the electrical efficiency of fracture (a) that is parallel to the direction of the current flow than the fracture (b) (from Herrick and Kennedy, 1993).	118
Figure 4-7: Effects of the rock properties on ultrasonic P-wave velocity (from Hilterman, 1998).	119
Figure 4-8: P-wave velocity (m/s) and porosity (%) in Fontainebleau sandstone as a function of net stress showing the significant stress-dependent of velocity in comparison to minimum change in porosity as the stress increase (modified from Han, 1986 as cited in Mavko, 2009).	120
Figure 4-9: Measured porosity (fraction) at ambient condition and porosity stress-corrected at 1500 and 5000 psi for group-A samples. See captions of Figure 3-5 and Figure 3-6 for porosity uncertainties in plotted values.	124
Figure 4-10: Helium permeability (mD) measured at the wide range of net stress (500 to 7300 psi) for samples in group A. See captions of Figure 3-5, Figure 3-6 and Figure 3-7 for permeability uncertainties in plotted values.	126
Figure 4-11: Normalized corrected helium permeability mD (Klinkenberg-corrected) for the whole range of net stress used that is low net stress 500 psi to reservoir high net stress 7300 psi for group-A samples. See captions of Figure 3-5, Figure 3-6 and Figure 3-7 for permeability uncertainties in plotted values.	127
Figure 4-12: Gas permeability against reservoir condition net stress in drawdown tests mimicking production scenario with fixed confining stress and decreasing pore pressure for group-A samples. See caption of Figure 3-6 for permeability uncertainties in plotted values.	127
Figure 4-13: Cross plot of corrected measured k_g at in-situ of 5000 psi net stress against corrected k_g measured at 500 psi net stress with 1:1 line (blue) indicating the great reduction in permeability at the high net stress for group-A samples. See captions of Figure 3-5 and Figure 3-6 for permeability uncertainties in plotted values.	128

Figure 4-14: Cross plot of corrected measured k_g at drawdown condition prior to abandonment against corrected k_g measured at 5000 psi net stress with 1:1 line (blue) indicating the less stress sensitivity of permeability measured at 5000 psi compared with the permeability measured at 7000 psi for group-A samples. See caption of Figure 3-6 for permeability uncertainties in plotted values..... 129

Figure 4-15: Gas permeability (Klinkenberg-corrected) (mD) against a wide range of net stress (psi) with the exponential regression fit for sample TS2-6. See captions of Figure 3-5, Figure 3-6 and Figure 3-7 for permeability uncertainties in plotted values. 130

Figure 4-16: An example of permeability measurements (mD) with 10% error bars at a range of equilibration "soaking" time sat different stresses for one of the samples..... 131

Figure 4-17: Correlation of slippage factor b (psi) against corrected permeability (mD). Both slippage factor and permeability are within 10% uncertainty. 132

Figure 4-18: Pore throat size distribution determined from mercury injection capillary pressure for all 15 samples in group-A. 133

Figure 4-19: NMR T_2 distributions for the 15 samples in group A are all less than 10 in μs indicating the dominance of the micro-pores. 134

Figure 4-20: Ultrasonic P-wave velocity (m/s) measured as a function of confining stress (psi) showing an increase in P-wave as the confining stress increases for group-A samples. 135

Figure 4-21: Normalized ultrasonic ($P\text{-wave}_{\text{stress}}/P\text{-wave}_{1000\text{psi}}$) for samples in group A. Samples TS2-3 and TS2-4 show steeper slopes indicating greater stress sensitivity compared to the remaining samples..... 135

Figure 4-22: Plot of the ultrasonic velocity P-wave (m/s) at 1000 psi against the porosity (fraction) stress-corrected to 1500 psi for group-A samples. See captions of Figure 3-5 and Figure 3-6 for porosity uncertainties in plotted values..... 136

Figure 4-23: Plot of the ultrasonic velocity P-wave (m/s) at 5000 psi against the porosity (fraction) stress-corrected to 5000 psi for samples in group A. See captions of Figure 3-5 and Figure 3-6 for porosity uncertainties in plotted values..... 137

Figure 4-24: Calculated resistivity (ohm-m) with $\pm 2\%$ uncertainties of the five samples in group A saturated with simulated brine (corrected at 25° C) under confining stress 1500, 3000 and 5000 psi..... 138

Figure 4-25: Normalized resistivity (corrected at 25° C) of the five samples in group A under 1500, 3000 and 5000 psi confining stress..... 139

Figure 4-26: Changes of formation resistivity factor FRF and porosity (fraction) as a function of stress increase (1500, 3000 and 5000 psi) for the five samples in group A. See captions of Figure 3-5, Figure 3-6 and Figure 4-24 for porosity and resistivity uncertainties in plotted values. ... 139

Figure 4-27: Calculated cementation exponent (m) plotted against measured porosity (fraction) under 1500 psi, in comparison with the two models presented by Cluff et al. (2009). See captions of Figure 3-5, Figure 3-6 and Figure 4-24 for porosity and resistivity uncertainties in plotted values..... 141

Figure 4-28: Diagram showing the relationship derived between the cementation exponent (m) and porosity (fraction) for the TS samples in group A. Note the exponent decreases as the porosity decreases in contrast to the Shell formula. 143

Figure 4-29: Cementation exponent m at 1500 psi against porosity (fraction) at 1500 psi for group-A samples in comparison with the fracture model. See captions of Figure 3-5, Figure 3-6 and Figure 4-24 for porosity and resistivity uncertainties in plotted values..... 144

Figure 4-30: Comparison of measured formation resistivity (FRF) at 1500 psi and calculated FRF using constant values of m , against 1500 psi stress-corrected porosity (fraction) in Pickett log-log plot for group-A samples. See captions of Figure 3-5, Figure 3-6 and Figure 4-24 for porosity and resistivity uncertainties in plotted values..... 145

Figure 4-31: Plot of the ultrasonic velocity P-wave (m/s) at 5000 psi against the porosity (fraction) stress-corrected to 5000 psi with colour coding corresponding to clay content in percentage for group-A samples. See caption of Figure 3-6 for porosity uncertainties in plotted values. 148

Figure 4-32: Comparison between normalized electrical conductivity (inverse of electrical resistivity) and normalized gas permeability (k_g) against confining net stress (psi) for the five samples showing higher stress dependency of permeability in group A. See captions of Figure 3-6, Figure 3-7 and Figure 4-24 for permeability and resistivity uncertainties in plotted values..... 151

Figure 4-33: Left: Plot of formation resistivity factor FRF against P-wave velocity (m/s) at low stress showing an exponential relationship with a correlation coefficient of 0.94. Right: Similar plot at 5000 psi showing an exponential relationship with less correlation coefficient 0.8..... 152

Figure 4-34: Plots of gas permeability k_g (mD) against P-wave velocity (m/s) at low net stress (left) and at in-situ stress of 5000 psi (right) for group-A samples. Both plots show no clear correlation..... 153

Figure 5-1: Schematic showing lithostatic pressure and fluid pressure that is often in between the lithostatic pressure and hydrostatic pressure (from Tiab and Donaldson, 2012)..... 157

Figure 5-2: An example of helium permeability measurements (mD) with 10% uncertainty against net stress (psi) during loading and unloading cycles performed prior to conducting the effective stress law measurements for sample TS7-4..... 163

Figure 5-3: Changing the confining pressure and pore pressure in steps during permeability measurements with several hours equilibrium after each confining or pore pressure change. The whole set of measurements takes 2 to 3 days..... 164

Figure 5-4: Helium permeability reduction ($\pm 10\%$ uncertainty) with increasing confining stress and different constant pore pressures for sample TS7-1..... 168

Figure 5-5: Helium permeability increases ($\pm 10\%$ uncertainty) due to the increase in pore pressure with different constant confining stresses for sample TS7-1..... 168

Figure 5-6: Measured helium permeability (mD) with $\pm 10\%$ uncertainty plotted against the simple effective stress that is $C_p - P_p$ (psi) for the five samples in group B. Black arrows indicate the direction of the pressure increase. 169

Figure 5-7: Best fitting of permeability (mD) vs modified effective stress (psi) with best effective-stress coefficient for permeability ($C_p - \chi P_p$) for the five samples in group B. 170

Figure 5-8: Helium permeability (mD) ($\pm 10\%$ uncertainty) of TS5-2 plotted against effective stress in power function with different coefficients (0.2, 0.4, 0.6, 0.8, and 1). $\chi = 0.8$ showed the best fit..... 171

Figure 5-9: Calculated permeability from the power law model (black circles) with helium permeability measured under low net stresses (blue) and higher in-situ net stresses (red) for sample TS5-2 with $\pm 10\%$ uncertainty..... 173

Figure 5-10: Effective stress coefficients reported from literature against their permeability measured (with 10% experimental error) at different net stresses (blue) (Keaney et al., 2004; Li et al., 2009; Qiao et al., 2012; Li et al., 2014) with coefficients determined for the TS samples in group B (orange). 175

Figure 5-11: Left: Simplified pore model developed by Zoback and Byerlee (1975) for $\chi > 1$ with low compressible quartz frame (black) and high compressible clay (grey) lining the pore walls shown in white. Right: Model proposed by Kwon et al (2001) for $\chi < 1$ with low compressible quartz shown in black and more compressible clay as connected matrix in grey. C_p is confining pressure (from Heller et al., 2014). 177

Figure 5-12: SEM image showing the clay surrounded by stiffer quartz grains with pore space at the center of the clay (black) with micropores and micro fluid paths (red) through which the gas penetrate the clay in sample TS5-5..... 178

Figure 5-13: Clay particle model showing the clay tangentially connected to the pore wall that is surrounded by the stiffer quartz (from Al-Wardy and Zimmerman, 2004). 179

Figure 5-14: SEM image showing the clay (red) with micropores (black) surrounded by stiffer quartz grains. Micropores of the clay particles (black) through which the gas penetrates the clay in sample TS7-1.	179
Figure 5-15: Plot of the dynamic bulk modulus K_{dyn} calculated from density and velocity at 1000 and 5000 psi ($\pm 5\%$ uncertainty) against static bulk modulus K_{stat} estimated using a correlation from tight sandstone in the Travis Peak formation for group-B samples with 1:1 line (black) (from Jizba, 1992).	182
Figure 5-16: Plot showing the difference between the dynamic dry modulus against the static dry modulus of North Sea chalk with higher differences in the fractured samples (from Oslen and Fabricius, 2006). ...	182
Figure 5-17: Increase in stress in the axial horizontal direction normal to the crack surfaces illustrates the closure of the crack with first image from left shows atmospheric pressure and the second and third show the closure of the opening as the stress increases to 1500 psi and 4500 psi respectively (from Batzle et al., 1980).	185
Figure 5-18: Comparison of pore pressure drop effect on permeability (with 10% uncertainty) due to production in a tight gas sandstone reservoir using Terzaghi net stress ($\chi = 1$) (black) and determined effective stress law ($\chi < 1$) (blue) for sample TS5-2.	186
Figure 5-19: 3-Points model (blue curve) using only 3 permeability measurements (blue points) in comparison with the original 12-points model (black curve). 3-points model also correlate well with permeability measurements under low effective stress (purple points) and higher effective stress (red points).	188
Figure 5-20: Klinkenberg corrected permeability (10% experimental error) plot for sample TS7-5 under confining stress of 6000 psi and reciprocals of pore pressures of 2000, 3000 and 4000 psi.	189
Figure 6-1: Geological structure with a minimum hydrocarbon height above free water level of rocks with different properties (from Arps, 1964).	194
Figure 6-2: Mercury injection capillary pressure curve in a semi-log graph showing the difference between the entry pressure (P_e) and the displacement pressure (P_d) (from Jennings, 1987).	196
Figure 6-3: Mercury injection capillary pressure curve showing the displacement pressure at 10% mercury saturation as defined by Schowalter (1979), and the threshold pressure at the inflection point as defined by Katz and Thomson (1987) (from Pittman, 1992).	197
Figure 6-4: Different pore throat sizes of a tight gas sandstone sample defined by the relationship between P_c and Hg-saturation using various methods (from Comisky et al., 2007).	198
Figure 6-5: Thomeer parameters (extrapolated displacement pressure, bulk volume occupied by mercury at infinite pressure and the pore geometrical factor) defining the shape of the hyperbola representing the mercury injection capillary pressure curve (from Thomeer, 1960).	200

Figure 6-6: Thomeer hyperbola showing different pore geometrical factors (G) (from Thomeer, 1960).....	201
Figure 6-7: MICP curve with plateau for a porous permeable sample (left) in comparison with a less porous less permeable sample with no plateau (right) (from Schowalter, 1979).....	202
Figure 6-8: Log-log plot of capillary pressure against Hg saturation following Thomeer's method (1960) with a 45° tangent line to determine the apex Swanson (1981) (from Pittman, 1992).....	203
Figure 6-9: Capillary pressure (psi) against water saturation percentage data combined from porous plate PP (the lower part) and vapour desorption VD (the upper part) for the nine samples in group C.	206
Figure 6-10: Water saturation S_w (%) against cumulative equilibration time (days) at 1660 psi capillary pressure in the vapour desorption chamber for group-C samples.	208
Figure 6-11: Water saturation S_w (%) against cumulative equilibration time (days) at 3236 psi capillary pressure in the vapour desorption chamber for group-C samples.	208
Figure 6-12: Water saturation S_w (%) against cumulative equilibration time (days) at 4443 psi capillary pressure in the vapour desorption chamber for group-C samples.	209
Figure 6-13: Water saturation S_w (%) against cumulative square root of equilibration time (days) ^{1/2} for all the capillary pressures 1660, 3236 and 4443 psi in the vapour desorption chamber for group-C samples.....	210
Figure 6-14: NMR normalized signal for sample TS4-11 showing different T_2 time in ms with different water saturations at different capillary pressures using PP and VD. Water trap in large pores after drainage process at high capillary pressures (red).	211
Figure 6-15: NMR cumulative signal for sample TS4-11 with different water saturations at different capillary pressures using PP and VD (lower value of T_2 indicates less water in the sample).	211
Figure 6-16: Normalized pore throat size distribution showing the pore throat radius in μm for group-C samples.....	213
Figure 6-17: Mercury injection capillary pressure curves showing mercury saturation (%) versus capillary pressure (psi) for group-C samples.....	213
Figure 6-18: Capillary pressure curves showing mercury saturation (fraction) versus capillary pressure (psi) obtained using PUCS under stress in comparison with the standard MICP for sample TS2-4	214
Figure 6-19: Pore diameter (μm) distribution obtained from PUCS under confining stress compared with distribution obtained from the standard MICP for sample TS2-4.	215

Figure 6-20: Measured gas permeability at 500 psi ($\pm 10\%$ uncertainty) against estimated permeability from MICP using Purcell and Swanson models for group-A samples.	216
Figure 6-21: Measured gas permeability at 500 psi ($\pm 10\%$ uncertainty) against estimated permeability from MICP using Winland and Thomeer models for group-A samples.	216
Figure 6-22: Comparison of water saturations determined from porous plate (PP) at 35 psi against the water saturations determined from the converted MICP at equivalent capillary pressure for group-C samples with 1:1 correlation (red line). All within ± 1 to 5% uncertainties.	217
Figure 6-23: Comparison of water saturations determined from porous plate (PP) at 75 psi against the water saturations determined from the converted MICP at equivalent capillary pressure for group-C samples with 1:1 correlation (red line). All within ± 1 to 5% uncertainties.	218
Figure 6-24: Comparison of water saturations determined from porous plate (PP) at 130 psi against the water saturations determined from the converted MICP at equivalent capillary pressure for group-C samples with 1:1 correlation (red line). All within ± 1 to 5% uncertainties.	218
Figure 6-25: Comparison of water saturations determined from vapour desorption (VD) at 1660 psi against the water saturations determined from the converted MICP at equivalent capillary pressure for group-C samples with 1:1 correlation (red line). All within ± 1 to 5% uncertainties.	219
Figure 6-26: Comparison of water saturations determined from vapour desorption (VD) at 3236 psi against the water saturations determined from the converted MICP at equivalent capillary pressure for group-C samples with 1:1 correlation (red line). All within ± 1 to 5% uncertainties.	220
Figure 6-27: Comparison of water saturations determined from vapour desorption (VD) at 4443 psi against the water saturations determined from the converted MICP at equivalent capillary pressure for group-C samples with 1:1 correlation (red line). All within ± 1 to 5% uncertainties.	220
Figure 6-28: Top: Capillary pressure (psi) plotted against water saturation S_w (%) obtained from MICP and converted to air-brine system (red) in comparison with capillary pressure determined from the combined porous plate PP (blue) and vapour desorption VD (green). Bottom: Same capillary pressure curves in semi-log plots for samples TS1-55, TS1-197 and TS1-305.	222

Figure 6-29: Top: Capillary pressure (psi) plotted against water saturation S_w (%) obtained from MICP and converted to air-brine system (red) in comparison with capillary pressure determined from the combined porous plate PP (blue) and vapour desorption VD (green). Bottom: Same capillary pressure curves in semi-log plots for samples TS4-4, TS4-11 and TS5-11. 223

Figure 6-30: Top: Capillary pressure (psi) plotted against water saturation S_w (%) obtained from MICP and converted to air-brine system (red) in comparison with capillary pressure determined from the combined porous plate PP (blue) and vapour desorption VD (green). Bottom: Same capillary pressure curves in semi-log plots for samples TS1-25, TS2-25 and TS3-47. 224

Figure 6-31: Schematic diagram showing the increase of the non-wetting phase saturation as a result of drainage process causes the discontinuity of the irreducible wetting phase (from Newsham et al., 2003)..... 226

Figure 6-32: Left: Smooth surface of a glass bead with disconnected craters (from Dullien et al., 1986). Right: Roughness of pore surface (yellow) and presence of connected micro-channels (red) through the sample TS4-4. 228

Figure 6-33: Schematic diagram of the triangular pore model at fully saturated stage (A) and at threshold capillary pressure (B) and high capillary pressure (C) (from Grattoni et al., 2003)..... 229

Figure 6-34: Comparison of gas permeability measured at 500 psi ($\pm 10\%$ uncertainty) and permeability at threshold pressure ($\pm 10\%$ uncertainty) of each sample in group A plotted against permeability estimated from MICP using Swanson model. 230

Figure 6-35: Permeability measured at 5000 psi stress plotted against predicted permeability using Katz and Thomson model from stressed MICP (left) and standard MICP (right). 231

1 Introduction

The global demand for gas has grown dramatically with the world natural gas consumption predicted to increase from 113 trillion cubic feet (TCF) in 2010 to 185 TCF in 2040 (US Energy Information Administration [EIA], 2016). Exploration for petroleum in the more complex unconventional reservoirs such as tight sandstones, coal beds and shales, has been dramatically increased as demand has risen and the easily produced conventional reservoirs have been depleted. Development of unconventional reservoirs began in North America but has recently expanded to places such as China, India, several European countries as well as Middle East and North Africa (Law and Curtis, 2002; Dong et al., 2012). Even though the unconventional resources are more complex to extract, they are more abundant than conventional resources (Figure 1-1). Unconventional gas resources are predicted to be the dominant source of natural gas in the United States until 2040 with tight gas reservoirs contributing approximately 20% of the total (Figure 1-2).

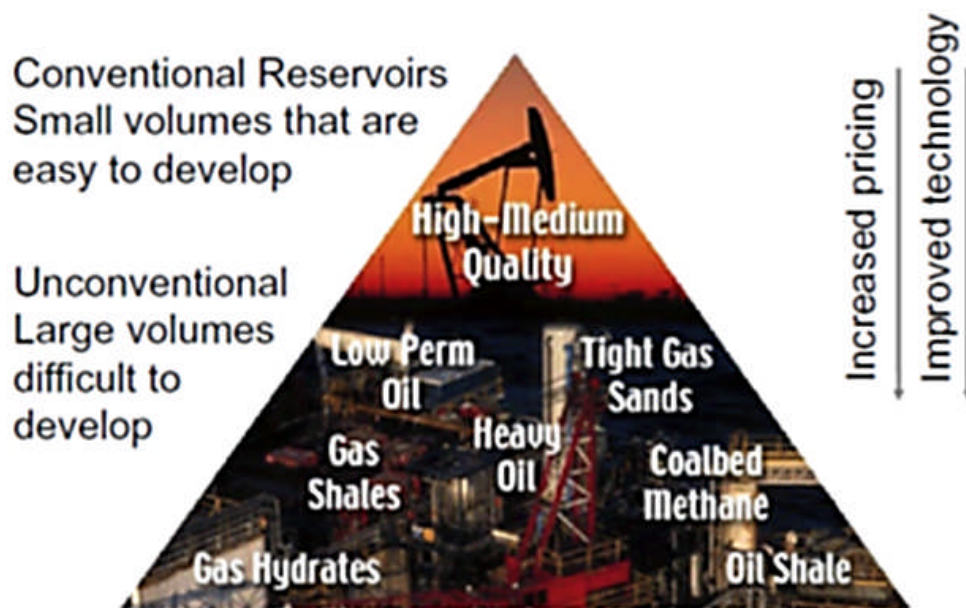


Figure 1-1: Resource triangle for natural gas (from Holditch, 2013).

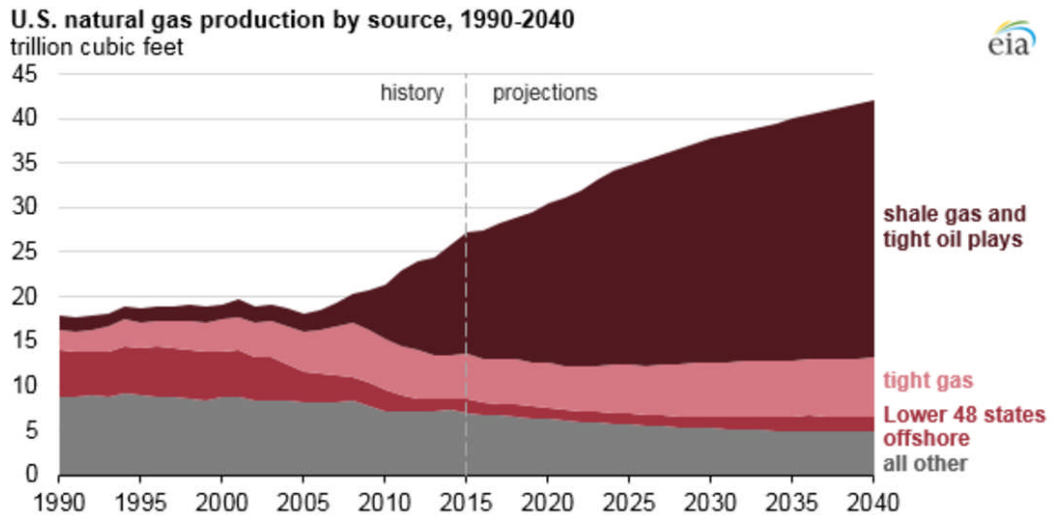


Figure 1-2: Prediction of unconventional gas resources to be the dominant source of natural gas in US with tight gas contributing approximately 20% (from EIA, 2016).

Estimating the amount of hydrocarbons present in the subsurface is a goal during the economic appraisal of potential oil and gas prospects. The volume of original gas in place, *OGIP*, can be calculated using Equation 1-1. It requires the knowledge of the gross rock volume between the top and the base of the reservoir, the rock storage capacity and the fraction of it that is filled with hydrocarbon “saturation”. The volume of the reservoir rock can be determined as the product of the reservoir area, *A*, and its thickness, *h*. The reservoir area is estimated from seismic data and often calibrated with data acquired from wells that are drilled at the exploration stage. The thickness is determined from lithological interpretation of wireline logs that are acquired from the exploration wells. The rock storage capacity “porosity” is determined from core samples or from wireline logs e.g. density-neutron measurements. The saturation can be derived from the electrical properties that are obtained from wireline logs. However, the rate at which the hydrocarbons can flow into the wellbore is another crucial parameter that is not used in the *OGIP* calculation. This parameter is referred to as permeability, and it is required to evaluate the rate at which hydrocarbons can be extracted. Permeability cannot be measured directly from wireline logs, but rather from core samples. Overall, accurate characterization of these key reservoir parameters is required for an effective appraisal of tight reservoirs (Newsham et al., 2002).

Equation 1-1

$$OGIP = \frac{43560 A h \phi (S_h)}{B_g}$$

where:

$OGIP$ = original gas in place (ft³)

43560 = conversion factor from acre-ft to ft³

A = area of reservoir (acres)

h = height or thickness of pay zone (ft)

ϕ = porosity (fraction)

S_h = hydrocarbon saturation (fraction)

B_g = formation volume factor for gas (reservoir ft³/scf)

Several factors can affect the porosity, fluid saturation and permeability of a reservoir, and hence affect the volume of the hydrocarbons and its producibility. Sandstone reservoirs are composed of different sizes of sand grains that have been deposited and buried through time. The porosity and permeability as well as saturation depend on the grain size, shape and sorting as well as how deep they are buried. Deep burial results in more compaction and cementation of the rock, which reduces both porosity and permeability and affects the fluid distribution. The deeper the rock is buried means the greater the impact on the properties. This explains why conventional “porous and permeable” reservoirs are often found at shallower depths compared with tight reservoirs “less porous and less permeable” that are found at greater depths.

Tight gas sandstone (TGS) reservoirs are more complex in the pore distribution and fluid saturation than conventional reservoirs that usually have uniform fluid (oil, gas and water) saturations. Fluid saturations in tight reservoirs vary greatly with the majority of hydrocarbons accumulations being in small pores with low to very low permeability (Zou et al., 2013). Flow rate analysis in TGS requires long-term testing due to their low permeability, and production from such tight reservoirs is often only marginally profitable. Large cost reductions can be achieved by identifying intervals with relatively higher porosity and permeability (Law, 2002), which are often referred to as ‘sweet spots’. This challenge requires advanced petrophysical analysis and obtaining a comprehensive understanding of the controls on the key petrophysical

properties of the reservoir such as porosity, permeability, and electrical resistivity that is a function of saturation (Holditch, 2006, 2013). Characterisation of unconventional reservoirs requires integration of all geological and engineering data. Drilling more wells and utilising the latest drilling technology such as horizontal drilling and hydraulic fracturing are the keys for developing the TGS reservoirs (Zee Ma, 2016).

The key problem with tight gas sandstones is that their petrophysical properties (e.g. porosity, permeability as well as electrical and elastic properties) vary significantly depending upon the stress and pore pressure conditions under which they are measured (Jones and Owens, 1980; Luffel et al., 1991; Holditch, 2006; Cluff et al., 2009; Smith et al., 2009; Smith et al., 2010; Lopez et al., 2016). Rock samples that are extracted through drilling and coring from deep reservoirs are exposed to significant changes in stress both during drilling and when they are brought to the surface; this could disturb their microstructures and hence their petrophysical properties. Hence the petrophysical properties measured in the laboratory may be significantly different to those of *in-situ* samples. This increases uncertainties regarding any volumetric or flow calculations that are made based on the results of core analyses.

This thesis analyses the stress dependencies of petrophysical properties of tight gas sandstone samples and the impact of the stress change on the fluid saturation and flow rate estimation. This is achieved by conducting petrophysical measurements such as porosity, permeability, electrical properties and ultrasonic velocity under ranges of net stresses. Permeability measurements under reservoir conditions that are likely to be experienced during production are also conducted; these are referred to as drawdown experiments. Time required for the samples to reach equilibrium prior to petrophysical measurements is called equilibration time, which is investigated by analysing measurements of a property after different periods of equilibration time. The impact of microstructures on such measurements is also investigated by analysing images obtained by scanning electron microscopy (SEM) and mineralogy of the samples. In addition, fluid saturations and the pore network of every sample obtained from capillary pressure data coupled with nuclear magnetic resonance technique is analysed.

This chapter presents background about the petrophysical properties of the reservoir rocks, and the commonly used techniques to measure and analyse such properties. Previous work is also reviewed in this chapter, with detailed literature review is discussed in each chapter. Depositional and diagenetic controls on porosity and permeability are discussed. Finally, the aim and the objectives of the thesis as well as the thesis outline are presented.

1.1 Background

Reservoir sandstone is composed of grains (minerals) that had been deposited and then buried over time. The pore space between grains contains fluids such as water and hydrocarbons. Petrophysics is the study of the physical properties of rocks and their interactions with the fluids they contain (Tiab and Donaldson, 2012). Reservoir rocks are examined and characterised based on their petrophysical properties: porosity, permeability and saturation. Porosity is the physical property that determines the volume of the pore spaces between the grains and thus how much fluid the rock can store. Permeability is a measure of the ease of the fluids stored in the rock to flow under lamina flow conditions; it determines the rate that the fluids can be extracted from the rock. Fluid flows through the rock due to differences in hydraulic potential or gravity and it is measured in relation to time. Saturation is the property that defines the proportion of different fluids stored in the rock (i.e. water, gas or oil); it is usually expressed as the pore volume filled by a particular fluid divided by the total pore volume. Generally, the volume of water in the reservoir is determined from electrical measurements, and petroleum is assumed to fill the remaining pore volume.

1.1.1 Porosity

Porosity, ϕ , is defined as the ratio of the pore spaces that are between the grains to the bulk volume of the rock that is the volume of the grains and the pore spaces (Hook, 2003). Porosity is divided into two categories, namely effective and total, based on the connectivity of the pore spaces. Effective porosity refers to the interconnected pore spaces, which is generally used in the reservoir engineering calculations, where the remaining isolated pore spaces are non-effective. The sum of the effective and isolated porosity is the total porosity, which is also referred to as the absolute porosity. Porosity can be measured from core taken from the wellbore or determined from the

wireline logs that are run into the borehole. Plugs are samples cut from cores, and measurement of porosity from core plug samples is conducted in petrophysical laboratories using devices such as pycnometers, which are used to measure the grain volume of the core plug. The pore volume is the difference between the measured bulk volume of the core plug and the determined grain volume. Porosity is then calculated using Equation 1-2.

Equation 1-2

$$\phi = \frac{B_v - G_v}{B_v}$$

where:

ϕ = porosity (in fraction)

B_v = bulk volume of the plug

G_v = grain volume

1.1.2 Permeability

Darcy (1855) conducted experiments in which he flowed water under the influence of gravity through a vertical pack of sand put inside an iron cylinder (Figure 1-3). He developed an empirical relationship to calculate permeability (Equation 1-3), which relates the fluid flow rates to the change in hydraulic potential. The most commonly used permeability unit is the Darcy, D . A rock with 1 D permeability, a length of 1 cm and a cross sectional area of 1 cm² will allow a fluid of viscosity of 1 cp to flow at a rate of 1 cm³/s under a hydraulic potential of 1 atm (Figure 1-4).

Equation 1-3

$$q = kA \frac{\Delta P}{\mu l}$$

where:

q = water flow rate (cm³/s)

k = constant of proportionality that is characteristic of the sand (D)

A = cross sectional area of the sand pack (cm²)

ΔP = difference in pressure across the sample (atm)

l = length (cm)

μ = viscosity (cp)

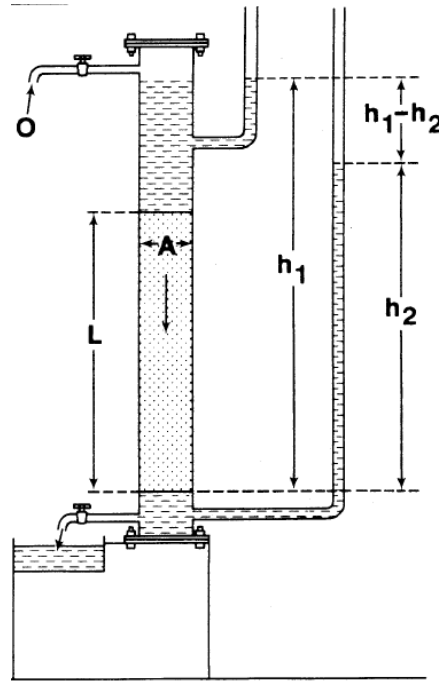


Figure 1-3: Apparatus used by Darcy for determining permeability by flowing water through a vertical pack of sand inside an iron cylinder (from Hubert, 1953).

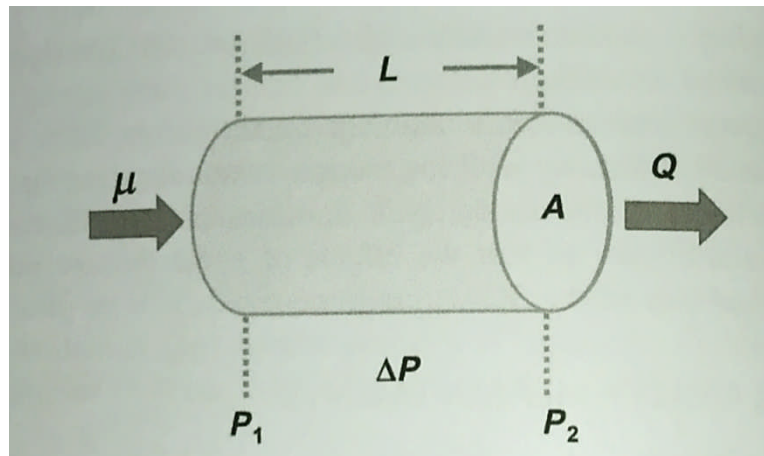


Figure 1-4: Diagram for the definition of permeability based on Darcy's law (from McPhee et al., 2015).

Permeability depends on the interconnected porosity and it is affected by the grain size and shape, degree of grain sorting in addition to the degree of cementation and compaction (Tiab and Donaldson, 2012). Thus, a rock with no porosity has no permeability, which is often referred to as "impermeable". Permeability of a core plug can be determined in the laboratory using permeameters that measure flow rates which are then used to calculate the permeability based on Darcy's law (Equation 1-3). Darcy's law is valid for incompressible fluids such as water. On the other hand, gas flow through a porous rock can result in an apparent permeability that is higher than the

true permeability due to gas molecules interacting with the pore walls; this is known as the slippage effect. Gas flows in porous media differently than liquid specifically under low pore pressure where the gas undergoes the influence of slip flow in addition to the Darcy flow (Klinkenberg, 1941).

Gas slippage is referred to the state where the gas molecules slip on the solid surface when the mean free path of the gas molecules is not negligible compared to the pore throat radius (Klinkenberg, 1941). Klinkenberg (1941) derived an expression to account for the gas slippage and to calculate the absolute permeability from the measured gas permeability. It was observed that measured or apparent permeability was inversely proportional to the mean pore pressure as expressed in Equation 1-4, which is used to determine the absolute “corrected” permeability.

Equation 1-4

$$k_g = k_l * \left(1 + \frac{b}{P}\right)$$

where:

k_g = gas permeability at pore pressure (mD)

k_l = absolute permeability (often referred to as liquid permeability)(mD)

b = gas slippage factor (atm)

P = pore pressure (atm)

Klinkenberg (1941) also derived an expression to determine the gas slippage factor, b , as a function of the gas properties, pore throat radius and the mean free path of the molecules under a mean pore pressure (Equation 1-5). Since the gas flow in porous media is controlled by the pore throat radii, gas slippage depends on the pore geometry and therefore its effect is more significant in tight gas sandstones (Davies and Davies 2001; Rushing et al., 2004).

Equation 1-5

$$b = \frac{4 k_l L P}{r}$$

where:

L = mean free path of gas molecule at pore pressure P

r = pore radius

The value of slippage factor, b , varies from one rock sample to another as it is a function of the pore radius distribution (Byrnes, 2005). An empirical correlation for air was presented by Heid et al. (1950) and another one was presented by Jones and Owens (1980) to estimate the general values for b in the Klinkenberg equation, (Equation 1-6) and (Equation 1-7) respectively.

Equation 1-6

$$b = 0.777 k_l^{-0.39}$$

Equation 1-7

$$b = 0.867 k_l^{-0.33}$$

1.1.3 Saturation

Electrical resistivity is one of the most important petrophysical properties of the reservoirs used to estimate the hydrocarbon saturation. Water saturation, S_w , which is referred to the fraction of the pore volume occupied with water, is determined using Archie's law (1942) (Equation 1-12), and thus the hydrocarbon saturation fraction, S_h , filling the remaining pore space is calculated as $S_h = 1 - S_w$.

Archie (1942) conducted laboratory studies and found that formation resistivity factor (FRF), also referred to as F , of a clay-free water filled rock is a constant defined by the ratio of the resistivity of the rock to the resistivity of the water (Equation 1-8). Archie also found that F varied with porosity of the rock as well as the tortuosity of the fluid path ways, a , and the degree of cementation, m , (Equation 1-9). Values of 1 and 2 were used by Archie for the tortuosity and cementation exponents, respectively.

Equation 1-8

$$F = \frac{R_0}{R_w}$$

Equation 1-9

$$F = \frac{a}{\phi^m}$$

where:

F = formation resistivity factor

R_0 = resistivity of the rock when fully saturated with water (ohm-m)

R_w = resistivity of the water (ohm-m)

a = tortuosity exponent

ϕ = porosity in fraction

m = cementation exponent

Archie (1942) also examined rocks filled with both water and hydrocarbon, and he defined the formation resistivity index, I , (Equation 1-10). He related the water saturation to the formation resistivity index by introducing the saturation exponent, n , (Equation 1-11).

Equation 1-10

$$I = \frac{R_t}{R_0}$$

Equation 1-11

$$S_w = \left(\frac{1}{I}\right)^{(1/n)}$$

where:

S_w = water saturation

I = formation resistivity index

R_t = true resistivity of formation containing hydrocarbon and water (ohm-m)

n = saturation exponent

Archie (1942) rearranged these four equations to introduce Equation 1-12, which is commonly used in the oil industry to calculate the water saturation. The resistivity and porosity values obtained either from wireline log measurements, or from core measurements in the laboratory. Archie's exponents, a and m and n , are also determined in the laboratory.

Equation 1-12

$$S_w = \left(\frac{R_0}{\phi^m R_t}\right)^{1/n}$$

1.1.4 Capillary pressure

Capillary pressure is defined as the difference in pressure across the interface between two immiscible fluids, the wetting phase and the non-wetting phase (Pickell et al., 1966). In gas reservoirs, brine is commonly the wetting fluid while gas is non-wetting.

Washburn (1921) was the first to suggest using the mercury injection technique to determine the pore size distribution in a porous medium (Equation 1-13). The capillary pressure required for a non-wetting fluid to pass through a pore throat is a function of the pore throat radius, the interfacial tension between petroleum and water as well as the three phase contact angle between the rock, brine and petroleum (Schowalter, 1979). Capillary pressure data can be obtained through several techniques, namely porous plate, centrifuge, vapour sorption as well as the mercury injection porosimetry. The fact that pore throat radius also controls single phase flow means that capillary pressure data has the potential to be used to calculate permeability. Capillary pressure data can also be used to estimate subsurface gas saturations if information is also available on the phase densities and the free water level of the reservoir (Schowalter, 1979).

Equation 1-13

$$r = \frac{2\sigma \cos \theta}{P}$$

where:

P = applied pressure (psi) (equivalent to the displacement pressure)

r = pore radius (μm)

σ = Hg-air surface tension (480 dynes/cm)

θ = Hg-air-rock contact angle (140°)

Purcell (1949) used the mercury injection technique to find the relationship between the volume of mercury injected and the capillary pressure curve for rock samples, which is known as the drainage process. Hydrocarbon migrating into the reservoir and displacing the initial water in-place is an example of the drainage process (Figure 1-5). Later, others examined the reverse, known as imbibition process, by reducing the injection pressure resulting in mercury withdrawal (Pickell et al., 1966; Wardlaw and Taylor, 1976). Newsham (1977) presented capillary pressure curves for different sandstone samples with different clay types to show the effect of clay on the shape of the curves (Figure 1-6).

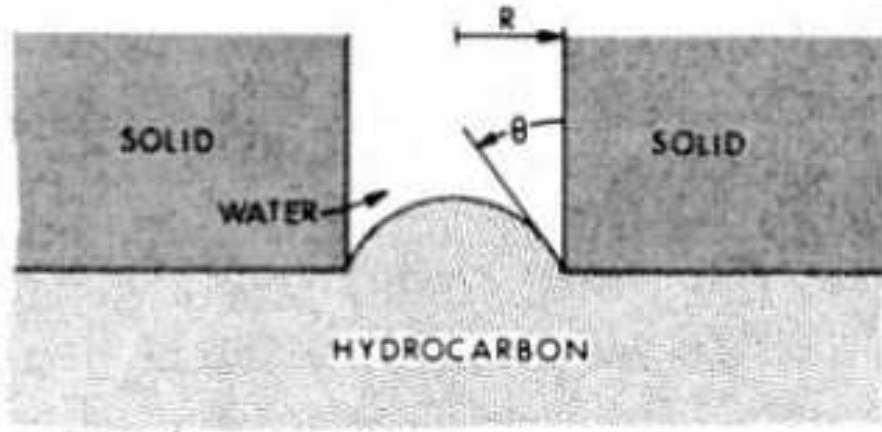


Figure 1-5: Diagram showing the drainage process that is the displacement capillary pressure for hydrocarbon as it migrates into the reservoir and displaces the initial water in the reservoir (from Schowalter, 1979).

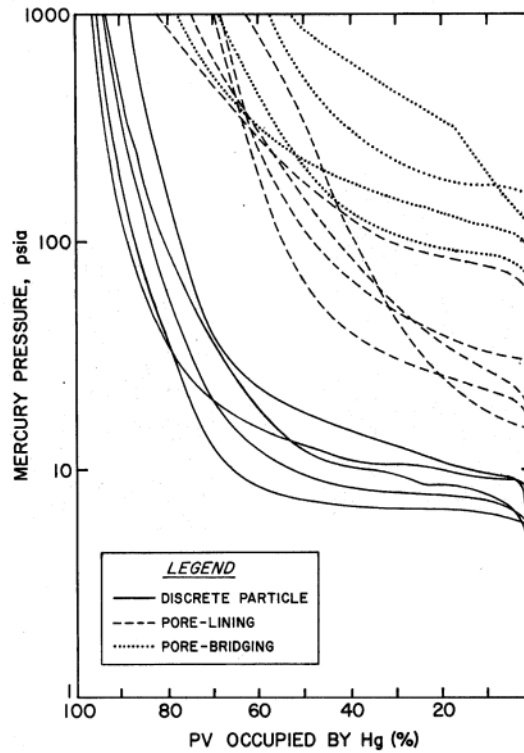


Figure 1-6: Capillary pressure curves for different sandstone samples with different clay types plotted as mercury pressure against Pore Volume (PV) occupied by mercury (%) (from Newsham, 1977).

1.1.5 Depositional controls on porosity and permeability

Porosity of freshly deposited sand depends on the grain packing arrangement and grain sorting rather than the grain size. Graton and Fraser (1935) showed that packing of uniform spheres in a cubic or wide-packing system would have a porosity of 47.6% while a rhombohedral or close-packing system would have approximately 26% porosity

(Figure 1-7). However, such packing systems are idealistic and sediments are never deposited in such perfect arrangements and often have a wide range of grain-sizes; hence petroleum reservoirs have a range of porosity between 5% and 40% but most frequently in the range of 10% and 20% (Tiab and Donaldson, 2012).

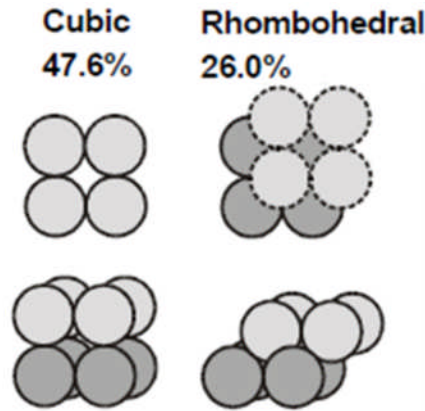


Figure 1-7: Porosity of different packing systems of uniform spheres (left) 47.6% for a cubic system and (right) 26% for a rhombohedral system (modified from Glover, 2016).

Sorting and packing depend on the degrees of roundness and sphericity of the grains as well as their grain-size distribution. Roundness describes the roughness of the grain, and it ranges from well rounded to very angular, while sphericity is related to the dimensions of the grain with reference to an equidimensional sphere (Figure 1-8). Sediments, resulting from the uplift and the exposure of bedrock, experience erosional processes during transport and deposition (Figure 1-9), which in turn affect the geometry and smoothness of the grains.

	Well rounded	Rounded	Subrounded	Subangular	Angular	Very angular
Low sphericity						
High sphericity						

Figure 1-8: Degrees of roundness and sphericity of grains based on the erosional processes during transport and deposition (from Pettijhon et al., 1987).

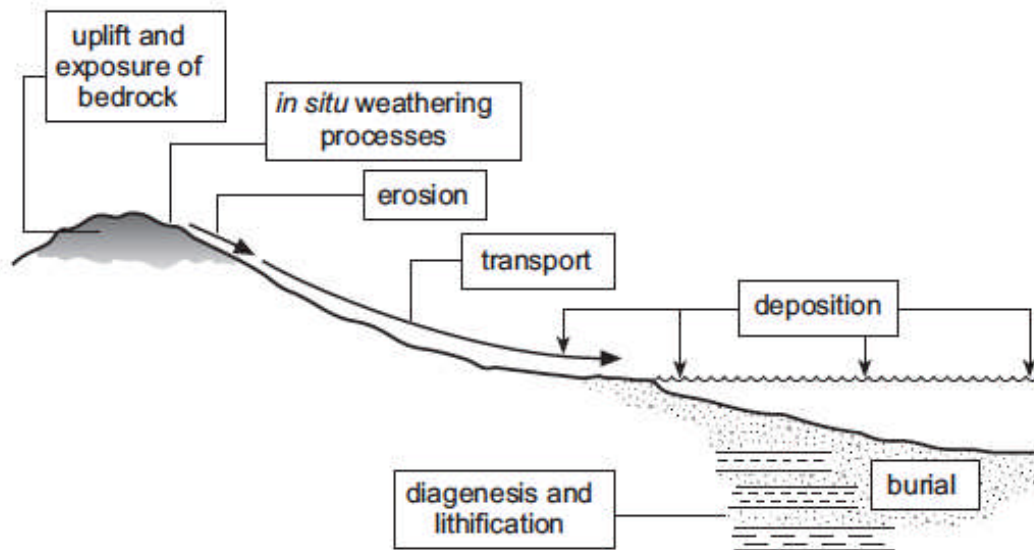


Figure 1-9: Erosional processes which sediments go through during transport and deposition that affect the geometry and smoothness of the grains (from Nichols, 2009).

Grain sorting is referred to the uniformity or the gradation of the grains in the rock. The porosity will significantly decrease if small grains like silt or clay are mixed with larger sand grains. Revil et al. (2002) provided a theoretical model that shows the impact of the sand to clay ratios on the porosity of the sediment (Figure 1-10). It is shown that porosity of well sorted clean sand with no clay content is 40% and the porosity of pure shale with no sand grains is 60%, while a mix of 60% sand and 40% shale would have a porosity of 24% (Revil et al., 2002).

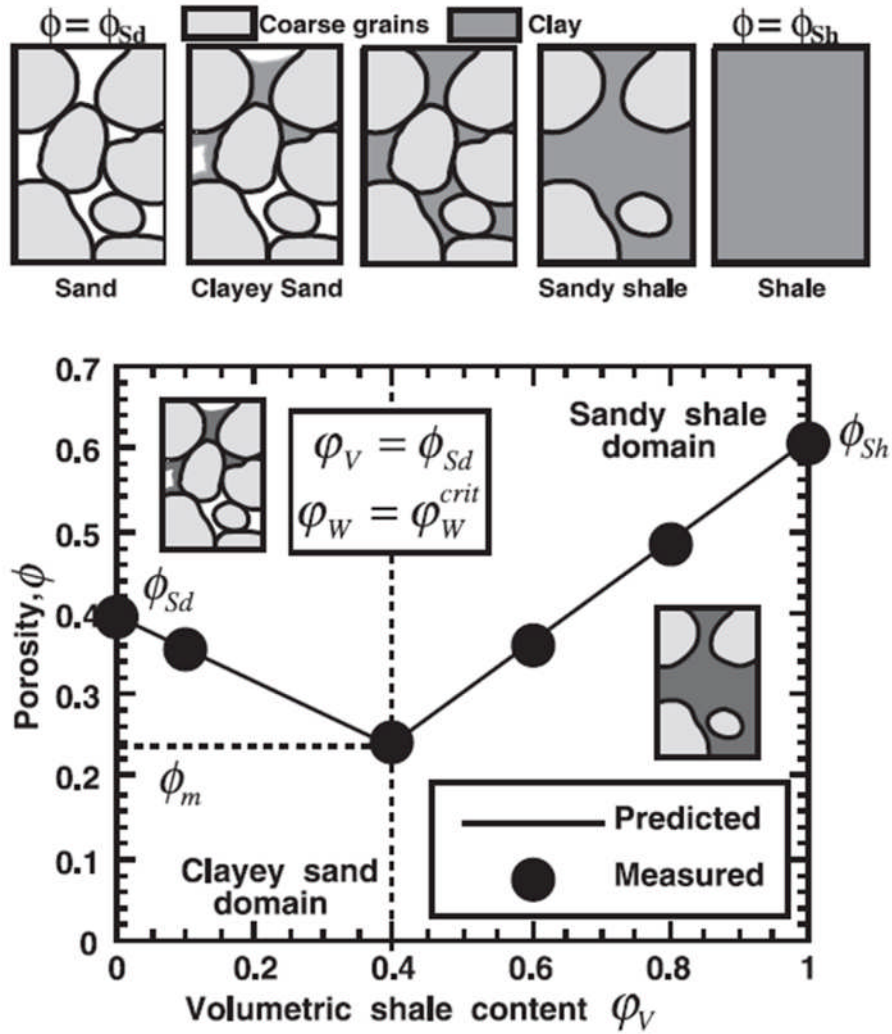


Figure 1-10: Diagram showing the impact of grain sorting that is sand to clay ratios on porosity with minimum porosity of 24% for a mixture of 60% sand and 40% clay (from Revil et al., 2002)

Permeability, on the other hand, is essentially controlled by the pore throat radius, r , which is controlled by the grain size and grain sorting. Small grains with poor grain sorting result in lower permeability compared with larger grains with better sorting. Numerical modeling shows the effect of grain size and grain sorting on both porosity and permeability (Figure 1-11). Thus, permeability of a petroleum reservoir is affected by the environment under which the rock was deposited. An example of the effect of the depositional environment on the porosity-permeability of different facies is presented in Figure 1-12. Figure 1-13 also shows a plot with different effects the different lithologies have on the porosity and permeability.

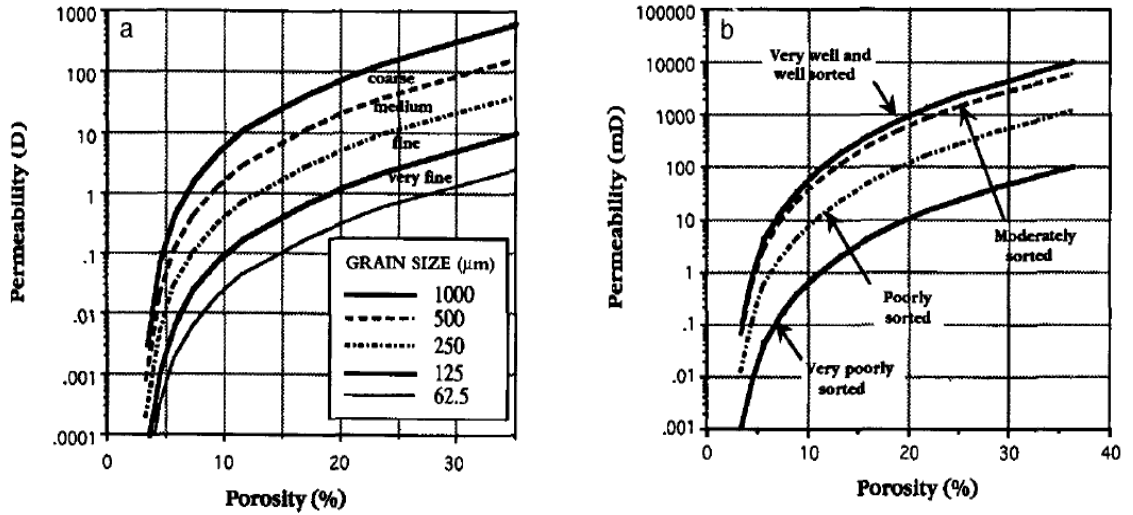


Figure 1-11: Effect of grain size (left) and grain sorting (right) on porosity and permeability based on the numerical modeling (from Cade et al., 1994).

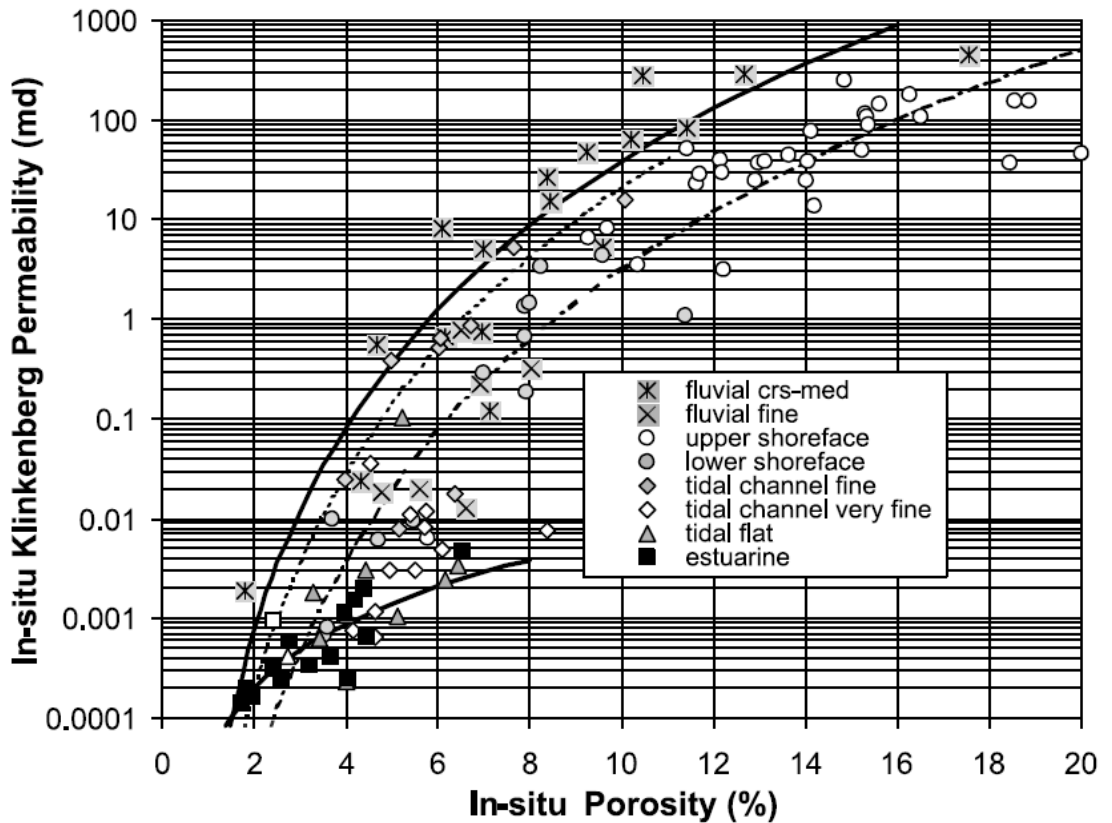


Figure 1-12: Cross plot of porosity and permeability at in-situ showing the effect of the different facies on the properties in Lower Silurian Sandstones in the Appalachian Basin (from Castle and Byrnes, 2005).

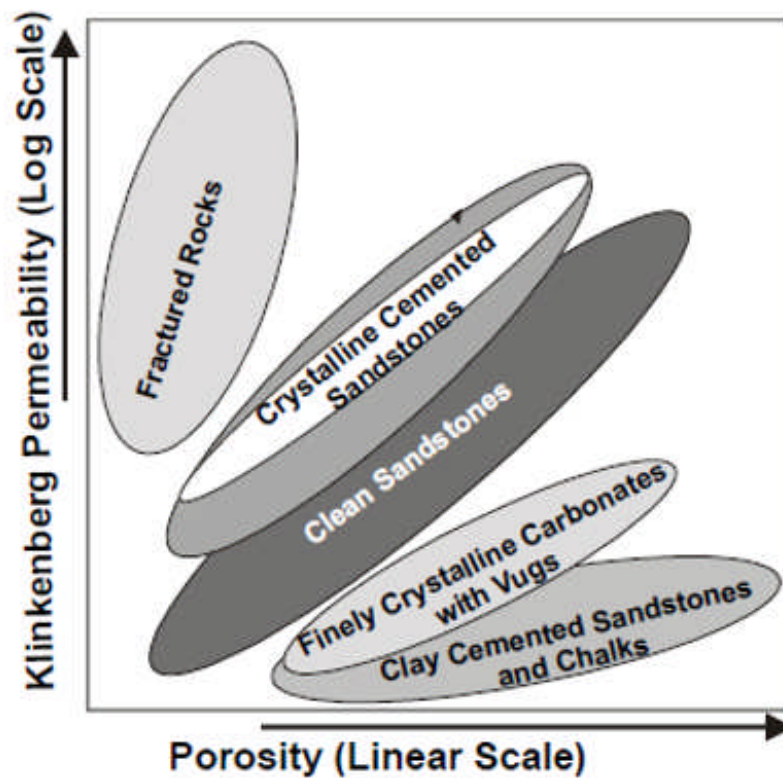


Figure 1-13: Semi-log plot of permeability (log scale) against porosity (linear scale) showing the relationship between porosity and permeability for different lithologies (from Glover, 2016).

1.1.6 Diagenetic controls on porosity and permeability

Sediments go through mechanical and chemical diagenetic processes after being deposited, which alter their microstructures as well as their petrophysical properties.

1.1.6.1 Mechanical compaction

Mechanical compaction is considered to be one of the most important processes causing reduction in porosity and permeability during diagenesis (Cade et al., 1994). It is defined as the reduction in porosity as a result of the reduction in the rock bulk volume caused by the increase of the overburden pressure. The increase of the pressure rearranges the sand grains, and may even crush and/or plastically deform grains (Figure 1-14).

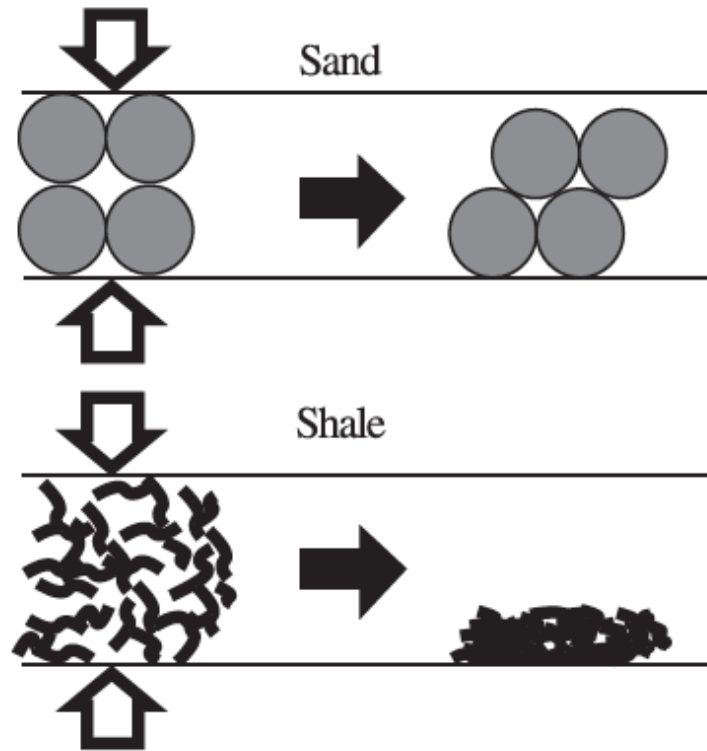


Figure 1-14: Sketch showing impact of mechanical compaction on rearranging sand grains and crushing shale particles affecting the porosity and permeability (from Revil et al., 2002).

1.1.6.2 Chemical processes

Chemical processes are the other type of diagenesis that impact the porosity as well as the permeability of the reservoirs particularly the unconventional ones. Porosity of sandstone reservoirs is classified, based on process under which the pore space was formed, into “primary” and “secondary”. Primary porosity is the matrix porosity that is formed during the deposition of the sand grains at the pre-diagenesis stage, while the secondary porosity is formed as a result of subsequent diagenesis (Tiab and Donaldson, 2012). Matrix permeability is referred to as the primary permeability, which also is formed at the pre-diagenesis stage. The secondary permeability could be evolved as a result of the diagenetic process including the formation of fractures and channels.

Secondary porosity is formed as a result of the subsequent diagenesis, and can be subdivided based on the diagenetic process. The main factors forming secondary porosity are fracturing, dissolution and shrinkage and each process varies significantly in its importance (Schmidt and McDonald, 1979), and how they affect the

permeability. Fractures are openings created by the structural failure of the reservoir rock as a result of the change in the hydraulic and mechanical stress state due to tectonic events and/or thermal expansion or contraction (Schmidt and McDonald, 1979; Choquette and Pray, 1970). Such activities could also contribute in enhancing the permeability by creating more pathways for the fluids in the reservoirs. It has been argued that dissolution could contribute to the porosity and could improve the permeability by forming channels or enlarging pores through circulating hot solutions (Tiab and Donaldson, 2012). However, in most situations the products from mineral dissolution are precipitated as new minerals in the surrounding pore-space, which means that the overall process may reduce permeability (Bjorlykke, 2015).

The presence of clay has a great impact on reservoir production especially in tight sandstones. The four most common types of clay encountered in the reservoir rocks, are kaolinite, smectite, illite and chlorite. Clay may be detrital in origin but also a large amount of clay within sandstones is formed after deposition with different sizes and shapes. Neasham (1977) categorized dispersed clay in sandstone, according to the clay crystal structure and its location in the pore system, into three types (1) discrete particle "kaolinite", (2) pore-lining "chlorite", and (3) pore-bridging "illite" (Figure 1-15). So the impact of clay on the porosity and permeability of the sandstone reservoir is based on their morphology and position.

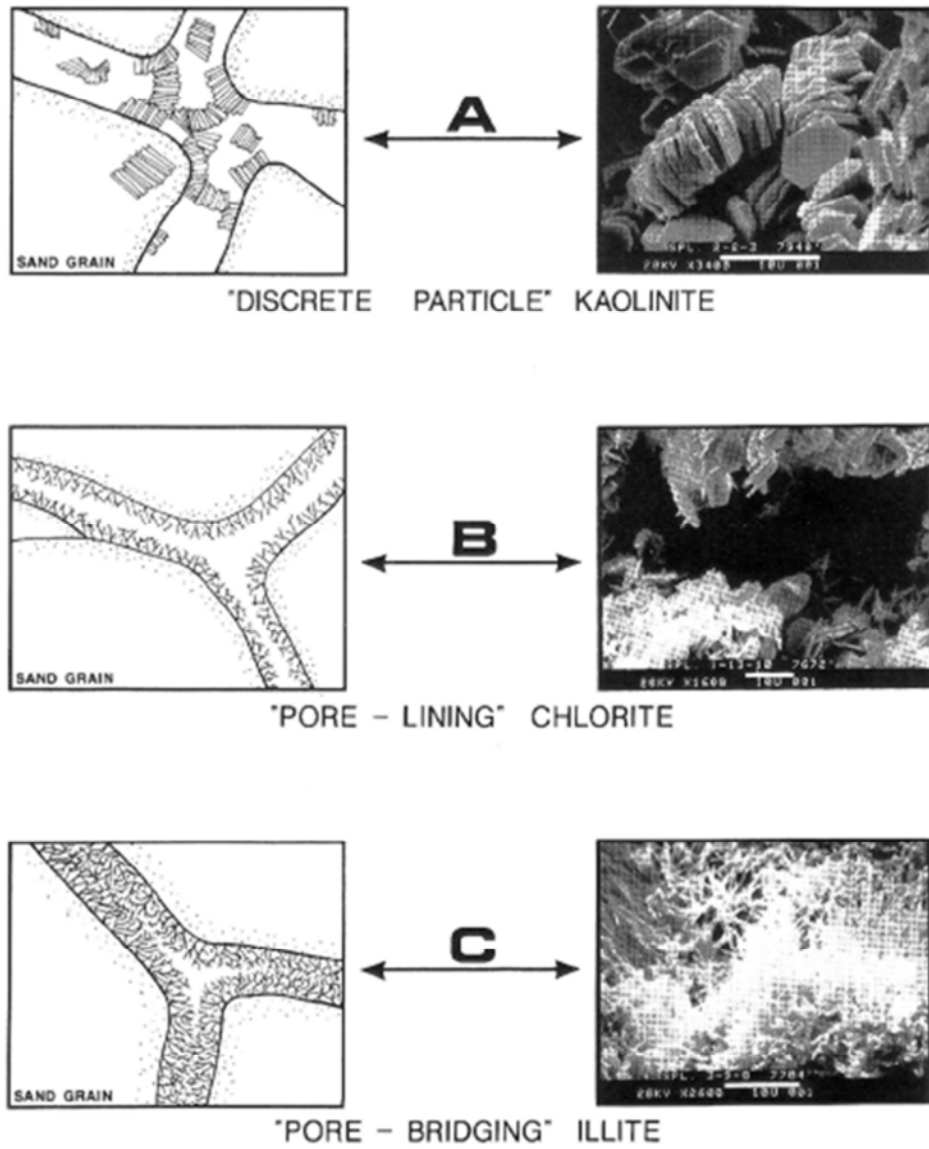


Figure 1-15: Classification of clay types based on their position in sandstones (from Neasham, 1977).

The effect of the clay type on the porosity and permeability have been documented in the literature. Sandstones with illite “pore bridging” show the lowest permeability for a given porosity compared with sandstones contain chlorite “pore lining” or kaolinite “discrete particles” for a given porosity; clean “clay-free” sandstones show the highest permeability (Figure 1-16) and (Figure 1-17).

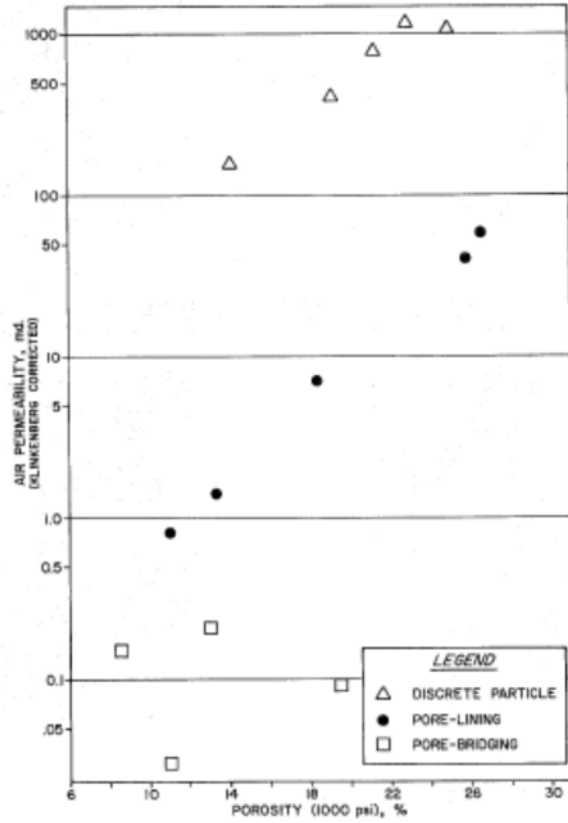


Figure 1-16: Porosity vs. air permeability for several sandstone samples with different types of clay (from Neasham, 1977).

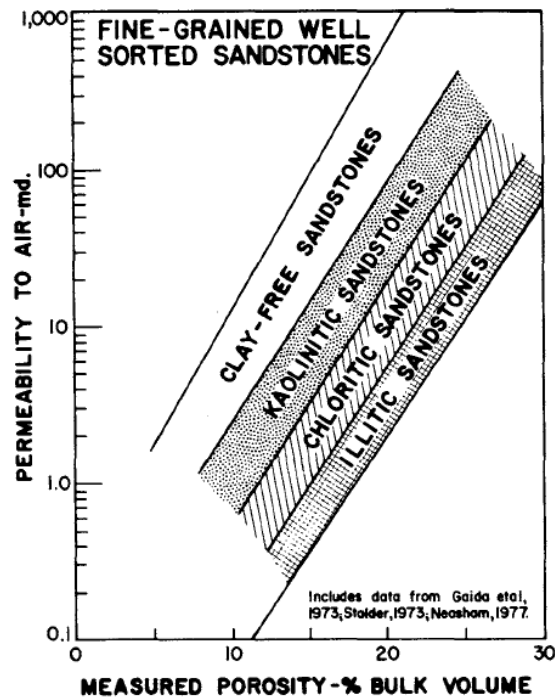


Figure 1-17: Relationships of porosity and permeability of clean sandstones (clay-free) and sandstones with different clay types (from Wilson, 1982).

Presence of clay can have a greater effect on the brine permeability more than gas permeability. According to Baptist and Sweeney (1954), liquid permeability of sandstone with clay content was reduced when measured using distilled water due to clay swelling compared to permeability measured with saline water. Lever and Dawe (1987) also reported clay swelling in sandstones with different clay contents as a result of using distilled water as the pore fluid to measure the permeability when compared with permeability measurements using brine with 30,000 ppm NaCl. They showed the effect of the brine salinity on the permeability measurements; they refer to it as water-sensitivity (Figure 1-18).

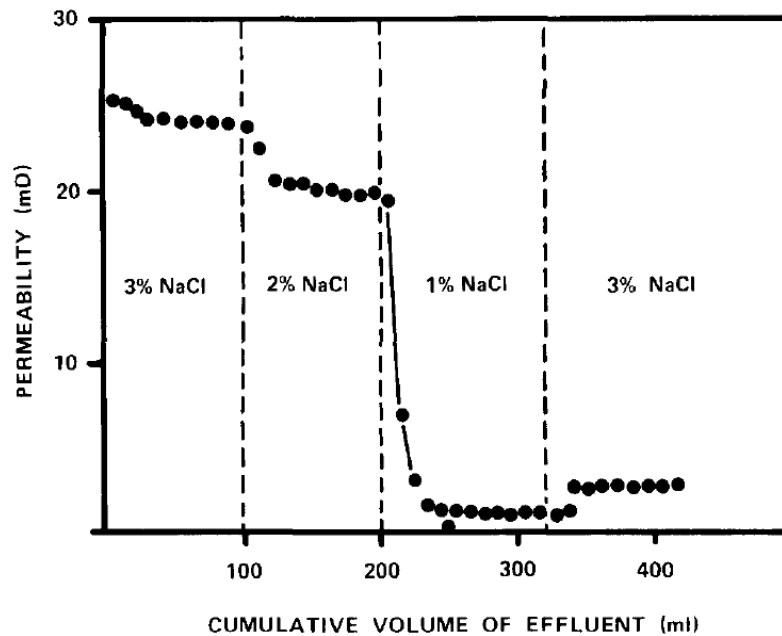


Figure 1-18: Water-sensitivity of the Spiney sandstone, Moray Firth Basin, showing the reduction in permeability based on the change in the salinity of the brine (from Lever and Dawe, 1987).

1.1.7 What are tight gas sandstones?

Tight gas sandstone reservoirs are not consistently defined. In the 1970s, the US government decided the standard definition of tight gas sand reservoirs are those with *in-situ* porosity and permeability of less than 10% and 0.1 mD respectively. This definition was made to support companies drilling and producing gas from tight reservoirs by receiving federal and/or state tax credits (Holditch, 2006). Holditch (2006) defines a tight gas sand reservoir as “a reservoir that cannot be produced at economic flow rates nor recover economic volumes of natural gas unless the well is

stimulated by a large hydraulic fracture treatment or produced by use of a horizontal wellbore or multilateral wellbores.” On the other hand, according to German Society for Petroleum and Coal Science and Technology (DGMK), tight reservoirs are defined to be the ones with effective gas permeability <0.6 mD (Naik, 2005). Blasingame (2008) considered a "modern" definition of tight gas reservoirs as sandstone reservoirs with permeabilities less than 0.001 mD.

Spencer (1989) subdivided tight clastic reservoirs into two main groups according to their porosity and permeability, namely high porosity (HP) and low porosity (LP) reservoirs. Both groups have permeability less than 0.1 mD. HP reservoirs have relatively high porosity (10-30%) while LP reservoirs have porosity in the range of 3 to 12%. HP tight reservoirs were defined as siltstone and very fine sandstone buried at shallow depths, with the low permeability due to the small silty grain size. LP tight reservoirs, on the other hand, may consist of larger sand grains compared to the HP, but their low permeability is caused by deep burial which increases the mechanical compaction resulting in diagenetic alteration such as quartz cementation and illitization (Spencer, 1989). According to Nelson (2009), pore throat diameters in conventional sandstones are greater than $2 \mu\text{m}$ while tight sandstones have pore throat diameters that are between 2 and $0.03 \mu\text{m}$ (Figure 1-19).

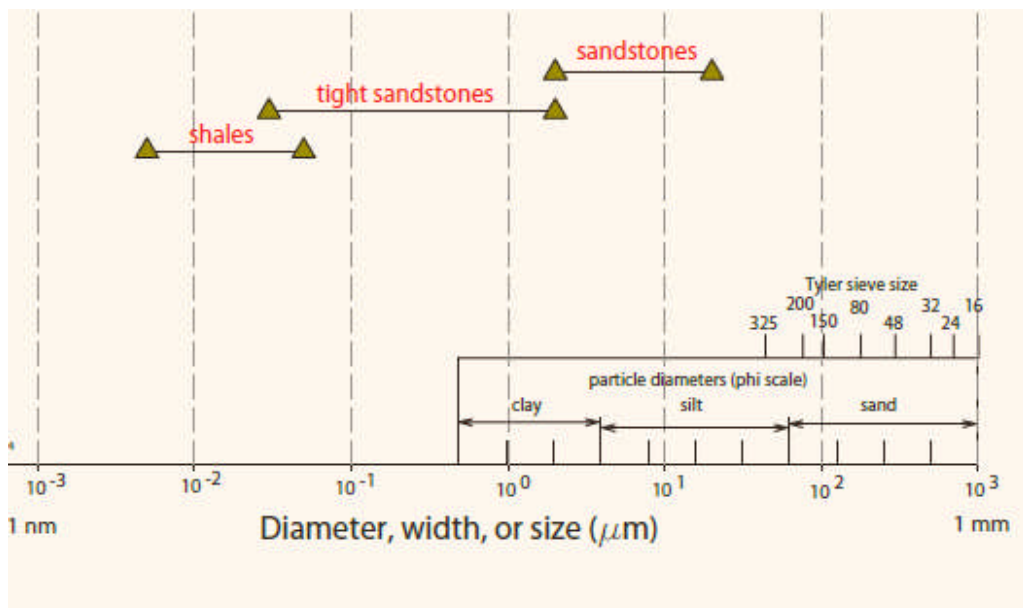


Figure 1-19: Pore throat size comparison between conventional sandstones and tight sandstones (modified from Nelson, 2009).

1.1.8 Effect of stress on petrophysical properties

The concept of the net stress law was first introduced by Terzaghi (1925) stating that net stress is the difference between confining stress and pore pressure. The net stress of a reservoir is defined as the difference between the total stress (i.e. weight of overburden and any tectonic stresses) and the pore pressure (Kilmer et al., 1987). The overburden stress is exerted by the overlying layers, and it is opposed by the pore pressure. Any change in the stress or pore pressure affects the petrophysical properties, and thus it is important to evaluate the reservoir under an effective net stress. Reservoir pressure decreases as a result of gas production, which in turn results in an increase in the net stress. Predicating the *in-situ* permeability and how it responds to the change in stress resulting from production is crucial in reservoir evaluation and fluid flow modelling. Although many experiments have been conducted on the stress dependency of petrophysical properties specifically permeability of clastic rocks (Fatt and Davies, 1952; Wyble, 1958; Dobrynin, 1962; Vairogs et al., 1971; Jones and Owens, 1980; Spence, 1989; Davies and Davies, 2001), less work has been focusing on the effect of the microstructures on such stress sensitivity.

Since the 1950's, reduction of permeability due to stress increase has been reported. Fatt and Davies (1952) were the first to study the effect of overburden pressure on permeability. Wyble (1958) examined the effect of radial pressure rather than overburden pressure on petrophysical properties, and reported that most reduction in permeability occurred below 3500 psi. McLatchie et al. (1958) also measured the oil permeability under pressure and found that reduction in permeability for sandstones with clay was greater than clean sandstones. Dobrynin (1962) analysed permeability measured under pressure based on two series of measurements, and suggested that pore channels contraction is the cause for the permeability reduction. About a decade later, it was reported that the effect of stress on permeability was greater for tight rock samples compared with more permeable rocks; this was reasoned to the smaller pores in the tight samples being stressed and the heterogeneity of the samples (Vairogs et al., 1971). It was reported that porosity of tight sandstones measured at reservoir pressure was generally 5-10% less than porosity measured at ambient condition while permeability at reservoir pressure is inconsistently less than permeability measured at low pressure (Spencer, 1989).

According to a laboratory study of Jones and Owens (1980), the permeability of tight gas sands is affected greatly by confining pressure. The study showed that permeabilities measured under hydrostatically applied confining pressure of 5000 to 6000 psi were reduced by almost 10-fold compared to routine core analysis measurements conducted at stresses of 150 to 250 psi. Permeability as well as electrical resistivity are both affected by the change in volume in addition to the changes in the pore shape and connectivity caused by compression while porosity is influenced only by the volume change (Saner et al., 1996). Permeability is arguably the petrophysical property that is most affected by stress; the lower the permeability the higher the effect. However, such behaviour is not completely understood and no unique relationship necessarily exists between permeability and stress (Davies and Davies, 2001).

It has been argued in the literature that the confining stress and the pore pressure could have different effects on the petrophysical properties of the reservoir. It is not clear whether the permeability of tight reservoirs for instance is more sensitive to the change in the confining stress or the pore pressure. Many experiments were conducted to determine which component of the net stress has more effect on the permeability (Zoback and Byerlee, 1975; Walls and Nur, 1979; Bernabe, 1986; Warpinski and Teufel, 1992; Kwon et al. 2001; Al-Wardy and Zimmerman, 2004; Li et al. 2009; Li et al. 2014). Several studies indicated greater effect of pore pressure on permeability than the confining stress (Zoback and Byerlee, 1975; Walls and Nur, 1979; Al-Wardy and Zimmerman, 2004). On the other hand, other studies reported less effect of the change in pore pressure than the change in confining stress on permeability (David and Darot, 1989; Shanley et al., 2004; Li et al., 2009; Qiao et al., 2012). Thus, it is critical to deal with every reservoir individually to determine the stress sensitivity of its petrophysical properties, particularly tight reservoirs.

1.2 Objectives

The aim of this thesis is to examine the effect of stress on permeability, velocity and electrical properties as well as capillary pressure measurements in tight gas sandstones, which are essential parameters in hydrocarbon exploration and development. The impact of equilibration time, which is the waiting time after

changing the pressure conditions of the samples and prior to taking the petrophysical measurement, is also analysed as it may affect the accuracy of the measurements. The objectives of this research project are the following:

- To analyse the stress dependencies of permeability, ultrasonic velocity and electrical properties caused by increasing the net stress, and to analyse the microstructures of the samples through SEM images, which maybe impact such dependencies.
- To determine effective stress law for permeability by measuring gas permeability under different combinations of confining stresses and pore pressures.
- To calculate Biot's coefficient for elastic volume deformation from quantitative mineralogy and ultrasonic velocity measurements and assess whether it is correlated with effective stress coefficients for permeability.
- To obtain capillary pressure data using porous plate and vapour desorption methods and to scan samples with NMR at different capillary pressure to monitor the drainage process and analyse the impact of equilibration time.
- To obtain capillary pressure from mercury injection to be compared with capillary pressure data from porous plate and vapour desorption.
- To conduct mercury injection capillary pressure under stress to analyse the effect of stress on capillary pressure data and permeability estimated from mercury-injection capillary pressure models.

1.3 Thesis outline

The thesis is divided into a further 7 chapters. Chapter 2 describes the samples analysed and the techniques and instruments used to prepare the samples, a simulated brine and to conduct the petrophysical measurements during this study. Chapter 3 presents the results of the core analysis (i.e. porosity, permeability, mineralogy, SEM images, mercury injection capillary pressure) conducted on three suites of tight gas sandstone samples and discusses the controls on porosity and permeability. Chapter 4 discusses the stress dependency of permeability, velocity and electrical properties of a suite of tight sandstones and the impact of microfractures on such dependency. Determination of the effective stress law for permeability and the

correlation between effective stress coefficients and Biot's coefficients for elastic volume deformation of another suite of tight samples is discussed in Chapter 5. Results of the capillary pressure measurements of the third suite of tight samples using porous plate, vapour sorption and mercury injection techniques, and comparison between the results is discussed in Chapter 6. Discussions about the impact of stress and equilibration time on the capillary pressure data obtained using different techniques coupled with NMR scans are also presented in Chapter 6. Chapter 7 presents a summary of all conclusions, implications and recommendations, with references cited in the thesis presented at the end.

2 Data and Methodology

2.1 Introduction

This chapter describes the samples analysed, the sample preparation procedures as well as the techniques used for measuring the petrophysical properties. All the measurements were conducted utilizing the instruments in the Wolfson Laboratory at University of Leeds. Different petrophysical measurements were made at ambient conditions, while others were measured under a range of net stresses by changing both confining and pore pressures.

2.2 Samples analysed

The analysed samples were taken from deep tight gas sandstone reservoirs of Carboniferous to Permian age, which were deposited in aeolian environments. The depth ranges from approximately 3000 to 4500 m. All core plugs were cut parallel to bedding plane and they were all nominally 5 cm in length and 3.7 cm in diameter. Simulated brine was prepared based on the chemical composition of the formation water from which the samples were taken.

A total of 29 samples were given the initials TS, which stands for "Tight Sand" due to confidentiality reasons. The first suite, group A, consists of 15 samples namely TS2-1 through TS2-10 and TS3-1 through TS3-5. This suite was taken from a gas field in Australia and it was used mainly for permeability, ultrasonic velocity and electrical properties stress dependency and drawdown experiments. The second suite, group B, consists of 5 samples TS5-2, TS5-5, TS7-1, TS7-4 and TS7-5, and they were taken from a gas field in North Sea. This suite was used for analyses of the effective stress law for permeability and elastic properties. The last suite, group C, was taken from a gas field in Oman and was used for the capillary pressure analyses. This suite consists of 9 samples named TS1-55, TS1-197, TS1-305, TS4-4, TS4-11, TS5-11, TS1-25, TS2-25, and TS3-47.

2.3 Sample preparation

All plugs were cleaned of hydrocarbon using Soxhlet apparatus with dichloromethane (DCM) solvent whose boiling temperature is about 40°C. In the Soxhlet apparatus,

DCM was heated to its boiling point where the vapour travelled through a tube and distilled into a chamber where the samples were placed. The solvent removed the hydrocarbon from the samples and dripped down back to the boiling chamber. Samples were left overnight in the apparatus chamber until the solvent in the chamber became clear indicating that no more hydrocarbons is present within the samples. The samples might contain some salts from the formation water at the end of this process. Thus, the samples were then extracted with methanol in the Soxhlet apparatus to remove any possible salts remaining (McPhee et al., 2015).

The plugs were then placed in the vacuum oven to be dried at about 60°C. Plugs were weighed before and after the cleaning and drying process to estimate the weight of the extracted fluids, hydrocarbon and/or water. For optimum results of petrophysical measurements, plugs were stored with desiccant to prevent water being adsorbed from the atmosphere. In addition, all samples were weighed before and after every measurement to ensure each sample was dry with a relatively consistent weight.

2.4 Bulk Density

Since all the sample plugs were cylindrical in shape, bulk volume of each plug was determined using Equation 2-1, where l and r are the length and radius of the sample respectively, which were measured using an electronic calliper. The mass, m , of every sample was measured using an electronic balance. Bulk density of the sample was then calculated using

Equation 2-2.

Equation 2-1

$$B_v = \pi * l * r^2$$

Equation 2-2

$$d_b = \frac{m}{V}$$

where:

d_b = bulk density (g/cm³)

m = mass (g)

V = volume of the sample (cm³)

2.5 Helium porosimetry

2.5.1 Helium pycnometer

Helium porosimetry relies on the gas expansion method that is based on Boyle's law, which under isothermal condition provides Equation 2-3. The apparatus used for this method is called helium pycnometer (Figure 2-1) and it basically measures the grain volume of the sample. The clean and dry sample was placed in chamber B (Figure 2-1), which was at atmospheric pressure and then valves 2 and 3 were closed. Helium was admitted into chamber A through valve 1 until pressure of approximately 150 psig, P_1 , is reached, then the valve was closed. The connecting valve 2 was then opened to expand the gas into the sample chamber. This resulted in a gas pressure drop as the gas would penetrate into the pore space of the sample. The gas was left for 30 seconds for pressure equilibrium, and the decreased pressure reading was recorded from the transducer as the final pressure P_f . Valve 3 was opened at the end of the measurements and sample was taken out of the chamber. All measurements were obtained under approximately constantly monitored laboratory conditions to avoid effects of temperature and barometric pressure changes on the measurements.

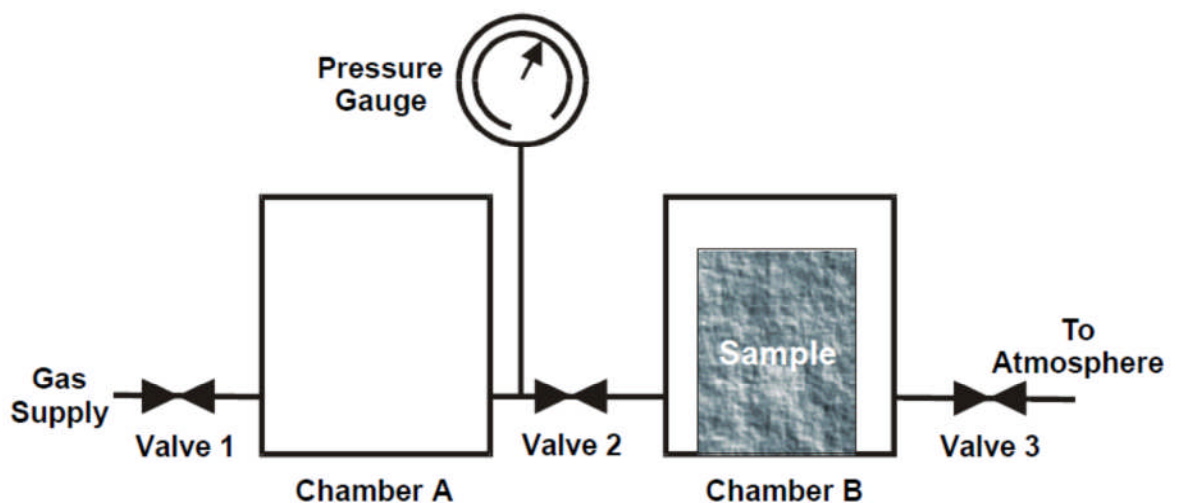


Figure 2-1: A schematic of the helium pycnometer used to determine the grain volume based on the gas expansion method (from Glover, 2016).

2.5.2 Pycnometer calibration

Calibration of the pycnometer is important prior to measurements to maximize the accuracy of the grain volume determination. Calibration was performed to obtain the accurate volumes of the reference chamber A, V_1 , and the sample chamber B, which were used in the grain volume calculation. The calibration was achieved once with empty chamber and another using a steel plug with a known volume. The volume V_2 is the total volume of the reference chamber volume, V_1 , and the empty sample chamber. The volume of the steel plug is referred to as V_s , and thus the final volume when calibrating using the steel plug would be V_f that is V_2 minus V_s . The calibration was conducted through the same procedures followed in Section 2.5.1.

Assuming isothermal condition, the first calibration was conducted with empty chamber. The recorded initial pressure P_1 was 250 psig and the pressure after expansion into the empty chamber P_2 was 80 psig; using Boyle's law (Equation 2-3) yielded ($V_1 = 0.32 V_2$). The calibration was repeated with a steel plug having a measured bulk volume $V_s = 29 \text{ cm}^3$ placed in the sample chamber. The initial recorded pressure P_1 was 256 psig and the final pressure after expansion into the chamber containing the steel plug was $P_f = 112$ psig. Using Equation 2-4 that is also based on Boyle's law yielded ($256 V_1 = 112 V_2 - 3248$). Substituting ($V_1 = 0.32 V_2$) that was obtained from the first calibration into the second calibration equation produced ($30 V_2 = 3248$). So the total volume of the reference chamber and the empty sample chamber $V_2 = 108 \text{ cm}^3$, and consequently the volume of the reference chamber in the pycnometer, V_1 , is 35 cm^3 . Uncertainty of all calibrations and measurements was approximately within $\pm 0.5\%$.

Equation 2-3

$$P_1 V_1 = P_2 V_2$$

Equation 2-4

$$P_1 V_1 = P_f V_f = P_f (V_2 - V_s)$$

where:

P_f = final pressure with the steel plug in the sample chamber (psig)

V_f = final volume for calibrating with steel plug ($V_2 - V_s$) (cm^3)

P_1 = initial pressure in V_1 (psig)

V_1 = volume of the reference chamber (cm^3)

P_2 = pressure after expansion with empty sample chamber (psig)

V_2 = total volume of the reference chamber and empty sample chamber (cm^3)

V_s = volume of the steel plug used for calibration (= 29 cm^3)

2.5.3 Porosity calculation

Following the procedures in Section 2.5.1, grain volume, G_v , of each sample was calculated using Equation 2-3 and the predetermined volume of the reference chamber, V_1 . Pore volume, P_v , is the difference between the bulk volume and grain volume. So porosity was calculated from the determined grain volume, G_v , and the measured bulk volume, B_v , using Equation 1-2. The accuracy of the measured grain volume would be within ± 0.2 percent of the true value corresponding to approximately $\pm 0.1 \text{ cm}^3$ in a sample that is approximately 5 cm long and 3.8 cm in diameter, if calibration was performed properly (Recommended practices for core analysis, 1998).

2.5.4 Stress-corrected porosity

Measured routine porosity was corrected for compressibility at net stress using the empirical relationships presented by Cluff et al. (2009) from the Mesaverde tight gas sandstones (Equation 2-5), (Equation 2-6) and (Equation 2-7) as the analysed samples showed similar properties to the Mesaverde tight gas sandstones.

Equation 2-5

$$\phi = \phi_{lab}[A \log \sigma' + B]$$

Equation 2-6

$$A = -0.00549 - \frac{0.155}{\phi_{lab}^{0.5}}$$

Equation 2-7

$$B = 1.045 + \frac{0.128}{\phi_{lab}}$$

where:

ϕ = corrected porosity

ϕ_{lab} = porosity at laboratory (ambient) condition

σ' = net stress

A and B are empirical fitting parameters

2.6 Permeability determination

The permeability of cores from conventional reservoirs is generally measured using the steady-state technique. In this method steady-state flow of gas or liquid is established through a core sample and the permeability is calculated from the measured flow rate and the pressure gradient. It would be very time-consuming, might take days for a single sample, to use the steady-state method to measure gas permeability of tight gas sandstone samples that are known to have very low permeabilities. So the gas permeability of such tight sandstone samples was measured using an unsteady-state instrument termed a pulse-decay permeameter (PDP).

2.6.1 Gas pulse decay permeameter

The unsteady-state technique is based on the transient flow method that was introduced by Brace et al. (1968). The set up introduced by Brace et al. (1968) was a cylindrical sample connected to two fluid reservoirs upstream and downstream, where a fluid pressure was suddenly increased in the upstream reservoir. Permeability was calculated from the observed pressure transient created as the fluid flows from the upstream to the downstream reservoir.

Measurements conducted during this study were made using a CoreLabs PDP200 permeameter that was limited to measure gas permeability with confining and pore pressures up to 3500 and 1200 psi respectively. The equipment was redesigned in Wolfson laboratory to measure permeability under confining pressure up to 5000 psi with pore pressure up to 1500 psi (Figure 2-2 – left). The system mainly consists of upstream and downstream gas reservoirs with known volumes, transducers to measure the differential pressure (ΔP) between upstream and downstream pressures with 0.5 psi accuracy, and a Hassler-type core holder connected to a pump to control the radial confining stress. Upstream and downstream gas reservoirs are connected to the helium gas cylinder and each reservoir is controlled with a separate valve. The reservoirs are connected to transducers to monitor the pressure evolution. The downstream volume is also connected to “bleeding” valve for venting the gas at the end of the measurement, and helium gas was used as the pore fluid to avoid interaction with the rock matrix (Figure 2-2 – right). To conduct the permeability measurement, the 5-cm plug sample was placed inside the Hassler-type core holder

with a rubber sleeve inside, and the confining pressure was applied on the rubber sleeve through a manual oil pump. A low differential pressure of about 10-50 psi was applied due to the samples ultra-low permeability. The transient pressure measurements were analysed automatically using a software, which is based on the algorithms presented by Jones (1972).

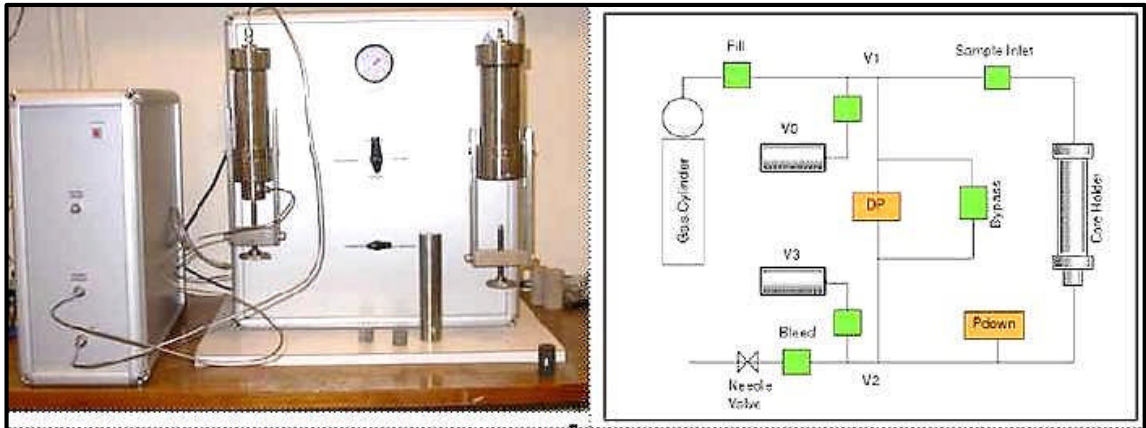


Figure 2-2: Left: A picture of the CoreLab PDP 200 redesigned in the Wolfson laboratory. Right: a schematic diagram of the pulse-decay permeameter (PDP) for gas permeability measurements under stress (from Wolfson laboratory website).

Permeability measurements under low confining stress (less than 3500 psi) were performed in two parts. First part was performed to examine the effect of stress on permeability. It was performed with a fixed pore pressure of 1000 psi and three different confining stresses starting with 1500 psi, followed by 2500 psi, and last test with 3500 psi. Second part was conducted to analyse the gas slippage effect. This was performed with a fixed confining stress and different pore pressures. At each step, the sample was left for a couple of hours to reach equilibrium. A tight sample would require several hours of soaking time than a relatively more permeable sample as gas needs longer time to reach equilibrium through the whole plug sample.

2.6.2 Klinkenberg permeability correction

Klinkenberg correction for gas slippage effect was performed by measuring the permeabilities of a sample under a constant confining stress of 3500 psi with different pore pressures of 1000, 700 and 400 psi. The permeability readings were cross-plotted against the reciprocal of the mean pore pressure ($1/P_p$) used for every pressure. A line was drawn through the points and it was extrapolated to intercept with permeability

y-axis indicating an infinite pore pressure (Klinkenberg, 1941). Then, Klinkenberg-corrected permeability, also known as the absolute permeability or k_i , was taken as the intercept value with the slope of the line defined as $(b*k_i)$ from the cross plot (Figure 2-3). The slippage factor, b , was then calculated using the Klinkenberg expression (Equation 1-4).

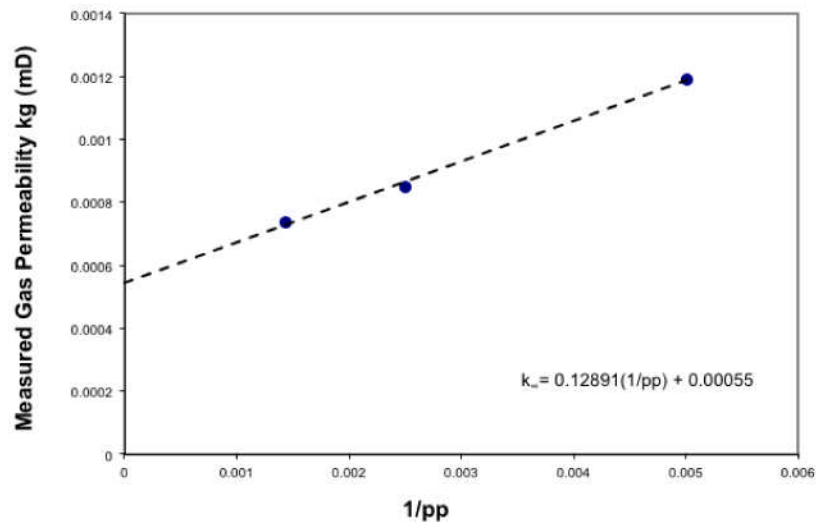


Figure 2-3: An example of estimating Klinkenberg-corrected permeability (mD) for TS2-5 by plotting permeability (mD) against the reciprocal of mean pore pressures (1/psi). Permeability measurements were within 10% error (based on Klinkenberg, 1941).

2.6.3 Drawdown experiments

Gas permeability measurements under higher stress were performed using a high pressure PDP permeameter, which had been up-graded in the Wolfson laboratory to work at confining pressures of up to 10,000 psi and gas pore pressures of up to 8,000 psi. The core holder was a hydrostatic “biaxial” rather than a Hassler-type one, to apply hydrostatic pressure radially and axially at the sample. Dimensions and pore volume determined for each sample were entered as parameters into the PDP program that runs and determine the permeability as a function of pressure change with time.

To perform the permeability measurements, the 5-cm plug sample was placed inside the hydrostatic core holder with a rubber sleeve inside, and the confining stress was applied on the rubber sleeve through an ISCO oil pump that is connected to the PDP system. Helium gas was used as the permeant for all gas permeability measurements and the pore pressure was controlled through an ISCO 100 DM pump. An initial of

1000 psi confining pressure was applied to the sample, and then helium gas was allowed to enter the sample at 500 psi. Confining and pore pressures were both increased with 1000 psi step simultaneously to the desired pressures. A differential pressure, which is the difference between upstream and downstream outlets, of approximately 10 to 50 psi was then imparted by opening the valve at the downstream. Pressure of the upstream volume dropped as gas flows through the core sample into the downstream, while the pressure of the downstream increased with time until it equilibrated with the upstream pressure. The upstream pressure and the differential pressure were recorded at 1-second intervals until the upstream and downstream pressures equilibrated. The transient pressure measurements were analysed automatically based on the algorithms by Jones (1972).

2.7 X-Ray Diffraction (XRD)

XRD has been used to quantify the mineralogy of the rock samples. The technique is based on the principle that the intensity of the XRD pattern of a mineral is proportional to its amount present in a mixture of the sample (Hardy and Tucker, 1988). A method to run XRD analysis is creating calibration curves that are based on the XRD analysis of several mixtures containing different proportions of an internal standard such as corundum. However, this method has not been widely used as a quantitative method because it requires preparation of samples with complete random orientations (Hillier, 1999; Brindley, 1984). A more recent technique has been developed that can be utilised without the need for preferred orientation even if the samples contain large percentages of clay (Hillier, 1999, 2000). The sample is ground with a standard (20 wt. % corundum), and then a slurry of the mixture is sprayed through an air brush into a tube furnace. This is performed to form approximately 30 μm layer of wide spherical aggregates with no orientation preferences as was required. The powder sample was then placed into the specimen holder in the XRD instrument to be analysed. A Rietveld method or reference intensity ratio (RIP) is then used to analyse the obtained diffraction results to get the mineralogical analyses. The analyses can be accurate to the 95% confidence level to $\pm X^{0.35}$ (X is the concentration in wt. %).

2.8 Scanning Electron Microscopy (SEM)

SEM images from thin sections were obtained for all core plugs to examine the microstructures, mineralogy and diagenetic history of the samples. Polished thin sections of the samples were prepared for microstructures analyses from 1.5 cm square and 0.5 cm thick blocks cut from the ends of core plugs using a diamond impregnated trimming saw. The block was then impregnated with a low viscosity resin. It was then mounted to a glass slide, trimmed and polished using a successively finer grained diamond that starts with 40 μm and cumulates with 1 μm diamond paste. The sample was carbon coated before being examined. The SEM instrument uses an electron beam to examine the thin section, hence samples must be carbon coated to be conductive. The samples were examined using a FEI Quanta 650 FEGSEM environmental SEM that is fitted with an Oxford Instruments INCA 350 EDX system/80 mm X-Max SDD detector. BSEM images were stored as 8 bit (tiff) files so they can be used for image analysis.

2.9 Ultrasonic velocities

Using the acoustic system in the Wolfson laboratory, ultrasonic velocities for all samples were measured dry under a range of confining stresses (1000, 2000, 3000, 4000, 5000 psi). The acoustic system has a universal instrumented triaxial test cell with transmission platens and ultrasonic receivers, and it runs at ambient laboratory temperature. It has split transducers capable of measuring compressional (P-waves) and two shear (S_1 and S_2 -waves) velocities. The frequency used to measure the P-wave velocities is 1 MHz and 0.6 MHz for the S-wave velocities.

2.10 Reservoir simulated brine preparation and properties

2.10.1 Brine preparation

Simulated brine was prepared based on the salinity of the formation brine which was provided as total dissolved salts (TDS) of 50,000 ppm with 80% NaCl, 10% CaCl_2 and 10% KCl. It was prepared by dissolving the equivalents of 40,000 ppm of NaCl, 5,000 ppm CaCl_2 and 5,000 ppm KCl in a litre of distilled water. As one litre of distilled water having the density of 1 g/cm^3 is equivalent to 1000 grams, the calculated TDS in grams per litre were 40, 5, and 5 grams respectively. The properties of the simulated brine are shown in Table 2-1.

Simulated Brine Properties			
Resistivity (ohm-m)	Density (g/cm ³)	Viscosity (cp)	Compressibility (1/atm)
0.18	1.06	1.07	-0.00057

Table 2-1: Properties of the simulated brine.

2.10.2 Brine resistivity

The conductivity of the simulated brine, C_w , was measured using a Siemens conductivity instrument in Wolfson laboratory. The conductivity was measured in siemens-cm, and an average was taken of several conductivity measurements with $\pm 2\%$ uncertainty. The reciprocal of the average reading was determined as the resistivity of the simulated brine, R_w . The resistivity was then temperature corrected to 25° C using Arp's empirical formula (1953) (Equation 2-8).

Equation 2-8

$$R_2 = \frac{R_1(Temp_1 + 21.5)}{(Temp_2 + 21.5)}$$

where:

R_2 = corrected resistivity at temperature $Temp_2$ (ohm-m)

R_1 = resistivity calculated at temperature $Temp_1$ (ohm-m)

$Temp_1$ = laboratory temperature at which resistance was measured (°C)

$Temp_2$ = correction temperature (°C)

2.10.3 Brine density

After dissolving the total of 50 grams of TDS in 1 litre of distilled water, the density of the simulated brine was calculated. A 50 mL pycnometer was filled with the brine, and it was weighed using an electronic balance after being zeroed to obtain the weight of the brine in the pycnometer. Average of three weight measurements was taken with $\pm 0.3\%$ error. Density of brine was then calculated using

Equation 2-2 (API, 1998).

2.10.4 Brine viscosity

Several measurements using Cannon-Fenske viscometer were taken by recording the time necessary for the distilled water and brine to pass from one mark point to

another. Different times were recorded for the distilled water and for the brine. With the known viscosity and density of distilled water as well as density of brine all at 25° C, the viscosity of the brine was calculated using Equation 2-9 (Maron and Prutton, 1958).

Equation 2-9

$$\frac{\eta_1}{\eta_2} = \frac{d_1 t_1}{d_2 t_2}$$

where:

η_1 = viscosity of brine (poise)

η_2 = viscosity of distilled water (poise)

d_1 = density of brine (g/cm³)

d_2 = density of distilled water (g/cm³)

t_1 = time brine flows through the capillary tube (s)

t_2 = time distilled water flows through the capillary tube (s)

2.10.5 Brine Compressibility

Using the water pump (Isco 100 DX), two readings of the simulated brine volume, in mm³ at different pressures, 130 and 200 psi, were taken with uncertainty of ±2.5%. The brine compressibility was then calculated using Equation 2-10.

Equation 2-10

$$C_w = \left(1 - \frac{V_2}{V_1}\right) \frac{1}{P_2 - P_1}$$

where:

C_w = brine compressibility (1/psi)

V_1 = volume at pressure P_1 (mm³ at psi)

V_2 = volume at pressure P_2 (mm³ at psi)

2.11 Saturating Samples with brine

After measuring the gas permeability and ultrasonic velocity under stress, samples then were saturated with the simulated brine for liquid permeability, electrical properties measurements, porous plate and vapour desorption capillary pressure and NMR scanning. The brine was placed in a vacuum chamber for degassing, and it was

left for 24 hours. Samples were placed in plastic cups filled with the degassed brine, and then they were all placed inside a vacuum chamber and left for 48 hours. Samples were left in the vacuum chamber to increase the imbibition process where brine was displacing air due to pressure drop while air was being vacuumed out of the chamber. The samples were then put under a pressure-saturation at approximately 1500 psi to maximize the brine saturation by displacing remaining air trapped inside the samples with the degassed brine. Samples were left under pressure-saturation for 24 to 48 hours.

2.12 Liquid pulse decay permeameter

Liquid pulse decay permeameter, *LPDP*, was used to determine the brine permeability for the samples. All brine permeability measurements were performed at 1500 psi confining stress with about 120 psi pore pressure. Differential pressure between upstream and downstream of about 10 psi was imparted as the samples showed very low measured gas permeability.

The sample was put in a rubber sleeve that was placed inside a Hassler-type steel core holder that is similar to the PDP setup. The confining stress transmitted to the sample radial surface through oil placed in-between the rubber sleeve and the steel holder. A pump (ISCO 100 DX) that was filled with the simulated brine, was connected to the upstream of the sample inside the core holder with a transducer to measure the pore pressure and the differential pressure. The downstream was connected to a reservoir filled with the brine. After the sample was placed inside the core holder, 1500 psi confining stress was applied using the manual pressure pump. Brine was pumped into both ends of the sample as upstream and downstream with pressure of approximately 130 psi. Each sample was left for about 48 hours for brine to reach equilibrium within the sample. After that, back pressure was reduced to about 120 psi to establish 10 psi differential pressure. The whole set up was connected to a computer running software 1.5 LPDP.

Pressure vs. time data acquired from the LPDP software was loaded into Cydar software as "Data Points". Atmospheric pressure was 14.696 psi and the experimental set up was set as volume-pressure with 9.815 cm^3 as the volume of the upstream reservoir V_1 . Properties of the simulated brine (Table 2-1) were input into "Fluid

Properties” box. Brine permeability was then determined using the absolute permeability model “PERM” with the best fitting “run optimum” command (Figure 2-4).

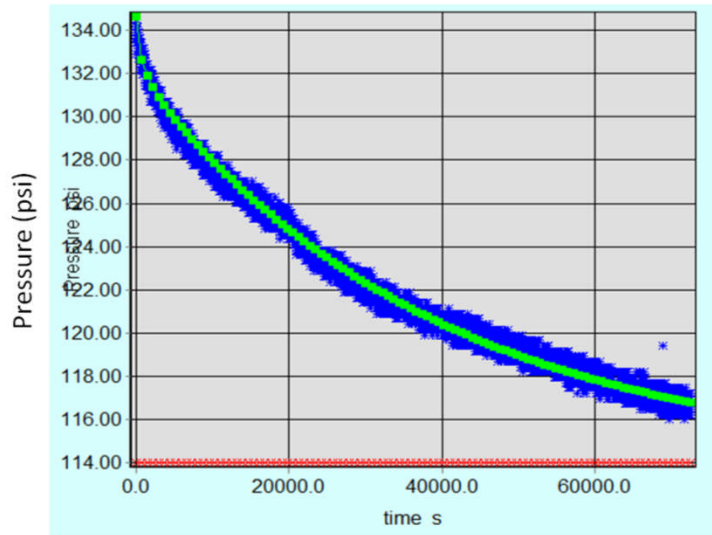


Figure 2-4: Brine permeability determined from pressure as a function of time modelled using CYDAR software that uses Newton-Raphson algorithm.

2.13 Electrical resistivity under stress

Electrical resistances were measured at a 2kHz frequency using a Quadtech 7600 RLC meter on fully saturated samples. A sample was placed in a Hassler-type core holder, and a confining pressure of 1500 psi was applied. Two pieces of tissue were cut, wetted with the simulated brine and placed on both ends of the core plug to ensure full contact between core sample and the steel end platens of the core holder. The two steel ends of the core holder, hence conductive, were connected to the electrical resistance instrument for measurement. Temperature was recorded with every measurement, as the electrical resistance is temperature dependant. As the electrical resistance is also pressure dependant, every sample resistance reading was monitored to ensure sample reaches equilibrium before taking final reading.

Samples were grouped based on their initial resistivity measured under 1500 psi due to the long waiting time needed for samples to reach equilibrium under higher stress prior to measuring the resistivity. A set of 5 representative samples of the first suite, TS2-2, TS2-4, TS2-7, TS3-1 and TS3-3, was picked to be examined for electrical properties under higher stresses. Resistivity of the five picked samples was measured under confining stress of 3000 psi, and then followed by a higher stress of 5000 psi.

Electrical resistivity, R_e , of a sample was calculated from the measured dimensions of the sample and its obtained electrical resistance under stress using Equation 2-11 at laboratory temperature. Arp's formula (1953) (Equation 2-8) was used to correct for the temperature effect. Formation resistivity factor, F , was then calculated using Equation 1-8. Cementation exponent m was then determined using Equation 1-9.

Equation 2-11

$$R_e = R \frac{A}{l}$$

where:

R_e = electrical resistivity ohm-metre (ohm-m)

R = electrical resistance (ohm, Ω)

A = cross sectional area of the sample (m^2)

l = length of the sample (m)

2.14 Nuclear magnetic resonance

Nuclear magnetic resonance, NMR, is a rapid non-destructive technique that does not require the typical sample drying and preparation, which is often destructive to the internal clay structure of the sample (Tyrologou et al., 2005). NMR is based on the responses of the nucleus of the hydrogen atom, (Coates et al., 1999), which is a compositional element of both water and hydrocarbons. NMR measures the longitudinal or spin-lattice relaxation time T_1 , and transverse or the spin-spin relaxation time, T_2 . Both relaxation times are related to the petrophysical properties of the rock such as the pore size and the surface-to-volume ratio (Equation 2-12) (Chen et al., 1998). NMR data is integrated with capillary pressure data to analyse the pore size distribution and the water saturations at different capillary pressures.

Equation 2-12

$$\frac{1}{T_2} = \rho \frac{S}{V}$$

where:

ρ = pore surface relaxivity

S/V = pore surface to volume ratio

NMR T_2 can be used to distinguish the type of fluids and their mobility. Fluids filling the pore spaces can be subdivided into non-moveable fluids, which are clay bound water and bulk volume irreducible (BVI) fluid, and the moveable or free fluid using T_2 cut off values (Georgi and Chen, 2007). A T_2 cut off value, $T_{2cutoff}$, is referred to the value below which the corresponding fluids are expected to be non-movable and above which the corresponding fluids are moveable (Figure 2-5). Default values of 33 millisecond and 92 millisecond are used as $T_{2cutoff}$ for sandstones and carbonates respectively in the absence of laboratory data (Coates et al., 1999).

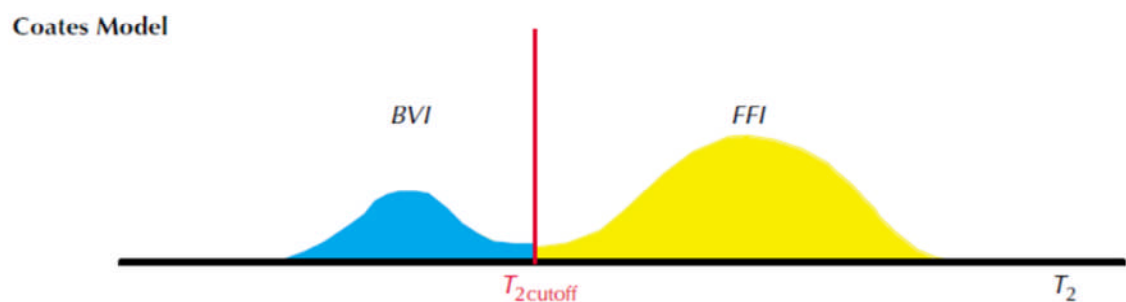


Figure 2-5: NMR T_2 relaxation time distribution (ms) with a $T_{2cutoff}$ value subdividing the fluids into non-movable (bulk volume irreducible BVI and clay bound water) and movable free fluid (free fluid index FFI) (from Coates et al., 1999).

2.14.1 NMR measurements

First, the samples were fully saturated with water as described in Section 2.11, and each sample was then gently rolled on a piece of paper tissue to adsorb excess of water on the sample. The sample was then weighed using the electronic balance to get the total weight of the sample and the water. The sample was wrapped with a piece of cling film before being placed into the sample chamber inside an Oxford MARAN Ultra NMR spectrometer to measure the relaxation time, T_2 . The cling film helps to prevent evaporation of water as the NMR instrument runs at about 35° C with operating frequency of 2 MHz. NMR data was acquired and saved into a computer that is connected to NMR instrument using CPMG software. Data was fitted, using WinFit and WinDXP programs as shown in Figure 2-6.

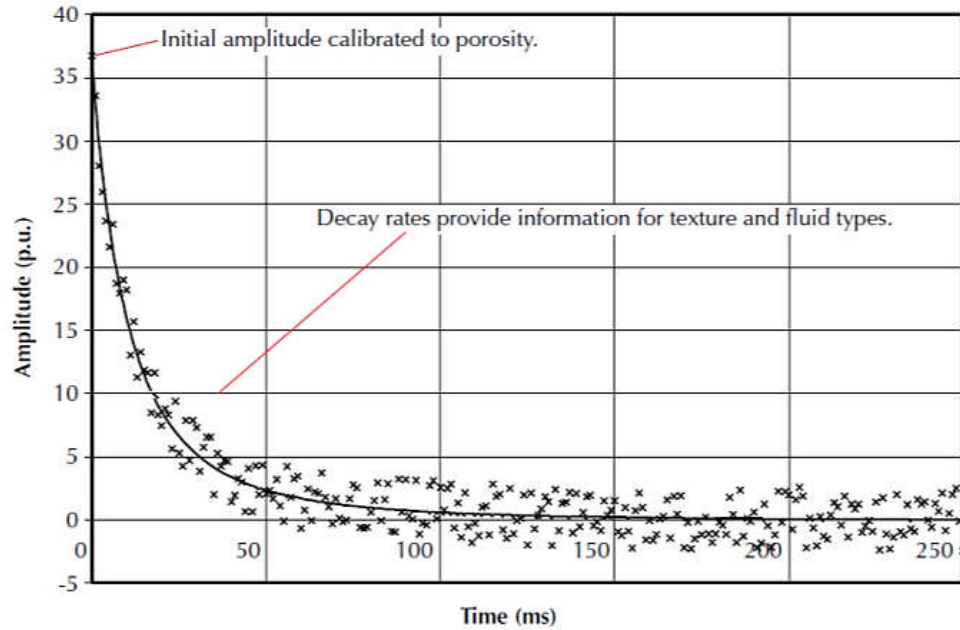


Figure 2-6: NMR amplitude signal decay against time in millisecond with measured raw data points and a fitting curve (from Coates et al., 1999).

NMR measurements were obtained for the samples at different saturation conditions. First when fully saturated with water ($S_w = 100\%$) and then after being partially desaturated at a certain drainage pressure ($S_w = \text{irreducible}$). After obtaining the NMR data, amplitude was converted to the cumulative porosity and incremental porosity in order to determine the values of $T_{2\text{cutoff}}$. First, the acquired amplitude data was divided by the number of NMR scans to convert them to pore volume, which was then divided by the measured dry bulk volume of the sample to obtain the porosity in percentage. The value of the $T_{2\text{cutoff}}$ was determined from the plot of the cumulative porosity curve by extrapolating the porosity of the irreducible water to intersect with the cumulative curve of the T_2 at $S_w = 100\%$ (Figure 2-7), where the intersection corresponds to the $T_{2\text{cutoff}}$ value at the certain capillary pressure.

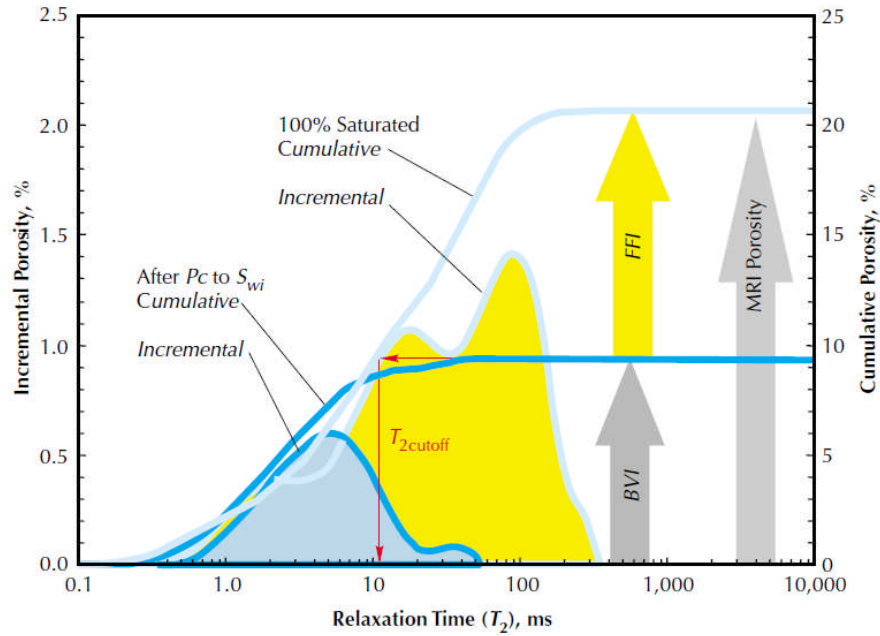


Figure 2-7: NMR T₂ distribution against incremental porosity (left y-axis) and cumulative porosity (right y-axis) in percentage, with the T_{2cutoff} determined at the intersection of the BVI cumulative porosity with the 100% saturated porosity (from Coates et al., 1999).

2.15 Capillary pressure measurements

2.15.1 Air-brine capillary pressure tests

Air-brine capillary pressure data was obtained using the porous plate and the vapour sorption in the humidity chamber techniques; these are described below.

2.15.1.1 Porous plate

Porous plate method is used to obtain the capillary pressure data for fully saturated samples. Samples saturated with simulated brine were placed on a porous diaphragm inside a porous plate chamber (Figure 2-8). This diaphragm has an entry pressure larger than the maximum entry pressure of the samples to allow the drainage of the wetting phase. To improve the capillary contact, clay paste was put between the samples and the diaphragm. After shutting and sealing the lid of the chamber, the pressure of the gas, non-wetting phase displacing water in this case, was increased to 35 psi initially. Equilibrium is the stage where no more brine is produced from the samples during the drainage process in the air-brine system, and this is when the pressure is increased to the next step. Volume of produced water was monitored until

it reached equilibrium indicating no more brine was produced at this pressure. The gas pressure was then increased to 75 psi as the second step, and finally to 130 psi. Volume of the brine produced was monitored during drainage at each pressure.

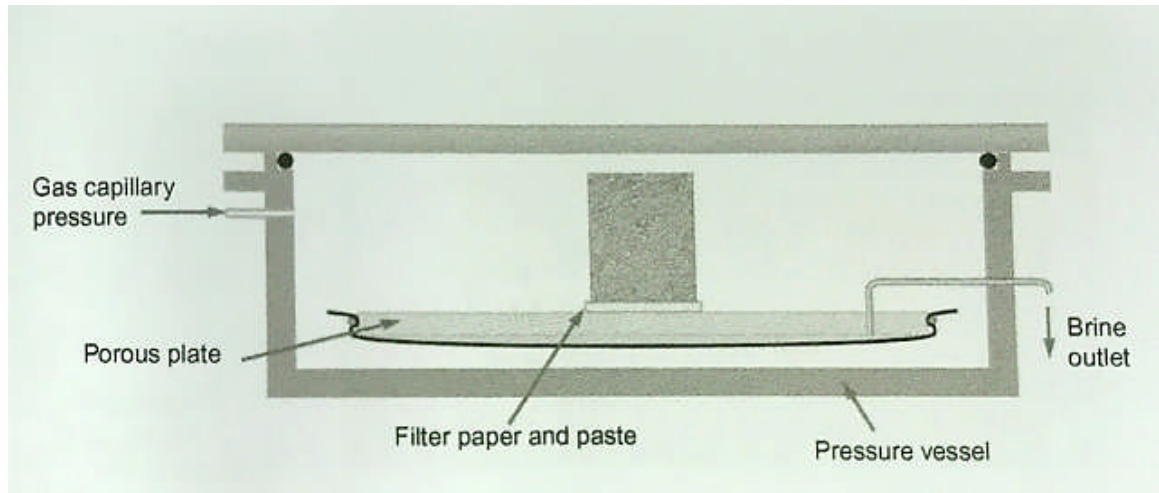


Figure 2-8: Porous plate chamber showing a core plug on top of a porous diaphragm used for capillary pressure measurements (from McPhee et al., 2015).

All samples were weighed when fully saturated with brine using an electronic balance. Every sample was weighed after every pressure step to determine the weight change due to water drainage. Every sample was also scanned with the NMR to determine the amount of water drained at each pressure. Capillary pressure curve for each sample was constructed by plotting the different determined water saturations in percentage against the different pressures. Steps followed are summarised below:

- The sample was weighed dry using an electronic balance
- It was fully saturated with simulated brine using vacuum chamber and pressurized to ensure maximum water saturation with no air remaining in the samples
- It was weighed then wrapped in cling film and scanned with NMR
- It was placed in the porous plate chamber starting with 35 psi pressure and monitor the amount of produced water until no more water was produced
- The sample was taken out of the chamber, weighed and scanned with NMR
- It was placed again in the porous plate and the pressure was increased to 75 psi and the samples were left for a couple of weeks with monitoring the amount of produced water
- It was weighed and scanned with NMR
- Last step in porous plate chamber with 130 psi for a couple of weeks

- Sample was finally weighed and scanned with NMR
- Volume of drained water was determined and plotted against the three different capillary pressures

2.15.1.2 Vapour desorption

Vapour-desorption method is based on the principle introduced by Thomson (Lord Kelvin) (1871) that the vapour pressure is a function of the liquid surface curvature. Since the capillary pressure data is also a function of the liquid surface curvature, both vapour pressure and capillary pressure are controlled by the liquid saturation in the porous rock (Newsham et al., 2004). Early workers used such method to obtain the relationship between the capillary pressure and the vapour pressure (Calhoun et al., 1949; Melrose, 1987). Controlling the vapour pressure in a porous media can be achieved by controlling the saturation equilibrium using humidity chambers with different salt concentrations that control the relative humidity in the chambers (Table 2-2). Capillary pressure can be determined from the relative humidity of different salt types using Equation 2-13 that is based on the classic Kelvin equation (Newsham et al., 2004).

Equation 2-13

$$P_c = -\frac{RT}{V_m} \ln\left(\frac{R_H}{100}\right)$$

where:

P_c = capillary pressure

R = universal gas constant

R_H = relative humidity

T = absolute temperature

V_m = molar volume of water (0.018016)

Salt type	RH % @ 25°C	Capillary pressure (psi)
Potassium sulphate	97	607
Potassium nitrate	92	1660
Potassium chloride	85	3236
Ammonium sulphate	80	4443
Ammonium nitrate	65	9518

Table 2-2: Relative humidity RH percentage with equivalent capillary pressure determined with different salt types.

The samples were placed in humidity chambers with different relative humidity to obtain the water saturation at the equivalent capillary pressure. The samples were weighed continuously until they reach constant weights indicating equilibrium that is no more water is drained. Difference in weights before and after a certain pressure is the weight of the water drained out of the sample. Volume of the drained water is calculated as this weight divided by the measured density of the water used (density of distilled water 1 g/cm^3). Water saturation was determined as the ratio of the brine volume to the pore volume of the sample. Capillary pressure was plotted against the determined water saturation, and capillary pressure data acquired from this method was combined with data acquired from the porous plate technique to obtain capillary pressure data at low pressures that cannot be obtained by vapour desorption. *PP-VD* combined capillary pressure is referred to the combined data from these techniques.

2.15.2 Mercury injection capillary pressure

Most MICP measurements that are now undertaken by industry are conducted using a high pressure system in which samples are placed under a confining pressure. The University of Leeds has, however, also built a unique MICP instrument that allows measurements to be made at a pre-determined confining pressure. These two tests are referred to as MICP and porosimetry under confining stress (PUCS) respectively and are described below.

2.15.2.1 Mercury injection capillary pressure

MICP was conducted using a Micromeritics Autopore IV 9520 Hg-injection system in the Wolfson laboratory with sample size of approximately 3 cm^3 . One 3-cm^3 sub-

sample was cut from each core plug using a diamond tooled trim saw. The sample was cleaned and dried before being placed in the sample chamber of the equipment where it was evacuated before injecting the mercury. Mercury, which is a non-wetting fluid, does not penetrate the sample spontaneously. Thus, it is forced into the sample by applying pressure in steps to allow for equilibrium at each step and to record the volume of the intruded mercury. An injection rate of 0.001 $\mu\text{l/g/s}$ was defined as the value below which the change of pressure step was applied. This change in pressure step can be applied at fixed times, commonly 15 seconds, rather than the injection rate. The change in the mercury volume as a result of the pressure change indicates the pore volume filled with mercury.

The lowest recorded pressure is referred to as the entry pressure at which mercury enters the pore system, which represents the minimum Hg saturation. The lowest pressure of nearly 2 psi corresponds to the largest pore size that is approximately 90 μm in diameter. Hg saturation at the maximum pressure of the equipment, which is 60,000 psi, is referred to as the maximum mercury saturation S_{HgMax} , and it corresponds to the smallest pore throat diameter of approximately 0.003 μm .

The sample was placed in a penetrometer that is a glass cup, which was initially filled with mercury at the pre-set step. The sample was then subjected to a series of low-pressure steps up to approximately 25 psi. After that, the penetrometer was transferred to the high-pressure set up where it was immersed in an oil bath inside a pressure vessel to apply hydraulic pressure in order to inject mercury at higher-pressure steps to the maximum pressure (Figure 2-9). The Hg-injection pressure was increased by applying more pressure to the oil. The volume of the mercury injected, saturation of mercury, was then plotted as a function of the injection pressure to construct the capillary pressure curve. Incremental mercury saturation was also plotted against the calculated pore throat diameters to obtain the pore throat size distribution plot. The blank correction was performed in the laboratory by running several penetrometer calibrations rather than the statistical blank correction.

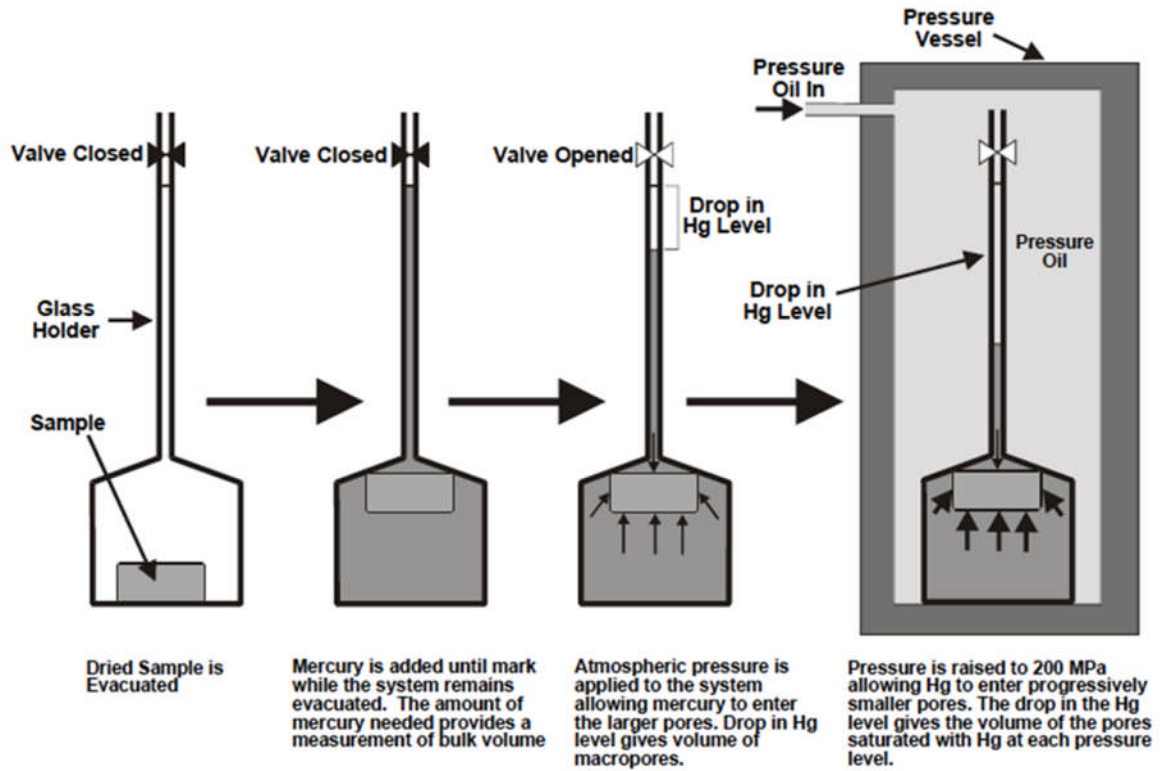


Figure 2-9: A schematic of the mercury injection porosimetry (from Glover, 2016).

The MICP data was converted to an equivalent air-brine system at laboratory conditions to be compared with data acquired from other methods, namely porous plate and vapour desorption. The conversion was obtained by using Equation 2-14 derived from Washburn (1921) expression (Equation 1-12). By incorporating the values of the interfacial tensions and contact angles into Equation 2-14, conversion expression for air-brine system is yielded (Equation 2-15). The conversion factor was also determined to be approximately 0.2 from a nomogram (Figure 2-10) that was presented by Schowalter (1979).

Equation 2-14

$$P_{c_{hw}} = P_{c_{aHg}} \frac{\sigma_{hw} \cos \theta_{hw}}{\sigma_{aHg} \cos \theta_{aHg}}$$

where:

$P_{c_{hw}}$ = capillary pressure (hydrocarbon-water system)

$P_{c_{aHg}}$ = capillary pressure (air-mercury system)

σ_{hw} = hydrocarbon-water interfacial tension (oil-water = 30 dynes/cm and gas-water = 70 dynes/cm)

σ_{aHg} = air-mercury interfacial tension (480 dynes/cm)

θ_{hw} = hydrocarbon-water contact angle (oil-water = gas-water = 0°)

θ_{aHg} = air-mercury contact angle (140°)

Equation 2-15

$$P_{c_{gw}} = 0.19P_{c_{aHg}}$$

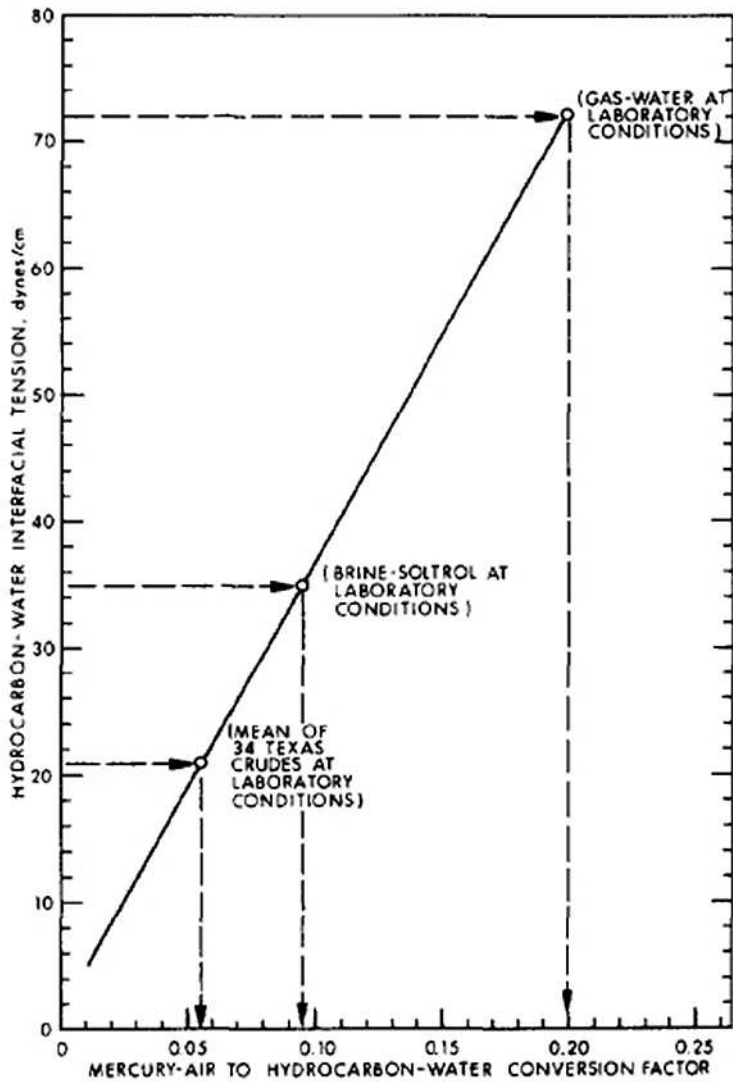


Figure 2-10: A nomogram to determine the conversion factor from mercury-air to air-water system at laboratory conditions (from Schowalter, 1979).

2.15.2.2 Mercury injection porosimetry under confining stress (PUCS)

The mercury injection under stress method was performed using Porosimetry under Confining Stress (PUCS) that was custom-built in the Wolfson Laboratory, which is capable of conducting mercury injection on a 38 mm core plug under confining stress

up to 75,000 psi (Guise et al., 2017). A few plug samples were picked for this test as the samples were contaminated with mercury and could not be used for further analysis after this test. A net stress, which is the difference between the confining stress and the pore pressure applied through the mercury injection, was kept constant during the entire test (Guise et al., 2017). First, the cleaned and dried core plug was loaded into a sample assembly to be evacuated. Then, the assembly was filled with mercury prior to placing it into the pressure vessel to apply the stress. Net stress was then applied and left overnight for approximately 12 hours. The setup was connected to a software that recorded the mercury volume and automatically controls the mercury pressure and the confining stress. Mercury was injected into the sample from one side, and the pressure step was changed when the injection rate reached below $0.001 \text{ mm}^3/\text{cm}^2/\text{s}$ (Guise et al., 2017). Since the core plug was evacuated, the sample was non-conductor. Thus, the moment the mercury spanned through the whole core plug, the resistivity significantly dropped indicating the breakthrough pressure (Guise et al., 2017).

3 Routine Core Analysis Results

3.1 Introduction

Porosity and permeability are two of the key petrophysical properties where porosity controls the volume of hydrocarbons and permeability is the property governing the hydrocarbon flow rate. Permeability cannot be measured directly from the wireline logs unlike porosity, and thus estimating the flow rate in tight gas sandstones is critical due to their marginal returns. Estimating permeability in tight gas sandstone (TGS) is more difficult than conventional reservoirs. This is due to the smaller grain size, the abundance of clay minerals and the impact of the depositional and diagenetic processes (Schmitt et al., 2015). Understanding the controls on the porosity and permeability is important to better evaluate such tight reservoirs and to optimize the fluid flow modelling.

This chapter presents all the results of the petrophysical properties measurements conducted in the Wolfson laboratory for three suites (group A, group B and group C) of tight sandstone core plugs used for this thesis. Porosity measured at ambient and brine permeability and gas permeability measured at different net stresses are presented. Quantitative mineralogy analyses with SEM images are presented. Mercury injection data are also plotted with SEM images of all samples for microstructures and pore size distributions analyses. The controls on porosity and permeability such as grain size and sorting, the confining stress, the presence of clay as well as microfractures are all discussed.

3.2 Methodology

The samples' preparation, involving cleaning and drying, is described in Section 2.3. The techniques and instruments used to determine the porosity and permeability are presented in Section 2.5 and 2.6 respectively while brine preparation and brine permeability are discussed in Sections 2.10 through 2.12. Analysis of the mineralogy of each sample was performed using the QXRD technique described in Section 2.7 with description of the scanning electron microscope used to obtain SEM images is described in Section 2.8. The capillary pressure data, presented in section 3.3.7, acquired using the mercury injection method is presented in Section 2.15.2.1.

3.3 Results

The samples of all suites have a gas permeability of less than 0.1 mD. Similar to most tight gas sandstone reservoirs, the samples have experienced a range of diagenetic processes. The diagenesis includes mechanical compaction, dissolution, quartz overgrowth and formation of clay in forms of grain coating and pore lining. The samples composed of mainly quartz followed by clay and K-feldspar as the minor minerals with traces of calcite and dolomite in some samples. The samples of the first suite (group A) proved to be even tighter, having less permeability and porosity, compared to other suites, group B and group C. Group A was taken from depth range (3940 to 3960 m) while group B and C were taken from depth ranges of (4310 to 4322 m) and (4838 to 4880m) respectively. Although all suites showed some heterogeneity, group A looked more heterogeneous, hence greater diagenesis, than the other two groups.

3.3.1 Porosity

Helium porosity measured at ambient condition for the 29 samples are presented in Table 3-1. The samples have an average porosity of 5.9% with a minimum porosity of approximately 2% and a maximum value of approximately 12% (Figure 3-1).

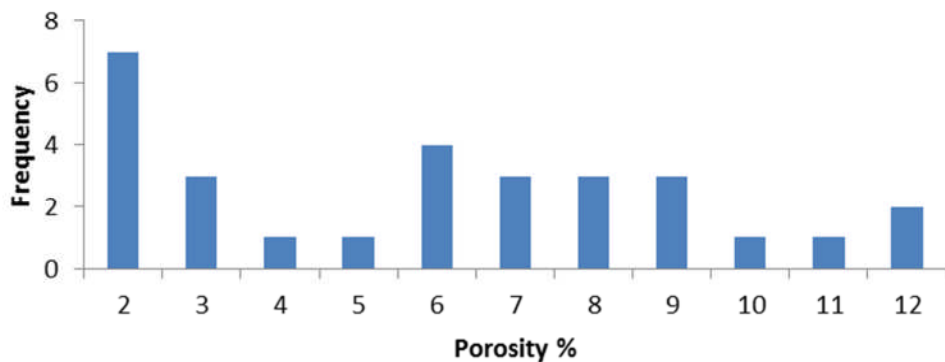


Figure 3-1: Histogram showing the porosity frequency in all the 29 analysed samples. The porosity values were rounded to the nearest whole number.

Sample No.	He (%) Porosity	k _w @ 1500 psi	k _g @ 500 psi	k _g @ 1500 psi	k _g @ 5000 psi	k _g @1500psi / k _w @1500psi	Grain Size	Grain Sorting
Group A								
TS2-1	2.3	0.000032	0.00097	0.00024	0.000008	7.5	M	W
TS 2-2	2.7	0.00011	0.00081	0.00038	0.000023	3.5	UF	M
TS 2-3	8.7	0.0002	0.0022	0.0012	0.00033	6	M	M
TS 2-4	7.2	0.00012	0.0017	0.00094	0.00045	7.9	M	W
TS 2-5	8.5	0.000076	0.0026	0.0022	0.00026	28.9	M	W
TS 2-6	5.1	0.000031	0.0017	0.0012	0.00005	38.7	UF	W
TS 2-7	6.4	0.000022	0.0022	0.001	0.00032	45.5	M	W
TS 2-8	2.3	0.000022	0.0012	0.0014	0.000052	63.6	UF	W
TS 2-9	3.8	0.000026	0.0023	0.0014	0.00013	53.8	UF	W
TS 2-10	1.7	0.00003	0.0004	0.0004	0.000001	13.3	UF	W
TS 3-1	1.5	0.000008	0.00034	0.0002	0.000004	25	UF	W
TS 3-2	1.8	0.000022	0.00091	0.00033	0.00001	15	UF	W
TS 3-3	1.8	0.000033	0.00083	0.00031	0.000012	9.4	UF	W
TS 3-4	2.6	0.000034	0.00073	0.00037	0.000018	10.9	M	W
TS 3-5	1.6	0.000047	0.00089	0.0005	0.00004	10.6	LF	W
Group B								
TS5-2	6.5	0.0046	0.024	0.021	0.0025	4.6	UF	M
TS5-5	11.3	0.0055	0.05	0.047	0.016	8.6	UF	W
TS7-1	6.4	0.0019	0.007	0.006	0.00083	3.2	LF	M
TS7-4	11.5	0.0068	0.035	0.035	0.0064	5.1	LF	M
TS7-5	8.3	0.0015	0.005	0.006	0.0012	4	VF	W

Group C								
TS1-55	7.6	0.0005	0.013	0.007	0.0014	14	UF	W
TS1-197	8.1	0.0026	0.025	0.016	0.0045	6	UF	W
TS1-305	12	0.0026	0.059	0.051	0.037	19.6	UF	W
TS4-4	6.9	0.008	0.037	0.033	0.029	4	LF	VW
TS4-11	6.1	0.0005	0.011	0.0077	0.0038	15.4	VF	W
TS5-11	9.7	0.023	0.17	0.16	0.13	6.8	VF	W
TS1-25	3	0.0011	0.053	0.04	0.007	36.4	UF	M
TS2-25	9.2	0.041	0.38	0.33	0.27	8	M	W
TS3-47	5.7	0.0019	0.029	0.024	0.015	12.6	UF	W

Table 3-1: Routine helium ambient porosity in percentage with $\pm 0.2\%$ error and brine permeability k_w at 1500 psi and gas permeability k_g at 500, 1500 and 5000 psi all within $\pm 10\%$ uncertainty, and k_g/k_w ratio at 1500 psi for the samples of the three suites. Grain size is shown as VF = very fine (grain size 0.0625 – 0.125 mm), LF = lower fine (grain size 0.125 – 0.177 mm), UF = upper fine (grain size 0.177 – 0.25 mm) and M = medium (grain size 0.25 – 0.5 mm) based on Wentworth scale (1922). Grain sorting is shown as very well sorted (VW), well sorted (W), moderately sorted (M).

3.3.2 Permeability

The geometric mean of the gas permeability measured at 500 psi is 0.0056 mD with a minimum and a maximum of 0.00034 mD and 0.38 mD respectively. The minimum gas permeability measured at 1500 psi is 0.0002 mD and the maximum is 0.33 mD. The geometric mean of the gas permeability measured under 1500 psi is 0.0048 mD, and it is 0.00053 mD for measurements at 5000 psi. The minimum measured gas permeability at 5000 psi net stress is 0.0000012 mD and the maximum is 0.27 mD. All samples showed a decrease in permeability as the net stress was increased to 500, 1500, 5000 psi as shown in Figure 3-2, Figure 3-3 and Figure 3-4 respectively.

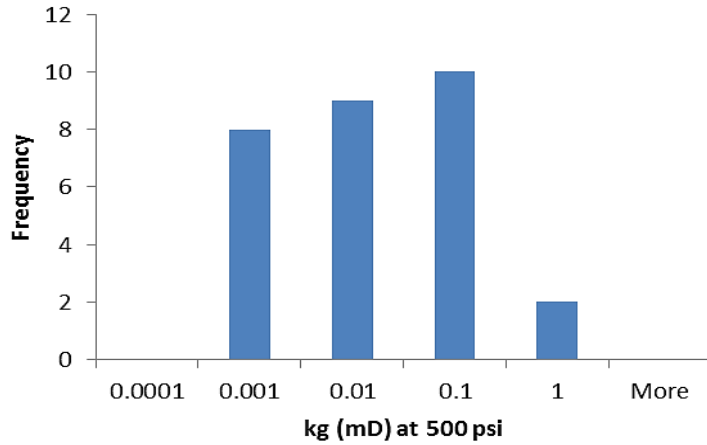


Figure 3-2: Histogram showing the range of the gas permeability measured at 500 psi stress ($\pm 10\%$ uncertainty). The permeability value in x-axis is the upper limit for the bin range.

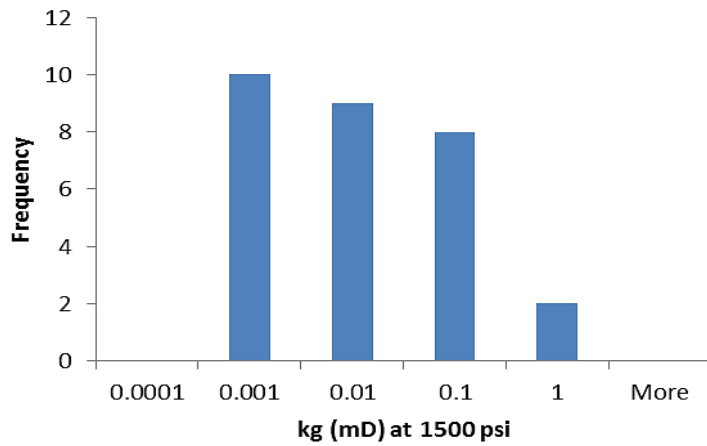


Figure 3-3: Histogram showing the range of the gas permeability measured at 1500 psi stress $\pm 10\%$ uncertainty. The permeability value in x-axis is the upper limit for the bin range.

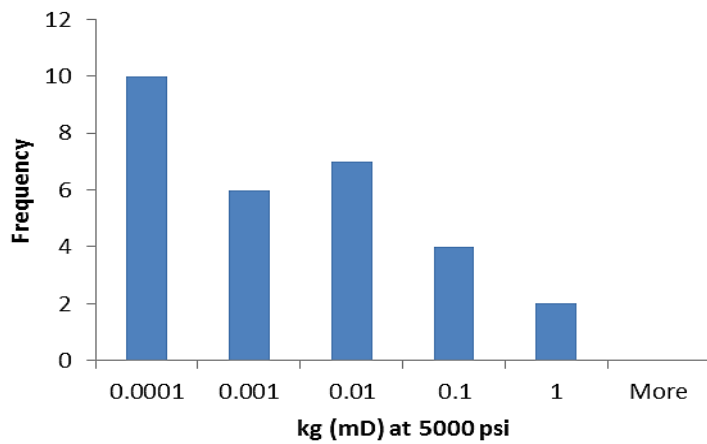


Figure 3-4: Histogram showing the range of the gas permeability measured at 5000 psi stress $\pm 10\%$ uncertainty. The permeability value in x-axis is the upper limit for the bin range.

3.3.3 Porosity permeability relationship

A plot of the porosity measured at ambient against permeability measured at low stress (i.e. 500 psi) is shown in Figure 3-5. A general trend shows that permeability increases as the porosity increases for all suites of samples with an exponential relationship (Equation 3-1) having a correlation coefficient of 0.64. Porosity stress-corrected at 5000 psi was plotted against gas permeability measured at 5000 psi net stress to evaluate the effect of stress on the porosity-permeability relationship. The increase in net stress improved the correlation between the porosity and permeability. The data of all three sets of samples was fitted with a power law (Equation 3-2) with a correlation coefficient of 0.75.

Equation 3-1

$$k_g = 0.0004194e^{44.48\phi}$$

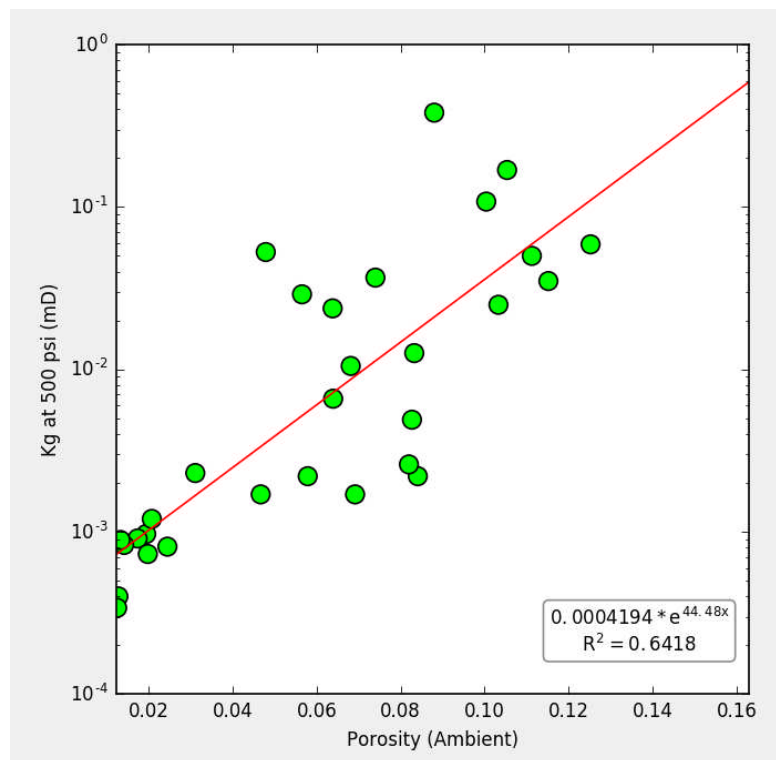


Figure 3-5: Plot of ambient porosity (fraction) with $\pm 0.2\%$ uncertainty vs. measured gas permeability (k_g) at 500 psi with $\pm 10\%$ uncertainty for all samples fitted with an exponential relationship having a correlation coefficient of 0.64.

Equation 3-2

$$k_g \text{ at } 5000 \text{ psi} = 27.51 \phi_{\text{at } 5000 \text{ psi}}^{3.254}$$

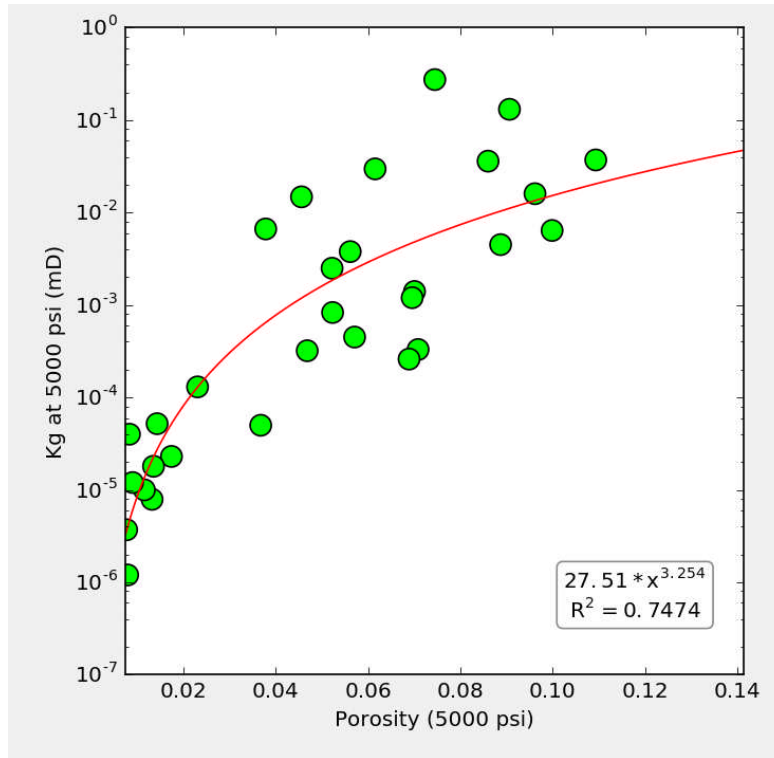


Figure 3-6: Plot of porosity (fraction) stress-corrected at 5000 psi with $\pm 1\%$ uncertainty vs. gas permeability (k_g) measured at 5000 psi net stress with $\pm 10\%$ uncertainty for all samples fitted with a power law relationship with a correlation coefficient of 0.75.

3.3.4 Brine permeability

Table 3-1 shows gas permeability and brine permeability both measured under 1500 psi net stress for all samples with the ratio of the gas permeability to the brine permeability (k_g/k_w). Brine permeability was plotted against gas permeability for comparison (Figure 3-7). A power law relationship exists between brine and gas permeabilities of all samples with a correlation coefficient of 0.91 (Equation 3-3). The measured brine permeability was lower than the gas permeability at the same stress of 1500 psi for all samples, and the difference is greater for samples with relatively lower permeability.

Equation 3-3

$$k_w = 0.1461 * k_g^{1.104}$$

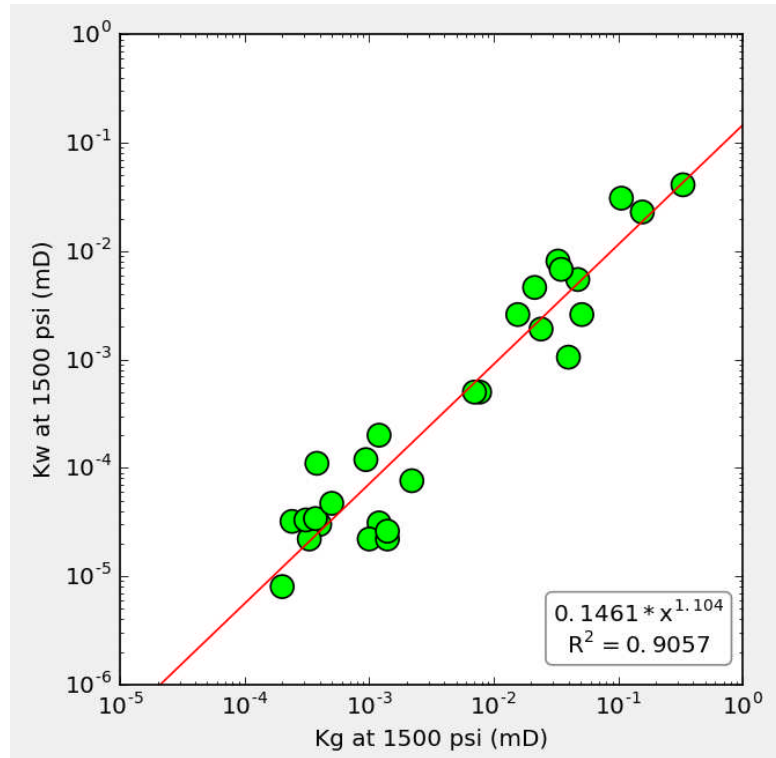


Figure 3-7: Plot of brine permeability (k_w) against the gas permeability (k_g) both measured under 1500 psi net stress and within $\pm 10\%$ uncertainty. A power law relationship exists with a correlation coefficient of 0.91.

3.3.5 Quantitative mineralogy

Table 3-2 shows the mineralogy composition in percentages determined for all the samples in the three suites using QXRD technique. The samples are composed of quartz and clay mainly with the presence of other minerals like calcite and dolomite at different fractions. The minimum and maximum quartz seen in the samples were 20.2 and 81.2% respectively. The maximum volume of clay was 38.7% and the minimum was 3.8%. Calcite cement was found only in the first suite of samples, which was in the range between 0 and 22.2%. Trace of calcite that is 0.3% was seen in sample TS1-25.

Sample No.	Quartz	Albite	Microcline	Calcite	Dolomite	Mica	Illite-smectite	Kaolinite	Chlorite	Siderite
Group A										
TS2-1	45.5	14.8	0.0	2.3	0.9	4.1	9.6	0.0	25.8	0.0
TS 2-2	47.0	22.0	4.6	0.0	0.0	8.7	8.6	0.0	9.1	0.0
TS 2-3	43.7	27.7	0.0	0.7	0.0	3.9	6.9	0.0	17.2	0.0
TS 2-4	49.0	21.4	0.0	8.7	0.0	3.4	6.2	0.0	11.4	0.0
TS 2-5	29.4	32.9	0.0	1.6	0.0	3.0	4.2	0.0	29.7	0.0
TS 2-6	20.2	30.1	0.0	0.9	1.1	6.8	13.7	0.0	25.0	0.0
TS 2-7	21.8	26.1	0.0	1.4	0.3	9.3	12.0	0.0	24.9	0.0
TS 2-8	42.2	22.3	0.0	3.2	0.8	2.4	13.8	0.0	17.2	0.0
TS 2-9	34.2	30.3	0.0	8.6	0.7	5.0	6.5	0.0	17.3	0.0
TS 2-10	43.5	12.7	0.0	16.5	0.4	3.0	5.1	0.0	18.7	0.0
TS 3-1	45.5	14.8	0.0	2.3	0.9	4.1	9.6	0.0	25.8	0.0
TS 3-2	40.7	18.3	0.0	10.6	0.0	5.6	9.2	0.0	15.6	0.0
TS 3-3	51.8	28.6	0.0	1.6	0.0	4.9	3.8	0.0	10.3	0.0
TS 3-4	40.6	18.8	0.0	22.2	0.0	5.2	5.9	0.0	11.1	0.0
TS 3-5	36.3	23.6	0.0	9.0	0.0	4.3	12.2	0.0	14.5	0.0
Group B										
TS5-2	75.5	0.0	0.0	0.0	6.8	2.2	2.7	8.6	0.0	3.5
TS5-5	79.3	0.0	0.0	0.0	4.6	5.3	0.0	9.5	0.0	0.0
TS7-1	76.4	7.7	1.8	0.0	4.7	3.9	5.4	0.0	0.0	0.0
TS7-4	66.4	13.3	4.7	0.0	5.5	5.8	4.4	0.0	0.0	0.0
TS7-5	65.0	14.4	6.5	0.0	0.0	6.5	7.6	0.0	0.0	0.0
Group C										
TS1-55	76.0	5.4	0.0	0.0	3.6	5.6	3.6	0.0	7.0	0.0
TS1-197	77.1	4.2	0.0	0.0	5.7	10.5	0.0	0.0	3.8	0.0
TS1-305	77.3	3.4	0.0	0.0	4.1	6.5	2.1	0.0	5.7	0.0
TS4-4	57.2	16.7	9.0	0.0	10.6	3.8	0.0	0.0	5.2	0.0
TS4-11	57.5	17.5	12.3	0.0	2.5	2.6	0.0	0.0	11.6	0.0
TS5-11	56.5	26.3	10.9	0.0	1.7	2.1	0.0	0.0	5.1	0.0
TS1-25	73.9	1.9	0.0	0.3	14.2	6.1	0.0	4.8	0.0	1.6
TS2-25	73.2	2.0	1.5	0.0	5.8	8.2	0.0	6.4	0.0	4.8
TS3-47	81.2	1.2	1.4	0.0	4.3	5.8	0.0	8.4	0.0	0.1

Table 3-2: Mineralogy (%) of all samples obtained using quantitative x-ray diffraction technique (QXR).

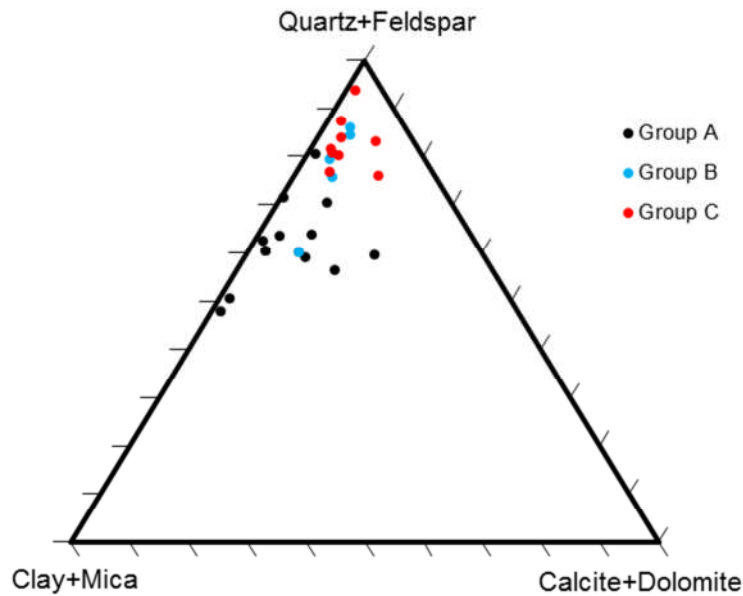


Figure 3-8: Ternary plot showing the major mineral composition of the samples in all three groups (group A, B and C).

3.3.6 SEM analysis

The group-A samples have experienced a range of diagenetic processes including microcrystalline quartz, K-feldspar, chlorite, calcite and illite precipitation. The first mineral to precipitate was microcrystalline quartz coating all detrital grains and filling most of the macroporosity of the samples. Remaining macroporosity was then filled with a combination of chlorite and calcite and to a lesser extent macrocrystalline quartz and illite. The mineral precipitation has been so intense that only microporosity is now available in the samples.

SEM image of sample TS2-1 indicates the sample has no macroporosity due to intense diagenetic alterations. The main diagenetic processes to affect the sample were microcrystalline quartz and calcite cementation. The precipitation of microcrystalline quartz occurs as a thin coating on all detrital grains. The sample contains also authigenic K-feldspar and illite bridging and blocking the pore spaces between quartz grains, and forming micro-porosity (Figure 3-9). This sample has the lowest permeability out of the 15 samples, with no clear microcracks shown. Microcracks and crack-like pores are defined as void spaces that have low aspect ratio, ϵ , which is the ratio of the short axis of the pore to its long axis (Li et al., 2009).

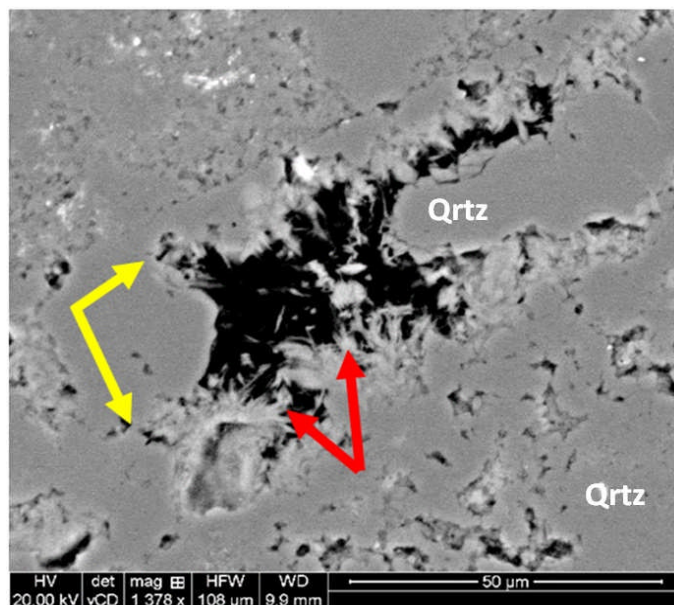


Figure 3-9: SEM image for sample TS2-1 showing clay (illite) (red arrows) blocking and bridging the pores and pore throats between quartz grains (Qrtz) and contributing in the formation of microporosity formation (yellow).

SEM images for sample TS2-4 (Figure 3-10) and sample TS2-7 (Figure 3-11) show the presence of microcracks and grain boundaries cracks that are microns to tens of microns in width. All images show how the samples are compacted and cemented, and such microcracks are present at ambient condition. The microcrystalline quartz and calcite cement are shown in (Figure 3-10 – Right) resulting from the diagenetic processes and deep burial that samples have been through. Figure 3-12 shows the diagenesis of the sample that has gone through major cementation and compaction. The sample is poorly sorted, and it also shows the presence of microfractures and microporosity.

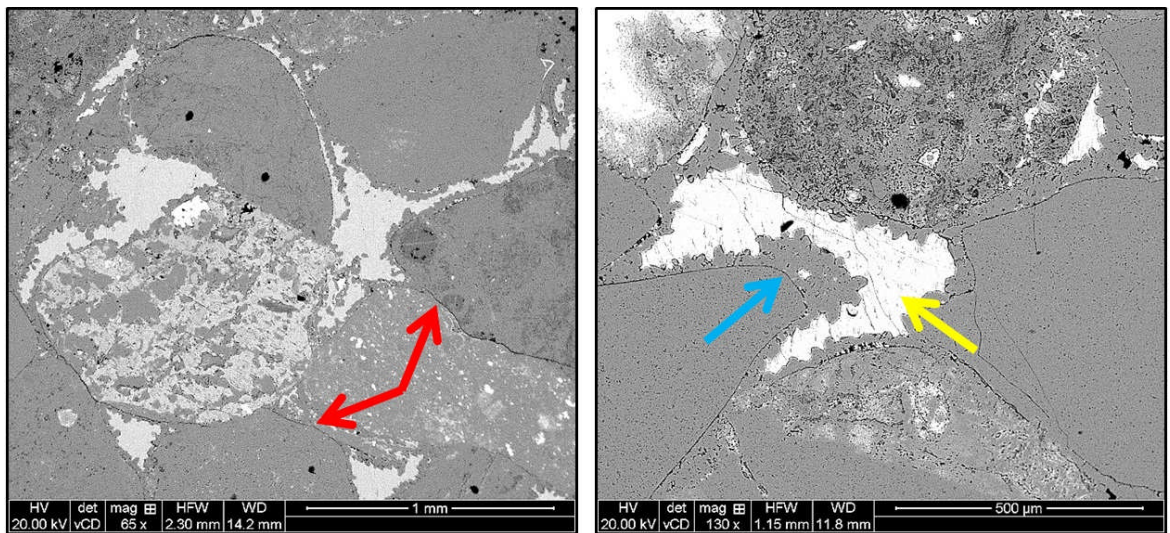


Figure 3-10: SEM images for TS2-4. Left: Abundance of microcracks and grain boundaries cracks (red). Right: microcrystalline quartz (blue) and calcite cement (yellow).

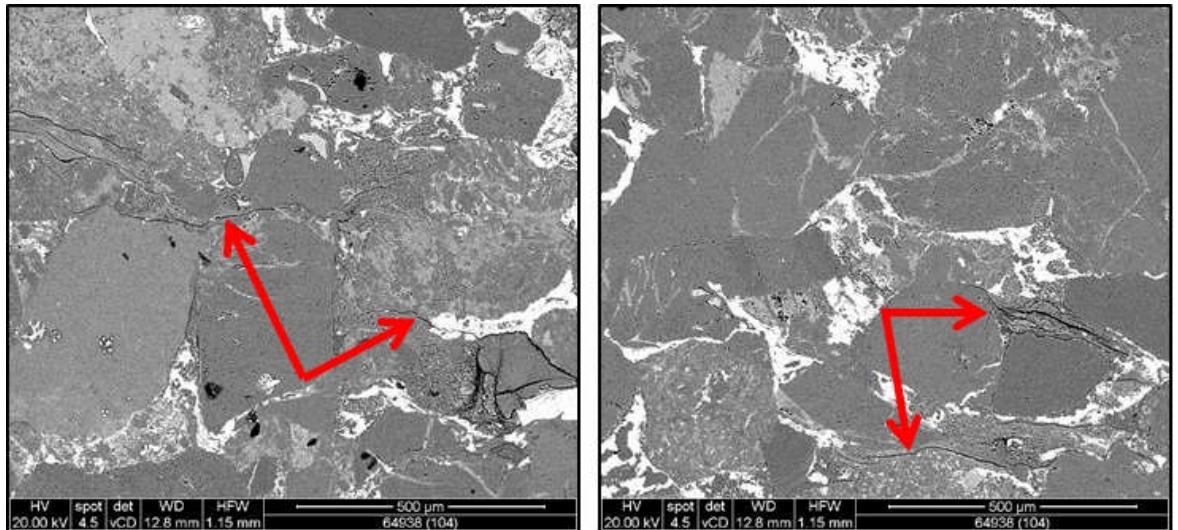


Figure 3-11: SEM images showing the microcracks (red) resulting from the change in stress state in sample TS2-7.

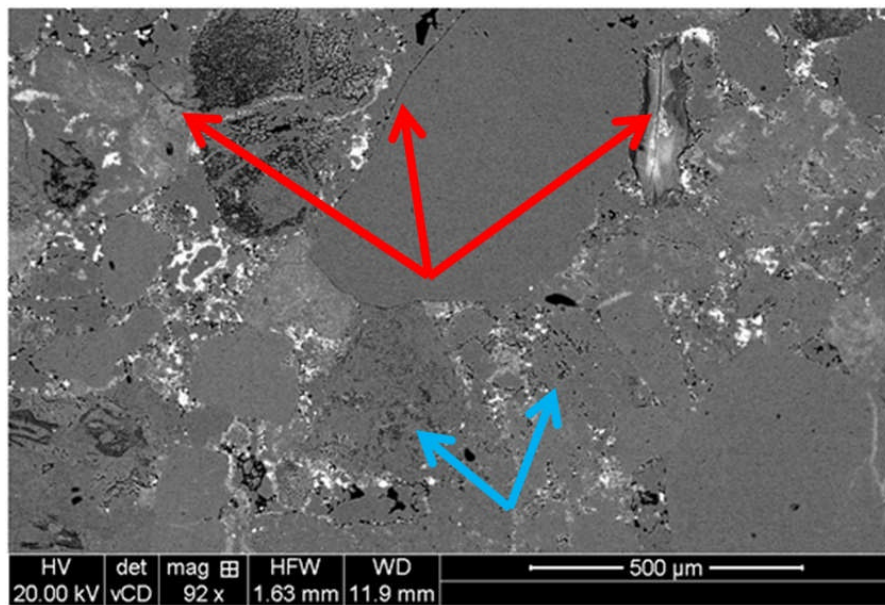


Figure 3-12: SEM image showing the microfractures (red) with the poorly sorted grains and the abundance of microporosity (blue) in sample TS2-3.

SEM images of sample TS2-9 show that the grains are poorly sorted, and well compacted and cemented indicating the deep burial of the samples (Figure 3-13). Microfractures are present in sample TS2-9, at ambient condition. SEM images of sample TS3-1 show the presence of micro-pores and clasts, with no abundance of microcracks (Figure 3-14). A micro-pore space filled with chlorite clay and illite coating the right surface of the pore in sample TS2-4 is shown in Figure 3-15.

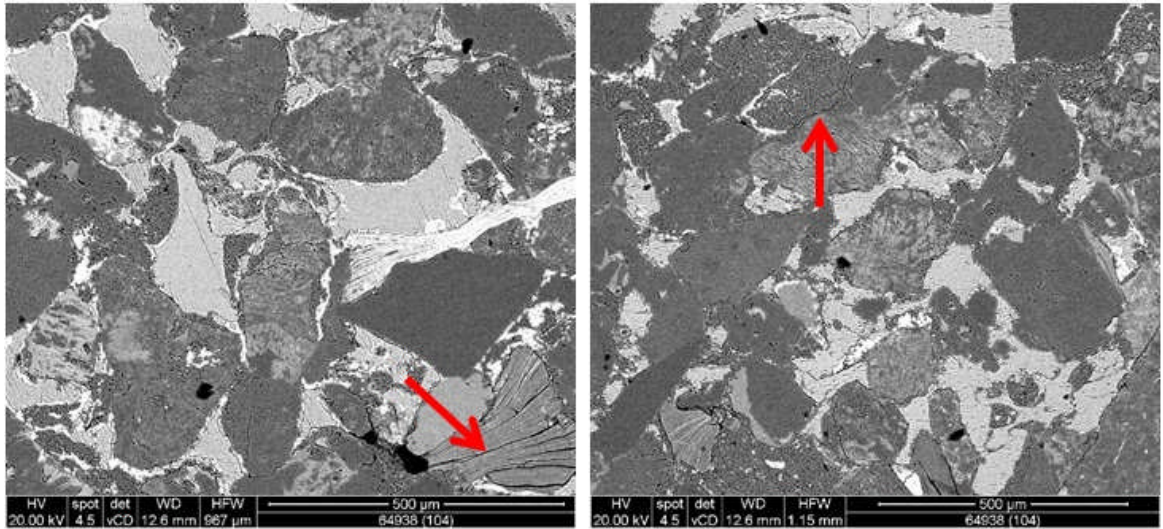


Figure 3-13: SEM images showing the poorly sorted grains which are compacted and cemented with the presence of micro-cracks (red) in sample TS2-9.

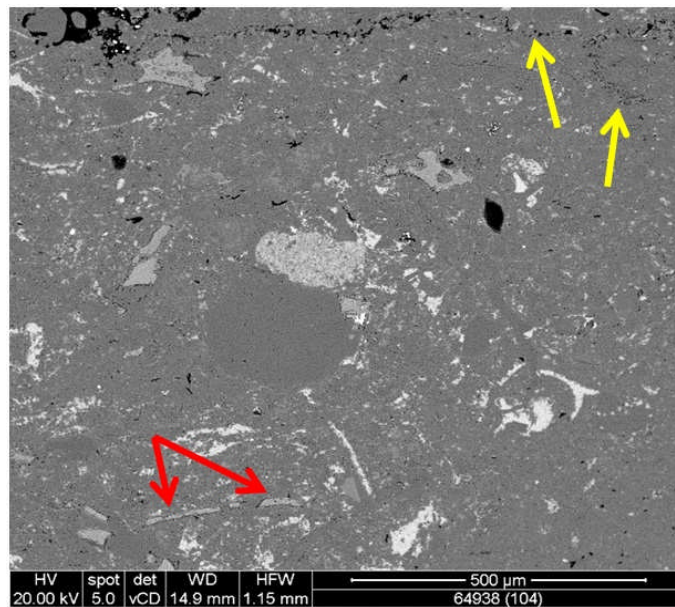


Figure 3-14: SEM image showing the micro-scale heterogeneity of the sample TS3-1 with micro-pores (yellow) and clasts (red).

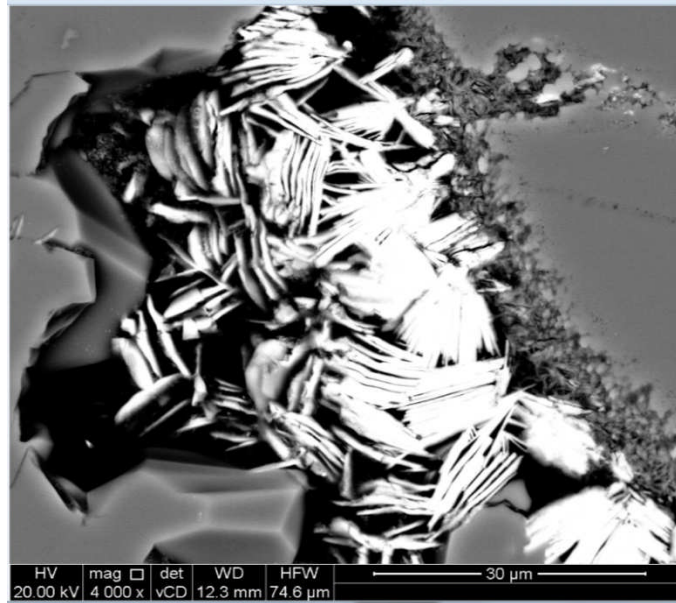


Figure 3-15: SEM image showing a micro-pore space filled with chlorite and illite coating the right surface of the pore in sample TS2-4.

The main diagenetic processes affecting the samples of the group B were dolomite, kaolin and quartz cementation and the precipitation of grain coating illite clay and quartz overgrowth. The dolomite cementation was the first diagenetic process to affect the samples. The dolomite were overgrown by large amounts of ferroan dolomite. Kaolin clearly precipitated after the dolomite but is partially overgrown by ferroan dolomite as well suggesting the two phases overlapped. Quartz cement is present in all samples and occurs as both overgrowths and outgrowths where the proportion of overgrowths to outgrowths decreases as the clay content increases. The kaolin is also frequently intergrown with illite and chlorite. The illite is probably a late stage precipitate.

SEM images of samples TS5-2 and TS5-5 (Figure 3-16) and (Figure 3-17) respectively showed the presence of kaolinite in these samples, which is also confirmed by mineralogy analyses obtained using QXRD (Table 3-2). Microcracks that are a few microns in width is shown in SEM image of sample TS7-5 (Figure 3-18). Figure 3-19 (left) is an SEM image showing the presence of illite coating the grains and filling the pore space in sample TS7-5.

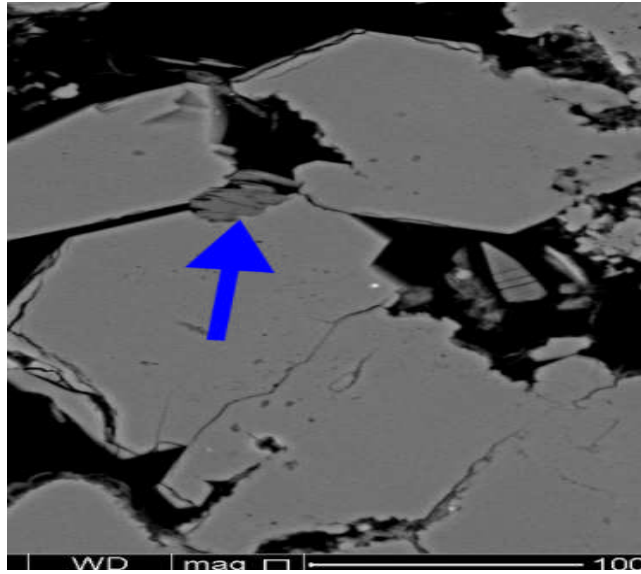


Figure 3-16: SEM image showing quartz overgrowth (red) and kaolinite filling the pore space (blue) in sample TS5-2.

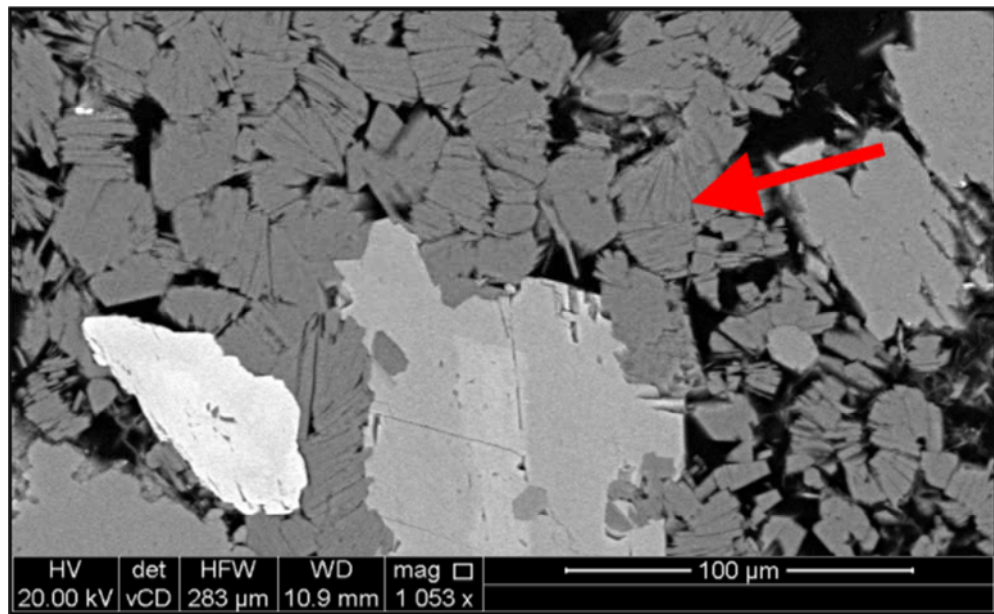


Figure 3-17: SEM image showing kaolinite filling the pore space (red) in sample TS5-5.

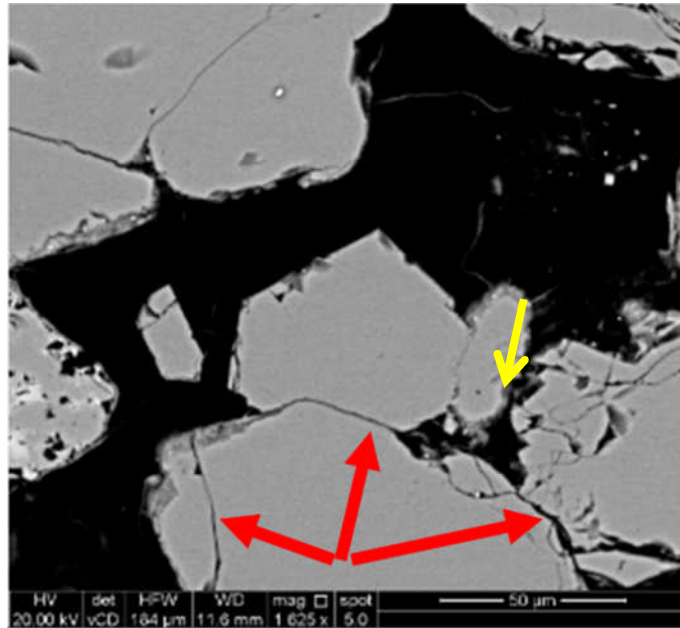


Figure 3-18: SEM image of sample TS7-5 with microcracks (red arrows) that are few microns to sub microns in width, and clay lining the pore (yellow arrow).

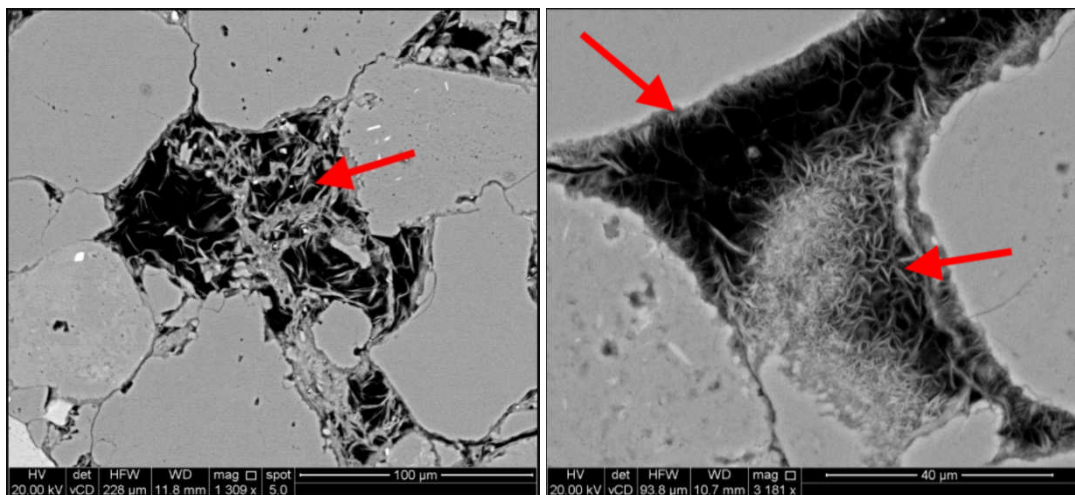


Figure 3-19: SEM image showing the presence of illite filling the pore space (red) of sample TS7-5 (left). SEM image showing hairy grain coating hairy illite (red) in sample TS1-55 (right).

Samples of the third suite, group C, were also affected by different diagenetic processes like precipitation of dolomite and chlorite during shallow burial. Extensive minor quartz, illite, Fe-dolomite as well as small but variable amounts of siderite happened during deeper burial. The precipitation of authigenic dolomite, chlorite and illite are the main diagenetic processes affecting the samples, where chlorite and illite occur as grain coats and pore filling cements. Hairy illite coating the grain is shown in SEM image of sample TS1-55 (Figure 3-19 – right). Grain coating illite and pore filling chlorite in sample TS1-305 are shown in Figure 3-20.

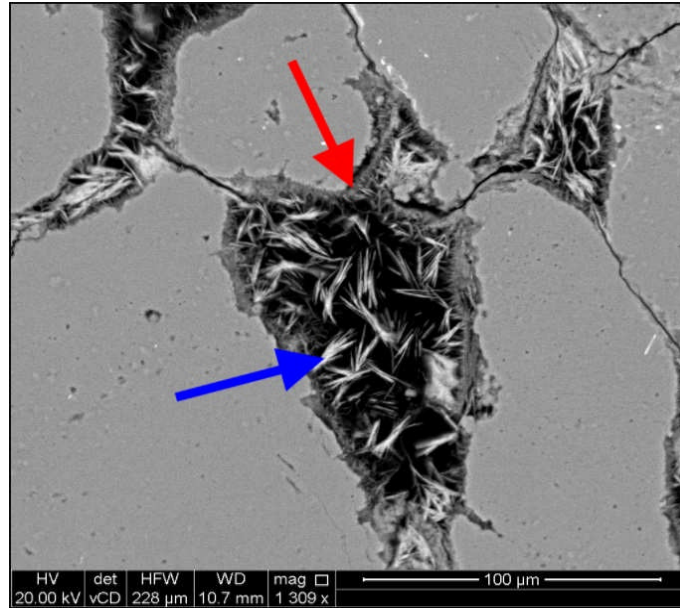


Figure 3-20: SEM image showing grain coating illite (red) and pore filling chlorite (blue) in sample TS1-305.

Quartz overgrowth is shown in SEM image of sample TS4-4 (Figure 3-21 – left). SEM image of sample TS4-11 showed the presence of chlorite clay filling and lining the pore space (Figure 3-21 – right), which is also confirmed by analyses of mineralogy obtained using QXRD (Table 3-2). The presence of dolomite and pore filling kaolinite in sample TS1-25 is shown in Figure 3-22. Pore filling kaolinite is shown in samples TS2-25 and TS3-47 (Figure 3-23) and (Figure 3-24) respectively, with the presence of dolomite in sample TS3-47.

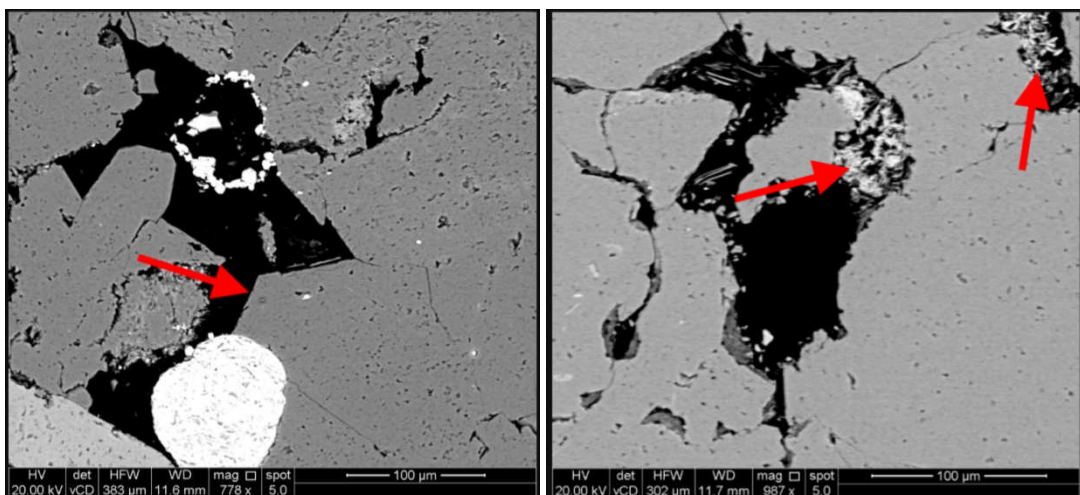


Figure 3-21: SEM image showing quartz overgrowth (red) in sample TS4-4 (left). SEM image showing the presence of chlorite filling and lining the pores (red) in sample TS4-11 (right).

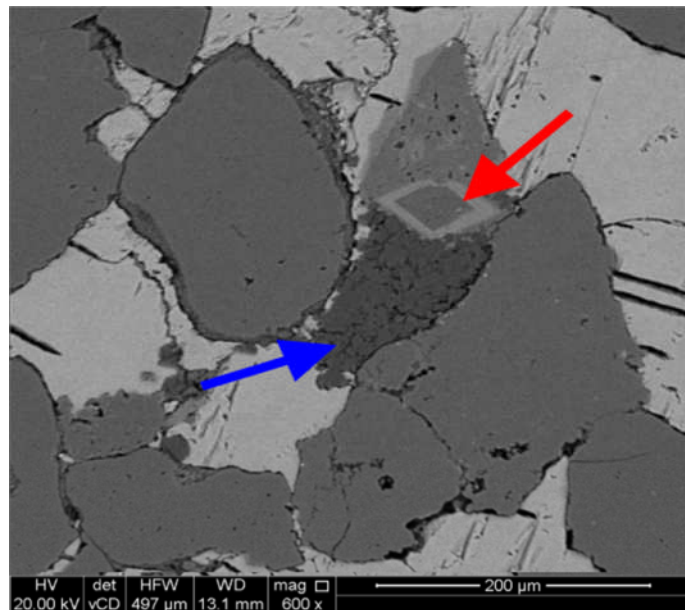


Figure 3-22: SEM image showing pore filling kaolinite (blue) and dolomite (red) in sample TS1-25.

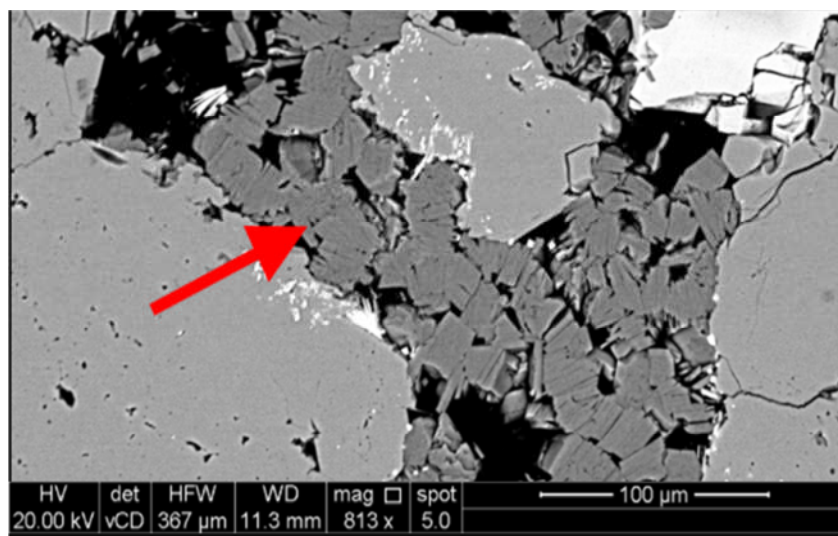


Figure 3-23: SEM image showing pore filling kaolinite in sample TS2-25.

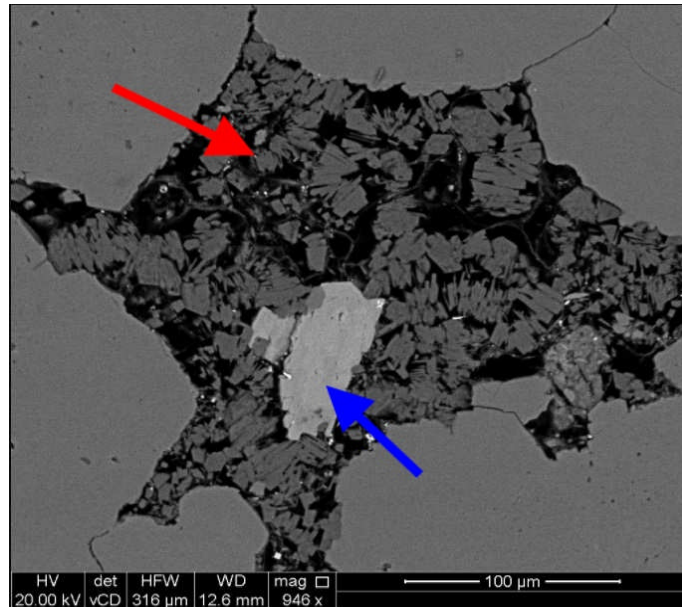


Figure 3-24: SEM image showing pore filling kaolinite (red) with the presence of dolomite (blue) in sample TS3-47.

3.3.7 Mercury injection capillary pressure data with SEM images

Montages showing the capillary pressure data combined with SEM images for all the samples are shown in Figure 3-25 through Figure 3-53. Each montage shows the mercury saturation against the capillary pressure, the pore size distribution and an SEM image showing the microstructures and the grain size and sorting in each sample. Porosity and permeability are also shown in the top for comparison between samples.

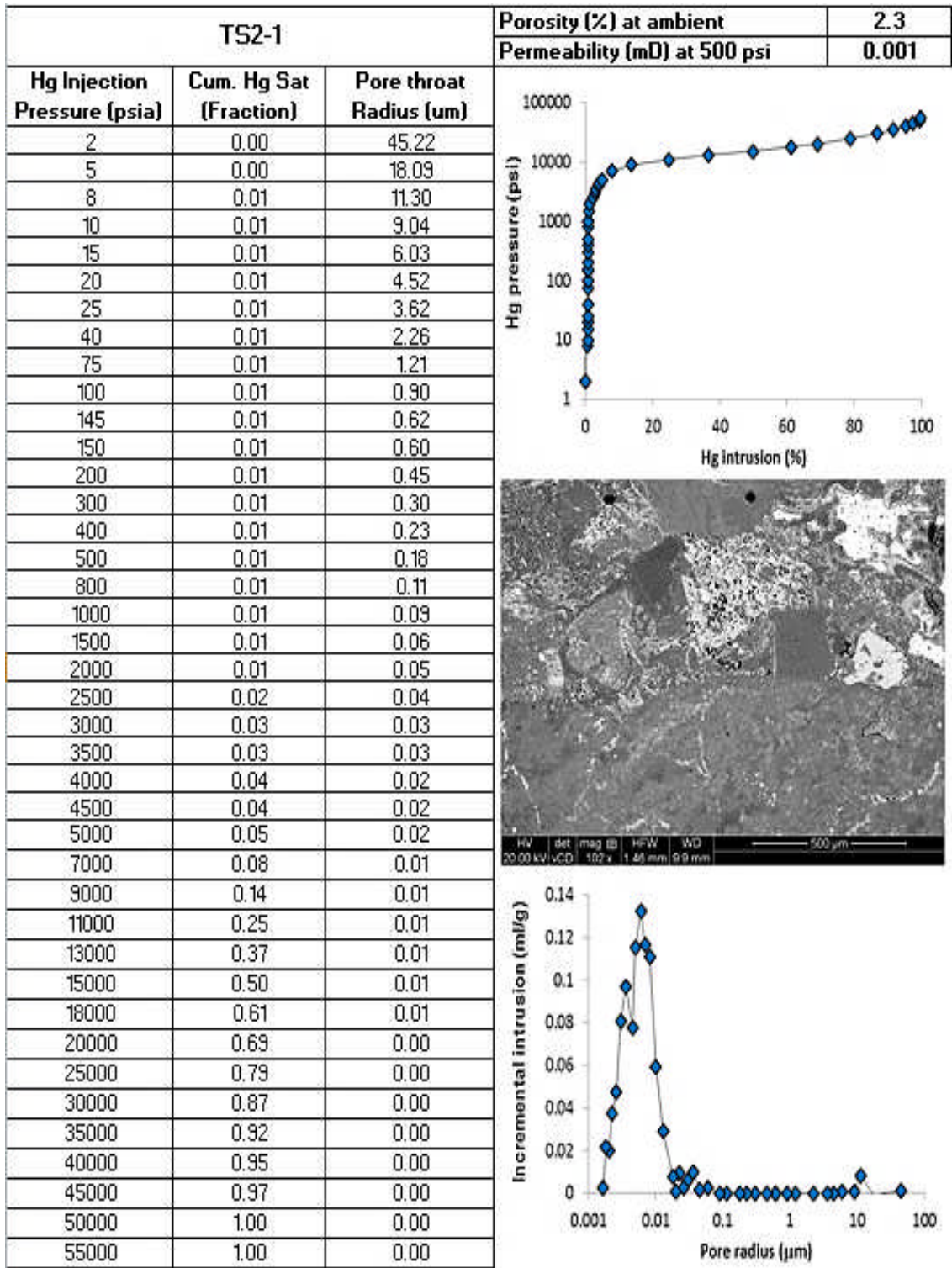


Figure 3-25: A montage showing the mercury injection data that is mercury saturation, capillary pressure, pore size distribution, SEM image and the porosity and permeability for sample TS2-1. See caption of Figure 3-5 for porosity and permeability uncertainties in plotted values.

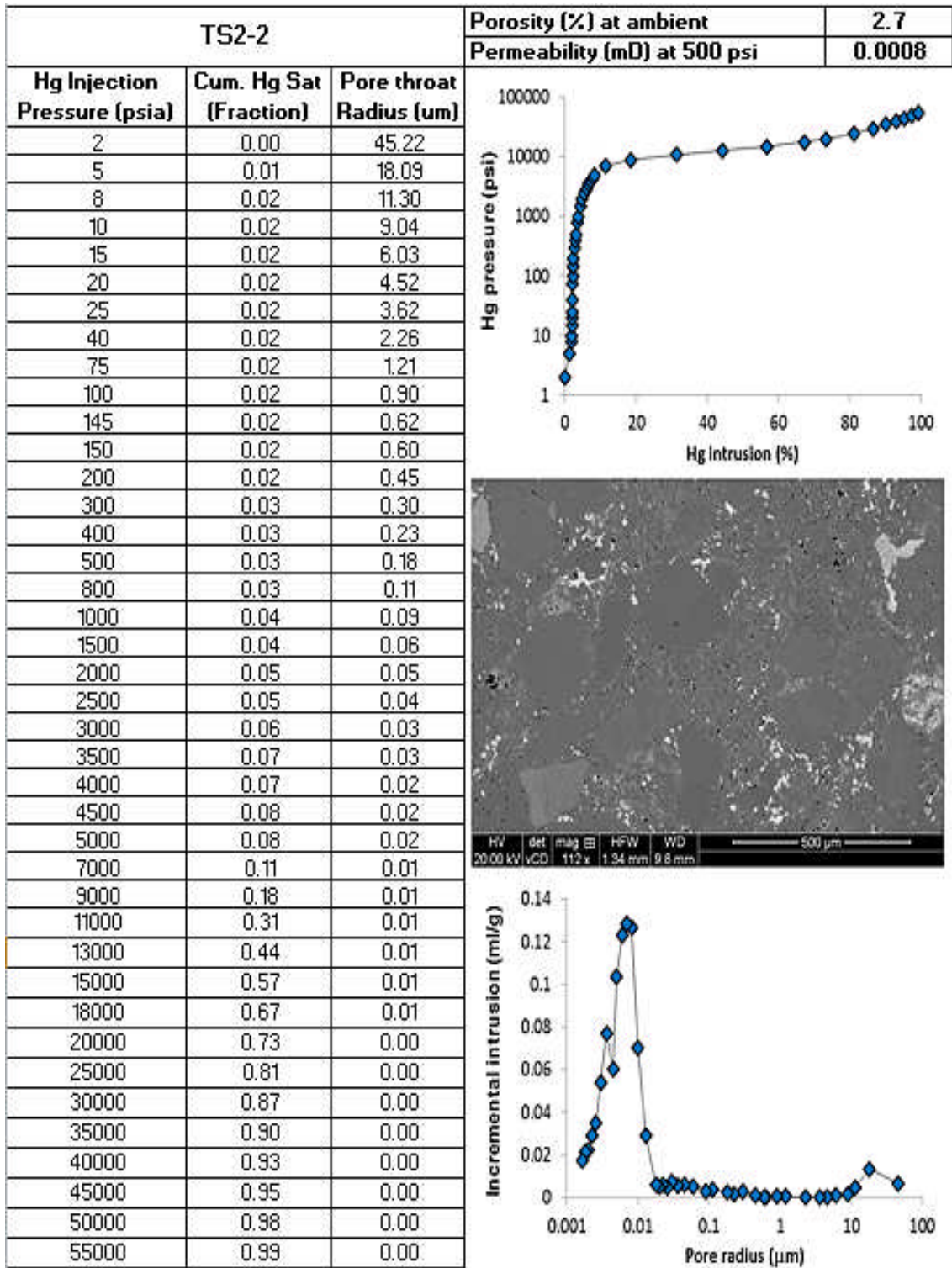


Figure 3-26: A montage showing the mercury injection data that is mercury saturation, capillary pressure, pore size distribution, SEM image and the porosity and permeability for sample TS2-2. See caption of Figure 3-5 for porosity and permeability uncertainties in plotted values.

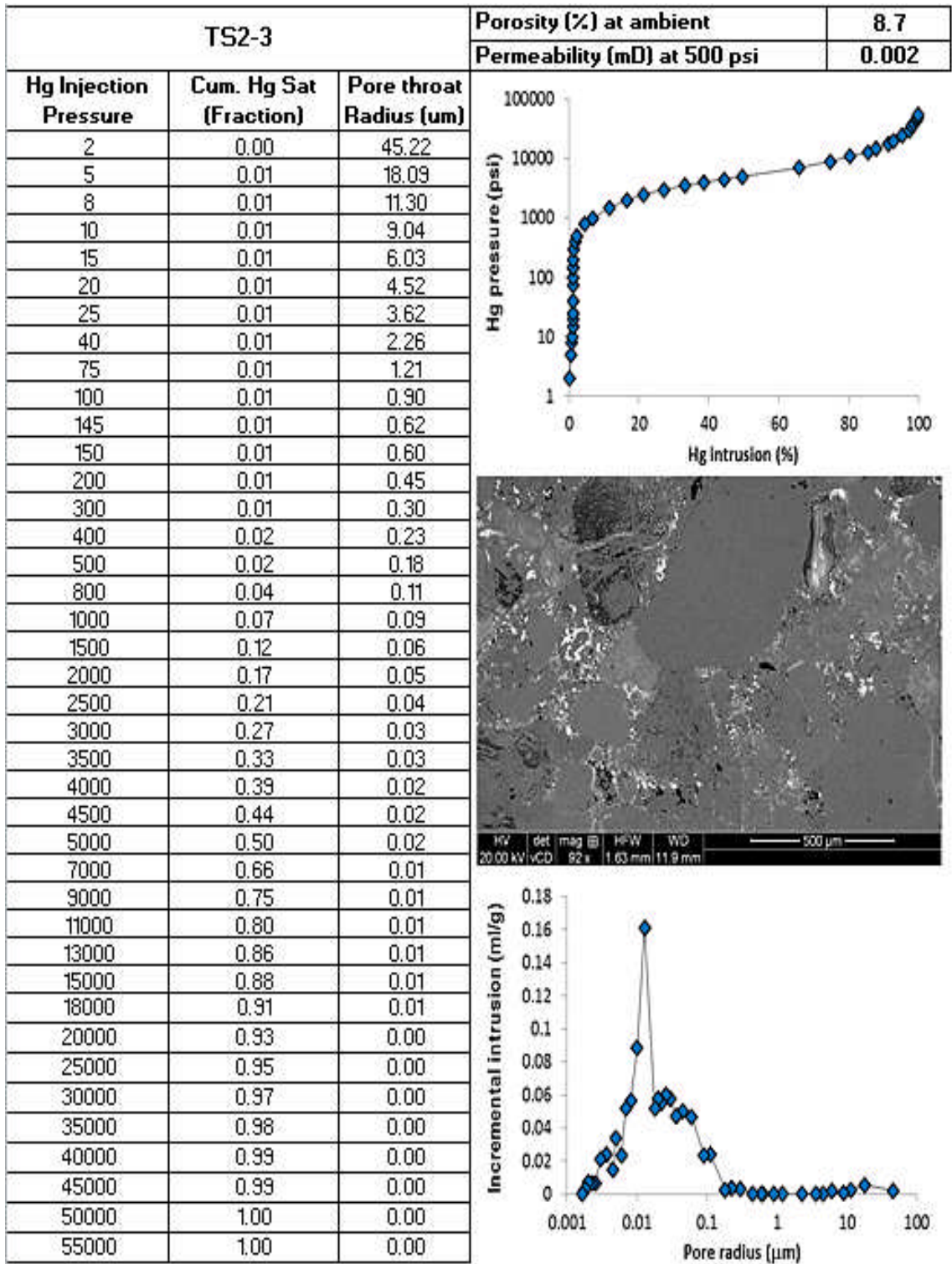


Figure 3-27: A montage showing the mercury injection data that is mercury saturation, capillary pressure, pore size distribution, SEM image and the porosity and permeability for sample TS2-3. See caption of Figure 3-5 for porosity and permeability uncertainties in plotted values.

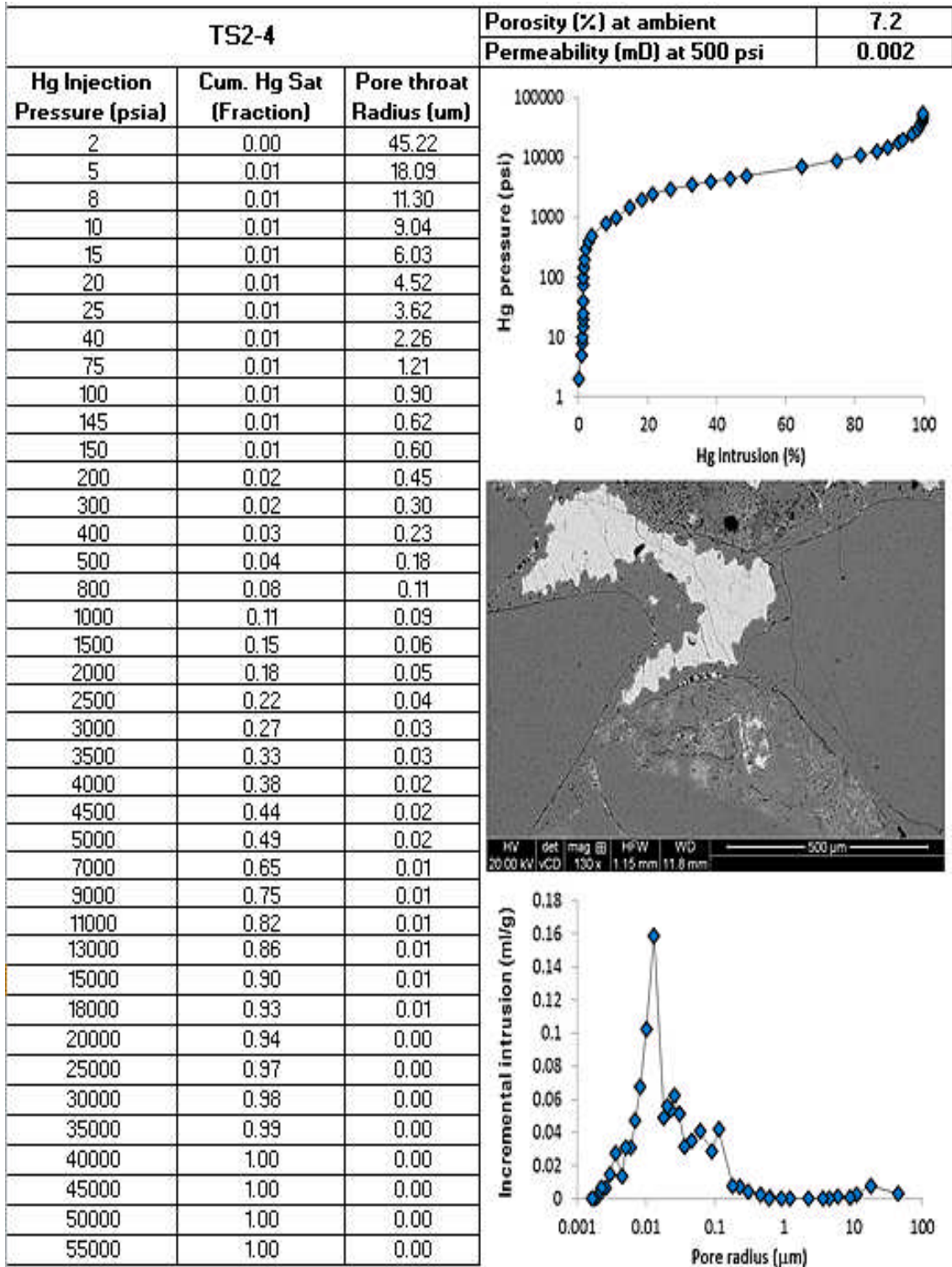


Figure 3-28: A montage showing the mercury injection data that is mercury saturation, capillary pressure, pore size distribution, SEM image and the porosity and permeability for sample TS2-4. See caption of Figure 3-5 for porosity and permeability uncertainties in plotted values.

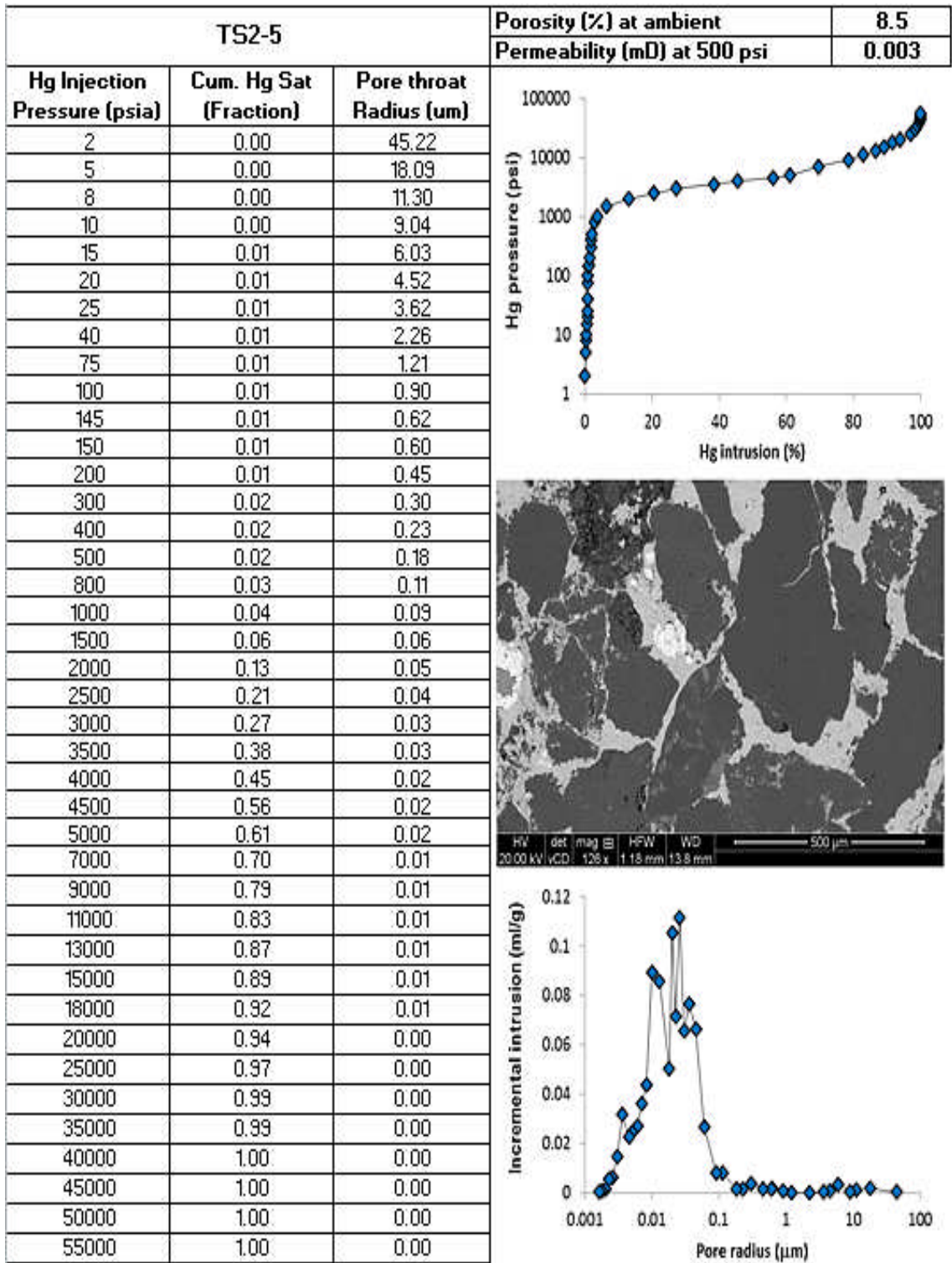


Figure 3-29: A montage showing the mercury injection data that is mercury saturation, capillary pressure, pore size distribution, SEM image and the porosity and permeability for sample TS2-5. See caption of Figure 3-5 for porosity and permeability uncertainties in plotted values.

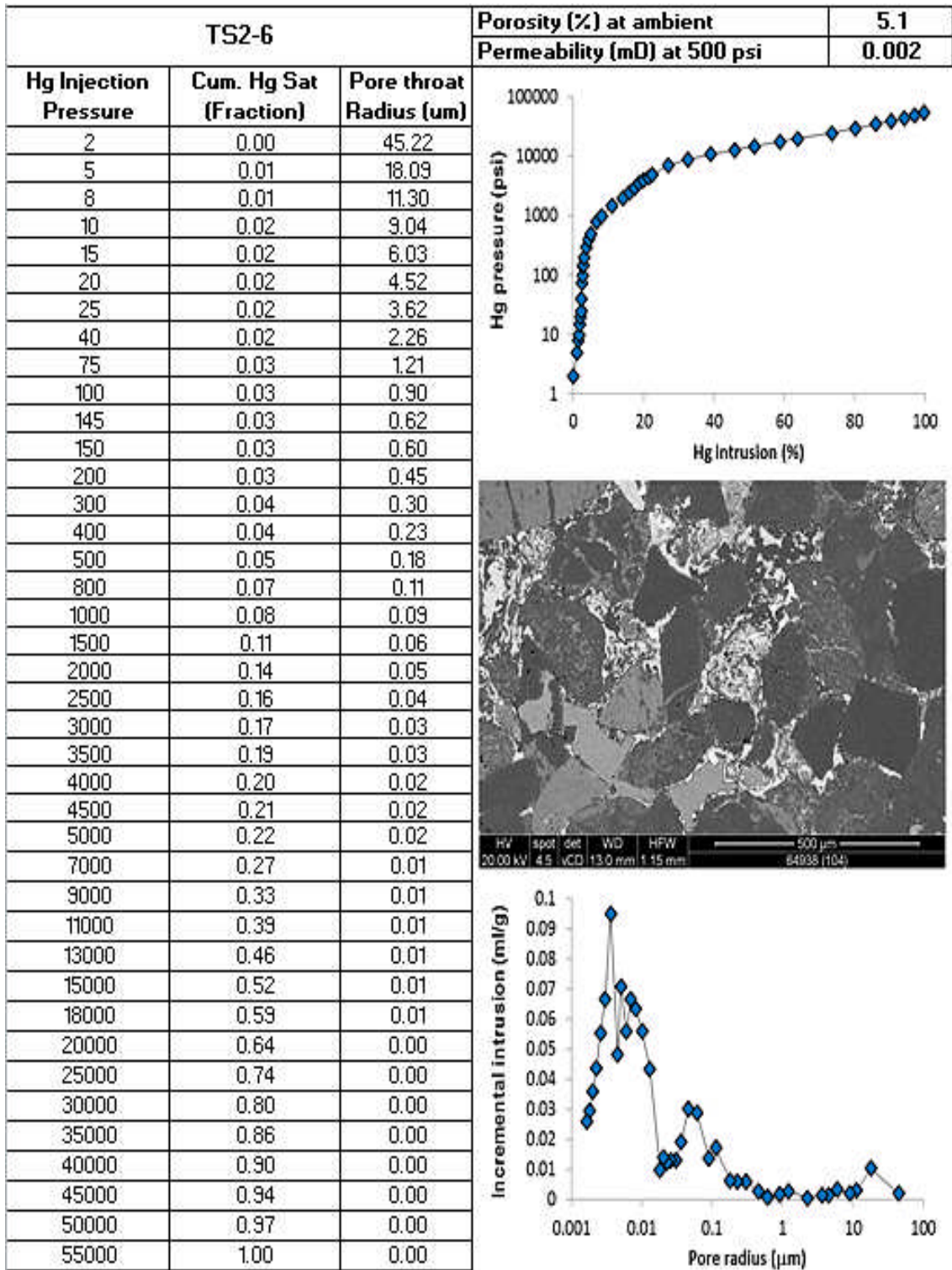


Figure 3-30: A montage showing the mercury injection data that is mercury saturation, capillary pressure, pore size distribution, SEM image and the porosity and permeability for sample TS2-6. See caption of Figure 3-5 for porosity and permeability uncertainties in plotted values.

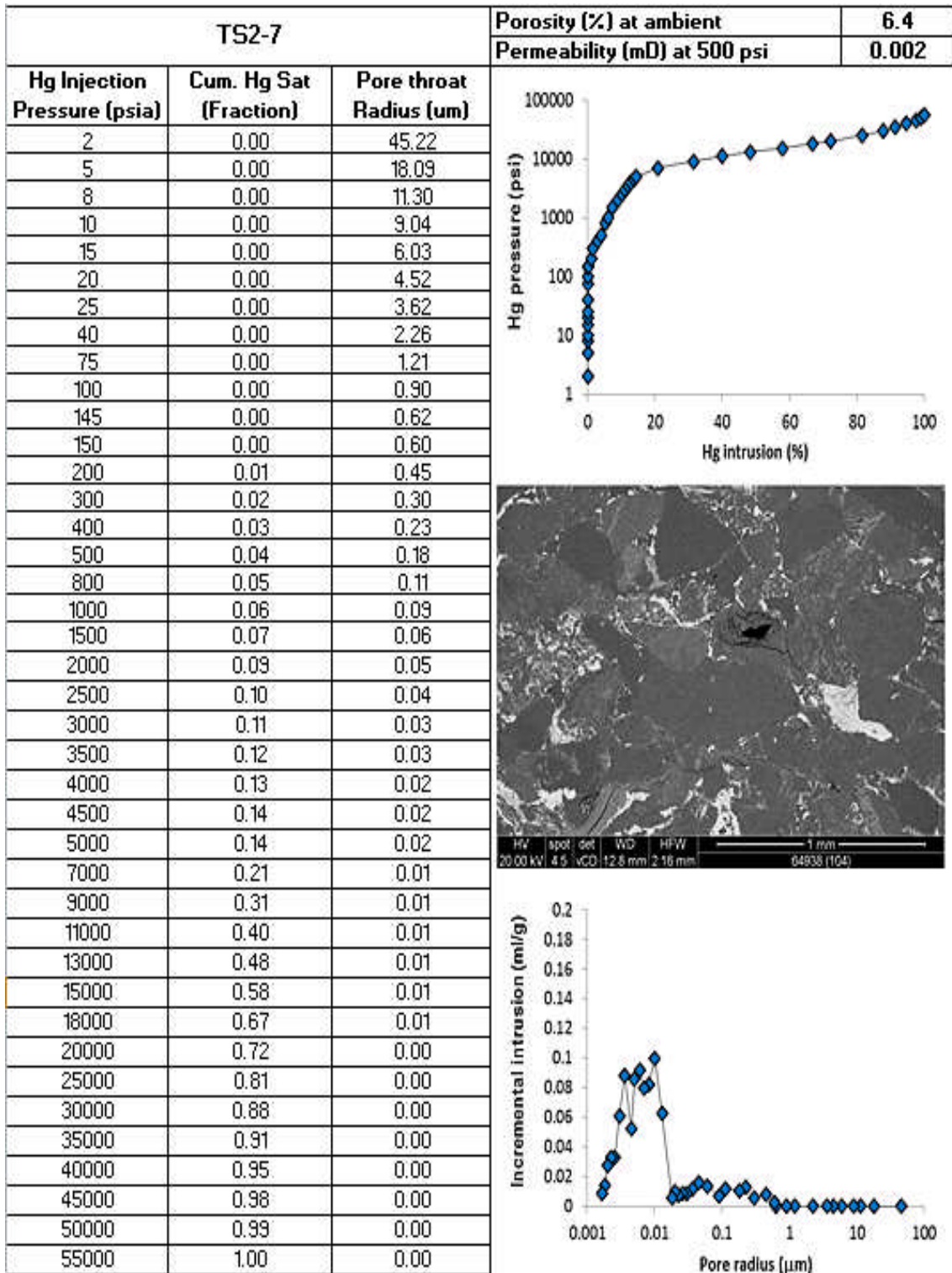


Figure 3-31: A montage showing the mercury injection data that is mercury saturation, capillary pressure, pore size distribution, SEM image and the porosity and permeability for sample TS2-7. See caption of Figure 3-5 for porosity and permeability uncertainties in plotted values.

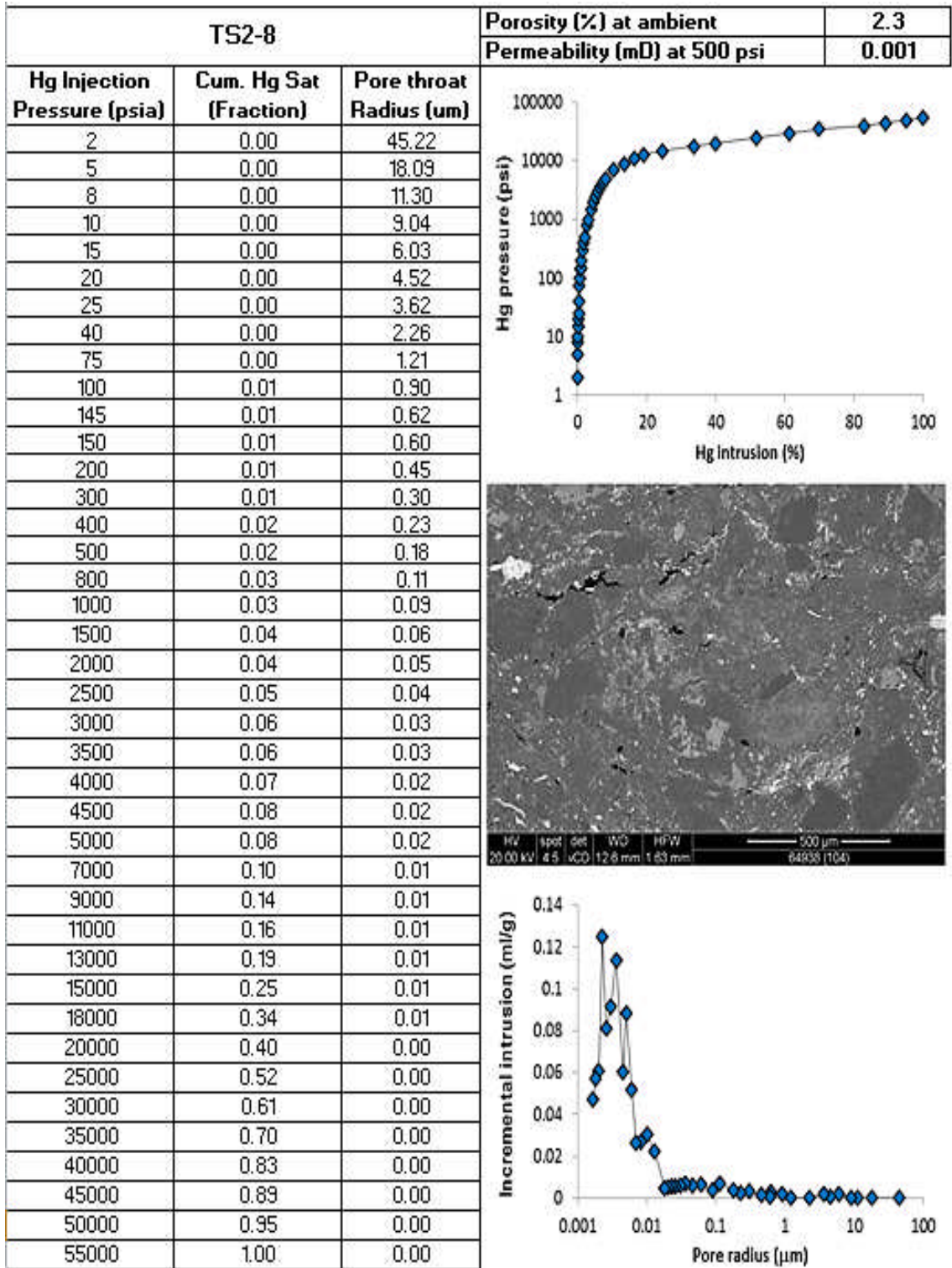


Figure 3-32: A montage showing the mercury injection data that is mercury saturation, capillary pressure, pore size distribution, SEM image and the porosity and permeability for sample TS2-8. See caption of Figure 3-5 for porosity and permeability uncertainties in plotted values.

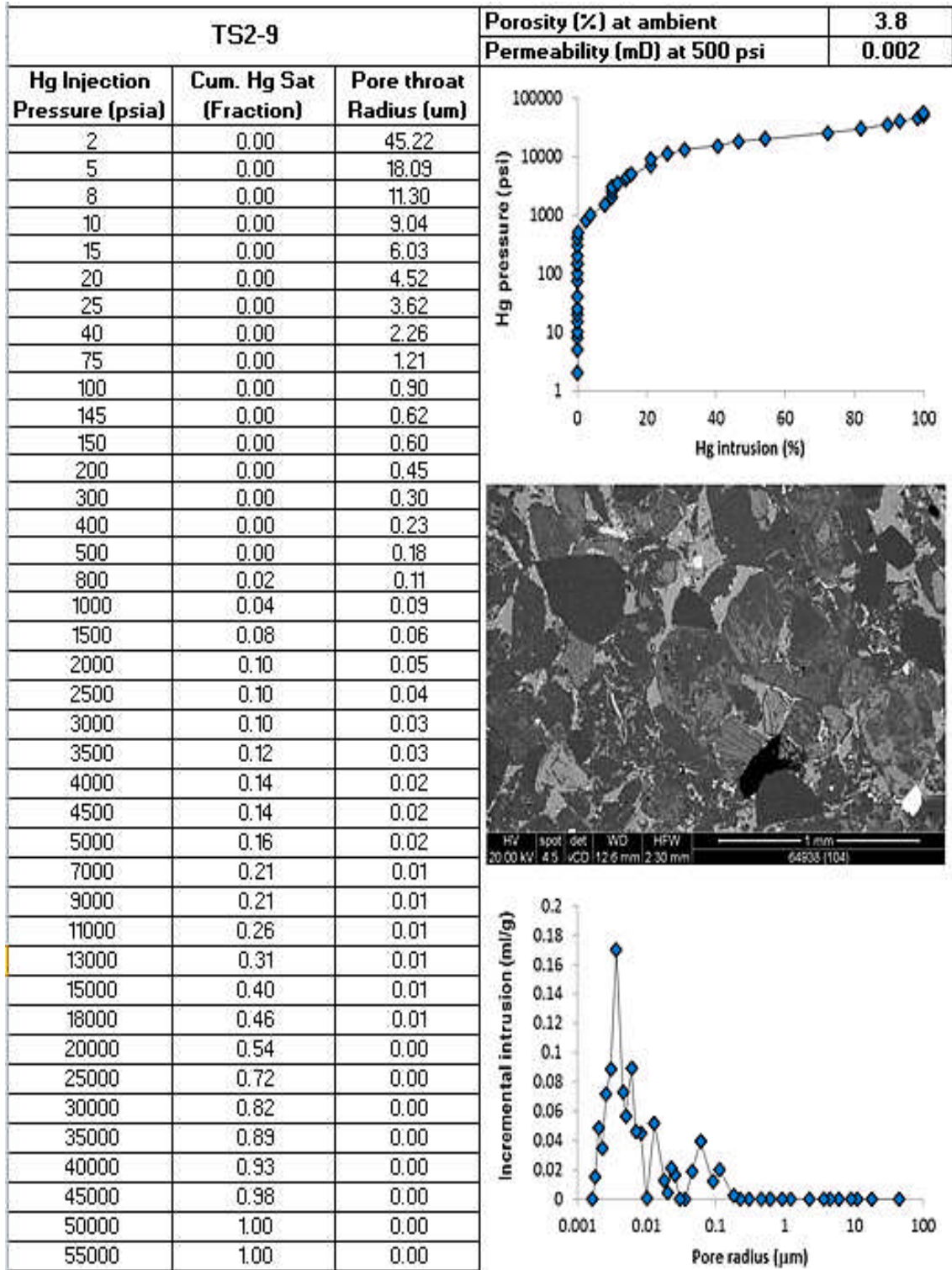


Figure 3-33: A montage showing the mercury injection data that is mercury saturation, capillary pressure, pore size distribution, SEM image and the porosity and permeability for sample TS2-9. See caption of Figure 3-5 for porosity and permeability uncertainties in plotted values.

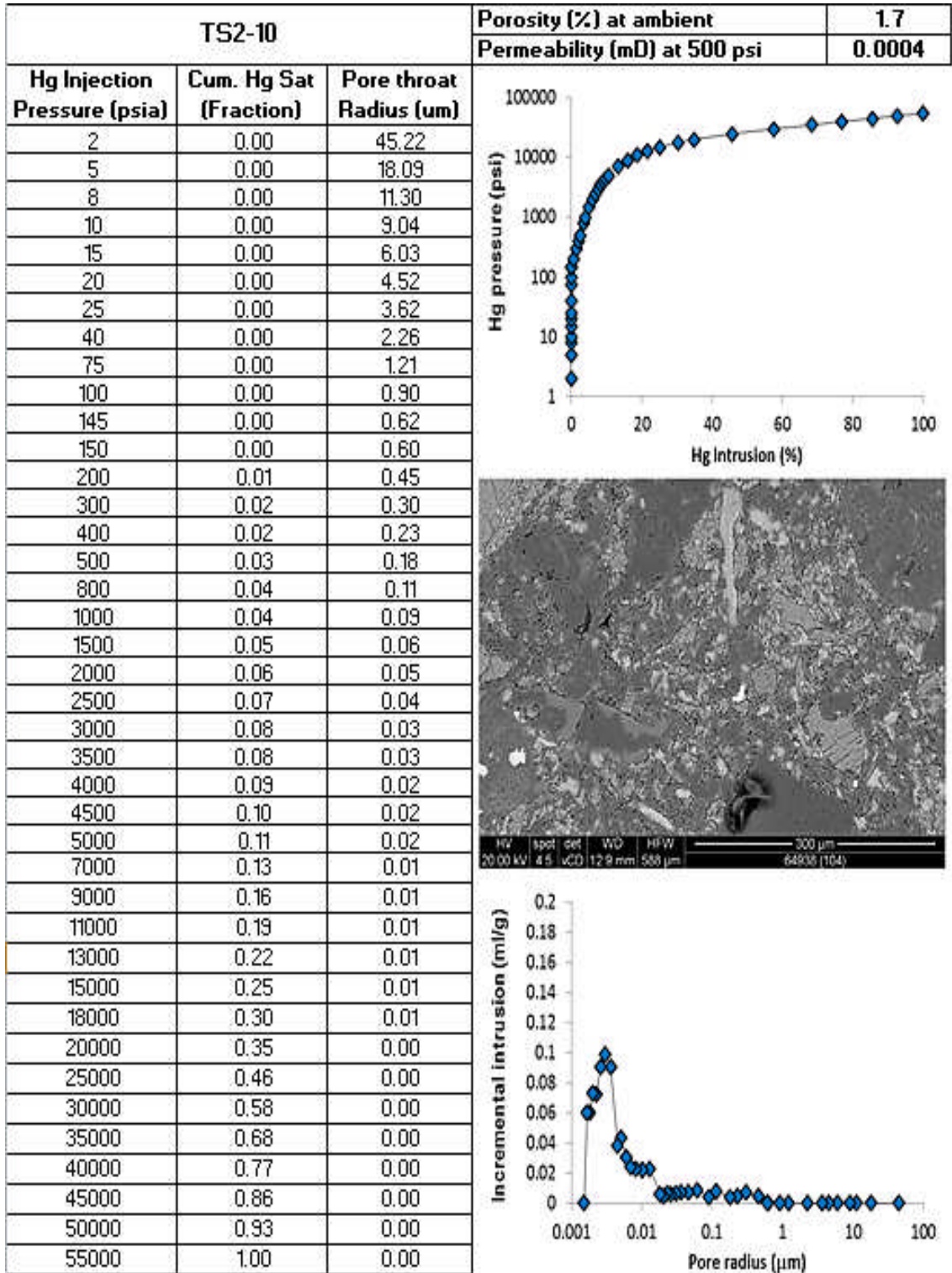


Figure 3-34: A montage showing the mercury injection data that is mercury saturation, capillary pressure, pore size distribution, SEM image and the porosity and permeability for sample TS2-10. See caption of Figure 3-5 for porosity and permeability uncertainties in plotted values.

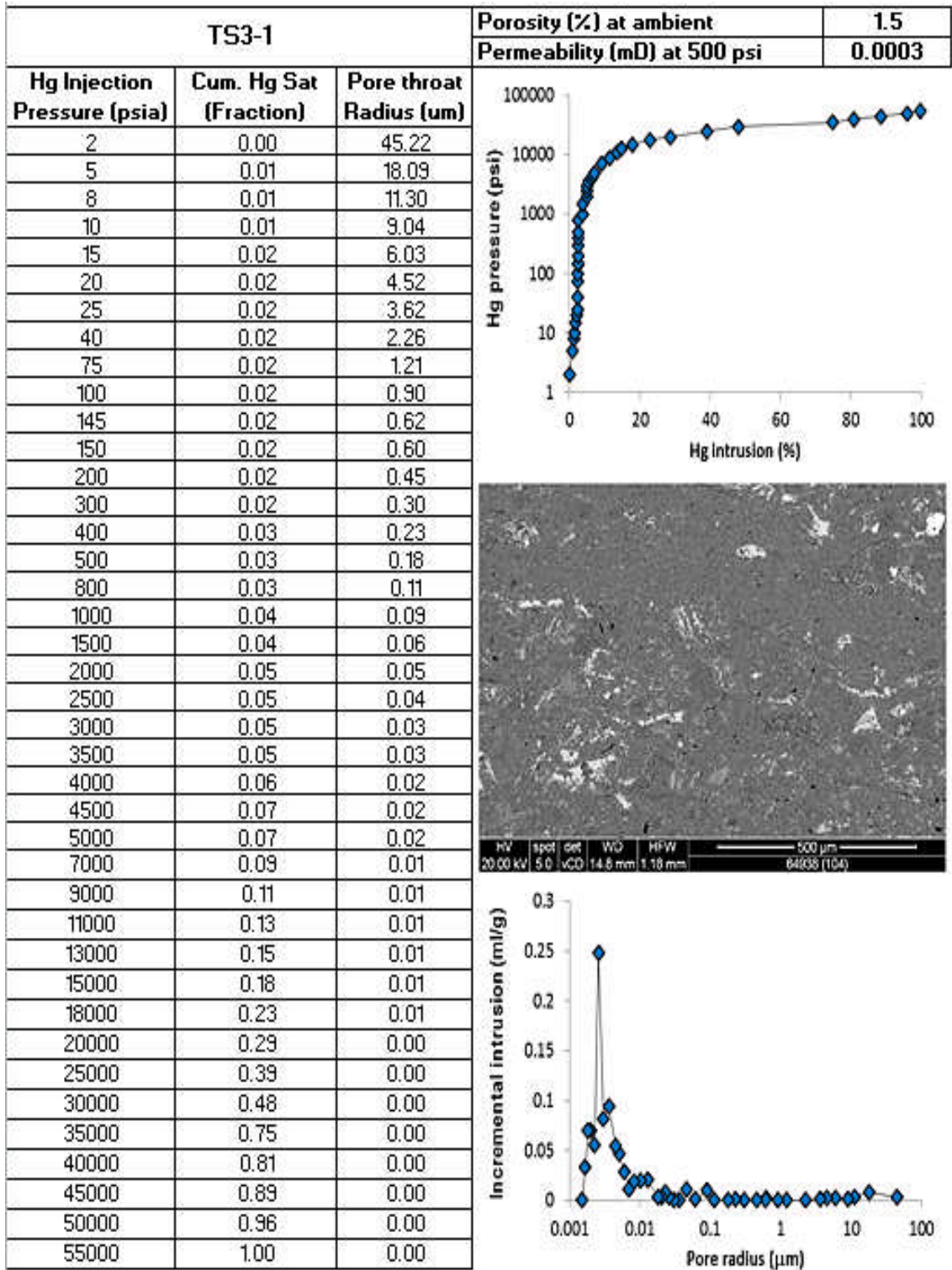


Figure 3-35: A montage showing the mercury injection data that is mercury saturation, capillary pressure, pore size distribution, SEM image and the porosity and permeability for sample TS3-1. See caption of Figure 3-5 for porosity and permeability uncertainties in plotted values.

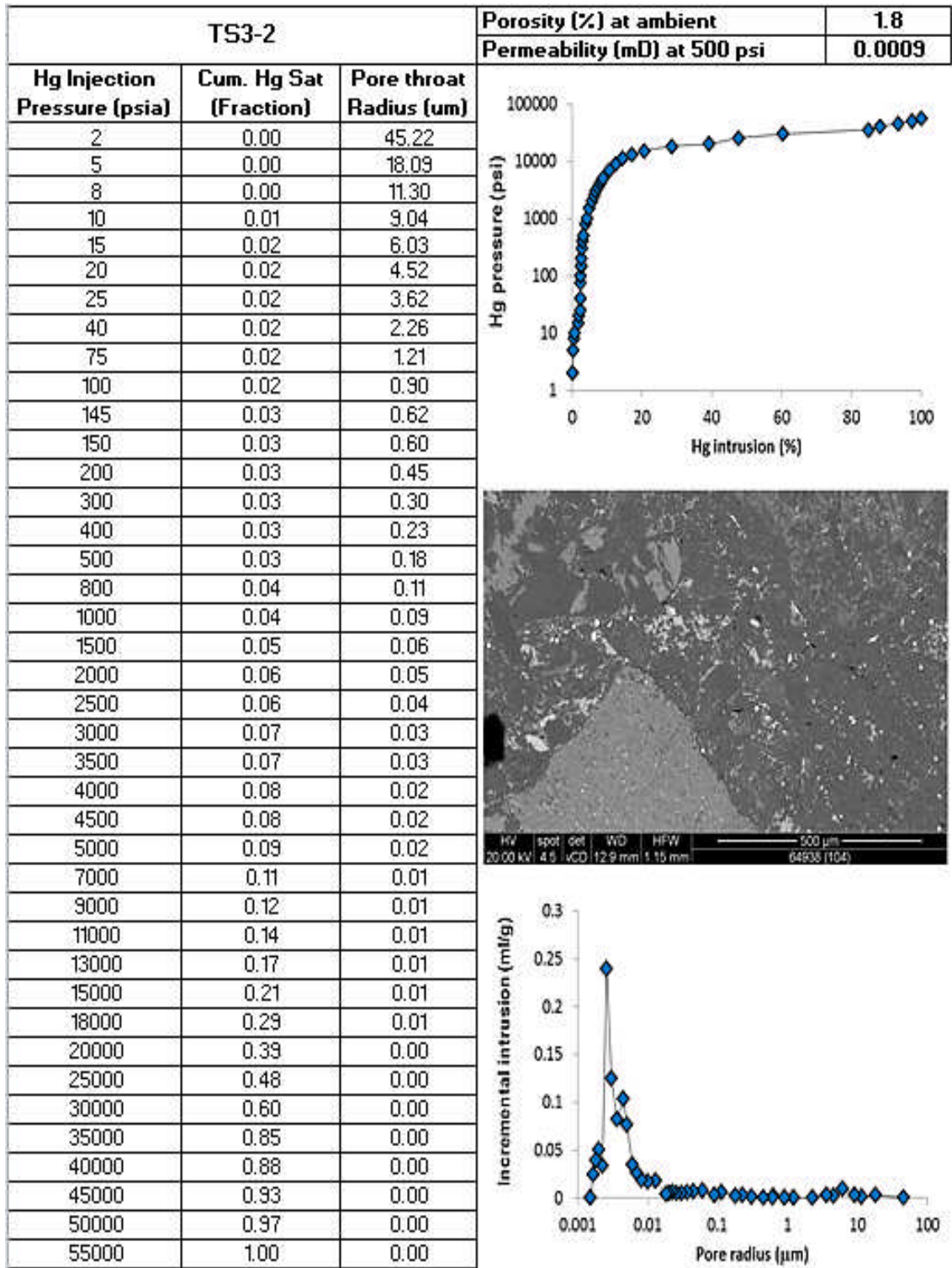


Figure 3-36: A montage showing the mercury injection data that is mercury saturation, capillary pressure, pore size distribution, SEM image and the porosity and permeability for sample TS3-2. See caption of Figure 3-5 for porosity and permeability uncertainties in plotted values.

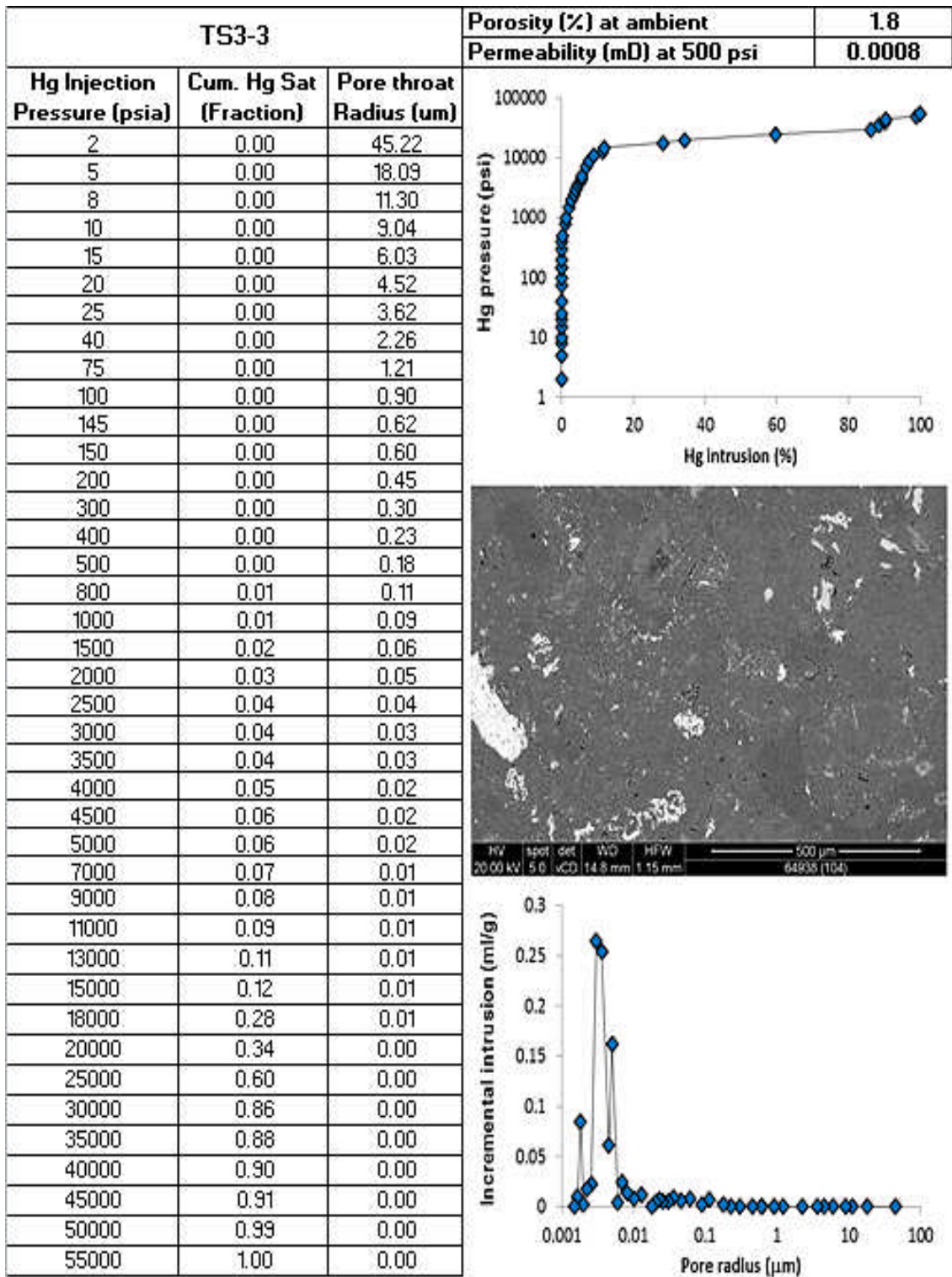


Figure 3-37: A montage showing the mercury injection data that is mercury saturation, capillary pressure, pore size distribution, SEM image and the porosity and permeability for sample TS3-3. See caption of Figure 3-5 for porosity and permeability uncertainties in plotted values.

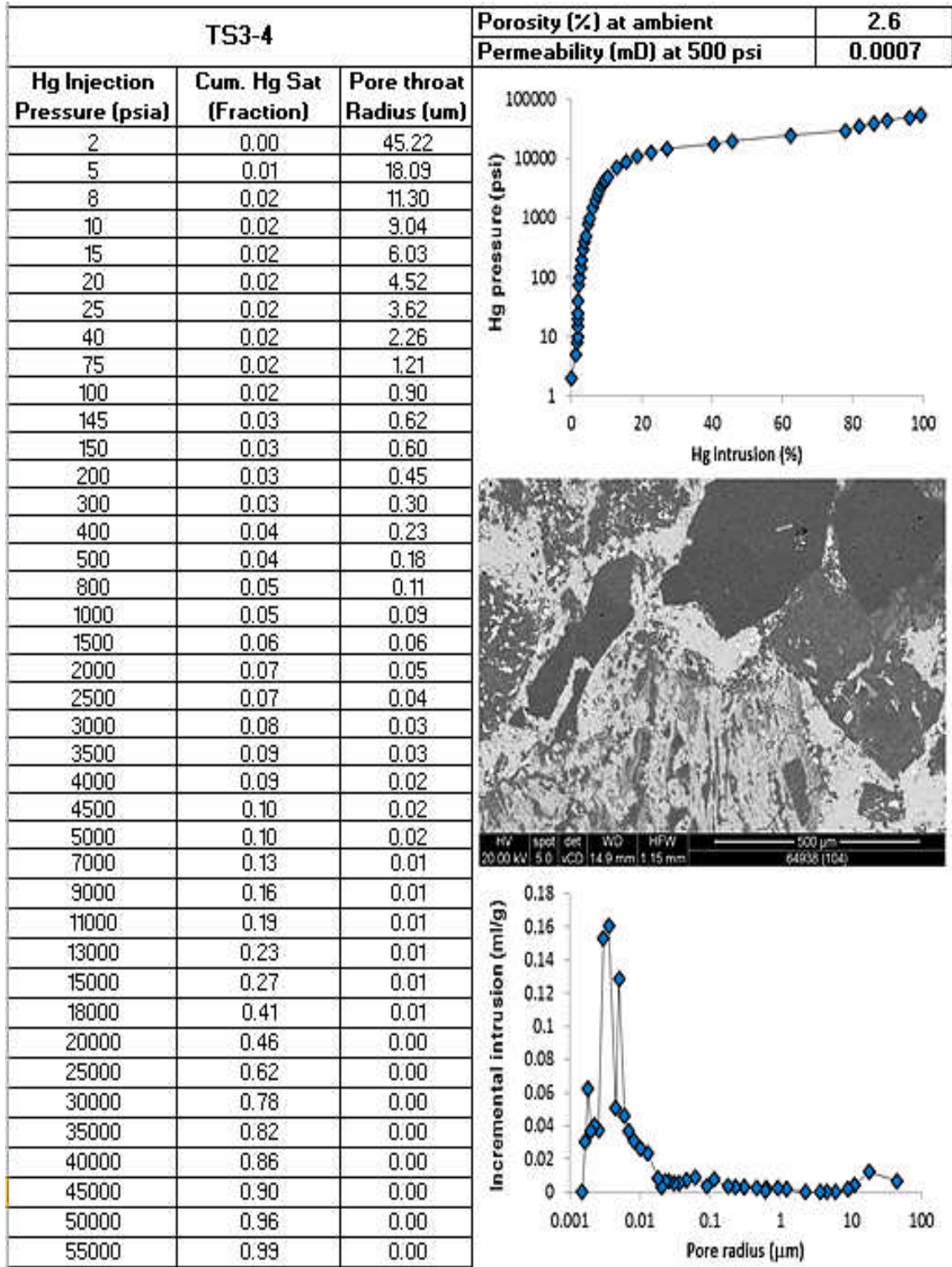


Figure 3-38: A montage showing the mercury injection data that is mercury saturation, capillary pressure, pore size distribution, SEM image and the porosity and permeability for sample TS3-4. See caption of Figure 3-5 for porosity and permeability uncertainties in plotted values.

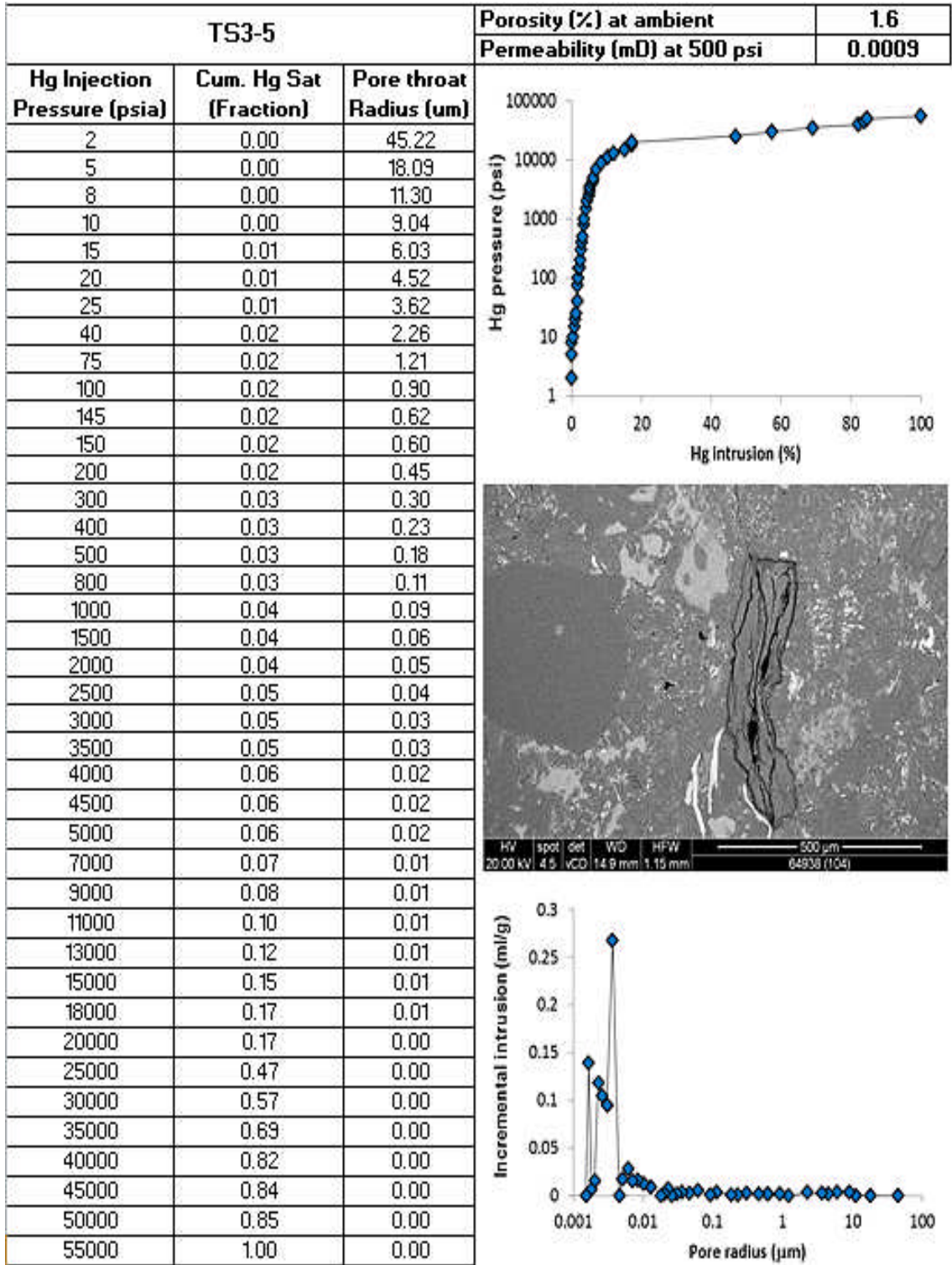


Figure 3-39: A montage showing the mercury injection data that is mercury saturation, capillary pressure, pore size distribution, SEM image and the porosity and permeability for sample TS3-5. See caption of Figure 3-5 for porosity and permeability uncertainties in plotted values.

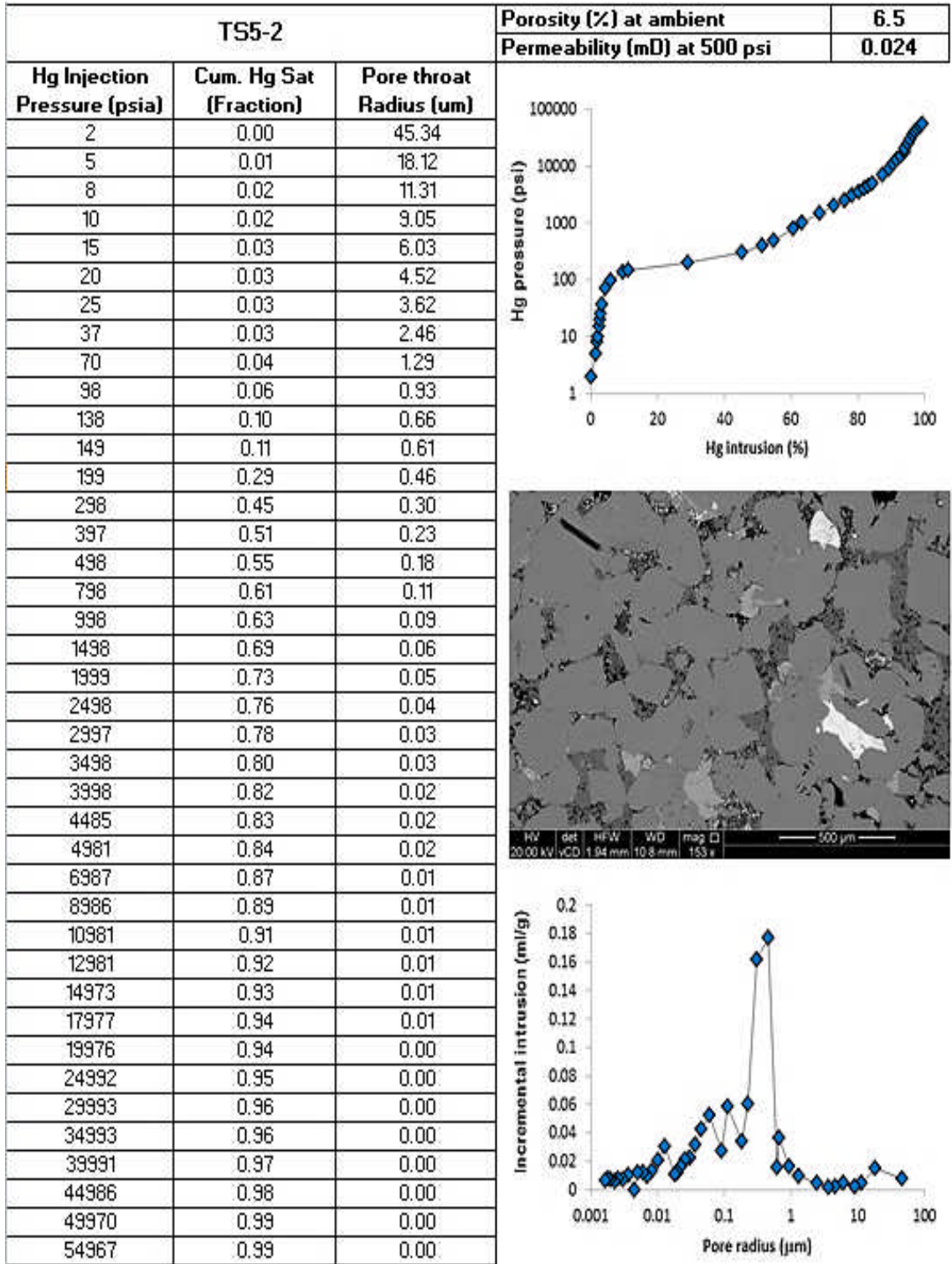


Figure 3-40: A montage showing the mercury injection data that is mercury saturation, capillary pressure, pore size distribution, SEM image and the porosity and permeability for sample TS5-2. See caption of Figure 3-5 for porosity and permeability uncertainties in plotted values.

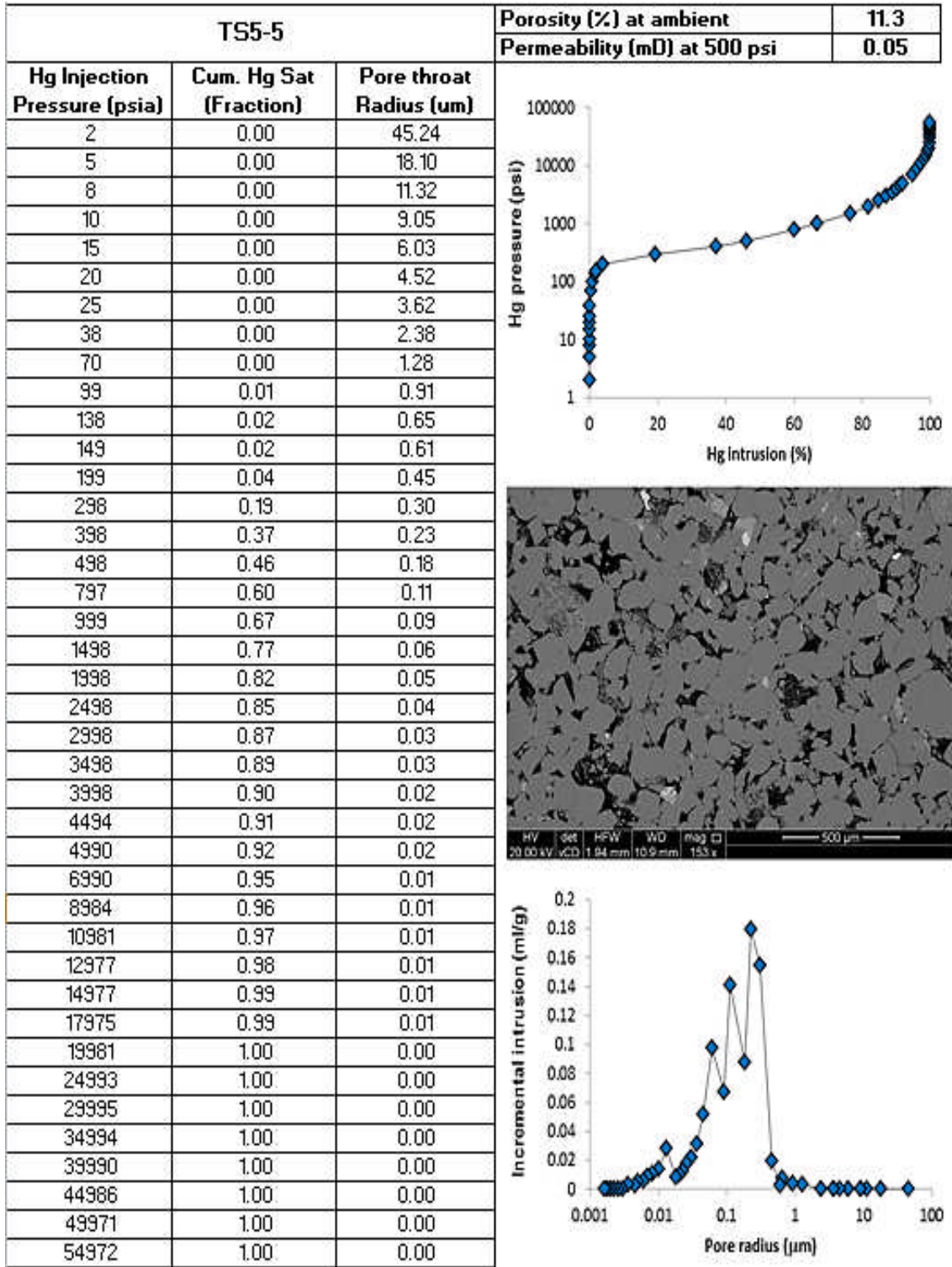


Figure 3-41: A montage showing the mercury injection data that is mercury saturation, capillary pressure, pore size distribution, SEM image and the porosity and permeability for sample TS5-5. See caption of Figure 3-5 for porosity and permeability uncertainties in plotted values.

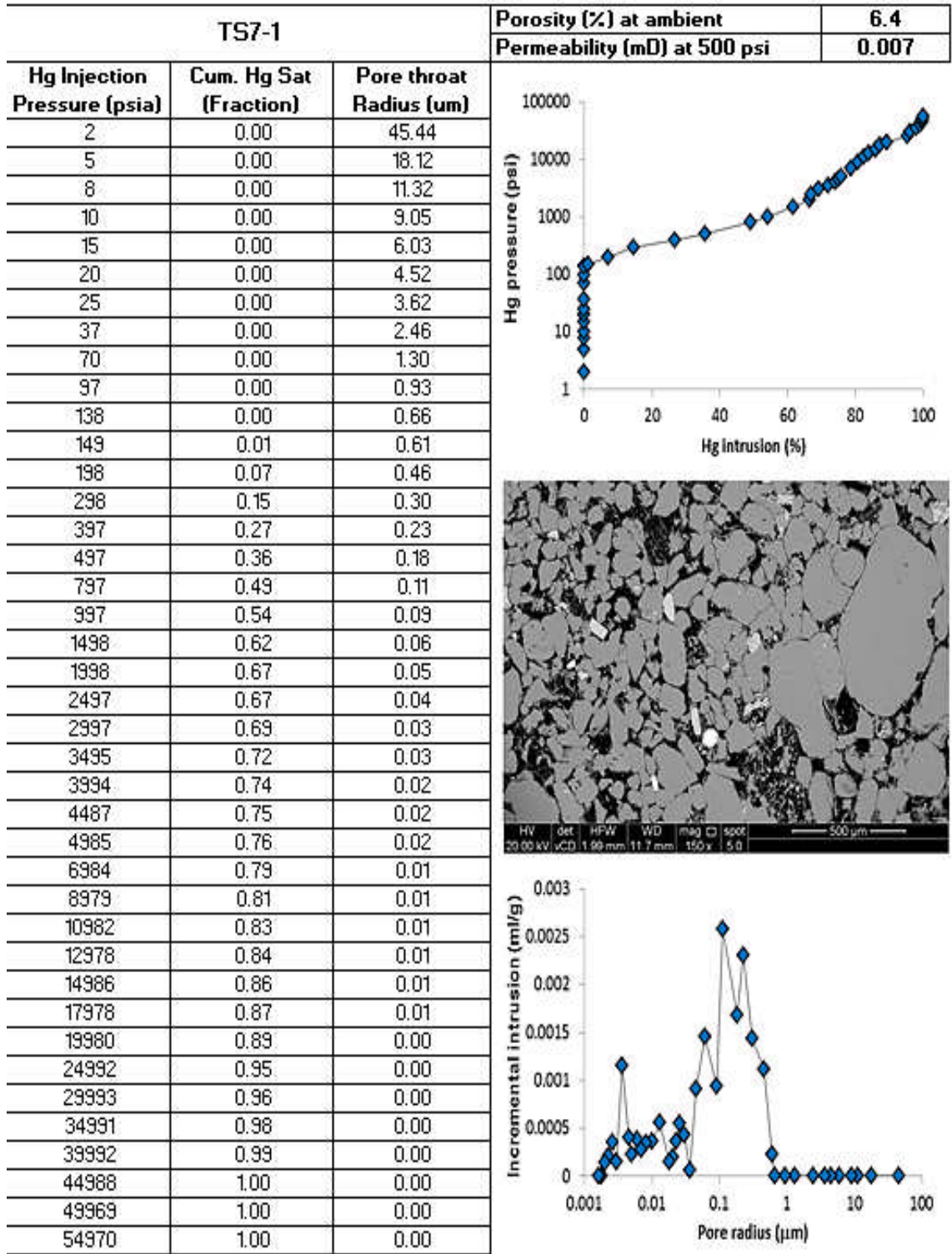


Figure 3-42: A montage showing the mercury injection data that is mercury saturation, capillary pressure, pore size distribution, SEM image and the porosity and permeability for sample TS7-1. See caption of Figure 3-5 for porosity and permeability uncertainties in plotted values.

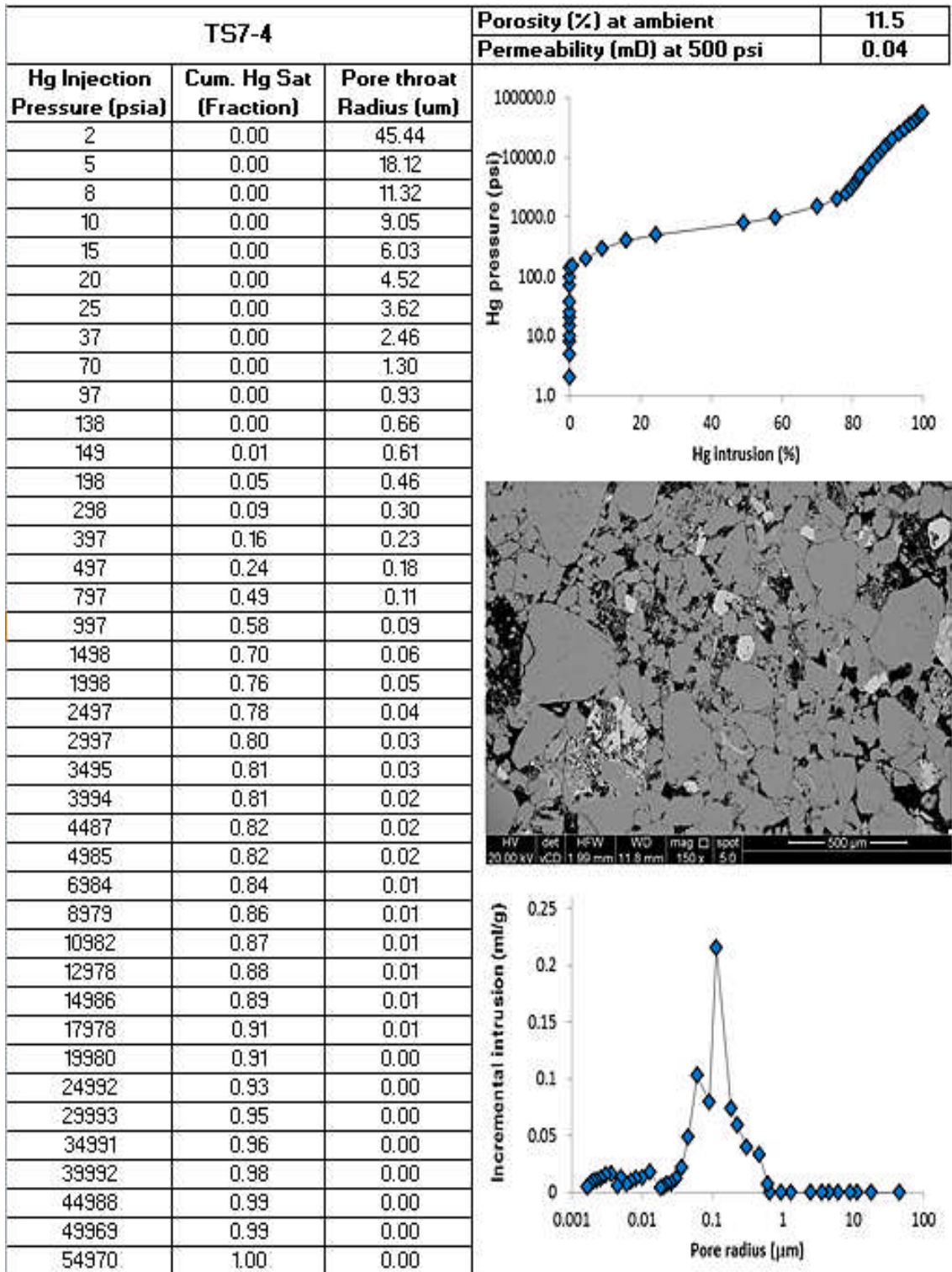


Figure 3-43: A montage showing the mercury injection data that is mercury saturation, capillary pressure, pore size distribution, SEM image and the porosity and permeability for sample TS7-4. See caption of Figure 3-5 for porosity and permeability uncertainties in plotted values.

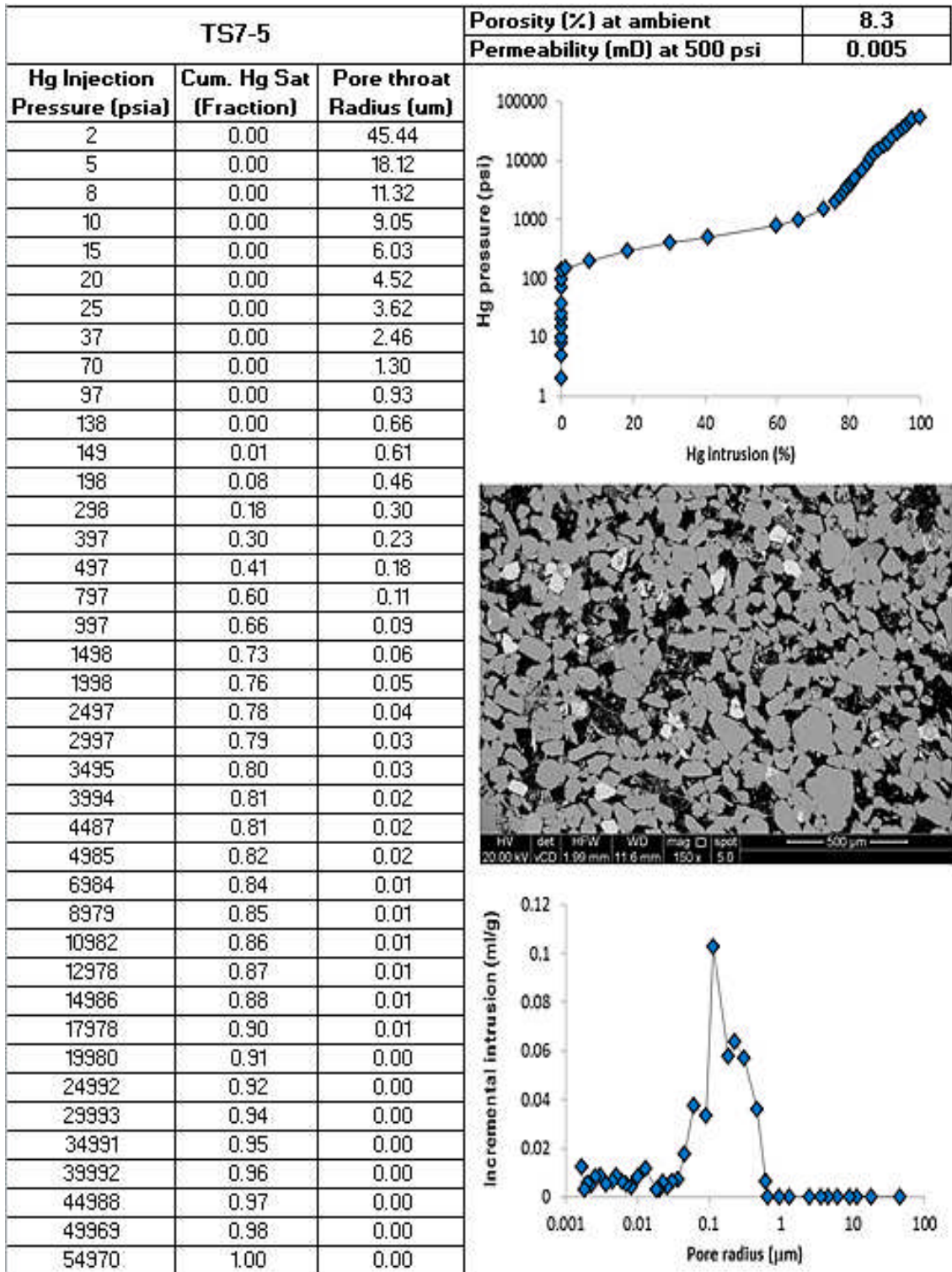


Figure 3-44: A montage showing the mercury injection data that is mercury saturation, capillary pressure, pore size distribution, SEM image and the porosity and permeability for sample TS7-5. See caption of Figure 3-5 for porosity and permeability uncertainties in plotted values.

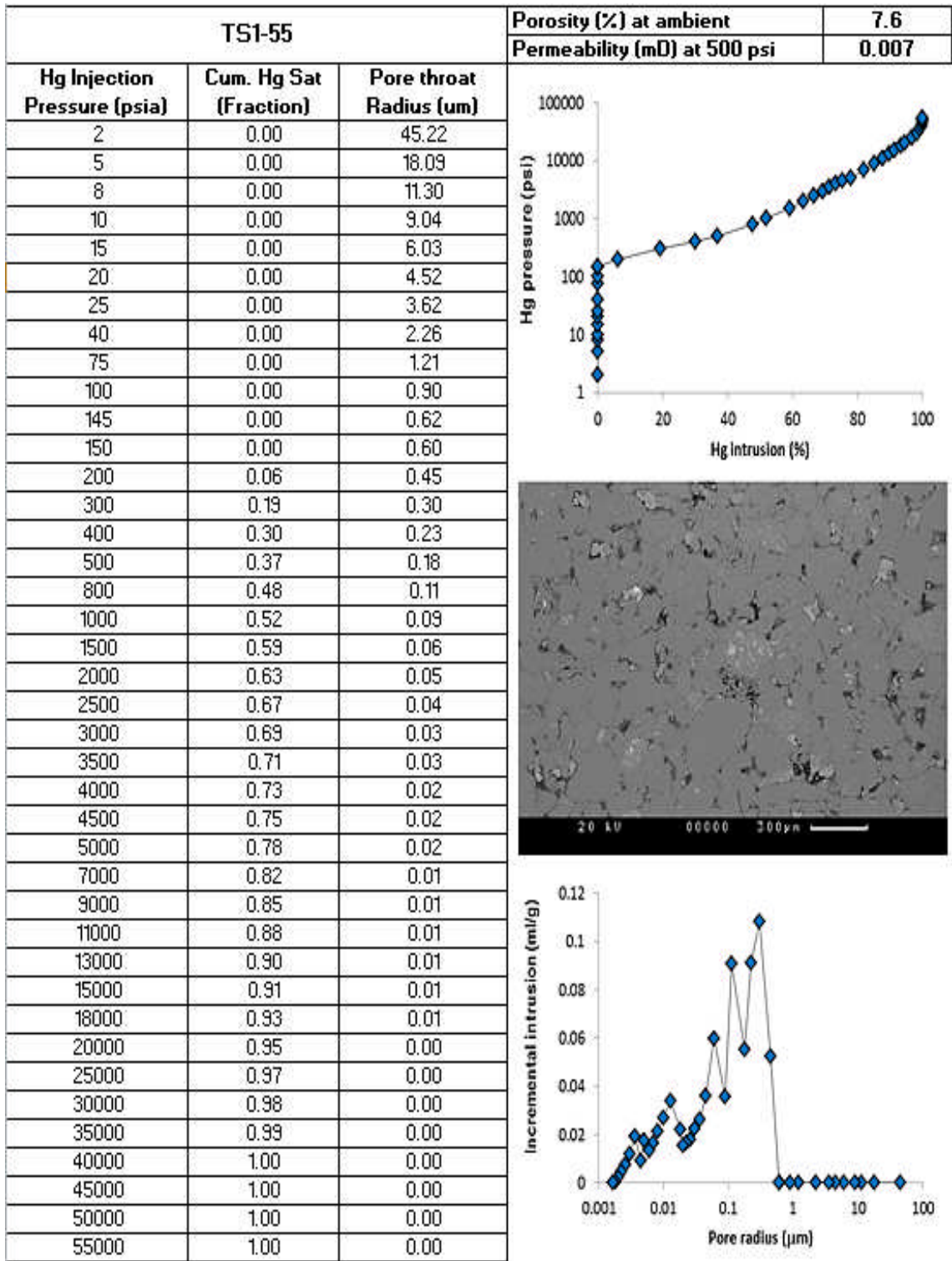


Figure 3-45: A montage showing the mercury injection data that is mercury saturation, capillary pressure, pore size distribution, SEM image and the porosity and permeability for sample TS1-55. See caption of Figure 3-5 for porosity and permeability uncertainties in plotted values.

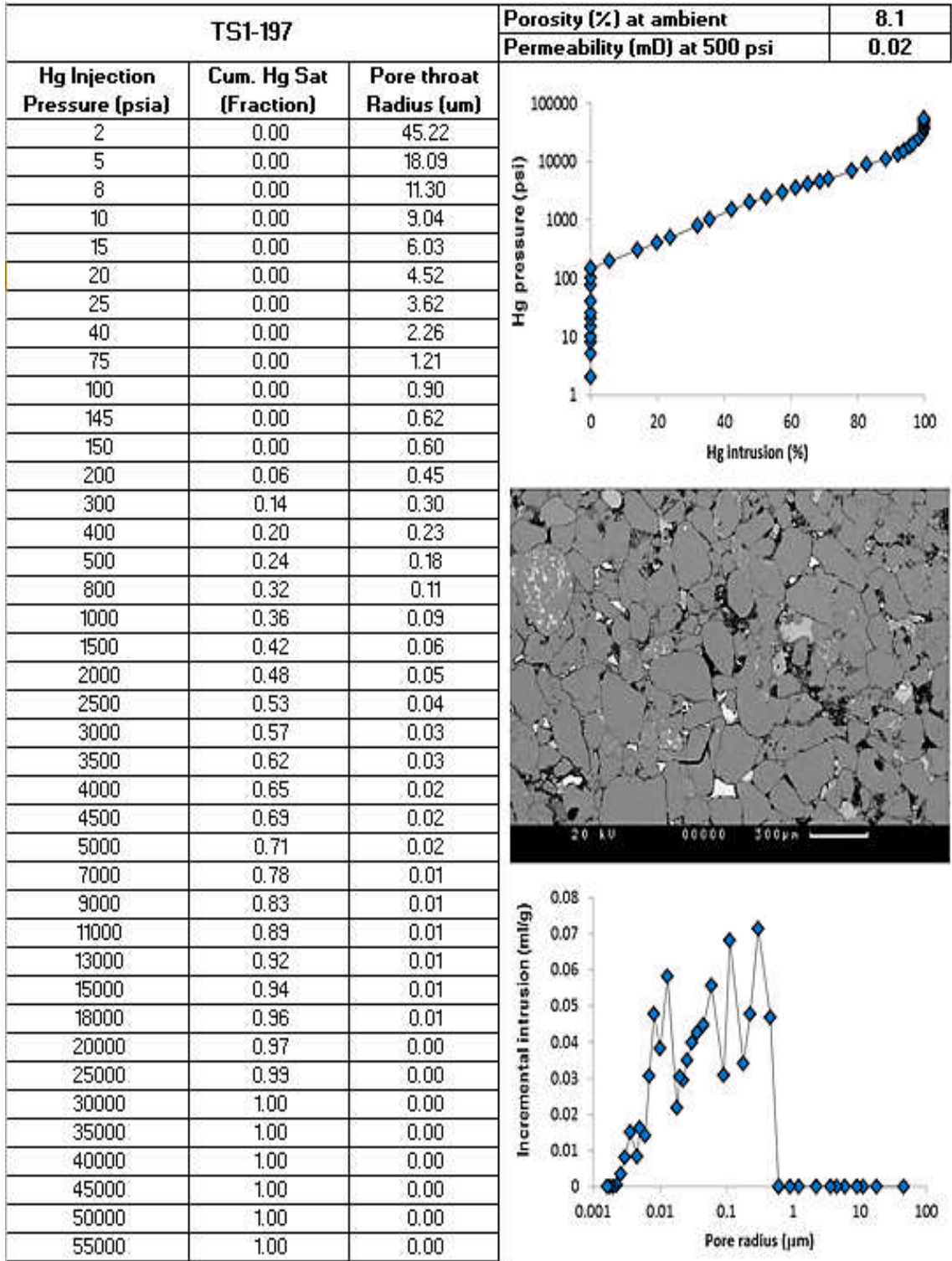


Figure 3-46: A montage showing the mercury injection data that is mercury saturation, capillary pressure, pore size distribution, SEM image and the porosity and permeability for sample TS1-197. See caption of Figure 3-5 for porosity and permeability uncertainties in plotted values.

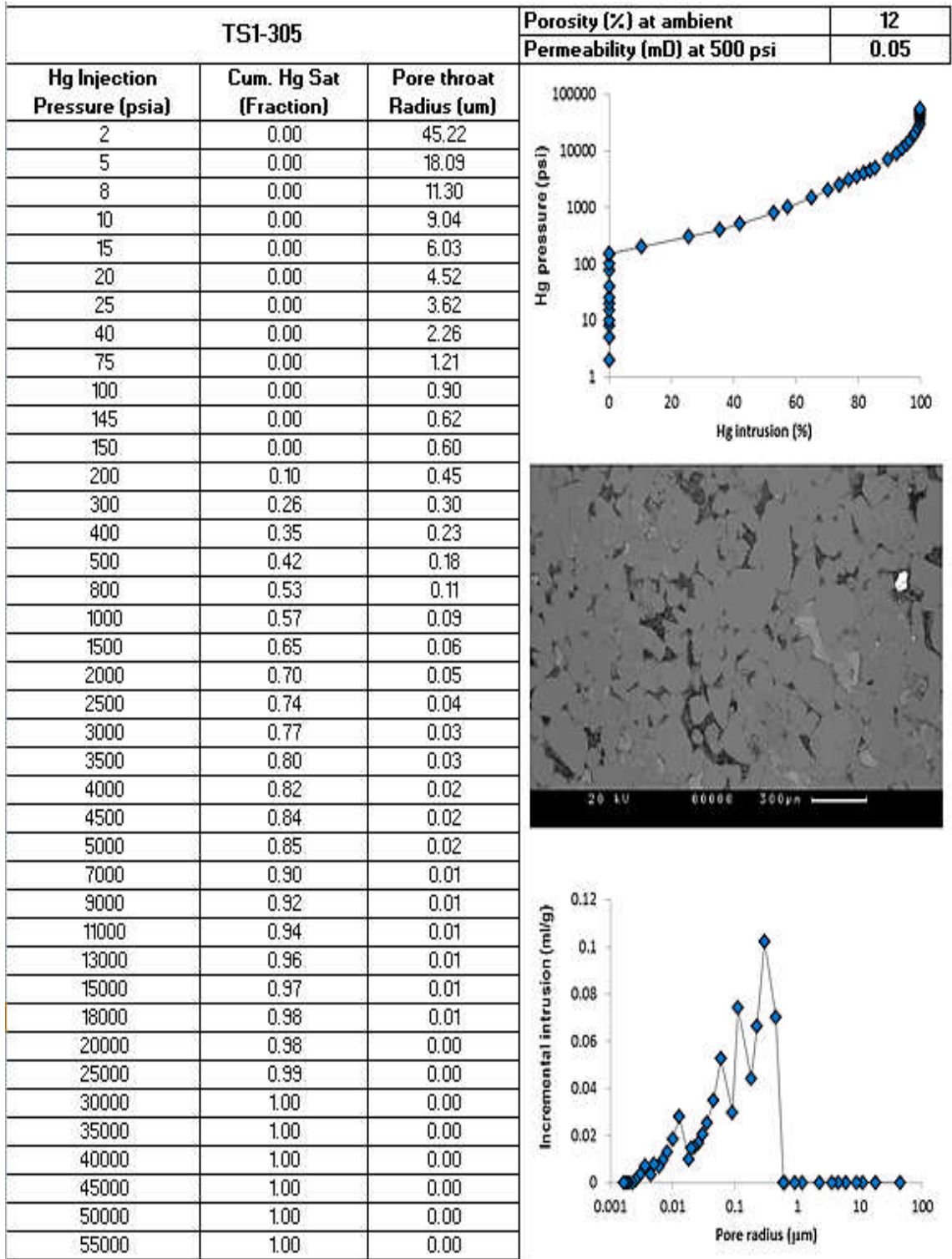


Figure 3-47: A montage showing the mercury injection data that is mercury saturation, capillary pressure, pore size distribution, SEM image and the porosity and permeability for sample TS1-305. See caption of Figure 3-5 for porosity and permeability uncertainties in plotted values.

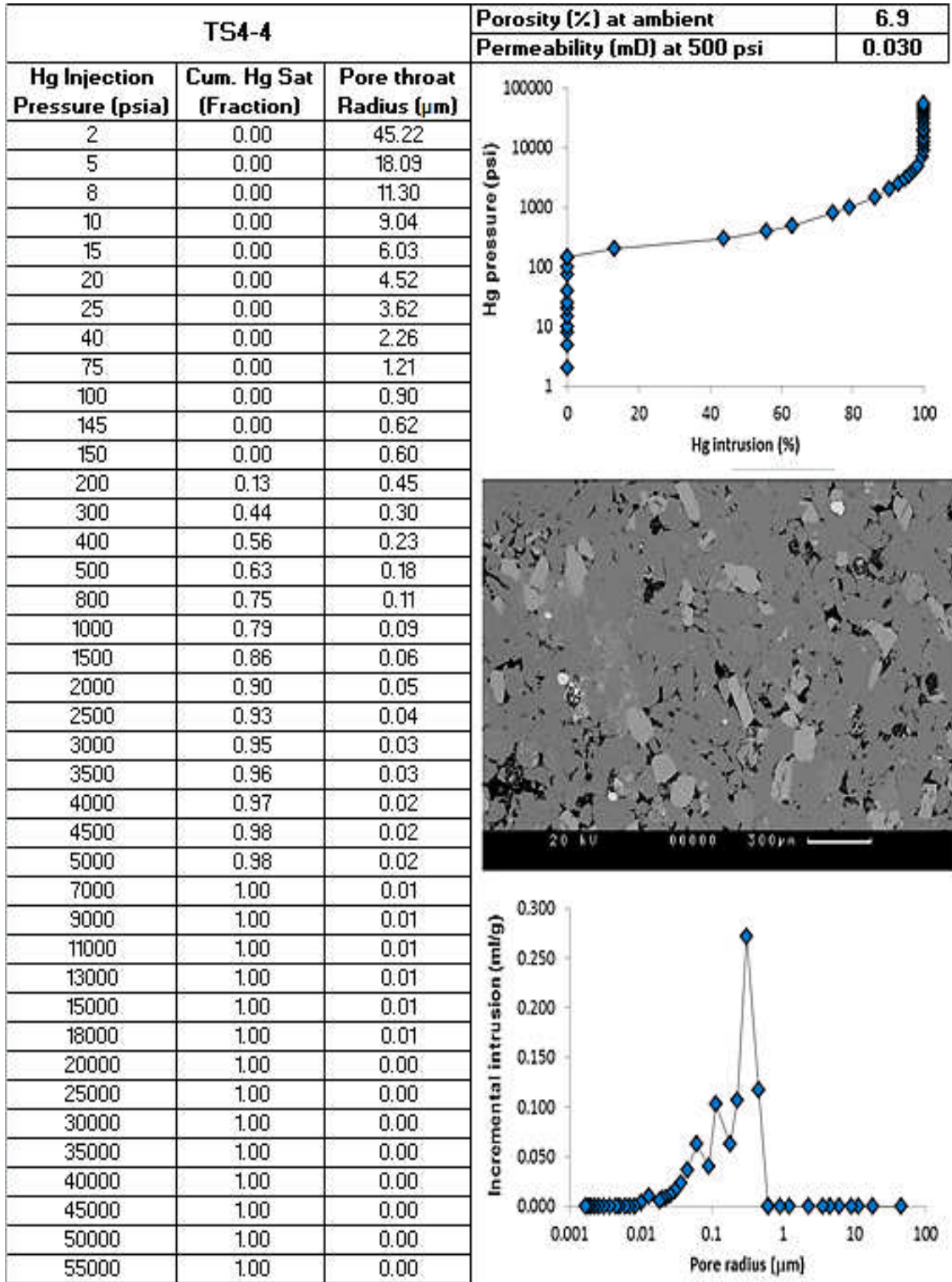


Figure 3-48: A montage showing the mercury injection data that is mercury saturation, capillary pressure, pore size distribution, SEM image and the porosity and permeability for sample TS4-4. See caption of Figure 3-5 for porosity and permeability uncertainties in plotted values.

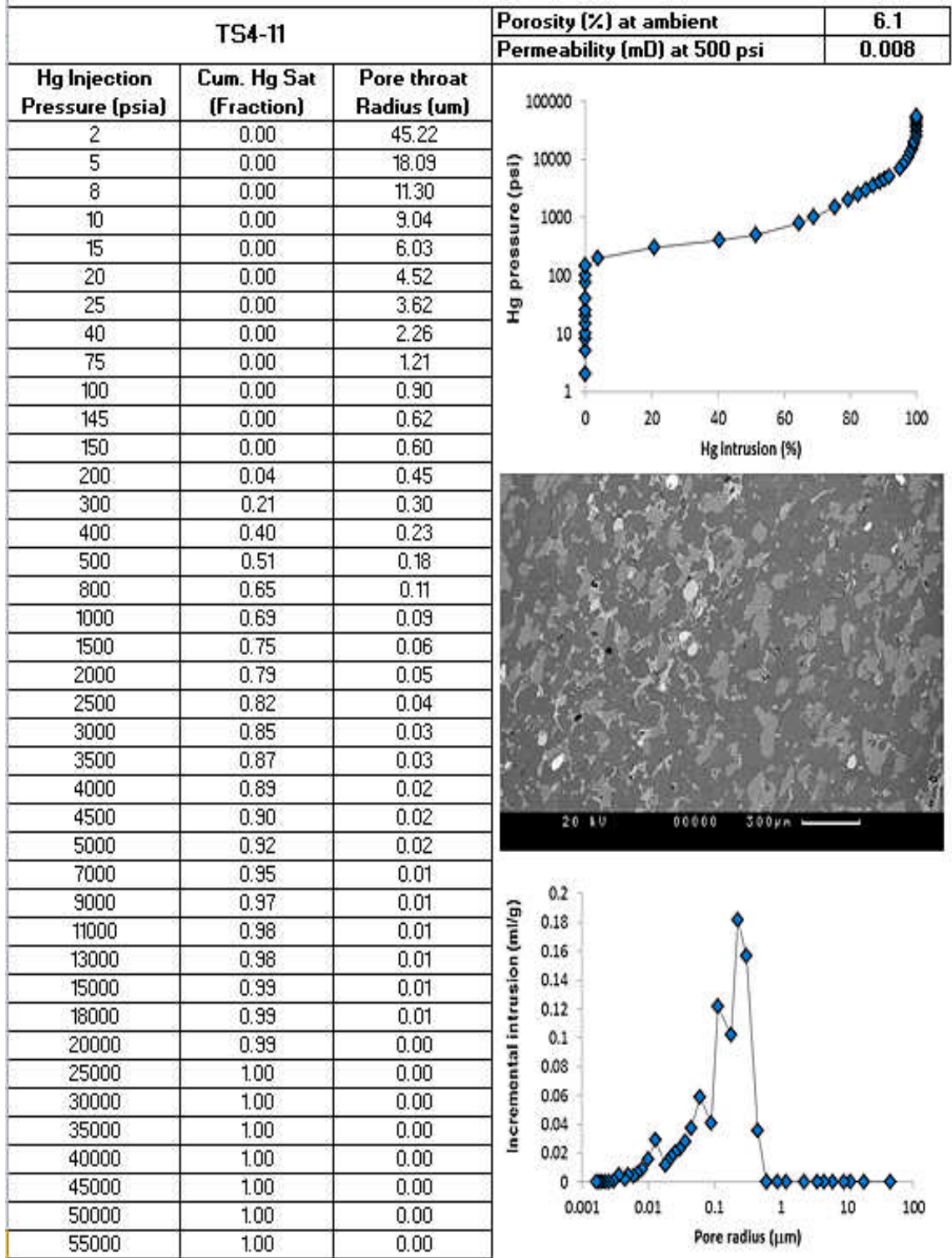


Figure 3-49: A montage showing the mercury injection data that is mercury saturation, capillary pressure, pore size distribution, SEM image and the porosity and permeability for sample TS4-11. See caption of Figure 3-5 for porosity and permeability uncertainties in plotted values.

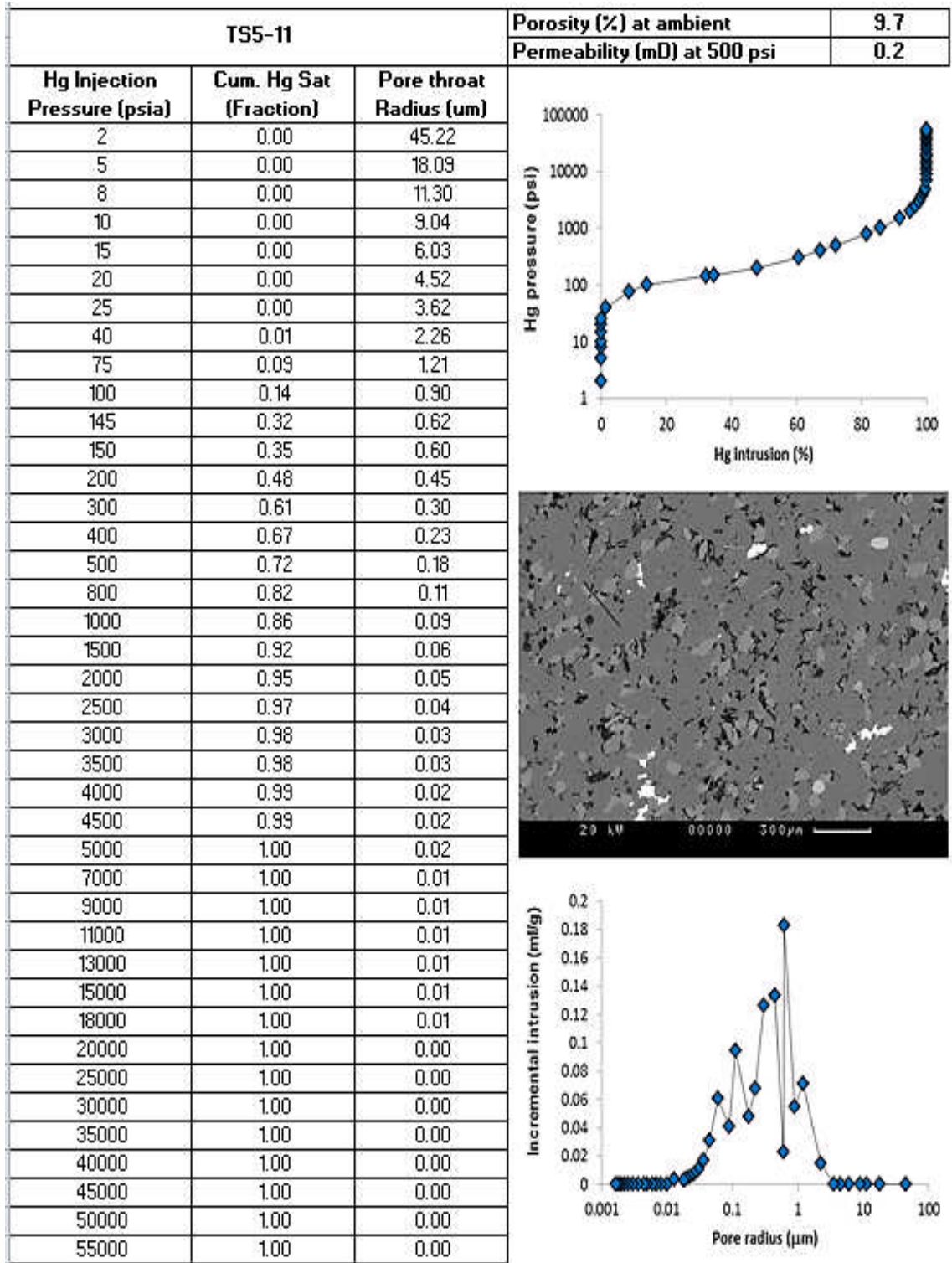


Figure 3-50: A montage showing the mercury injection data that is mercury saturation, capillary pressure, pore size distribution, SEM image and the porosity and permeability for sample TS5-11. See caption of Figure 3-5 for porosity and permeability uncertainties in plotted values.

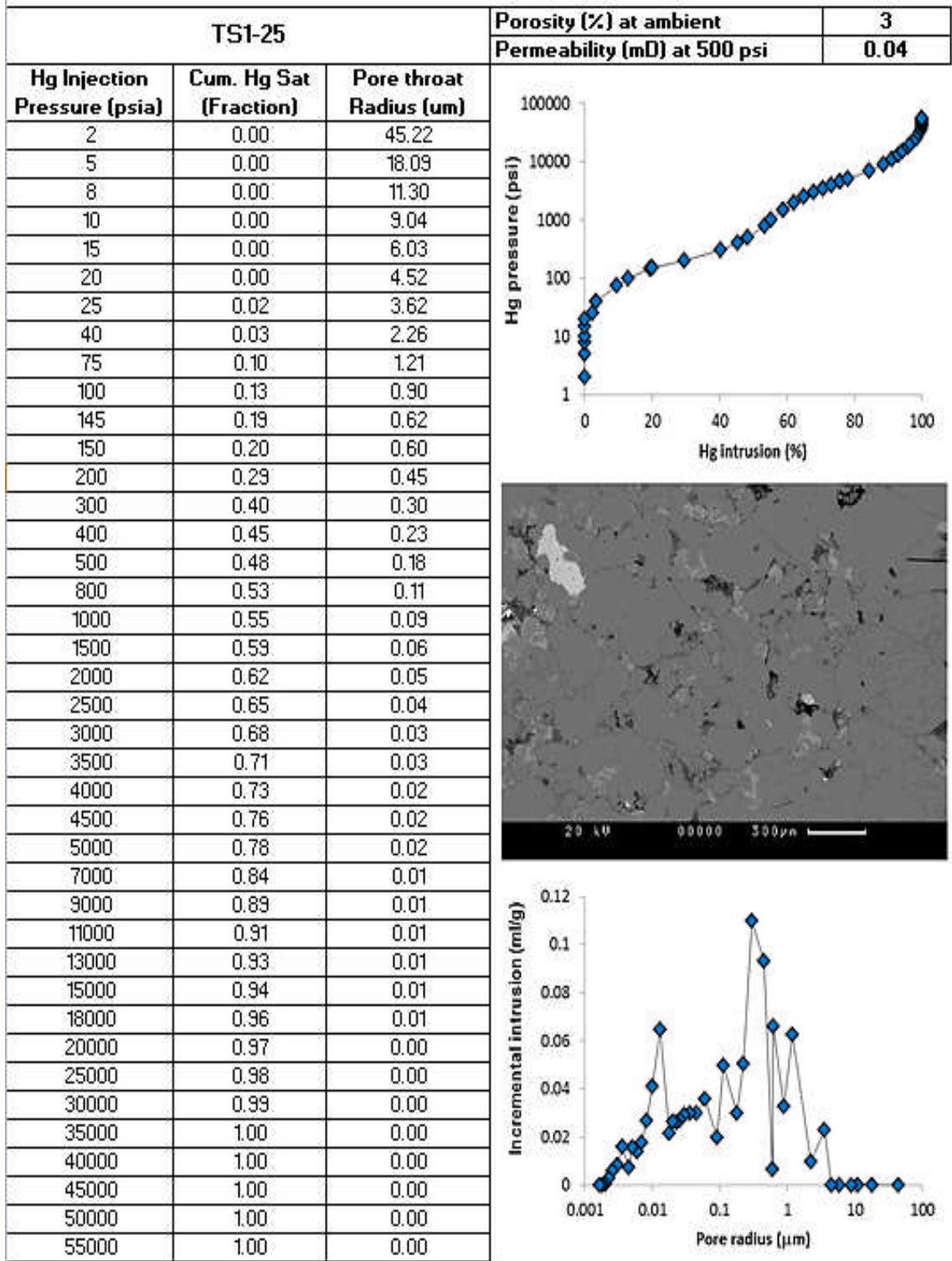


Figure 3-51: A montage showing the mercury injection data that is mercury saturation, capillary pressure, pore size distribution, SEM image and the porosity and permeability for sample TS1-25. See caption of Figure 3-5 for porosity and permeability uncertainties in plotted values.

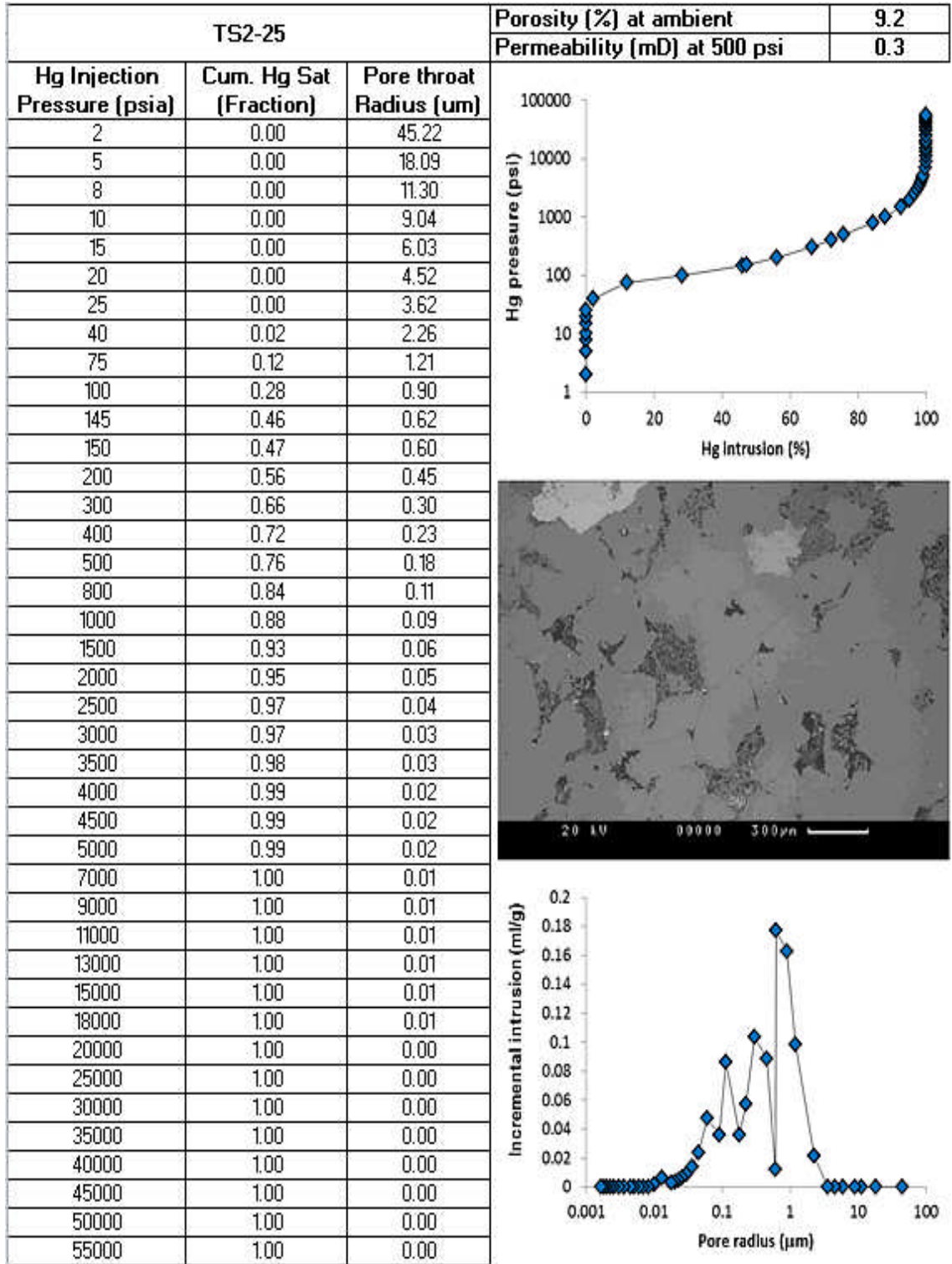


Figure 3-52: A montage showing the mercury injection data that is mercury saturation, capillary pressure, pore size distribution, SEM image and the porosity and permeability for sample TS2-25. See caption of Figure 3-5 for porosity and permeability uncertainties in plotted values.

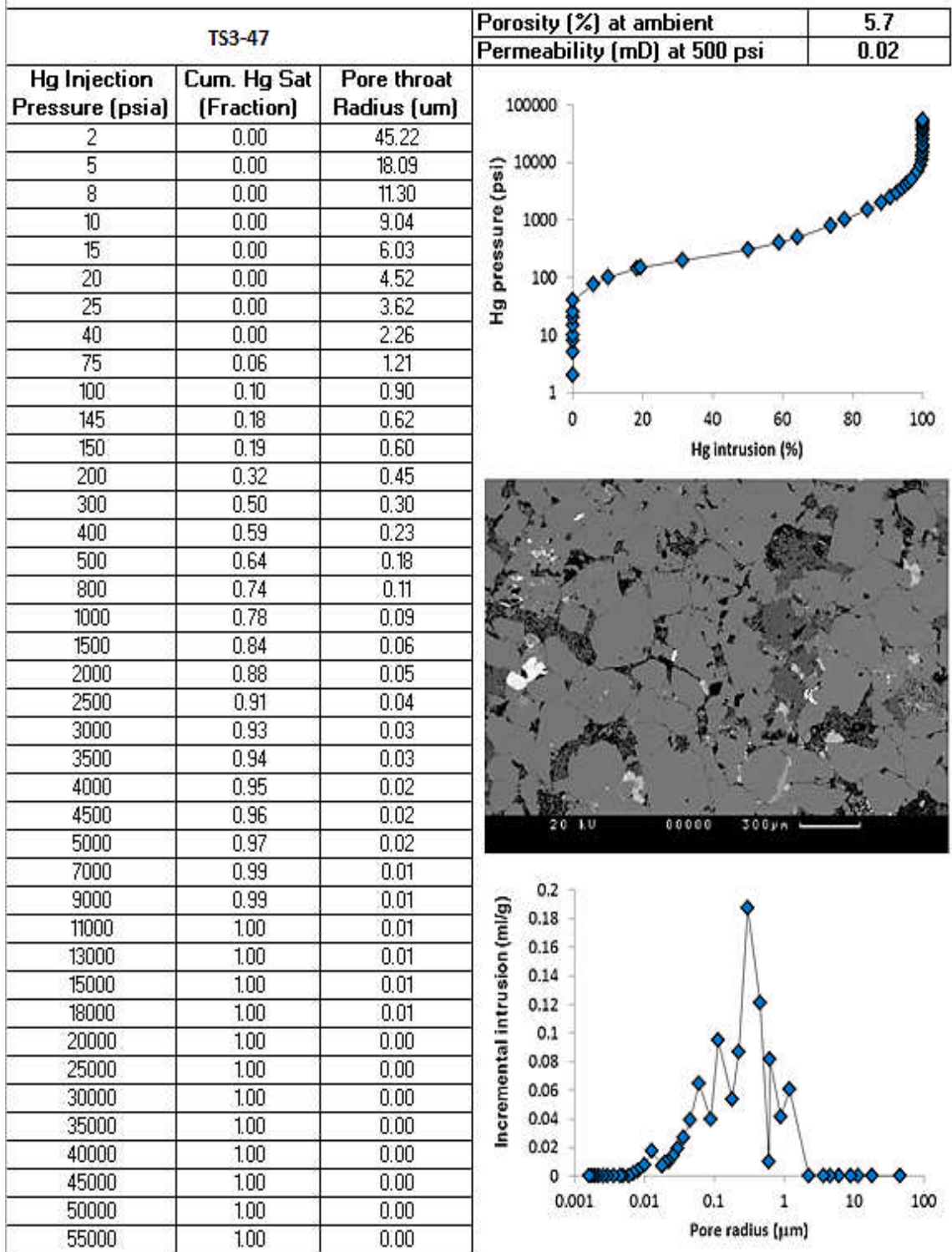


Figure 3-53: A montage showing the mercury injection data that is mercury saturation, capillary pressure, pore size distribution, SEM image and the porosity and permeability for sample TS3-47. See caption of Figure 3-5 for porosity and permeability uncertainties in plotted values.

3.4 Discussion

3.4.1 Controls on k_g/k_b ratios

The analysed samples show that the measured brine permeabilities at 1500 psi are all lower than the measured gas permeabilities at the same stress (Table 3-1). Figure 3-7 shows that a correlation exists between the brine and gas permeabilities for all three suites of samples examined during this study even though they are from different reservoirs. The results agree with the previous study conducted by Jones and Owen (1980) showing brine permeability lower than the absolute permeability measured for more than 100 tight sandstone samples (Figure 3-54). The determined power law relationship (Equation 3-3) could be used to estimate the effect of water on permeability, which can be used to optimize modelling the reservoir fluid flow.

QXRD analyses indicate the presence of different clay types at different percentages in the samples (Table 3-2), which is also consistent with the observation of the presence of different clay types from the SEM image analyses shown in Section 3.3.6. So, the water permeability was performed with the simulated brine that contains 40,000 ppm NaCl (Section 2.10.1) rather than distilled water to minimize the effect of clay swelling that could result in permeability reduction. Significant permeability reduction could result from using distilled water to measure the liquid permeability of sandstones with clay contents (Baptist and Sweeney, 1954; Lever and Dawe, 1987). So, measuring water permeability of tight sandstones that contain clay with fresh water can increase the water-sensitivity by interacting with clay particles present in the samples (Figure 1-18), which would underestimate the permeability leading to inaccurate modelling of the fluid flow.

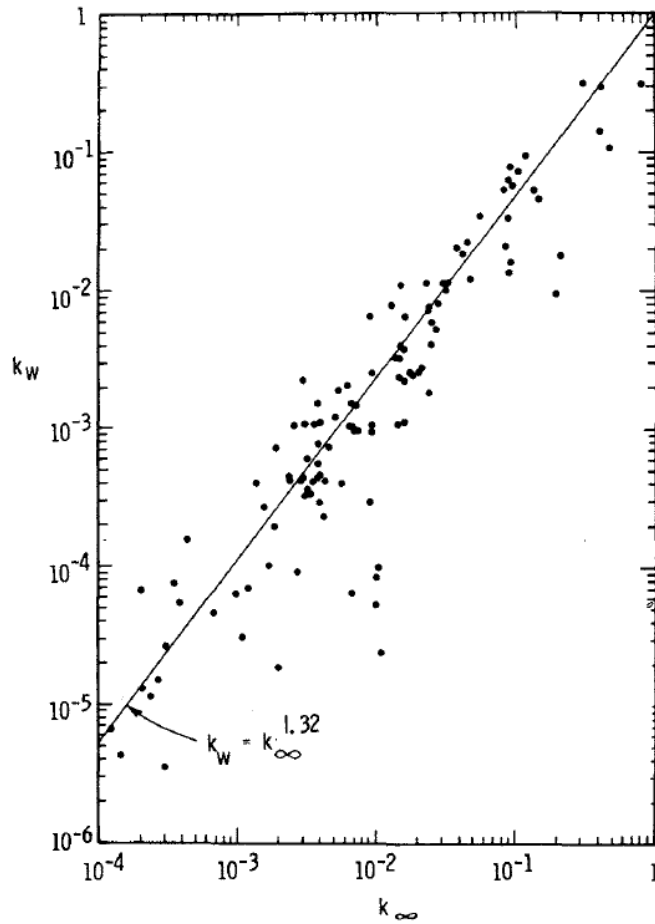


Figure 3-54: Cross plot of brine permeability (k_w) and absolute gas permeability (k_∞) for tight sandstone samples showing lower brine permeability for all the samples (from Jones and Owen, 1980).

3.4.2 Controls on porosity and permeability of sandstones

Porosity has an impact on permeability because generally more connected pore spaces would mean more fluid pathways, and hence higher permeability. Porosity is often plotted against permeability in a semi-log plot to determine how porosity controls permeability, and hence permeability can be determined from a porosity-permeability relationship. The low correlation coefficient indicates that factors other than porosity are controlling the permeability in tight sandstones (Figure 3-5). Pore-throat size, which is a function of the grain size, grain sorting and packing and cementation play a major role in controlling permeability of such tight rocks (Castle and Byrnes, 2005).

3.4.2.1 Grain size and sorting

Grain size and grain sorting play an important role in controlling the porosity and permeability of conventional sandstones reservoirs (Figure 1-11). Figure 3-55 shows a

cross plot of the porosity against permeability of the samples with colour coding corresponding to the grain size classified based on Wentworth scale (1922) where very fine (VF are grains between 0.0625 and 0.125 mm), lower fine (LF between 0.125 and 0.177 mm), upper fine (UF between 0.177 and 0.25 mm) and medium sand grains (M between 0.25 and 0.5 mm). The grains of the samples vary in sizes with no relationship can be found for all the samples between the grain size and the position of samples on the porosity-permeability cross-plot. Another plot of the porosity-permeability with colour coding corresponding to the grain sorting is shown in Figure 3-56. No correlation can be found between the degree of grain sorting of the samples and their positions on the porosity-permeability cross-plot. A better correlation of such plots may exist for samples from single formations or rock types, and so variation would be expected based on samples taken from different formations. This is in agreement with the results of the analyses of the porosity-permeability based on the lithofacies of the samples taken from the Lower Silurian Sandstones in the Appalachian Basin (Figure 1-12). Another reason would be the extensive various diagenetic processes the analysed samples had been through, which also might affect the correlation between the grain size and sorting and the porosity-permeability seen in conventional rocks. Diagenetic processes such as compaction and cementation alter the pore geometry which impacts the porosity and permeability relationship (Davies and Davies, 2001).

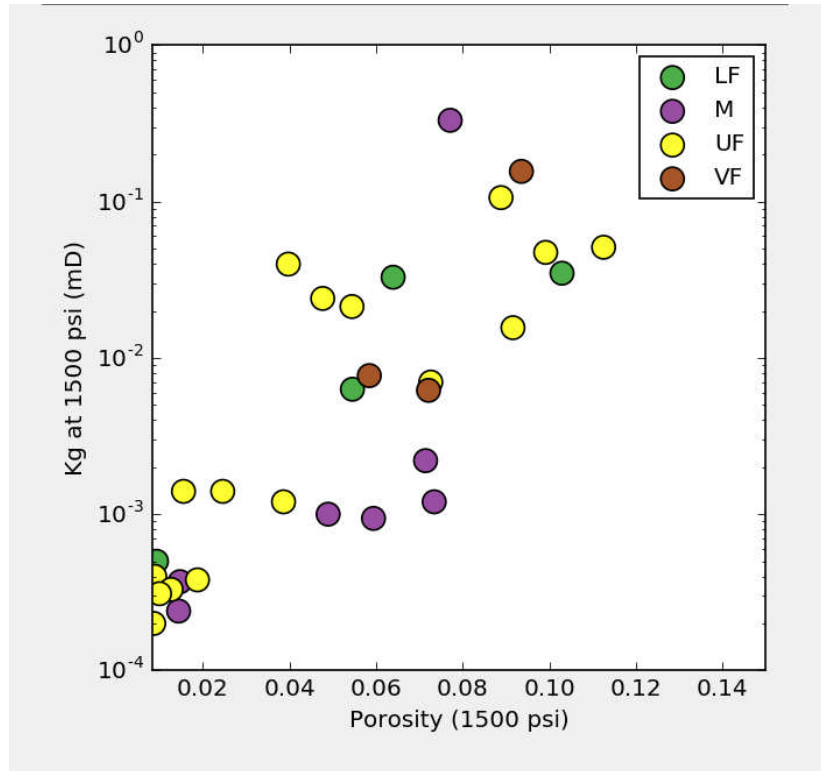


Figure 3-55: Porosity-permeability plot with colour coding for grain size. See caption of Table 3-1 for grain size definitions. No clear correlation exists between the grain size and the position of samples on porosity-permeability. See caption of Figure 3-5 for porosity and permeability uncertainties in plotted values.

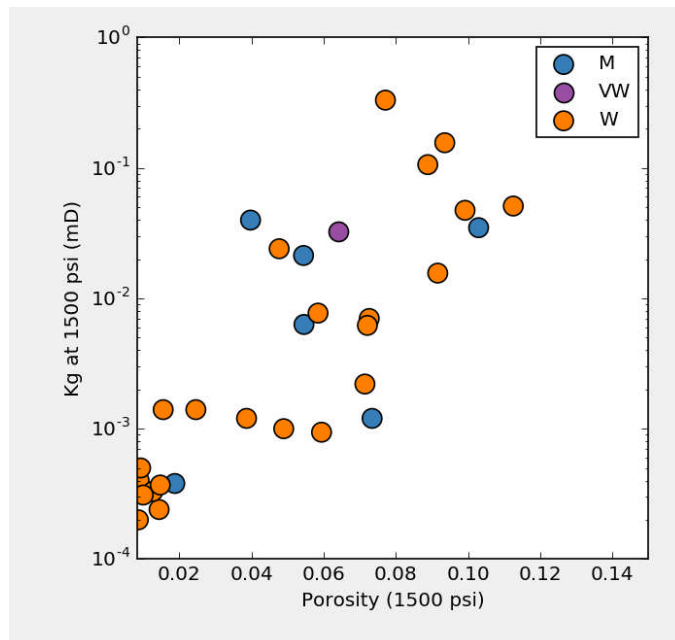


Figure 3-56: Porosity-permeability plot with colour coding for grain sorting. See caption of Table 3-1 for grain sorting definitions. No relationship found between the grain sorting and the position of the samples in the porosity-permeability cross plot. See caption of Figure 3-5 for porosity and permeability uncertainties in plotted values.

However, examining the samples individually shows some impact of the grain sorting on the porosity and permeability that is indicated from the mercury injection data. The grains of sample TS5-11 are very fine in size and well sorted as shown from SEM image (Figure 3-50). This sample has a high porosity of approximately 10% and the second highest permeability among all the samples (0.2 mD). In comparison, sample TS1-25, having a porosity of 3% with a relatively low permeability of 0.04 mD, shows poorly sorted grains and hence more heterogeneous pore system (Figure 3-51). The capillary pressure curve derived from the mercury injection data indicates the bimodal pore network resulting from the poorly sorted grains in sample TS1-25 in comparison with the monomodal pore system resulting from the relatively better grain sorting in sample TS5-11 (Figure 3-57). This is in agreement with the analyses of tight gas sandstones showing bimodal pore size distribution derived from MICP by Schmitt et al. (2015) and a study reported on a carbonate reservoir in Saudi Arabia (Clerke, 2009).

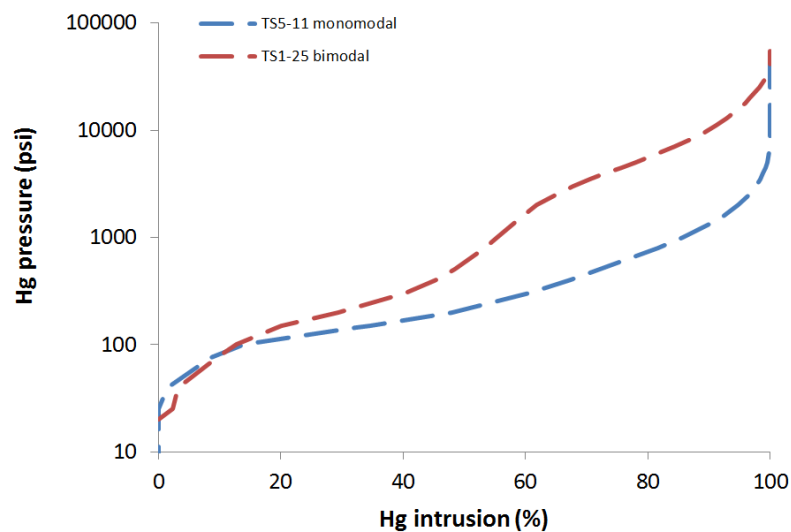


Figure 3-57: Mercury injection capillary pressure showing the monomodal for sample TS5-11 indicating the homogeneous pore system from the well sorted grains (blue) and the bimodal curve for TS1-25 indicating heterogeneous pore system resulting from the poorly sorted grains (red).

Moreover, samples TS1-197 and TS1-305 have similar permeability measured at 500 psi, but sample TS1-197 shows less porosity of approximately 8% compared to 12% porosity of TS1-305. Grain size of the both samples are in the upper fine range, but sample TS1-197 shows to be poorly sorted with broader pore size distribution as indicated from the MICP curve (Figure 3-46) compared to sample TS1-305

(Figure 3-47). Sample TS1-305 shows narrower pore size distribution plot derived from MICP, which indicates less heterogeneous pore system compared to the sample TS1-197 (Figure 3-58). Broader size distributions derived from MICP have been reported to be common in tight sandstones more than homogenous conventional rocks (Cao et al., 2016).

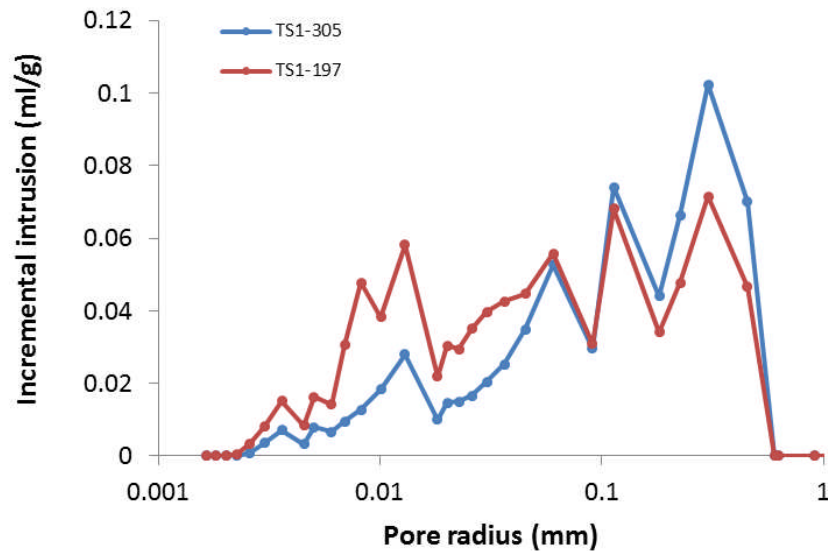


Figure 3-58: Pore size distribution derived from MICP showing narrower pore size distribution for sample TS1-305 indicating the homogenous pore system as a result from the well sorted grains (blue) and the broader pore size distribution curve for TS1-197 indicating heterogeneous pore system resulting from the poorly sorted grains (red).

3.4.2.2 Presence of microfractures

The presence of microfractures shows more effect on permeability than porosity, which can be seen in the analysed samples where several samples show higher measured permeabilities at low stress even though their measured porosities are low (Figure 3-5). For example, ambient porosities of samples TS2-3 and TS2-9 are approximately 9% and 4% respectively. Yet, the measured gas permeabilities of both samples at 500 psi net stress are similar, that is 0.002 mD. Analysis of the microstructure of the samples shows that microfractures are more abundant in sample TS2-9 as shown in the SEM image (Figure 3-13), which indicates that microfractures contribute more to the permeability. Microfractures don't contribute much to the porosity, but form connected networks that control the path ways for the fluid to flow, and hence increase the permeability (Shanley et al., 2004; Glover, 2016). The results

are consistent with the plot (Figure 1-13) where fractured rocks showing higher permeability than clean sandstone even though the clean rocks have higher porosity than the fractured ones (Figure 1-13).

3.4.2.3 Confining stress

Both stress-corrected porosity and measured gas permeability decrease as the confining stress increases. The increase in the confining stress results in greater reduction in permeability with less decrease in the determined porosity at 5000 psi (Figure 3-6) in comparison with porosity-permeability determined at ambient condition (Figure 3-5). The increase in stress resulted in a better porosity-permeability relationship (correlation coefficient of 0.75) than the correlation obtained at ambient low stress (a correlation coefficient of 0.64). This is consistent with the concept of closing microfractures due to net stress increase. Increasing the confining stress from low stress to 5000 psi resulted in more significant reduction in the permeability (Figure 3-59 – left) and the lower the permeability the greater the effect. The reduction in porosity is not significant compared with permeability (Figure 3-59 – right), but the higher the porosity the greater the effect of the stress. These results agree with previous studies reporting greater effect of stress on permeability than on porosity (Thomas and Ward, 1972; Byrnes, 1996). The stress dependency of permeability is discussed in more detail in Chapter 4.

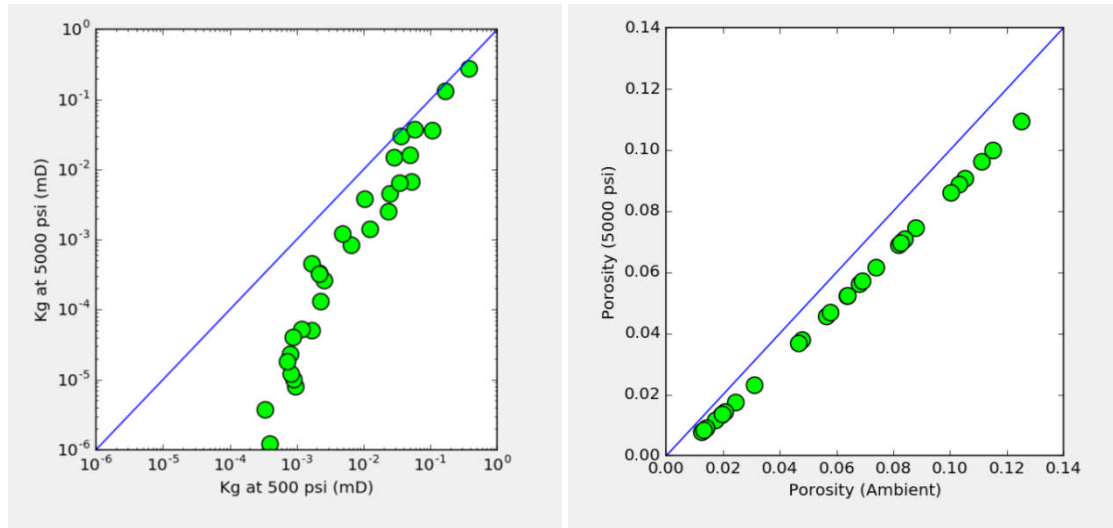


Figure 3-59: Left: Plot of gas permeability measured at 500 psi net stress against permeability measured at 5000 psi with 1:1 correlation (blue line). Right: Porosity measured at ambient against porosity determined at 5000 psi with 1:1 correlation (blue line). See caption of Figure 3-5 for porosity and permeability uncertainties in plotted values.

3.4.2.4 Clay type

Different clay types are observed in most of the samples as indicated by the SEM images of the samples presented in Section 2.8 and confirmed by QXRD data (Table 3-2), which are consistent with Figure 1-14. A plot of porosity-permeability with colour coding corresponding to the clay type is shown in Figure 3-60 to analyse the impact of the clay type in the porosity and permeability. Generally, no clear trend exists between the clay type and the position of the samples in the porosity-permeability plot of all the three suites of samples. This could be due to the samples being collected from different reservoirs. However, samples that contain clay “illite” coating the grains and bridging the pores show lower permeability than samples with pore filling clays for a given porosity. Samples with a porosity between 0.08 and 0.1 show that sample with low clay has highest permeability, followed by samples having pore filling and pore bridging, respectively. These results are generally consistent with the studies of Neasham (1977) and Wilson (1982).

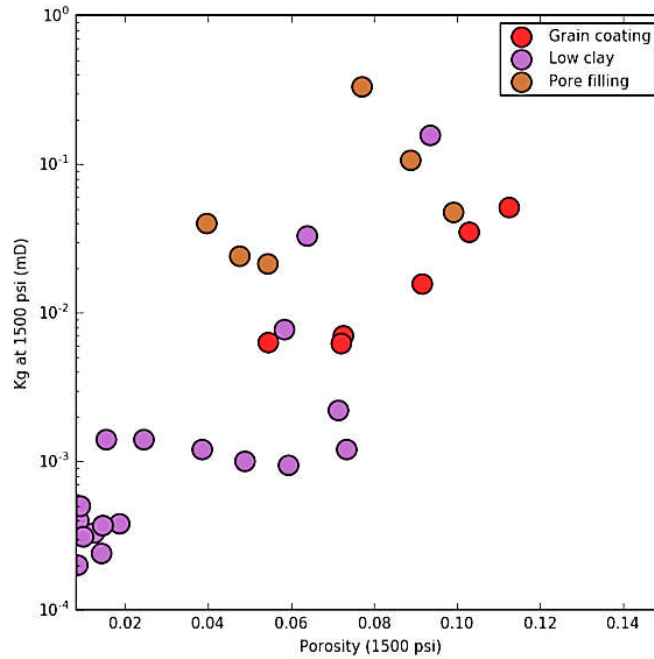


Figure 3-60: Plot of porosity-permeability with different types of clay present in the samples as indicated by the colours (Red = grain coating illite, Purple = low clay samples and Brown = pore filling clay). See caption of Figure 3-5 for porosity and permeability uncertainties in plotted values.

3.5 Conclusion

Analyses of the porosity and permeability showed that there is a control of porosity on the permeability of the samples where permeability increased as the porosity increased. Porosity-permeability data was fitted with an exponential relationship with a correlation coefficient of 0.64. The grain size and sorting theoretically have an impact on the porosity and permeability of the samples. Examination of samples individually indicated that samples with poorly sorted grains appeared to have lower permeability due to their bimodal pore system observed from the mercury injection capillary pressure curves and the pore size distribution plots as well as SEM images. However, no clear correlation could be found between these properties in the whole tight gas sandstone database generated during the current study. This could be explained by the different lithofacies of the samples and the extensive diagenetic processes the samples had been through.

The presence of microfractures could have a greater impact on permeability than porosity. Samples with different measured porosities appeared to have similar measured permeabilities. Examination of the SEM images of the samples indicated

that the presence of microfractures enhanced the permeabilities of the samples with the lower porosities. Stress-correction for porosity indicated the reduction of porosity is lower for the less porous samples. The increase of confining stress reduced the permeability of all samples with greater reduction for relatively tighter samples. This could be caused by the closure of microfractures.

The clay impact on the porosity and permeability depend on the clay type and distribution. Clean sandstones (i.e. those with little or no clay) showed to have the highest porosity and permeability. The grain coating Illite that bridges the pore space showed to have the greatest effect in reducing the permeability compared to other clay types at a given porosity. Permeability of sandstones with pore filling chlorite or the discrete kaolinite particles had a higher permeability than those containing illite for a given porosity. Thus, the presence of the clay has great impact on the quality of the tight sandstones reservoirs, which also depends on the content and distribution of the clay.

4 Stress-Dependent Permeability, Ultrasonic Velocity and Electrical Properties of Tight Gas Sandstones

4.1 Introduction

The stresses and pore pressures often used to measure the properties of tight gas sandstones in the laboratory are often far lower than those that are encountered in the subsurface (e.g. 500 psi compared to 5000 psi net stress). This creates a major problem in calculating the gas volume in place and determining the producibility in tight sandstone reservoirs because their petrophysical properties are stress dependent. In general, the stresses encountered in the subsurface are not equal in all directions (i.e. $\sigma_1 \neq \sigma_2 \neq \sigma_3$) (Tiab and Donaldson, 2012). The maximum stress encountered in the subsurface, expressed as σ_1 , is that imposed by the overburden in an extensional tectonic regime. However, in a thrust or strike-slip regime, the horizontal stresses could be higher than the vertical stress. After drilling and cutting cores from the formation, the stress state of the core changes into hydrostatic state where all stresses become equal (i.e. $\sigma_1 = \sigma_2 = \sigma_3$) (Farquhar et al., 1993). Rapid change of stress state of the rock after being buried for millions of years may alter the pore structure of the rock resulting in significant alteration of the petrophysical properties (Farquhar et al., 1993). Measuring petrophysical properties such as permeability, electrical resistivity and velocity under ambient condition is therefore not representative of the *in-situ* stress condition prior to the pore structure alteration. Stress sensitivity of petrophysical properties is defined as the ratio of the measured property at an effective net stress to its value measured under different stress and pore pressure conditions.

Permeability is a key parameter used for predicting productivity, selecting well completion intervals with the optimum fracture stimulation design (Luffel et al., 1991). Permeability of tight gas sandstone reservoirs is more sensitive to stress than conventional rocks having relatively higher permeability (Kilmer et al., 1987) especially when examined at low net stresses. Thus, it is important to have permeability measurement that is representative of the reservoir condition to accurately model subsurface fluid flow. Such measurement is achieved by either measuring permeability

at reservoir stress or by applying the proper stress correction to permeability measured at low confining pressure.

Properties of tight samples are stress sensitive in the laboratory but may not be in the field as microcracks are not as abundant in the sub-surface as in the laboratory. Thus, flow rate would be overestimated if calculated based on routine core analysis data i.e. permeability measured under ambient condition (Ostensen, 1983), or stress-corrected using conventional core formulas. Velocity that is used to estimate the porosity and the elastic properties of the rock, would overestimate the porosity and the elasticity of the rock if stress state is not considered. Measuring electrical properties without considering the effect of stress will also result in incorrect water saturation and hence erroneous gas saturation in place. Abandonment pressure, which is a function of the permeability, could also vary more significantly in unconventional reservoirs than the conventional formations. Thus, it is important to analyse the stress dependency of the petrophysical properties of each tight reservoir and not to assume all reservoirs respond equally to the change in stress.

To provide further insight into the stress dependency of the petrophysical properties of tight sandstones, gas permeability, ultrasonic velocity and electrical properties were measured under a range of net stresses. Permeability measurements were conducted to analyse the causes of the stress dependency on the fluid flow. Gas permeability was also measured under reservoir condition with drawdown experiments to analyse the stress dependency at *in-situ* stress. Ultrasonic velocity was measured under different stresses to analyse the impact of stress on the elastic properties and the porosity of the tight samples. Electrical resistivity was also measured at various stresses to analyse the effect of stress state on the electrical parameters used to estimate the water saturation in the samples. All measurements were coupled with SEM images to analyse the microstructure of the samples that could affect the stress dependency of the properties.

This chapter presents the results of the permeability, ultrasonic velocity and electrical properties measurements under a range of stresses conducted on 15 core plugs that were taken from tight heterogeneous sandstone reservoirs. The permeability measurements at *in-situ* stress and prior to abandonment condition corresponding to a

production scenario are also presented. Analyses of the microstructures of the samples from SEM images are presented. The controls on the stress dependencies of the properties and correlations between their dependencies are discussed. A discussion regarding the errors in calculating the gas in place using wrong values of electrical properties is presented. Implications of gas slippage and stress dependency of permeability in production are also discussed.

4.1.1 Background

Reservoir pressure drops during gas production causing an increase in the effective net stress which affects the permeability due to compaction of the reservoir rock (Vairogs et al., 1971). It is crucial to examine and quantify the stress dependency of permeability to evaluate the likely flow rates for tight gas sandstones when put on production, and permeability enhancement that might occur due to gas slippage effect resulting from pore pressure reduction. Understanding the impact of stress and pore pressure on the permeability of tight gas sandstones would allow industry to better plan production strategies such as whether it is worth producing gas at lower rates but high pressure to increase the total gas production. This process is referred to as restricted rate practice where gas wells may flow for longer periods at a nearly constant low rate (Dong et al., 2015).

4.1.1.1 Electrical properties

The formation resistivity factor can be calculated using one of the Archie's formulas (1942) discussed in Chapter 1 (Equation 1-8) and (Equation 1-9). The exponent m , which is often referred to as the porosity exponent (Guyod, 1944), can be determined as the slope of the formation resistivity factor cross-plotted against porosity in a log-log plot, which is known as the Pickett Plot (Figure 4-1).

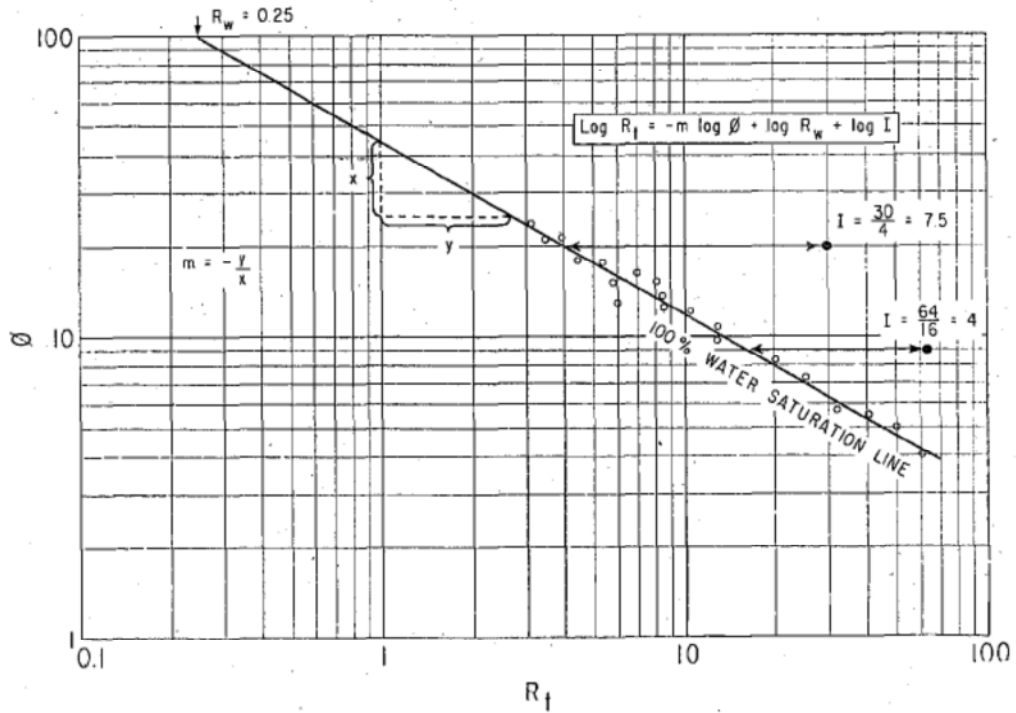


Figure 4-1: A schematic of the Pickett plot used to determine the cementation exponent m as the slope of the porosity vs formation resistivity in log-log scale (from Pickett, 1966).

One of the early formulas presented to correlate the cementation exponent m with porosity is the Shell formula (Equation 4-1), which shows that the exponent m increases as the porosity decreases (Figure 4-2). However, results from experiments conducted on Mesaverde tight gas sandstones presented by Cluff et al. (2009) showed that the exponent m decreases as the porosity drops. Their models are an empirical reduced major axis (RMA) (Equation 4-2), and an ordinary linear regression analysis (LRA) (Equation 4-3) as shown in Figure 4-3. This could be explained by the presence of fractures (Watfa and Nurmi, 1987) or the presence of aligned slot-like pores acting as conductive cracks (Cluff et al., 2008).

Equation 4-1

$$m = \frac{0.019}{\phi} + 1.87$$

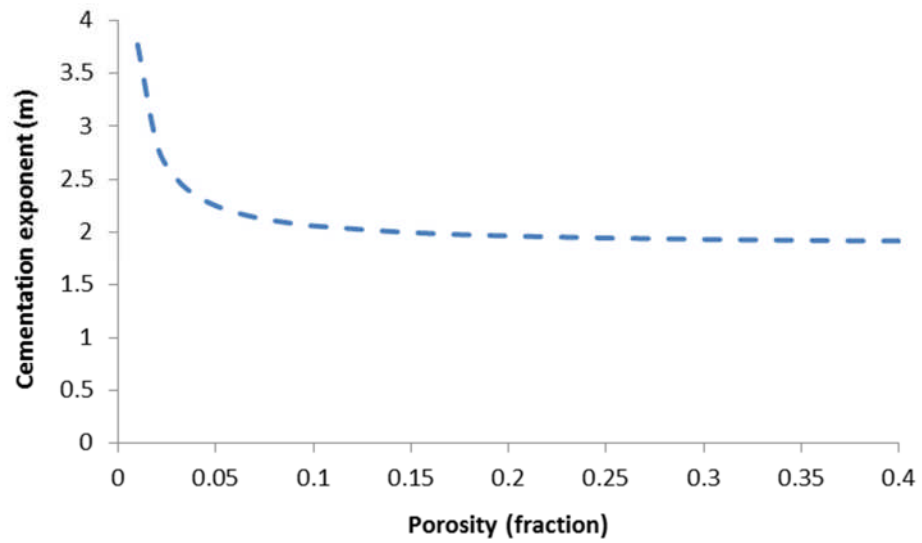


Figure 4-2: Relationship between the cementation exponent (m) and porosity (fraction) based on the Shell formula suggesting that m increases as the porosity decreases (from Neustaedter, 1968).

Equation 4-2

$$m = 0.653 \log \phi + 1.248$$

Equation 4-3

$$m = 0.53 \log \phi + 1.344$$

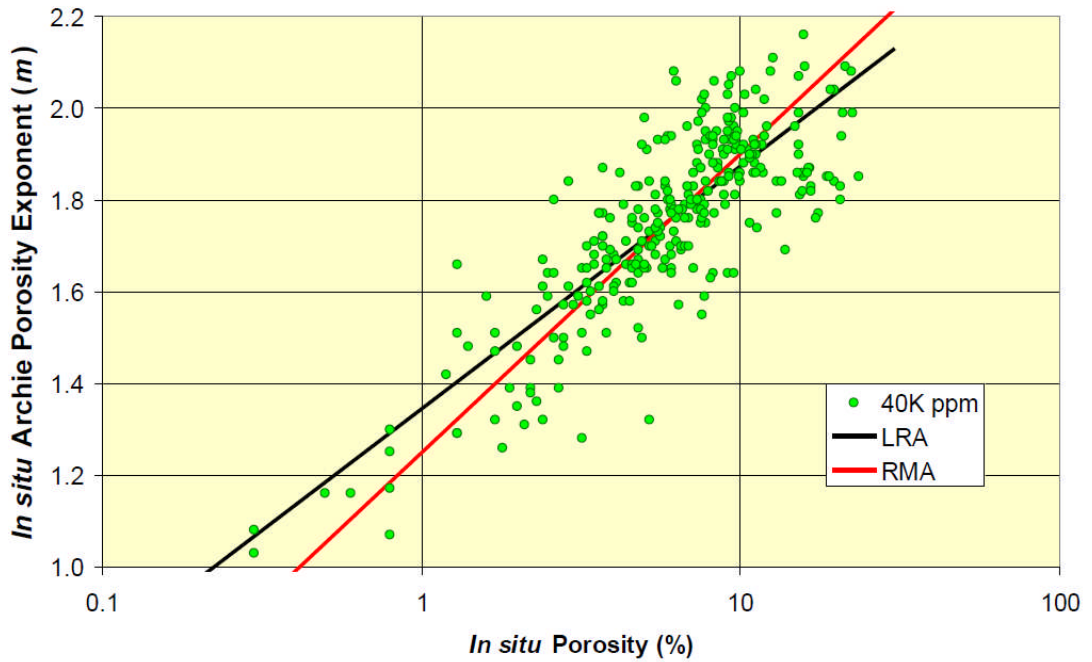


Figure 4-3: Cross plot of the in-situ Archie exponent (m) against in-situ porosity (%) in semi-log graph showing correlation using reduced major axis RMA (red) and linear regression analysis LRA (black) for Mesaverde tight gas sandstones (from Cluff et al., 2009).

It is assumed that the presence of microfractures supports the current flow parallel to the matrix. In such case, the dual porosity model can be used to describe the variation in m with porosity (Equation 4-4) (Cluff et al., 2009). It is vital to carefully choose the value of m to be used in hydrocarbon estimation as slight errors in the value of m could cause large uncertainties in saturation calculation especially in tight formations (Figure 4-4).

Equation 4-4

$$m = \log [(\phi - \phi_2)^{m_1} + \phi_2^{m_2}] / \log \phi$$

Where:

ϕ = bulk porosity (fraction)

ϕ_2 = fracture porosity (fraction)

m_1 = matrix porosity exponent

m_2 = fracture porosity exponent

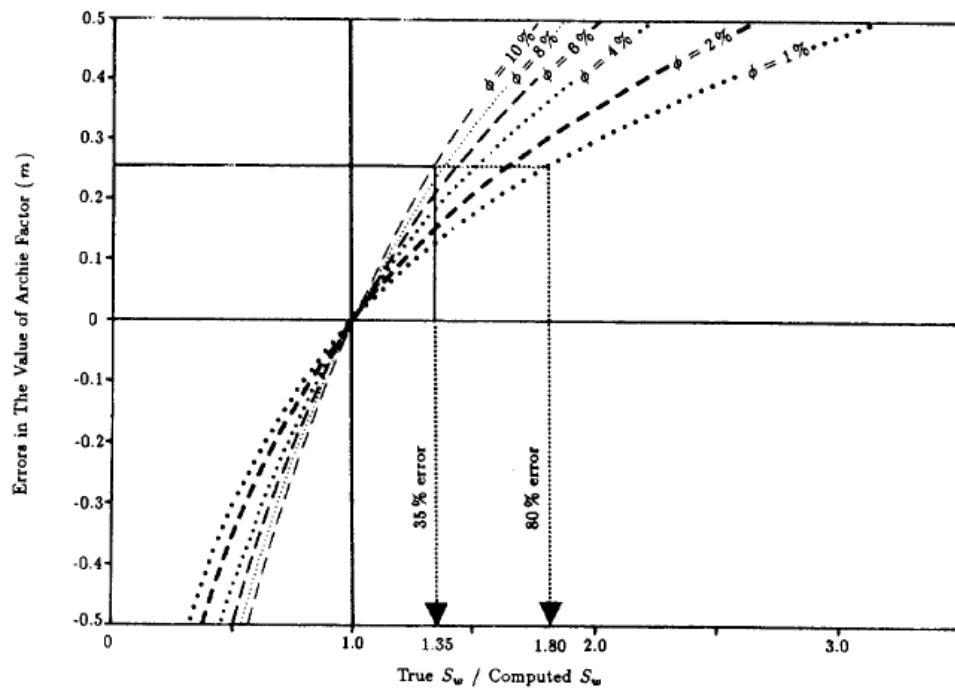


Figure 4-4: Large errors in water saturation calculation as a result of using wrong values of the cementation exponent m in Archie's law (from Watfa and Nurmi, 1987).

Herrick and Kennedy (1993) defined an electrical efficiency, E , which is inversely related to the exponent m , and a function of the pore throat geometry rather than the pore volume. They showed that the electrical efficiency can be increased in tight rocks by the presence of fractures despite their low porosity (Figure 4-5). They also discussed how the orientation of the fractures play a major role in affecting E . Fractures that are parallel to the direction of the current flow contribute more to the electrical efficiency than fractures that are perpendicular to the current flow (Figure 4-6).

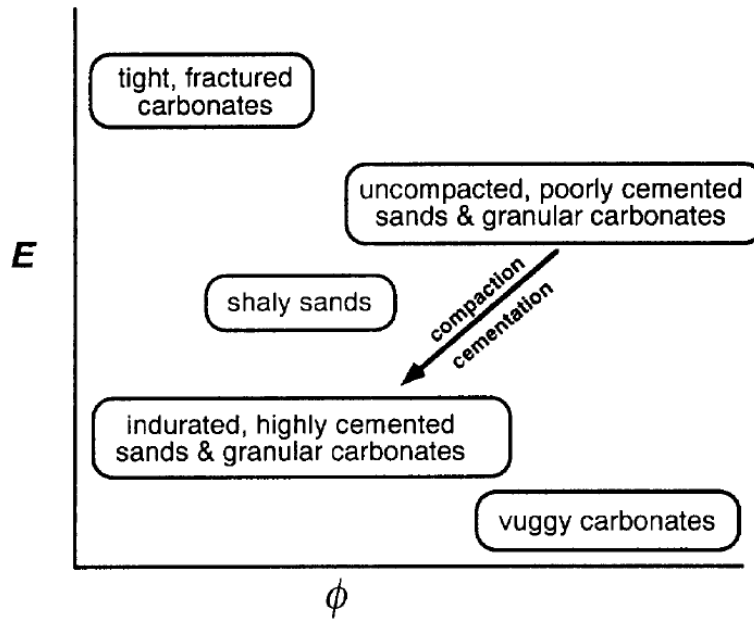


Figure 4-5: Effect of the pore geometry (i.e. fractures) in increasing the electrical efficiency of tight rocks despite their low porosity (from Herrick and Kennedy, 1993).

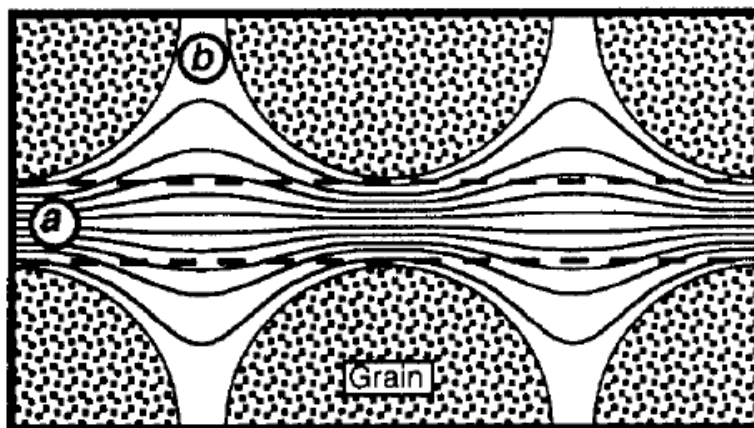


Figure 4-6: A schematic demonstrating the higher contribution to the electrical efficiency of fracture (a) that is parallel to the direction of the current flow than the fracture (b) (from Herrick and Kennedy, 1993).

4.1.1.2 Ultrasonic velocity

The ultrasonic P-wave velocity at any stress state is controlled mainly by the composition of the rock, its porosity and cementation (Figure 4-7). Ultrasonic velocity is used extensively in the analysis of tight gas sandstone reservoirs. Wyllie et al. (1956, 1958, 1963) and Raymer et al. (1980) were among the earliest who determined

empirically the porosity of porous media using the compressional velocity measurements. Han (1986) suggested that clay content could affect the velocity-porosity relationship and that taking into account the clay content improved the ultrasonic velocity calculation. P-wave velocity and porosity measurements under different net stresses were conducted on Fontainebleau sandstone by Han (1986). It was reported that the increase in net stress had greater impact on the velocity than the porosity (Figure 4-8). Nur et al. (1991, 1995) introduced the concept of critical porosity stating that ultrasonic velocity should fall between the velocities of the minerals of the sample at zero porosity and the velocity of a suspension of the material at high porosity.

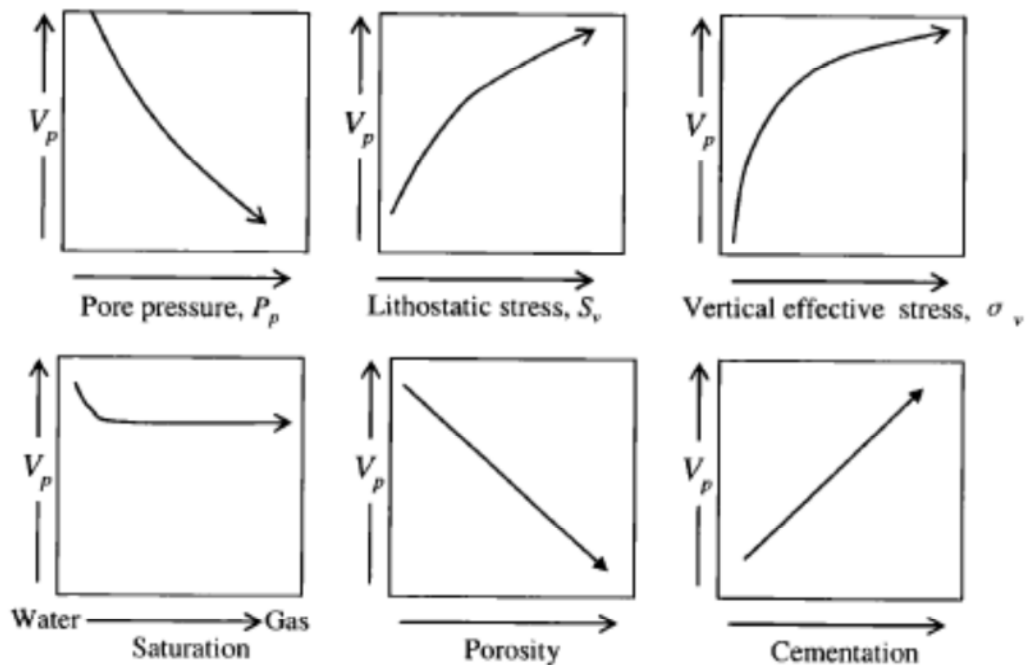


Figure 4-7: Effects of the rock properties on ultrasonic P-wave velocity (from Hilterman, 1998).

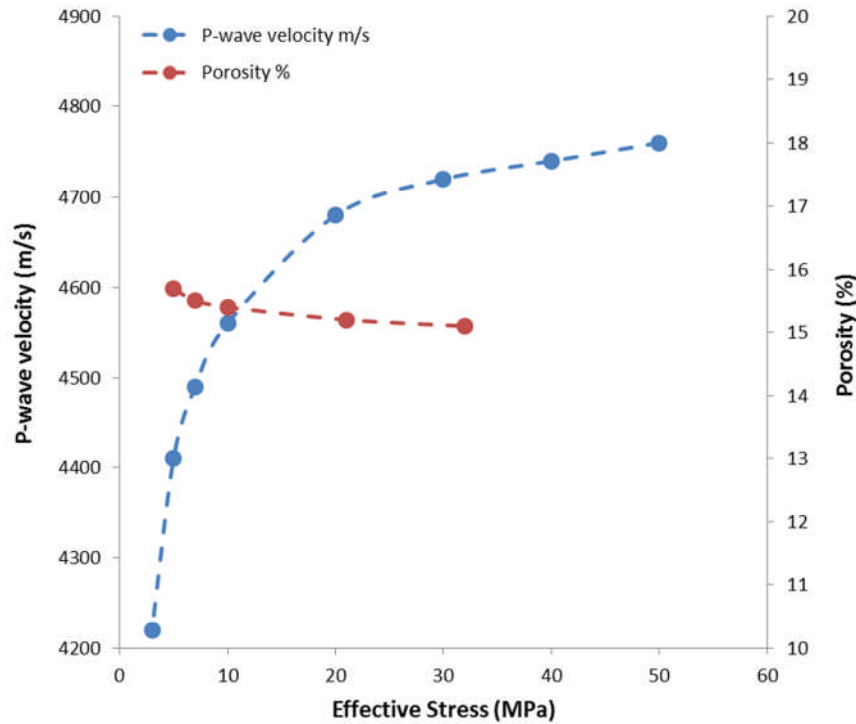


Figure 4-8: P-wave velocity (m/s) and porosity (%) in Fontainebleau sandstone as a function of net stress showing the significant stress-dependent of velocity in comparison to minimum change in porosity as the stress increase (modified from Han, 1986 as cited in Mavko, 2009).

4.1.1.3 Controls on the stress dependency of properties

Many experiments have been conducted to examine the stress sensitivity of permeability and other petrophysical properties of clastic rocks. However, less work has been done to examine the effect of the microstructure on the different stress dependencies of the properties. Reduction of permeability with the increase in the confining stress has been proved since the 1950's. Fatt and Davies (1952) were the first to examine the effect of overburden pressure on the permeability. They examined eight clean dry sandstone core plugs, and they observed the most reduction of permeability to be in the range of 0 – 3000 psi overburden pressure. They reported that at 3000 psi overburden with pore pressure at about atmospheric condition, permeability decreased in the range of 11 to 41 percent of the initial unstressed permeability. Later, Fatt (1958) published the first relationship between porosity and formation resistivity factor under compression. Wyble (1958) examined the effect of radial pressure rather than overburden pressure on petrophysical properties of sixteen sandstone samples. He reported asymptotic reduction in corrected permeability and

porosity as well as electrical conductivity. He observed the most effect of pressure on such properties to occur in the range of 0 to 3500 psi. An increase in the cementation exponent with pressure was also reported.

McLatchie et al. (1958) measured the oil permeability under a range of effective overburden pressure from 0 to 8000 psi for sandstone samples. They referred to the permeability at 0 psi as the reference permeability. They attributed the permeability reduction to the compressibility of the rock. It was found that reduction of permeability as a result of the overburden pressure increase was greater in sandstones with clay content compared to clean sands.

Dobrynin (1962) analysed the effect of overburden pressure on some petrophysical properties of consolidated sandstones with two series of measurements. One series with pore pressure equal to atmospheric pressure and the second one with pore pressure of 1800 psi. Overburden pressure in the range 0-20000 psi was used with both series, and he defined the net overburden pressure as $(P_e - 0.85 P_i)$ where P_e is the overburden pressure and P_i is the pore pressure, and 0.85 is a coefficient indicating less effect of the pore pressure. He assumed permeability reduction under stress is due to pore channels contraction. Brace et al. (1968) examined the fluid permeability and electrical conductivity of Westerly granite sample as a function of the effective stress. They reported reduction in both properties with increase in pressure and proposed a permeability-electrical resistivity relationship as a function of pressure.

Vairogs et al. (1971) examined tight sandstone samples under a stress, and reported that effect of stress on permeability of tight rocks was greater than the effect on samples with higher permeability due to smaller pore sizes being stressed. It was also reported that heterogeneity of the samples such as shale streaks and hairline fractures could increase the permeability stress-dependency. Thomas and Ward (1972) reported a reduction of about 75 percent of gas permeability under 3000 psi net stress, and 80 to 90 percent reduction at 6000 psi of tight sandstone samples. They reported greater permeability reduction for the similar tight samples with microfractures where 95 percent of permeability reduction occurred under 3000 psi net stress.

The stress-sensitivity of permeability depends on the geometry of the micro-pores where different pore shapes result in different stress dependencies (Ostensen, 1983). Brower and Morrow (1985) showed that sheet-like pores in an unconfined core could not be impregnated with the casting material when the core sample was put under 5000 psi stress indicating an alteration in the pore size distribution by tightening or even complete closure of crack-like pores and constrictions.

Davies and Davies (2001) examined the stress dependent permeability in two sets of sandstones, tight gas sandstones and unconsolidated high porosity ones. They showed the greatest reduction in permeability occurred in the tight consolidated sandstones compared with better quality unconsolidated samples. Yet, they stated that no unique relationship necessarily exist between permeability and stress. Shanley et al. (2004) also demonstrated in their study that impact of confining stress on permeability is greater for sandstone reservoirs with measured routine permeability of 0.5 mD or less.

4.2 Materials and methods

Gas permeability and ultrasonic velocity measurements were performed under a wide range of stresses. The samples were then saturated with simulated brine for brine permeability and electrical resistivity measurements under stress. The samples used for the analyses and their preparation are discussed in Section 2.2 and 2.3 respectively. Details of preparing the simulated brine and its properties (resistivity, density, viscosity and compressibility) are discussed in Section 2.10.

4.2.1 Porosity

The technique used to measure the porosity at ambient as well as the stress-correction of porosity at 1500 and 5000 psi is described in Section 2.5.

4.2.2 Permeability measurements and Klinkenberg correction

The technique used to measure the gas permeability using pulse decay permeameter at a range of net stresses is presented in Section 2.6.1. The Klinkenberg correction is described in more details in Section 2.6.2.

4.2.3 Drawdown experiments

High-pressure gas pulse decay was used to measure permeability in a drawdown test representing a production scenario. More details of the technique are presented in

Section 2.6.3. During production, net stress is increased as the reservoir pore pressure is reduced while the stress of the overburden is fixed. The production is mimicked by measuring the permeability at various pore pressures with a fixed confining stress of 10,000 psi, which is the pressure exerted by a 10,000 ft of overburden with a gradient of 1 psi/ft. Reducing the pore pressure of the plug samples represents the drop in reservoir pressure. The permeability was measured under a range of pore pressure (5000, 4500, 4000, 3500, 3000 and 2700 psi) with fixed confining stress of 10000 psi. Six permeability measurements were performed for each sample (Table 4-1). Confining and pore pressures were both monitored all the time and the confining pressure was kept always higher than pore pressure.

# of Measurements	Confining Stress (psi)	Pore Pressure (psi)
1	10,000	5000
2		4500
3		4000
4		3500
5		3000
6		2700

Table 4-1: Total of 6 gas permeability measurements under a fixed confining stress and varying pore pressure in drawdown tests conducted for each sample.

4.2.4 Equilibration time

Equilibration or soaking time that is referred to as the period of time a sample is left under certain confining and pore pressures to reach equilibrium before measuring permeability. Each sample was left for approximately two hours soaking time after each confining pressure increment to minimize measurements errors. This 2-hour interval was estimated to be the minimum soaking time for the samples to have reasonably constant permeability measurements with less than 10% error. At a fixed pore pressure and a certain confining pressure, permeability was measured repeatedly after the sample was left for different periods of time, that is 5 minutes, 30 minutes, an hour, 2 hours, 6 hours, and 24 hours.

4.3 Results

4.3.1 Porosity

The average ambient porosity for this suite of samples was approximately 3.9%, with the range between approximately 1.5% and 9% (Table 3-1). Porosity measured at ambient condition as well as stress-corrected porosity at 1500 and 5000 psi are presented in Figure 4-9. The average difference in porosity measured at ambient condition and porosity corrected at 1500 psi was 10% reduction. The reduction in porosity between the ones determined at 1500 and 5000 psi was less than 5% in average.

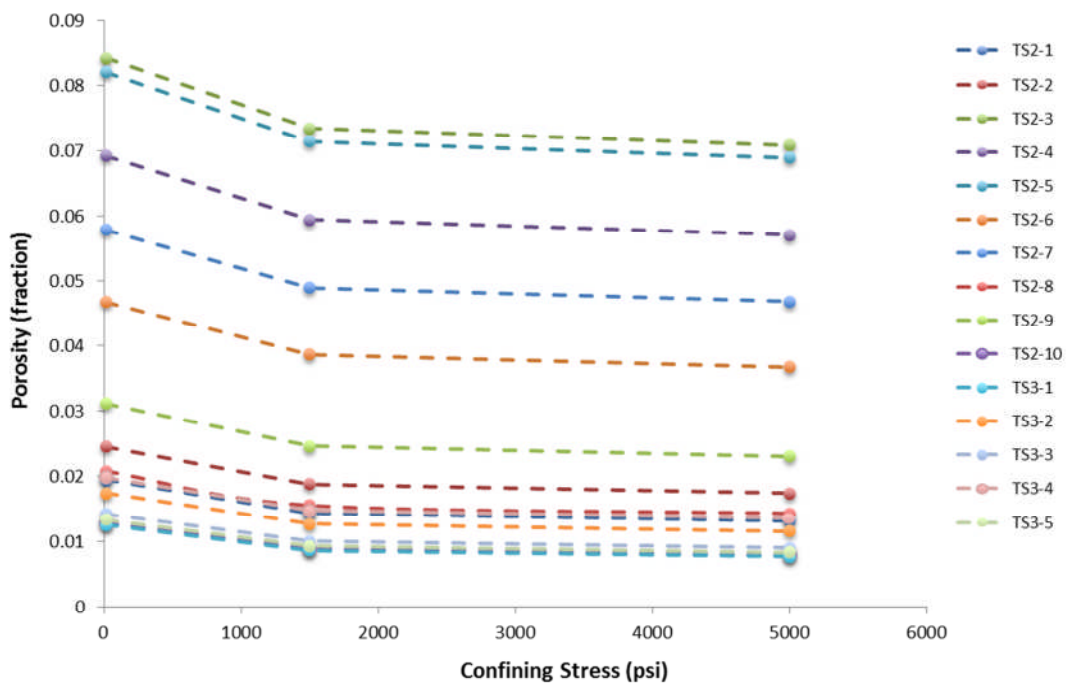


Figure 4-9: Measured porosity (fraction) at ambient condition and porosity stress-corrected at 1500 and 5000 psi for group-A samples. See captions of Figure 3-5 and Figure 3-6 for porosity uncertainties in plotted values.

4.3.2 Gas permeability

All permeability measurements, Klinkenberg corrected, under the range of net stress up to 3300 psi are presented in (Table 4-2) and the drawdown measurements presented in (Table 4-3). The gas permeability of all samples decreased with increasing the net stress with the most reduction occurring below the 3000 psi net stress (Figure 4-11). The reduction from initial permeability measured at confining net stress of 500 psi to the ones measured at *in-situ* stress of 5000 psi varied significantly within

the set of the samples. For example, permeability of sample TS2-1 decreased from 0.0005 mD at 500 psi to 0.0001 mD at 2500 psi while TS2-9 decreased one order of magnitude from approximately 0.003 mD at 500 psi to 0.0007 mD at 2500 psi net stress. Sample TS2-9 has the highest measured permeability out of all the samples despite having a low ambient porosity of 3.8%. However, the permeability reduction during the drawdown measurements, that is net stress of 5000 psi and dropping to stress prior to abandonment condition, was relatively small between the samples (Figure 4-12).

Confining Stress (psi)	1500	2500	3500	3500	3500	3500
Pore Pressure (psi)	1000	1000	1000	700	400	200
Net Stress (psi)	500	1500	2500	2800	3100	3300
TS2-1	4.7E-04	2.5E-04	1.1E-04	7.0E-05	1.1E-04	1.4E-04
TS2-2	5.9E-04	3.8E-04	2.6E-04	2.1E-04	1.2E-04	2.4E-04
TS2-3	1.9E-03	1.2E-03	8.3E-04	7.5E-04	5.9E-04	6.9E-04
TS2-4	1.3E-03	8.2E-04	7.5E-04	6.5E-04	6.0E-04	7.5E-04
TS2-5	8.6E-04	5.5E-04	3.9E-04	5.5E-04	5.4E-04	5.5E-04
TS2-6	1.6E-03	1.3E-03	3.7E-04	4.3E-04	3.8E-04	3.4E-04
TS2-7	2.4E-03	1.2E-03	7.0E-04	9.3E-04	5.5E-04	5.2E-04
TS2-8	1.9E-03	1.5E-03	7.5E-04	6.1E-04	6.6E-04	4.4E-04
TS2-9	2.9E-03	1.3E-03	7.0E-04	5.7E-04	7.1E-04	8.3E-04
TS2-10	4.6E-04	4.6E-04	2.9E-04	1.8E-04	1.3E-04	8.7E-05
TS3-1	3.5E-04	3.1E-04	1.5E-04	9.4E-05	8.8E-05	9.4E-05
TS3-2	6.6E-04	2.8E-04	1.5E-04	1.2E-04	1.0E-04	1.2E-04
TS3-3	6.9E-04	2.2E-04	1.2E-04	1.5E-04	1.1E-04	1.1E-04
TS3-4	3.4E-04	1.9E-04	7.2E-05	1.2E-04	1.6E-04	1.4E-04
TS3-5	8.9E-04	3.9E-04	1.6E-04	2.0E-04	1.3E-04	1.8E-04

Table 4-2: Corrected helium permeability (mD) under a range of confining stresses (psi) with different pore pressures (psi) with maximum net stress of 3300 psi for group-A samples. See captions of Figure 3-5 and Figure 3-7 for permeability uncertainties in plotted values.

Draw-down with confining stress of 10,000 psi						
Pore Pressure (psi)	5000	4500	4000	3500	3000	2700
Net Stress (psi)	5000	5500	6000	6500	7000	7300
TS2-1	1.3E-05	9.8E-06	6.4E-06	3.7E-06	3.5E-06	2.5E-06
TS2-2	2.4E-05	1.5E-05	1.8E-05	8.9E-06	1.4E-05	-
TS2-3	1.5E-04	1.2E-04	1.0E-04	8.6E-05	8.7E-05	7.5E-05
TS2-4	8.4E-05	5.1E-05	4.5E-05	4.3E-05	4.1E-05	4.2E-05
TS2-5	2.9E-04	2.5E-04	2.4E-04	2.1E-04	2.1E-04	2.1E-04
TS2-6	8.0E-05	6.2E-05	4.8E-05	4.0E-05	2.9E-05	2.9E-05
TS2-7	4.3E-05	3.6E-05	2.8E-05	2.4E-05	2.3E-05	2.1E-05
TS2-8	5.5E-05	5.7E-05	4.8E-05	4.4E-05	4.4E-05	4.1E-05
TS2-9	2.4E-04	1.5E-04	1.2E-04	9.6E-05	8.6E-05	8.4E-05
TS2-10	1.3E-06	4.5E-07	1.0E-06	9.8E-07	5.1E-07	1.0E-06
TS3-1	4.0E-06	2.7E-06	2.4E-06	1.3E-06	7.0E-07	1.2E-06
TS3-2	1.0E-05	8.5E-06	7.7E-06	5.0E-06	4.3E-06	7.1E-06
TS3-3	1.2E-05	4.8E-06	6.6E-06	3.4E-06	2.5E-06	1.6E-06
TS3-4	1.9E-05	1.0E-05	1.0E-05	9.4E-06	6.2E-06	-
TS3-5	4.1E-05	2.7E-05	2.2E-05	1.4E-05	1.3E-05	-

Table 4-3: Corrected helium permeability (mD) under a drawdown measurements with confining stress of 10000 psi with pore pressure in the range 5000-7300 psi for group-A samples.

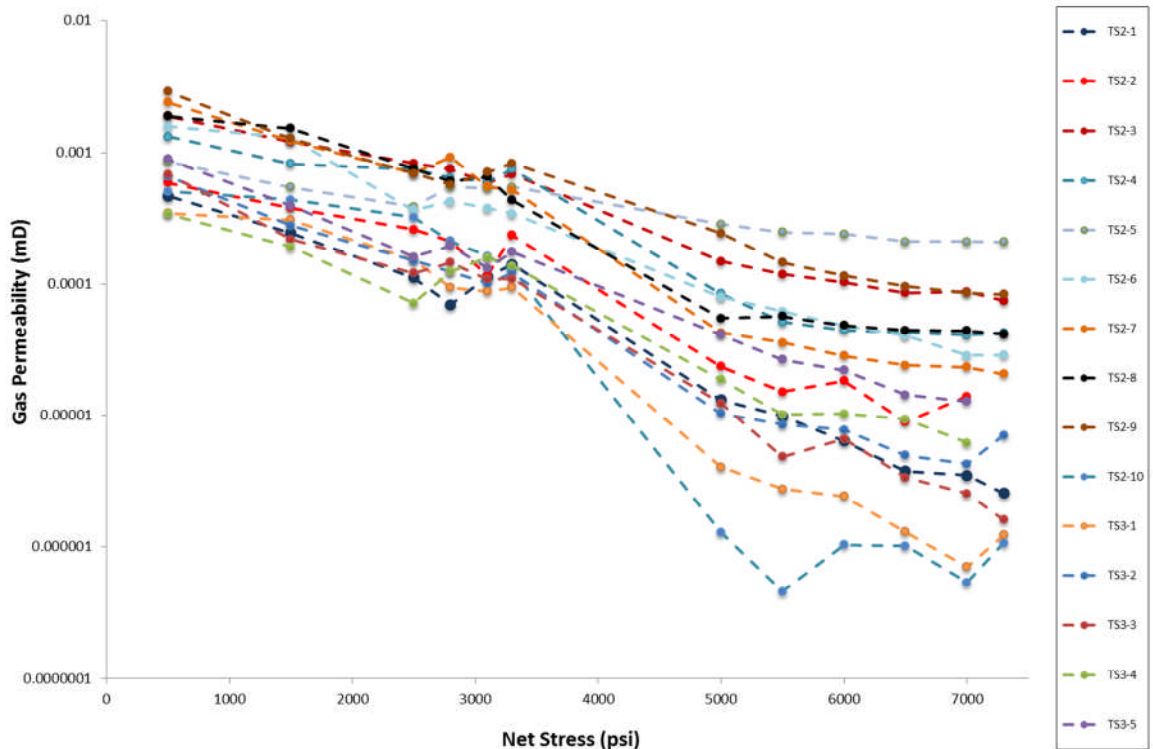


Figure 4-10: Helium permeability (mD) measured at the wide range of net stress (500 to 7300 psi) for samples in group A. See captions of Figure 3-5, Figure 3-6 and Figure 3-7 for permeability uncertainties in plotted values.

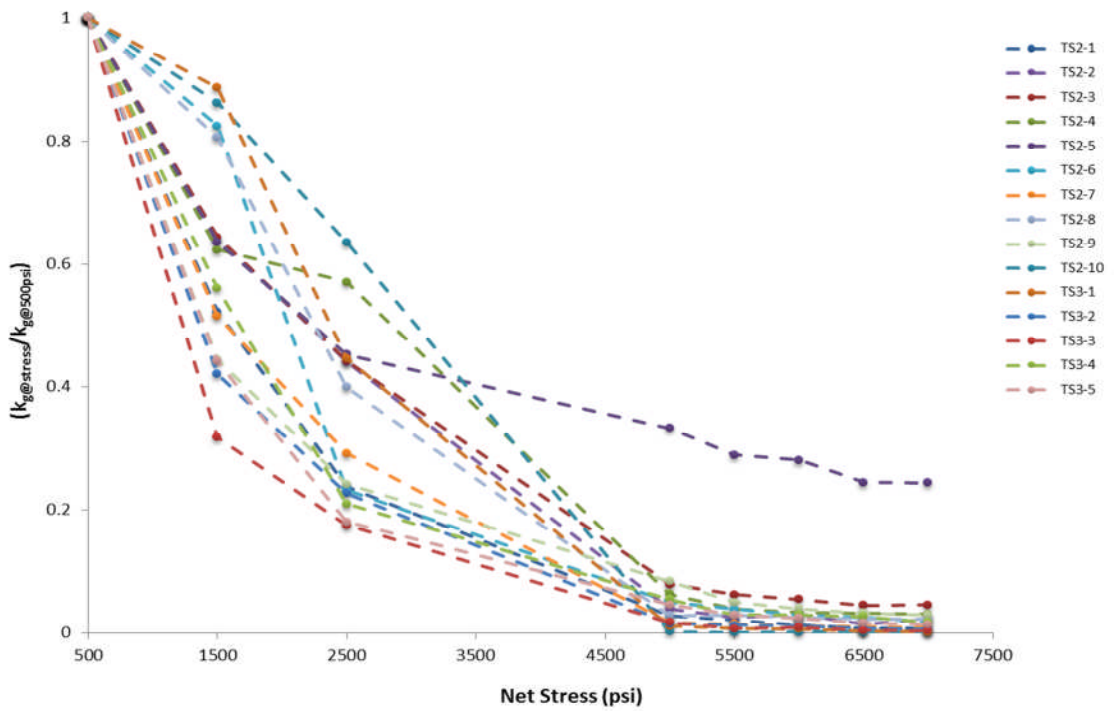


Figure 4-11: Normalized corrected helium permeability mD (Klinkenberg-corrected) for the whole range of net stress used that is low net stress 500 psi to reservoir high net stress 7300 psi for group-A samples. See captions of Figure 3-5, Figure 3-6 and Figure 3-7 for permeability uncertainties in plotted values.

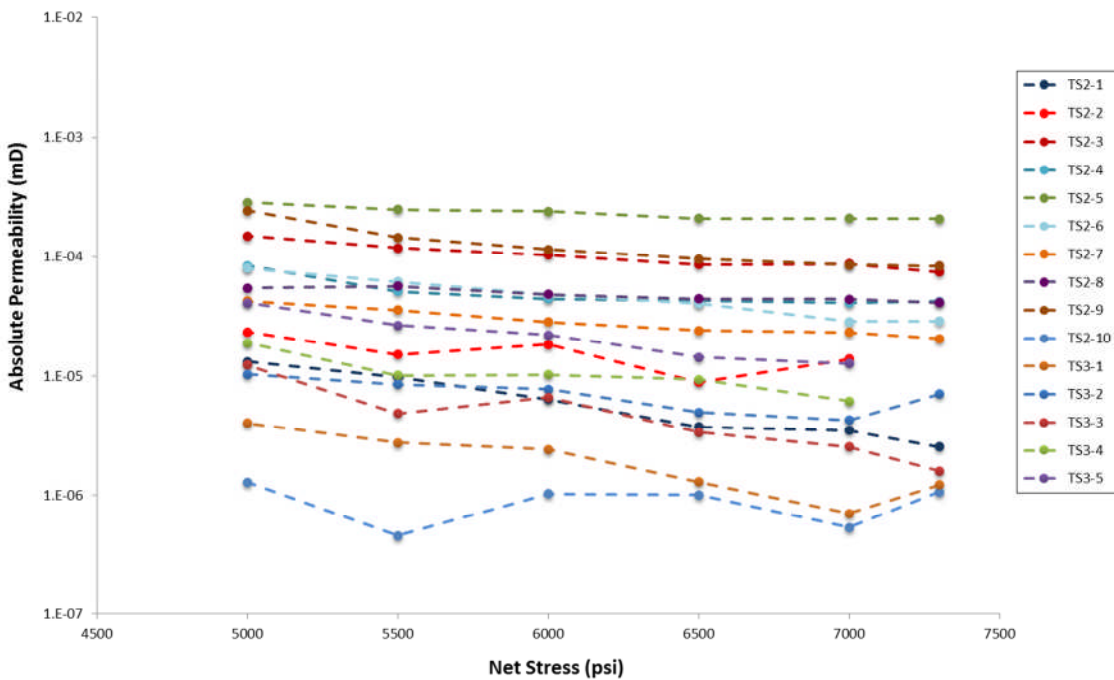


Figure 4-12: Gas permeability against reservoir condition net stress in drawdown tests mimicking production scenario with fixed confining stress and decreasing pore pressure for group-A samples. See caption of Figure 3-6 for permeability uncertainties in plotted values.

Permeability measured at ambient condition (i.e. 500 psi) was plotted against permeability measured at *in-situ* condition (5000 psi net stress) and prior to abandonment condition that is 7000-7300 psi net stress to analyse the stress dependency under different conditions. Samples with initial low permeability showed higher stress sensitivity than the ones with relatively higher absolute permeability. The stress sensitivity of permeability was also higher when the sample was stressed from ambient condition into higher stress (500 to 5000 psi) in comparison with the stress sensitivity due to stress increase from *in-situ* to higher net stress during drawdown experiments (Figure 4-13) and (Figure 4-14) respectively.

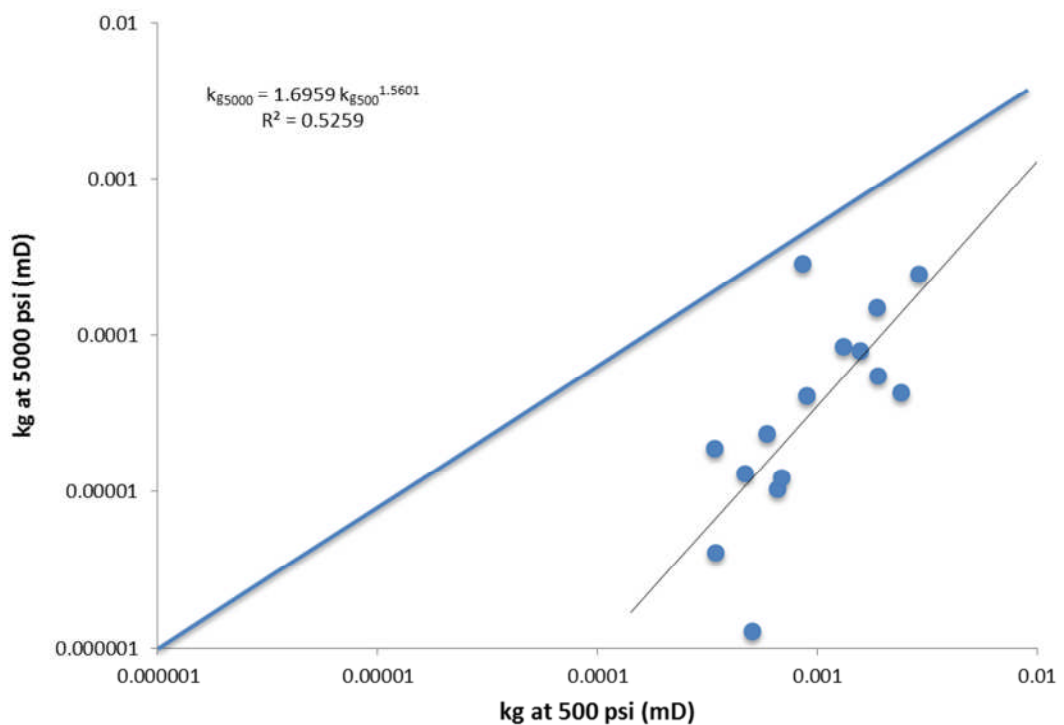


Figure 4-13: Cross plot of corrected measured kg at in-situ of 5000 psi net stress against corrected kg measured at 500 psi net stress with 1:1 line (blue) indicating the great reduction in permeability at the high net stress for group-A samples. See captions of Figure 3-5 and Figure 3-6 for permeability uncertainties in plotted values.

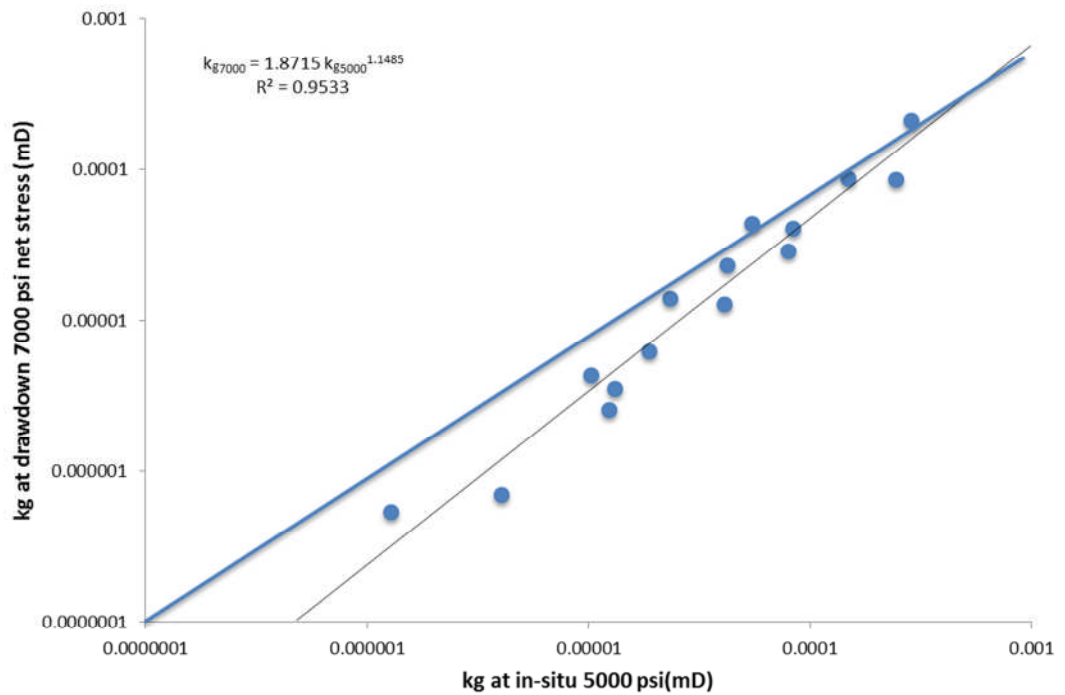


Figure 4-14: Cross plot of corrected measured k_g at drawdown condition prior to abandonment against corrected k_g measured at 5000 psi net stress with 1:1 line (blue) indicating the less stress sensitivity of permeability measured at 5000 psi compared with the permeability measured at 7000 psi for group-A samples. See caption of Figure 3-6 for permeability uncertainties in plotted values.

Permeability of sample TS2-5 dropped from 0.00086 to 0.00029 mD when increasing net confining stress from 500 to 5000 psi, and it only dropped to 0.00021 mD when measured under 7300 psi. Some samples experienced less than an order of magnitude reduction in permeability while other samples such as TS2-4 and TS2-7 decreased two orders of magnitude. Their permeabilities decreased from 0.0013 and 0.0024 mD under 500 psi to 0.000084 and 0.000043 mD under 5000 psi respectively. Yet, their permeabilities dropped only one-fold when stressed under 7300 psi net. Another example of the significant stress sensitivity is sample TS2-1 having porosity of 2.5%. Its measured permeability was 0.0005 mD under 500 psi net stress, and it dropped two orders of magnitude to 0.000006 mD when measured under a reservoir condition of 6000 psi.

Permeability was plotted against the wide range of the net stress to find a relationship that enables the prediction of permeability at reservoir condition from routine core data. All samples showed exponential regression best-fit trend, expressed in

Equation 4-5, with correlation coefficients of 0.92 to 0.99 for 14 samples with sample TS2-10 having 0.88. A plot of sample TS2-6 with the exponential regression is presented in Figure 4-15.

Equation 4-5

$$k_g = ae^{-b\sigma'}$$

where:

k_g = gas permeability

σ' = effective stress (assumed here to be equal to net stress that is effective stress coefficient 1)

The parameters a and b are empirical constants.

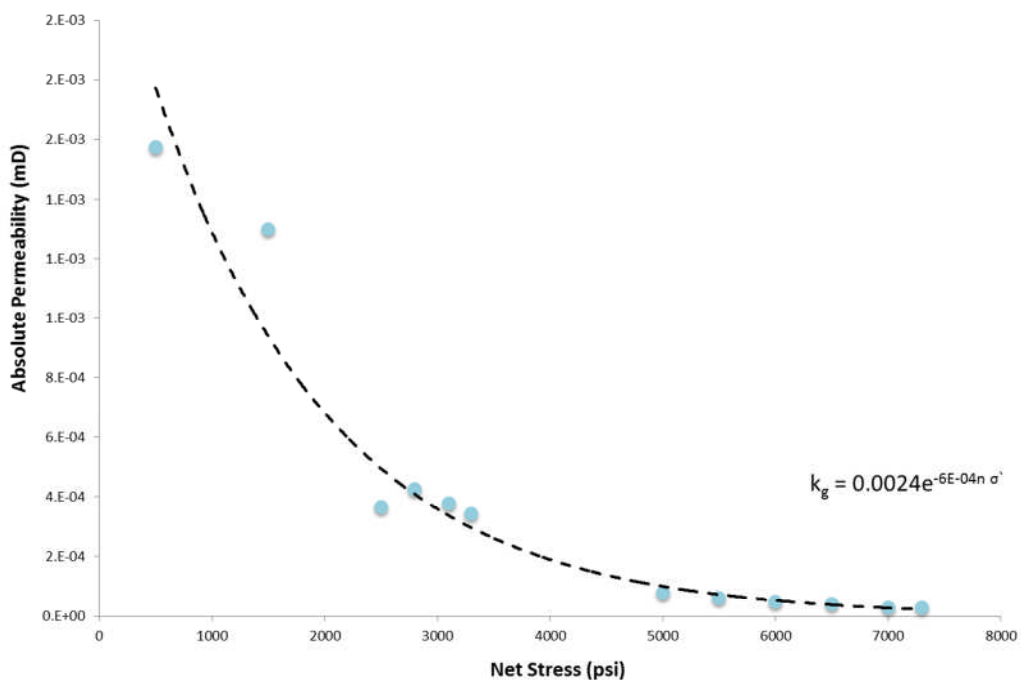


Figure 4-15: Gas permeability (Klinkenberg-corrected) (mD) against a wide range of net stress (psi) with the exponential regression fit for sample TS2-6. See captions of Figure 3-5, Figure 3-6 and Figure 3-7 for permeability uncertainties in plotted values.

4.3.2.1 Equilibration time prior to permeability measurement

Permeability readings were not constant when the sample was left for less than an hour, and it maintained an approximately constant reading above one hundred minutes. Figure 4-16 shows an example of equilibration times in minutes for the measured gas permeability at several net stresses with 10% error bars for one of the sample.

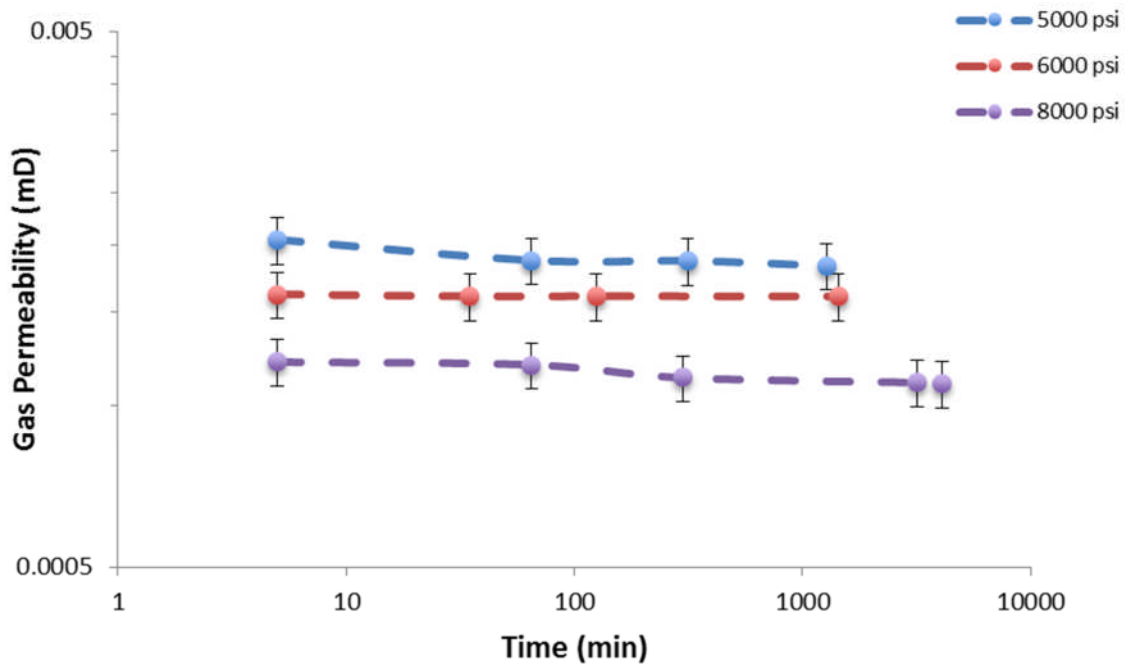


Figure 4-16: An example of permeability measurements (mD) with 10% error bars at a range of equilibration "soaking" time sat different stresses for one of the samples.

4.3.2.2 Klinkenberg correction

The gas slippage factor b determined for the samples using Klinkenberg technique (1941), are presented in Table 4-4. A cross plot of the factor b against corrected permeability is shown in Figure 4-17. Experimental errors in permeability measurements under different pressures for each sample might be the reason for errors in the determined b values causing wide scattering. It is believed that much of the scatter in such relation is caused by the variations in the pore patterns of the core samples (Heid et al., 1950). The best fit for the samples yields Equation 4-6.

Sample No.	Slippage Factor-b
TS2-1	89
TS2-2	57
TS2-3	146
TS2-4	90
TS2-5	234
TS2-6	114
TS2-7	23
TS2-8	37
TS2-9	170
TS2-10	150
TS3-1	124
TS3-2	157
TS3-3	229
TS3-4	37
TS3-5	58

Table 4-4: Determined slippage factor b (psi) with 10% uncertainties for all samples under 3500 psi confining stress with varying mean pore pressures (1000, 700 and 400 psi).

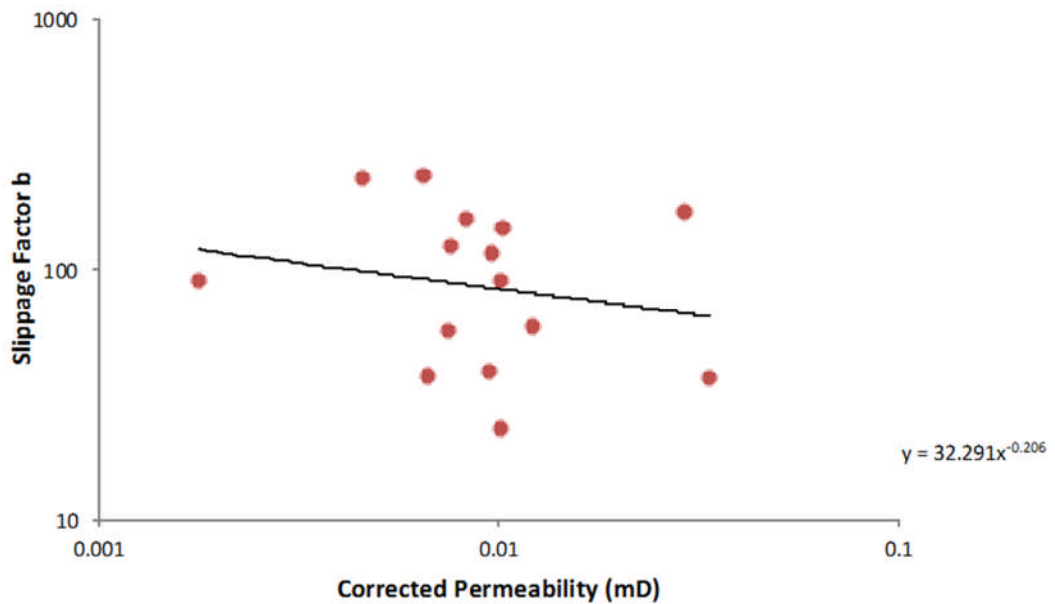


Figure 4-17: Correlation of slippage factor b (psi) against corrected permeability (mD). Both slippage factor and permeability are within 10% uncertainty.

According to Ostensen (1983), the exponent of the best fit in Equation 4-6 should be around -0.3 if the flow is controlled by slit-like apertures compared with an exponent of -0.5 for uniform cylindrical capillaries. Heid et al. (1950) determined an exponent of -0.39 (Equation 1-6) for the set of samples they examined, while Owens and Jones

(1980) presented -0.33 (Equation 1-7) as the best fit exponent for their samples; where both described the pores to be irregular in shape with low aspect ratios. The samples show a best fit with an exponent of -0.206 (Equation 4-6) indicating that the pores are more like cracks with irregular shapes than regular capillaries.

Equation 4-6

$$b = 32.291 k_g^{-0.206}$$

4.3.3 Pore size distribution

Pore throat size distributions determined using mercury injection capillary pressure indicate that fluid flow in the samples is dominated by micro to nano pore throats with radii less than 0.1 μm (Figure 4-18). Pore size distribution of every sample is shown in more details in Section 3.3.7. Results of NMR show that majority of the samples have relaxation time, T_2 , less than 1 μs with a few samples showing T_2 between 1 and 10 μs , which relate to the pore size from the pore surface to volume ratio based on Equation 2-12. This is an indication of the dominance of the micro-pores network rather than macro-pores in the analysed samples (Figure 4-19).

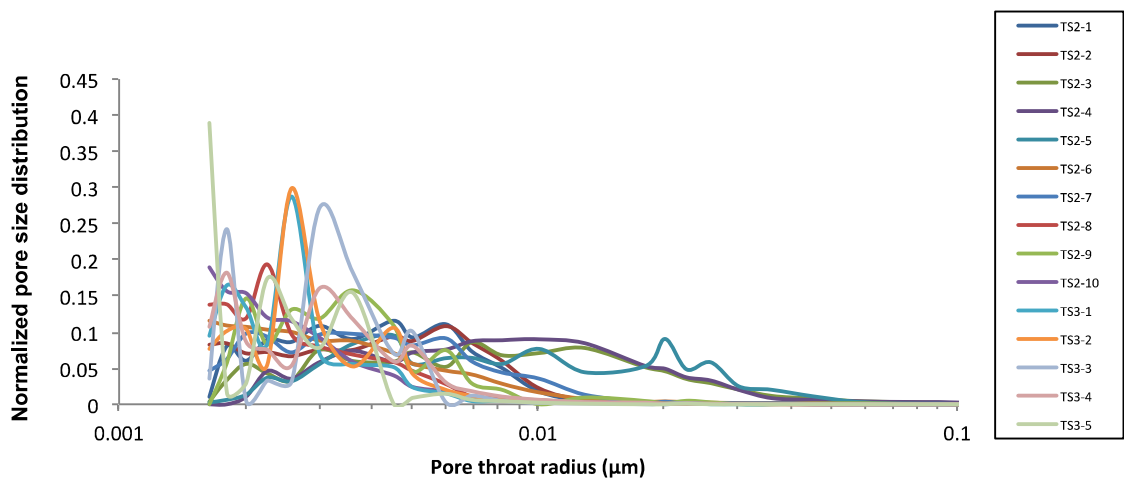


Figure 4-18: Pore throat size distribution determined from mercury injection capillary pressure for all 15 samples in group-A.

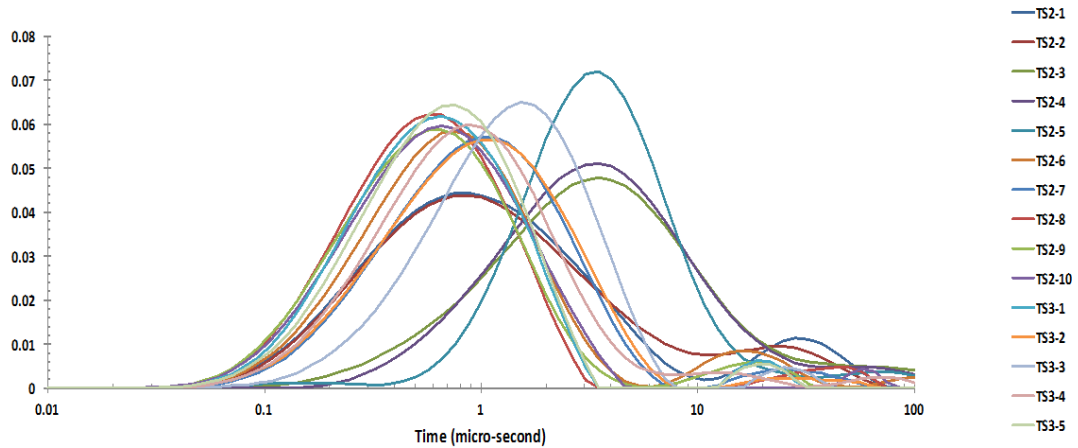


Figure 4-19: NMR T_2 distributions for the 15 samples in group A are all less than 10 μs indicating the dominance of the micro-pores.

4.3.4 Ultrasonic velocities

The ultrasonic P-wave velocities for all samples increased with increasing the confining stress (Figure 4-20). Table 4-5 shows all ultrasonic velocity measurements for the samples. The measured velocity was in the range between 4230 and 5348 m/s at 1000 psi, and between 4554 and 5487 m/s at 5000 psi. The velocity increased by an average of approximately 280 m/s with the increase in stress from 1000 to 5000 psi. The average ratios of P-wave to S-wave (V_p/V_s) were 1.58 and 1.62 at 1000 and 5000 psi respectively. The velocities showed a general higher increase at the range of 1000 to 3000 psi compared to velocity at higher stresses. Samples TS2-3 and TS2-4 appeared to have the highest increase in velocities compared with the remaining samples (Figure 4-21); their velocities increased from 4248 to 4853 m/s, and from 4598 to 5134 m/s respectively with increasing the confining stress from 1000 to 5000 psi. A cross plot of the porosity against the velocity for the samples showed a general trend of increasing velocity as the porosity decreased, but no correlation could be found (Figure 4-22). Porosity stress-corrected at 5000 psi was plotted against P-wave velocity measured at 5000 psi to evaluate the effect of stress on porosity-velocity relationship (Figure 4-23); no correlation could be found.

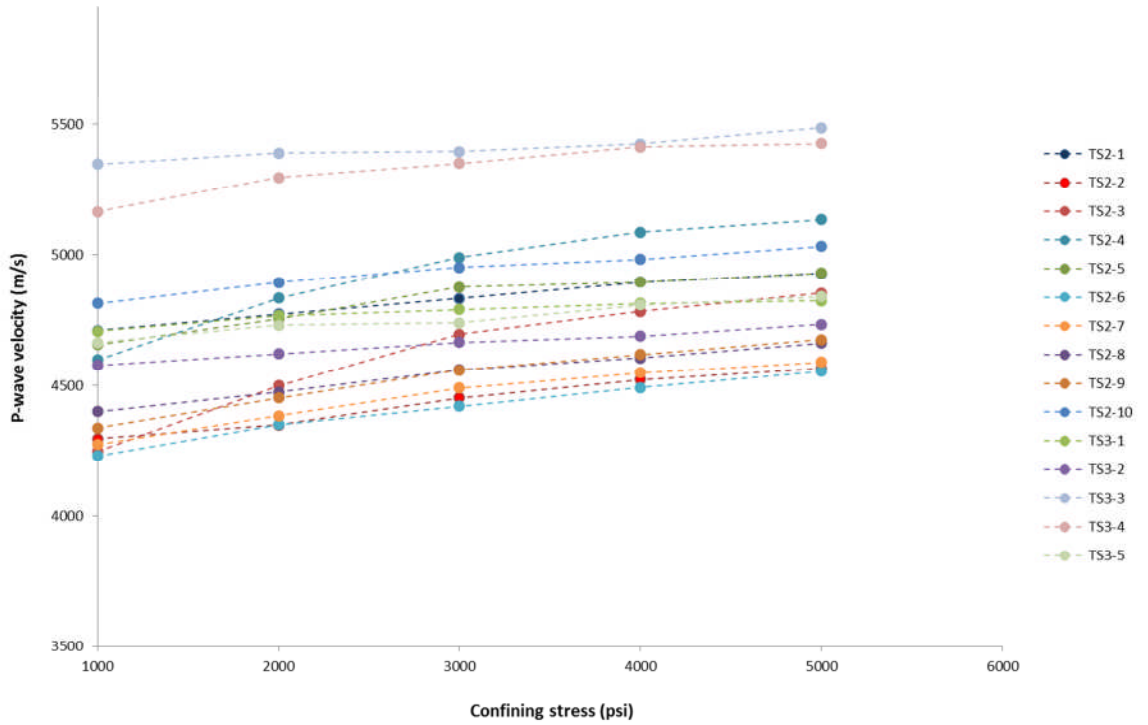


Figure 4-20: Ultrasonic P-wave velocity (m/s) measured as a function of confining stress (psi) showing an increase in P-wave as the confining stress increases for group-A samples.

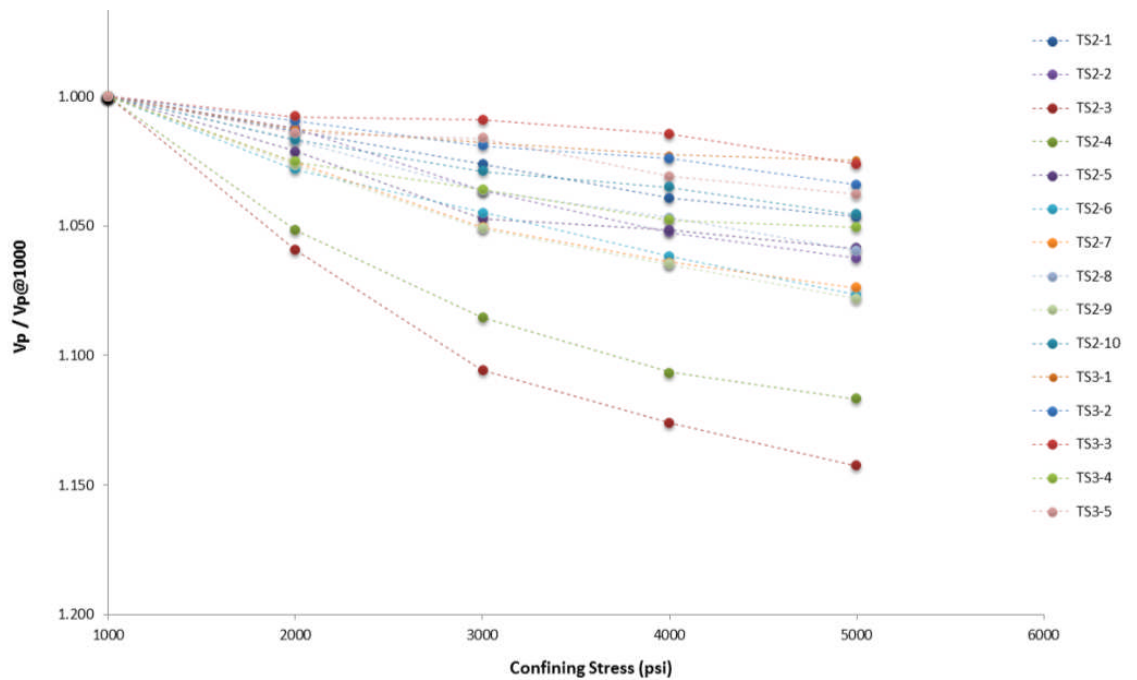


Figure 4-21: Normalized ultrasonic ($P\text{-wave}_{\text{stress}}/P\text{-wave}_{1000\text{psi}}$) for samples in group A. Samples TS2-3 and TS2-4 show steeper slopes indicating greater stress sensitivity compared to the remaining samples.

Sample No.	P-wave (m/s) at Confining Stress (psi)					Vp/Vs at 1000 psi	Vp/Vs at 5000 psi
	1000	2000	3000	4000	5000		
TS2-1	4710	4773	4833	4895	4929	1.59	1.62
TS2-2	4296	4349	4452	4522	4564	1.57	1.60
TS2-3	4248	4499	4696	4783	4853	1.49	1.58
TS2-4	4598	4835	4990	5087	5134	1.56	1.62
TS2-5	4657	4755	4877	4896	4930	1.60	1.64
TS2-6	4230	4349	4419	4492	4554	1.56	1.62
TS2-7	4274	4384	4491	4548	4590	1.56	1.61
TS2-8	4400	4475	4560	4606	4662	1.60	1.65
TS2-9	4337	4452	4558	4618	4675	1.59	1.64
TS2-10	4814	4895	4953	4983	5033	1.62	1.66
TS3-1	4707	4767	4790	4814	4823	1.56	1.58
TS3-2	4578	4621	4665	4688	4733	1.64	1.65
TS3-3	5348	5389	5395	5426	5487	1.57	1.59
TS3-4	5165	5296	5350	5413	5427	1.63	1.65
TS3-5	4664	4730	4739	4808	4841	1.60	1.63

Table 4-5: Ultrasonic P-wave velocity (m/s) measurements under a range of confining stresses 1000, 2000, 3000, 4000 and 5000 psi with the ratio of P-wave to S-wave (V_p/V_s) at 1000 and 5000 psi for group-A samples.

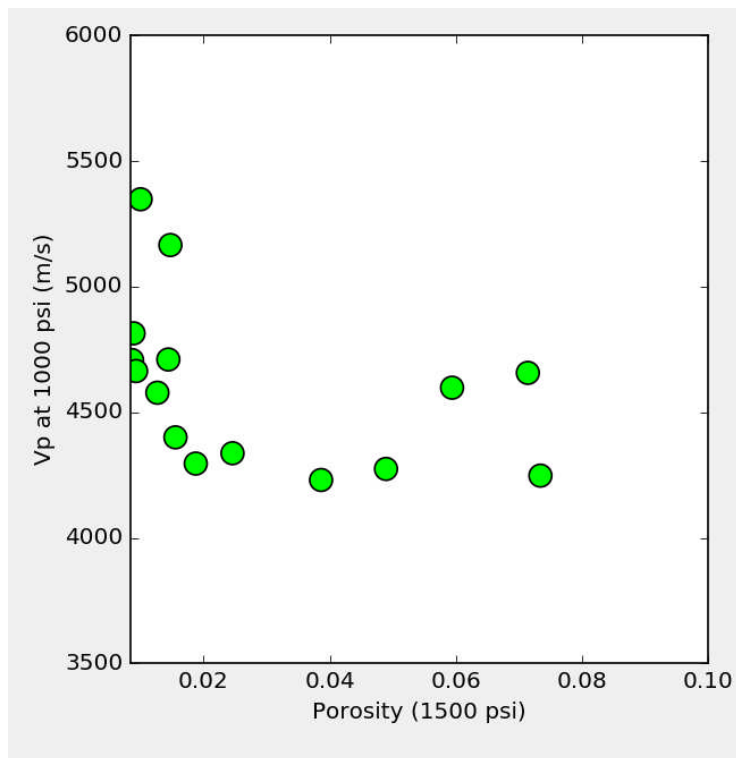


Figure 4-22: Plot of the ultrasonic velocity P-wave (m/s) at 1000 psi against the porosity (fraction) stress-corrected to 1500 psi for group-A samples. See captions of Figure 3-5 and Figure 3-6 for porosity uncertainties in plotted values.

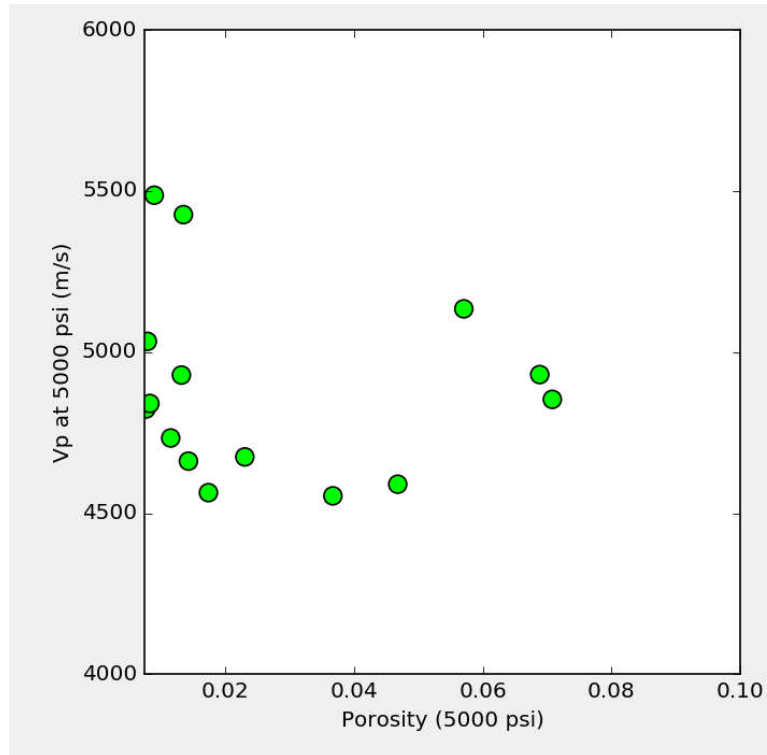


Figure 4-23: Plot of the ultrasonic velocity P-wave (m/s) at 5000 psi against the porosity (fraction) stress-corrected to 5000 psi for samples in group A. See captions of Figure 3-5 and Figure 3-6 for porosity uncertainties in plotted values.

4.3.5 Electrical properties under stress

Calculated electrical resistivity under higher stress corrected to 25° C for the five selected samples are shown in Table 4-6. The samples show an increase in resistivity as a result of increasing the confining stress (Figure 4-24). Normalized corrected resistivity plotted against confining stress (Figure 4-25) shows the stress-sensitivity for each sample. Sample TS2-4 showed the highest stress-sensitivity with resistivity increasing from approximately 49 ohm-m to 62 ohm-m with stress increase from 1500 psi to 5000 psi. Resistivity of the samples TS2-2 and TS2-7 increased from 44 to 50 ohm-m and from 31 to 38 ohm-m respectively due to the increase in stress from 1500 to 5000 psi, while samples TS3-1 and TS3-3 both showed the least stress sensitivity under the same stress condition. FRF and stress-corrected porosity of the five samples were plotted as a function of net stress to further evaluate the effect of stress on both properties (Figure 4-26). FRF showed to be more sensitive to the change in stress than the determined porosity.

Sample No.	Resistivity (ohm-m) Under 1500 psi	Resistivity (ohm-m) Under 3000 psi	Resistivity (ohm-m) Under 5000 psi
TS2-2	44.0	46.3	50.7
TS2-4	48.7	54.5	61.7
TS2-7	31.0	33.8	37.6
TS3-1	55.2	56.2	60.3
TS3-3	244.4	251.7	268.9

Table 4-6: Calculated electrical resistivity measurements (ohm-m) for the five representative samples in group A under a range of stress 1500, 3000 and 5000 psi. All measurements were corrected to 25° C and within ±2% uncertainties.

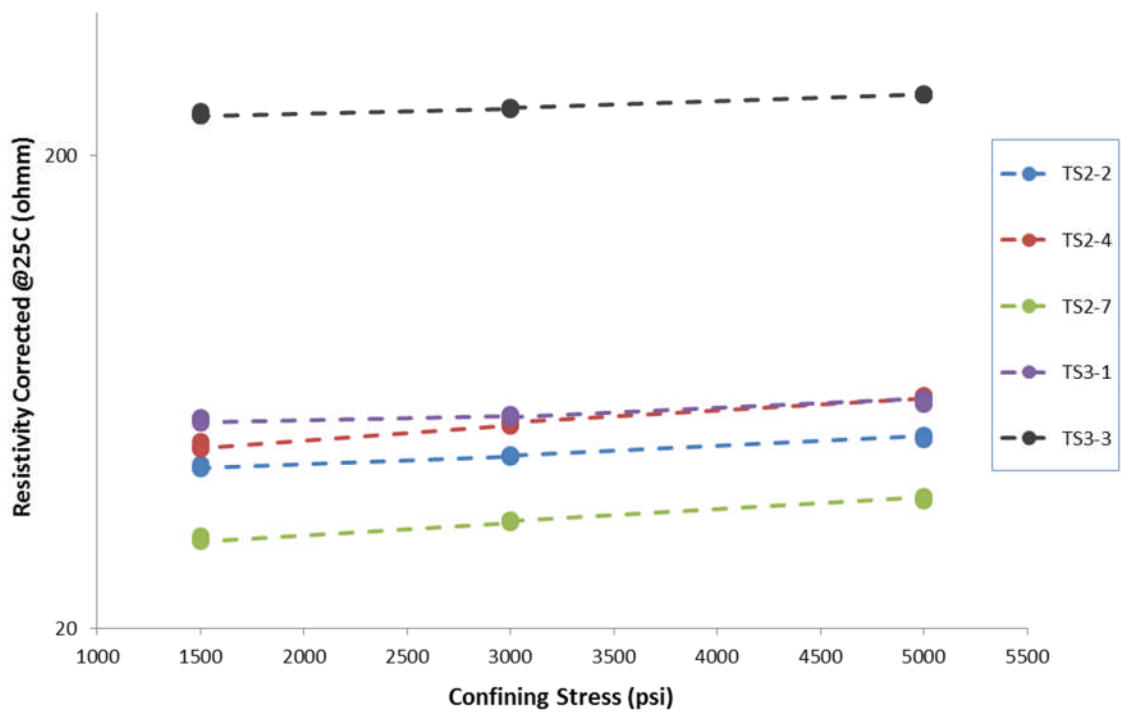


Figure 4-24: Calculated resistivity (ohm-m) with ±2% uncertainties of the five samples in group A saturated with simulated brine (corrected at 25° C) under confining stress 1500, 3000 and 5000 psi.

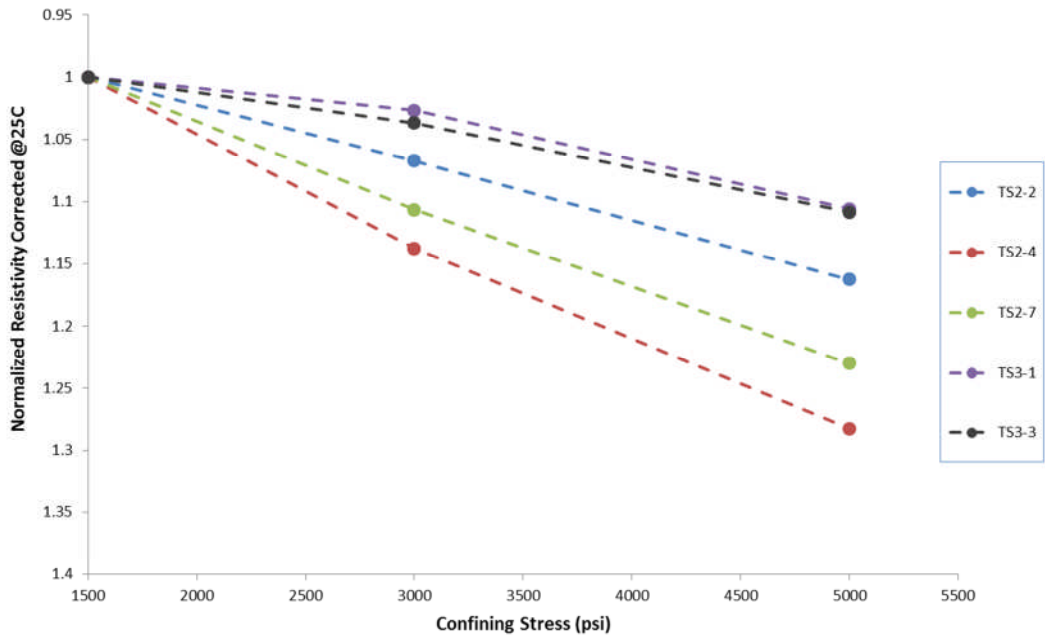


Figure 4-25: Normalized resistivity (corrected at 25° C) of the five samples in group A under 1500, 3000 and 5000 psi confining stress.

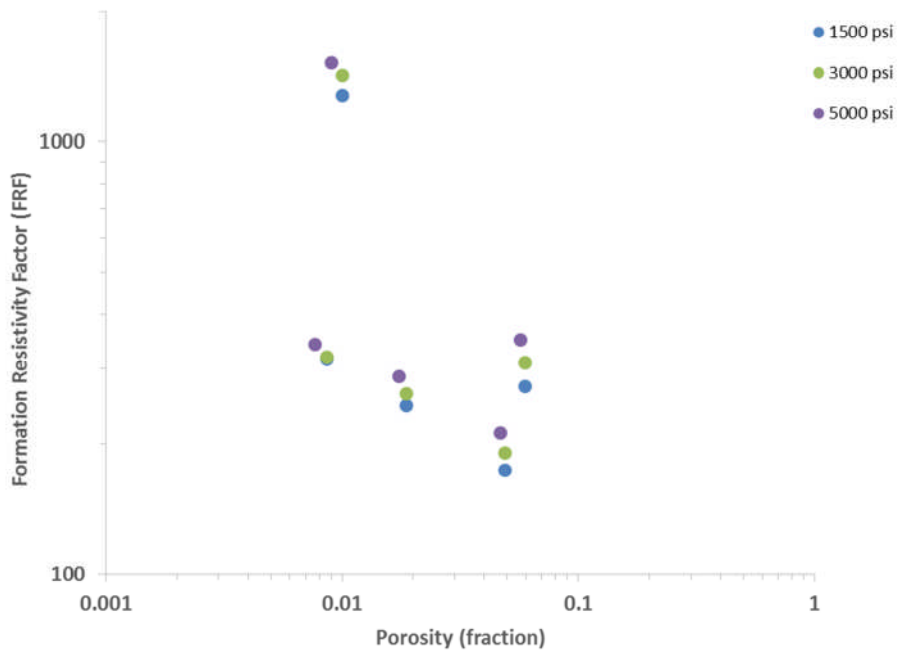


Figure 4-26: Changes of formation resistivity factor *FRF* and porosity (fraction) as a function of stress increase (1500, 3000 and 5000 psi) for the five samples in group A. See captions of Figure 3-5, Figure 3-6 and Figure 4-24 for porosity and resistivity uncertainties in plotted values.

The cementation exponents, m , were calculated from the measured electrical properties and porosity determined at 1500 psi. The exponents showed a minimum and a maximum values of 1.2 and 2 respectively (Table 4-7). Stress corrected (at 1500 psi) porosity in fraction was plotted against the calculated cementation exponent (Figure 4-27). Two models presented by Cluff et al. (2009) were also plotted for comparison. The trend in Figure 4-27 shows a good correlation between the decreases in m values as the porosity decreases with m approaching 1.2 for samples having porosity of approximately 0.01. The relationship can be expressed with Equation 4-7. The decrease in m is more pronounced in samples with porosity less than 0.05, whereas samples with porosity higher than 0.06 showed values of approximately 2. Results agree with the studies presented by Cluff et al. (2009).

Equation 4-7

$$m = 0.3281 \ln(\phi) + 2.7852$$

Sample No.	FRF (Ro/Rw)	Calculated m	Porosity (fraction)
TS2-1	442	1.4	0.01
TS2-2	246	1.4	0.02
TS2-3	175	2.0	0.07
TS2-4	272	2.0	0.06
TS2-5	184	2.0	0.07
TS2-6	186	1.6	0.04
TS2-7	174	1.7	0.05
TS2-8	235	1.3	0.02
TS2-9	226	1.5	0.03
TS2-10	380	1.3	0.01
TS3-1	314	1.2	0.01
TS3-2	235	1.3	0.01
TS3-3	1274	1.6	0.01
TS3-4	677	1.5	0.02
TS3-5	222	1.2	0.01

Table 4-7: Formation resistivity factor (FRF) determined at 1500 psi and porosity (fraction) stress-corrected at 1500 psi and calculated cementation exponent (m) for all samples in group A. See captions of Figure 3-5, Figure 3-6 and Figure 4-24 for porosity and resistivity uncertainties in plotted values.

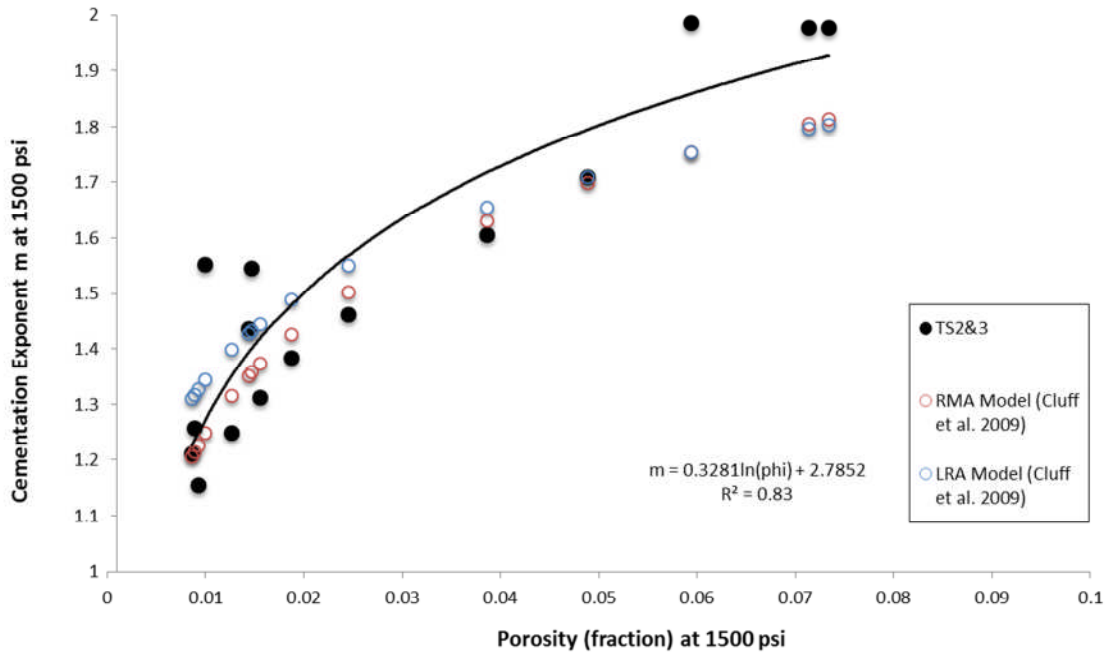


Figure 4-27: Calculated cementation exponent (m) plotted against measured porosity (fraction) under 1500 psi, in comparison with the two models presented by Cluff et al. (2009). See captions of Figure 3-5, Figure 3-6 and Figure 4-24 for porosity and resistivity uncertainties in plotted values.

4.4 Discussion

The measurements of the petrophysical properties under a range of net stress show that the stress dependency of the properties varies from one property to another (Figure 4-11), (Figure 4-21) and (Figure 4-25). The stress dependency even varies for the same property of samples taken from the same reservoir. The formation of microcracks (microfractures) in tight sandstones due to the rapid change in the stress state of the rocks after drilling and coring alters their pore and grain structures from their original *in-situ* state (Farqhur et al., 1993). Altering the microstructures (i.e. microfractures formation) could be the cause of the stress dependency. The variation in the stress dependencies of the different petrophysical properties measured at low stress condition may not necessarily reflect the stress dependencies that exist in the reservoir. Every property will be affected by the stress change differently and probably even every rock sample as well.

4.4.1 Controls on stress dependency of permeability

The permeability measurements at different net stresses prove that permeability is stress dependent for all samples. The most reduction in permeability occurs at net

stress range between 500 and 3000 psi, which agrees with the literature (Fatt and Davis, 1952; Mclatchie et al., 1958; Wyble, 1958). Stress dependency of permeability appears to be higher at low net stress compared to *in-situ* condition. The permeability measured at 5000 psi is reduced significantly compared to permeability measured at ambient (i.e. 500 psi) (Figure 4-13). The results are consistent with the theory of the permeability stress dependence caused by microcracks or crack-like pores that tend to close at high confining stress (Jones and Owens, 1980; Ostensen, 1983; Bernabe, 1986). The presence of microfractures are confirmed from the SEM images of the samples (Figure 3-11); (Figure 3-12) and (Figure 3-13).

The permeability at high net stress range (i.e. 5000 to 7000 psi) seems to be less stress dependent in comparison with permeability measurements at lower net stress (500 to 5000 psi). The reduction in the permeability at near abandonment pressure of 7000 psi is minimal when plotted against permeability measured at 5000 psi, especially for samples with permeability <0.0001 mD (Figure 4-14). Fluid flow in tight samples is affected by the formation of microcracks observed in the SEM images of the samples, which is also indicated by the relatively high permeability measured at ambient condition. So increasing the net stress from 5000 psi to 7000 psi shows no significant reduction in permeability. This is in agreement with the assumption of microfractures closure at high net stress, which is consistent with studies reporting the stress sensitivity of permeability caused by closing of microcracks and crack-like pores that probably not present at the reservoir condition (Keighin and Sampath, 1982; Sampath and Keighin, 1982; Spencer, 1989).

Moreover, several samples, TS2-7 and TS2-9 as an example, with similar initial routine permeability show large contrast in permeability readings measured at reservoir condition indicating a wide range of stress dependencies (Figure 4-10). On the other hand, samples TS2-2 and TS3-5 having identical *in-situ* permeabilities, but their measured permeabilities at ambient condition differ (Figure 4-10). This various stress dependencies of permeability for the different samples might be explained by the orientation of the microfractures. Partial or complete closure of microcracks that have their surface parallel to the fluid flow direction will reduce the permeability more significantly than closure of microcracks that are perpendicular to the flow.

4.4.2 Controls on electrical properties

According to Archie law (1942), high values of m would be required to relate the high measured formation resistivity factor with the low determined porosity. However, the samples experienced a decrease in the cementation exponent m as the porosity decreases (Figure 4-27), which disagrees with the correlation presented by Shell stating that the exponent m increases as the porosity decreases (Figure 4-28). The reason could be explained by the presence of microcracks acting as conduits that contribute to the electrical current flow particularly when oriented parallel to the bedding (Cluff et al., 2008). To assess the impact of microfractures concentration on the exponent m , the fracture model (Equation 4-4) was used with different percentages of fractures. The model shows most of the samples have microfractures occupying 10% or more of the porosity, and approximately 1% for other samples (Figure 4-29). This is consistent with the microfractures observed in the SEM images, which supports the theory of m decreasing with the decrease of porosity.

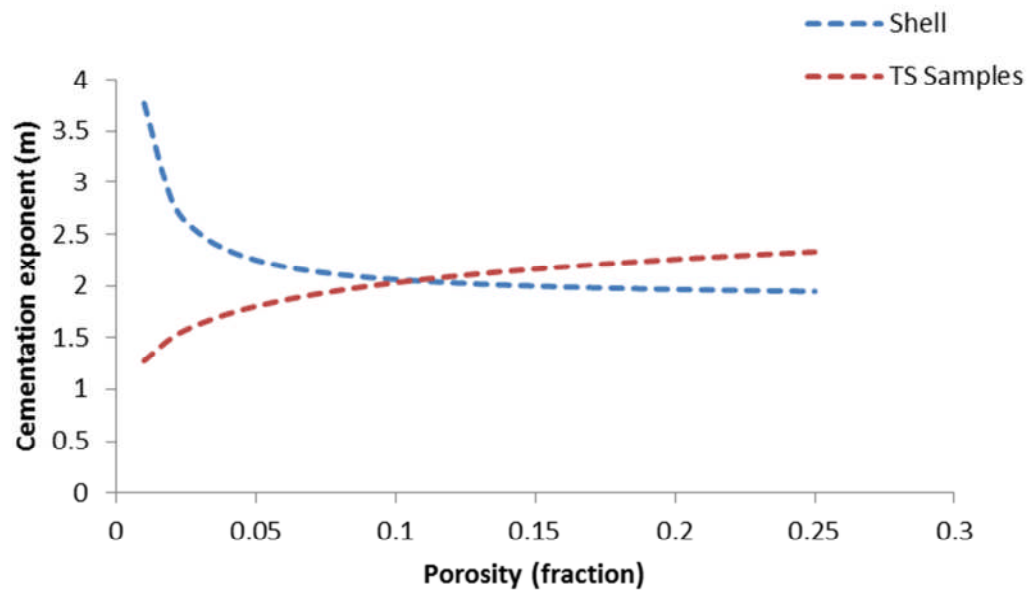


Figure 4-28: Diagram showing the relationship derived between the cementation exponent (m) and porosity (fraction) for the TS samples in group A. Note the exponent decreases as the porosity decreases in contrast to the Shell formula.

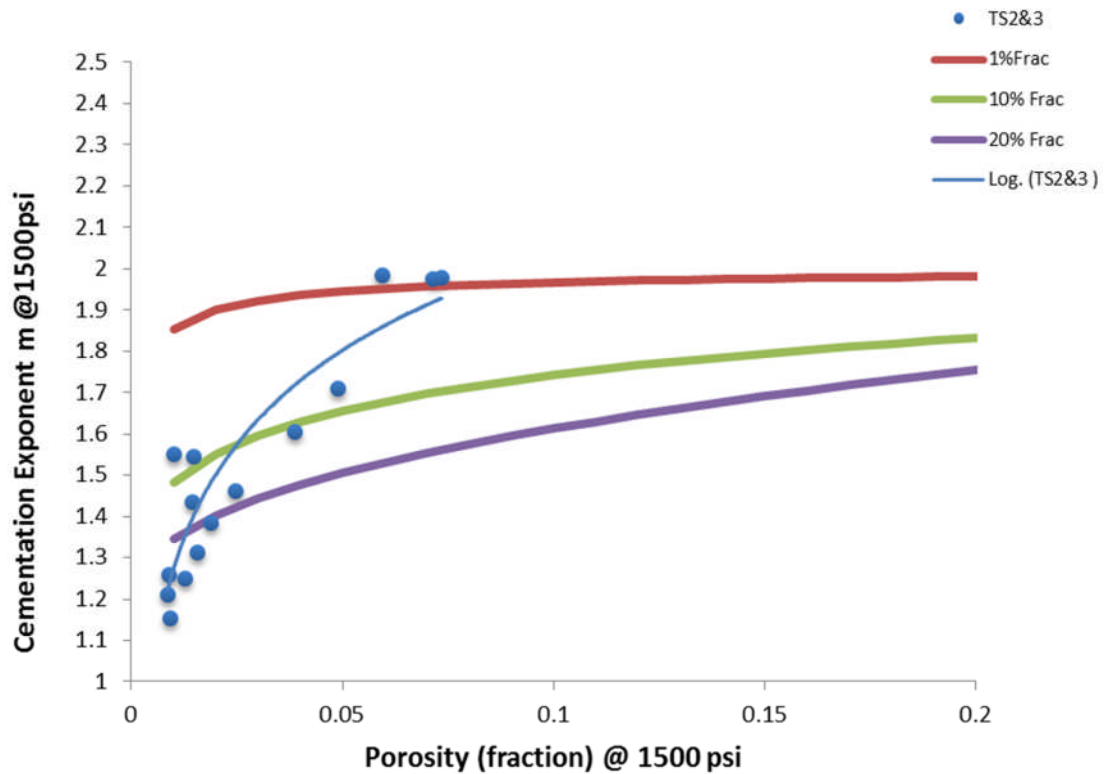


Figure 4-29: Cementation exponent m at 1500 psi against porosity (fraction) at 1500 psi for group-A samples in comparison with the fracture model. See captions of Figure 3-5, Figure 3-6 and Figure 4-24 for porosity and resistivity uncertainties in plotted values.

FRF values determined from measurements were correlated with FRF estimated theoretically to analyse the impact of using a single value of the cementation exponent for the whole set of samples. FRF determined for the samples from the resistivity measurements (Equation 1-8) were plotted against FRF values calculated using Equation 1-9 with constant values of the exponent m ; this was plotted in Pickett log-log plot (Figure 4-30). Constant values of 1, 1.5 and 1.75 for the exponent m were used to calculate FRF . The plot shows that using a single constant value of m won't fit all the samples. The large discrepancies show that analysing the samples with a constant value of the cementation exponent would result in inaccurate FRF . It also indicates the severe degree of heterogeneity between the samples even though those taken from the same reservoir.

impact on the electrical properties than the pore volume. This is consistent with the observation of microcracks in the SEM images of the samples. Increasing the confining stress results in altering both the pore shapes and distributions, which affect the electrical properties (Tiab and Donaldson, 2012). So it is critical to determine the porosity-*FRF* relationship under stress for tight reservoirs rather than at ambient condition, which is often the case in characterising conventional reservoirs.

4.4.4 Implication in calculating GOIP

Calculating water saturation with electrical parameters measured under ambient condition results in underestimated water saturation when compared with electrical properties determined under reservoir conditions (Saner et al., 1996). An example is presented here to illustrate the impact of using different values of *m* in calculating the gas volume in place. Gas volume in place is calculated for a gas field that has an area, *A*, of 2000 acres, a thickness, *h*, of 150 feet and a gas formation volume factor, *B_g*, of 0.0035 (reservoir ft³/scf) using Equation 1-1. Table 4-8 shows the water saturation calculated based on a base case of *m* = 2 and (+ and – 20% of the value of *m*) at different porosities using Archie formula (Equation 1-12), where *R_t* and *R_w* are 30 and 0.01 ohm-m respectively, and the exponents *a* and *n* are assumed to be 1 and 2 respectively. The impact of 20% error in the value of *m* in the calculations of the STGOIP is shown in Table 4-9. For example, using the wrong value of *m* at a porosity of 10%, results in incorrect calculations of gas in place with errors between 8% smaller and 13% larger volumes. The results show greater errors at lower porosities, which are consistent with the study by Watfa and Nurmi (1987).

Saturation <i>S_w</i> (fraction) based on changing <i>m</i> values at different porosities			
	Φ = 0.1	= 0.08	Φ = 0.06
<i>m</i> = 1.6	0.12	0.14	0.17
<i>m</i> = 2	0.18	0.23	0.30
<i>m</i> = 2.4	0.29	0.38	0.53

Table 4-8: Water saturation *S_w* calculated from Archie formula using different values of *m* at different porosities.

STGOIP (billion cubic ft) based on changing m values at different porosities			
	$\Phi = 0.1$	$\Phi = 0.08$	$\Phi = 0.06$
(-20%) m = 1.6	330.36	257.56	185.19
Base case m = 2	305.20	230.53	155.85
(20%) m = 2.4	265.33	185.73	104.36
Relative difference error %			
	$\Phi = 0.1$	$\Phi = 0.08$	$\Phi = 0.06$
(-20%) m = 1.6	-8%	-12%	-19%
Base case m = 2	0%	0%	0%
(20%) m = 2.4	13%	19%	33%

Table 4-9: Calculated volume of gas in billion cubic feet based on base case of m=2 and +/- 20% of the value of m at different porosities. Relative differences show error in percentage of using different m values with larger error at lower porosity.

4.4.5 Controls on velocities

The increase in the confining stress increases the P-wave velocity as indicated by the measurements of the samples (Figure 4-20). The effect of the porosity on velocity is indicated in Figure 4-22 where the decrease in porosity results in an increase in the velocity. This is in agreement with studies reporting increase in the velocity resulting from the decrease in porosity (Wyllie et al., 1956; Nur et al., 1995). A cross plot of P-wave velocity and porosity both at 5000 psi with colour coding corresponding to the clay content in the samples is shown in Figure 4-31. No clear relationship can be found between the clay and the position of the sample in the cross plot, which disagrees with the study of Han et al. (1986). The disagreement could be explained by the diagenetic effects on the analysed samples.

Velocity can also be affected by the presence of microfractures and their concentration (Smith et al., 2010). SEM images of samples TS2-4 and TS2-7 show the presence of microfractures in both samples. However, velocity of the sample TS2-4 measured at 1000 psi is higher than the velocity of TS2-7 measured at the same stress, even though both samples have similar porosity of approximately 7%. The microfractures have the greatest effect on the P-wave velocity when the microfractures orientation is perpendicular or nearly so to the propagation direction of the elastic wave (Mavko et al., 2009). The difference in the velocities of the two

samples can be interpreted to be caused by the concentration and the orientation of the microfractures. So the microfractures in sample TS2-4 might be parallel to the direction of the waves causing less impact on the velocity. Moreover, the microfractures seen in SEM images are in two dimensions, and so the microfractures might be less concentrated through the whole core plug TS2-4 than the plug sample TS2-7.

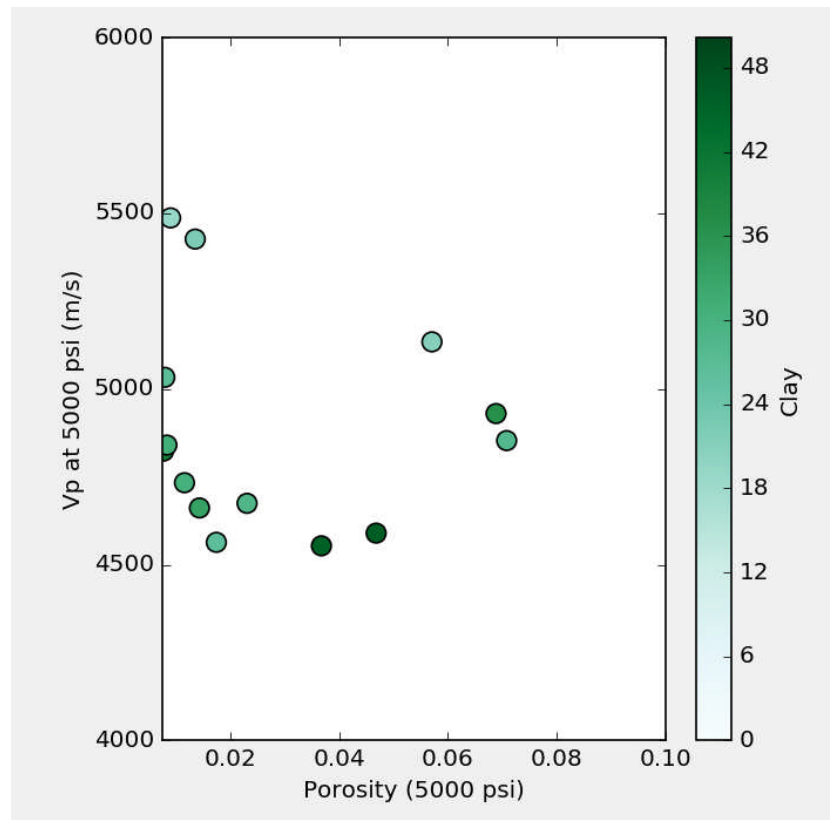


Figure 4-31: Plot of the ultrasonic velocity P-wave (m/s) at 5000 psi against the porosity (fraction) stress-corrected to 5000 psi with colour coding corresponding to clay content in percentage for group-A samples. See caption of Figure 3-6 for porosity uncertainties in plotted values.

4.4.6 Controls on the stress dependency of velocities

The measurements of all the samples prove the P-wave velocity to be stress dependent. However, the velocities of the samples show various stress dependencies (Figure 4-21). For example, samples TS2-3 and TS3-5 having similar measured velocities at 1000 psi stress show different velocities measured at 5000 psi (Figure 4-20). Microfractures appeared to be more abundant in TS2-3 as indicated by the SEM images of the samples (Figure 3-12), which probably be the cause of the different stress dependences between the samples. In contrast, other samples that have

different measured velocities at 1000 psi appear to have similar velocities measured at 5000 psi (e.g. TS2-4 and TS3-2) shown in Figure 4-20. Analysis of SEM images confirms the presence of microfractures in sample TS2-4 (Figure 3-10). This is consistent with the concept that velocity stress dependency is controlled by the closure of microcracks, which also agrees with the results of P-wave velocity measurements under stress for Fontainebleau sandstone conducted by Han (1986) (Figure 4-8). Greater stress dependency of velocity compared with the less affected porosity determined at higher stresses indicates that high stress closes the very thin cracks (Mavko, 2009), hence more impact on velocity.

The velocity was also plotted against the porosity of all samples at higher stress to analyse the effect of microfractures on stress dependency of the velocity. The lack of correlation between P-wave velocity and porosity at two different confining stresses (low net stress shown in Figure 4-22) and (5000 psi net stress shown in Figure 4-23) could be explained by the presence of microfractures seen in SEM images at different orientation, which could have greater impact on the velocity. This is in agreement with the study of tight samples reported by Smith et al. (2010) showing the zero-porosity intercept not crossing with the velocity axis at a value corresponding to the pure mineral forming the rock. They suggested that the presence of cracks caused such behavior.

Moreover, samples TS2-3 and TS2-4 having the highest porosity among the samples, with microfractures present in both, show a minor decrease in the stress-corrected porosity with the increase in the confining stress. Yet, a significant increase in the velocity is observed for the two samples at 5000 psi, which are consistent with the study by Han (1986). Thus, the best way to estimate the stress-dependency of velocity for tight reservoir is to measure the P-wave velocity under reservoir conditions.

4.4.7 Relationship between the stress dependencies of different properties

All the properties measured at different stresses prove to be stress dependent with the determined stress-corrected porosity appearing to be the least stress dependent. The stress-dependencies of permeability, electrical properties and P-wave ultrasonic velocity seem to be all controlled by microcracks, and so relationships between the stress dependencies of the properties might exist.

4.4.7.1 Relationship between stress dependencies of electrical properties and permeability

Stress dependencies of gas permeability and electrical resistivity both are controlled by the presence of microcracks. The stress dependency of gas permeability appears to be higher than the stress dependency of the electrical resistivity. Permeability shows greater reduction when the two properties are normalized and plotted against net stress of the five selected samples (Figure 4-32). Note the plot in Figure 4-32 is the normalized electrical conductivity that is the inverse of the electrical resistivity, which is used only for the purpose of comparison. Reduction in permeability for sample TS2-4 was approximately twice the reduction in conductivity, and it reached up to nine times for other samples like TS3-1. The reason is that permeability of a crack is controlled by the square of the mean crack width, w , (Equation 4-8) (Zimmerman and Bodvarsson, 1994), which means reduction in crack width due to stress increase results in greater reduction in permeability than electrical resistivity. This is consistent with the study reported by Brower and Morrow (1985) stating that reduction in permeability was close to the cube of the reduction in the electrical conductivity for tight rocks with low aspect ratio cracks.

Equation 4-8

$$k = \frac{w^2}{12}$$

Where:

k = permeability

w = mean crack width

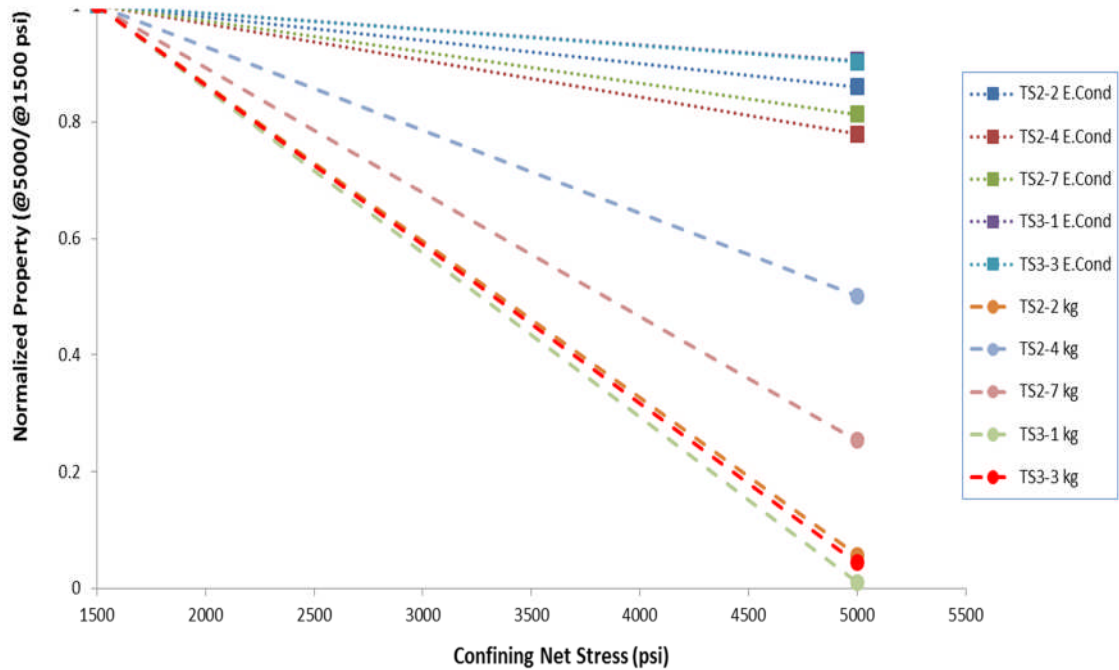


Figure 4-32: Comparison between normalized electrical conductivity (inverse of electrical resistivity) and normalized gas permeability (k_g) against confining net stress (psi) for the five samples showing higher stress dependency of permeability in group A. See captions of Figure 3-6, Figure 3-7 and Figure 4-24 for permeability and resistivity uncertainties in plotted values.

4.4.7.2 Relationship between stress dependencies of electrical properties and ultrasonic velocity

The stress dependencies of both electrical properties and P-wave velocity are both affected by the presence of microfractures. A correlation between *FRF* and P-wave velocity might exist at high net stress since microfractures are expected to be closed at 5000 psi stress. Two cross plots of *FRF* against P-wave velocity at low and high stresses are constructed (Figure 4-33). The plot at low stress indicates the observed microfractures are open, while the second plot at 5000 psi assumes microfractures are closed. Both plots show exponential relationship, but the correlation coefficient at low stress is higher than the one at reservoir stress. This could be explained by the connectivity of the microcracks, which controls *FRF* unlike the velocity that is controlled by the density of microcracks rather than their connectivity. So the two properties respond differently to different aspects of the microfractures. This is consistent with the results of the study by Smith et al. (2010) showing greater impact of the microcracks closure on the velocities than the electrical properties of tight

sandstone samples. In addition, this also agrees with the concept that microcracks oriented parallel to core axis will have more impact on the resistivity than on the velocity; velocity is more controlled by microfractures perpendicular to its propagation direction (Mavko et al., 2009).

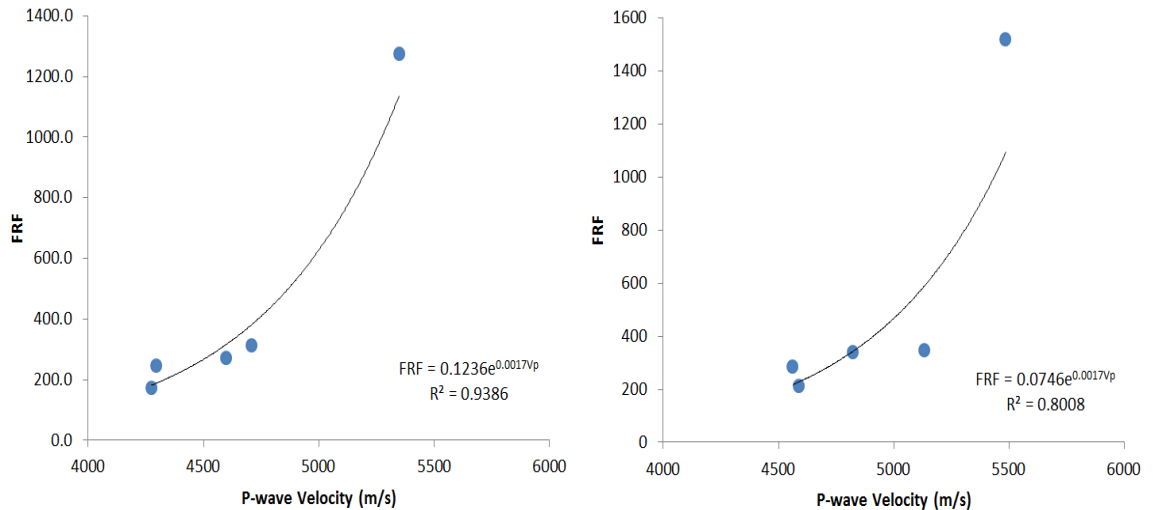


Figure 4-33: Left: Plot of formation resistivity factor FRF against P-wave velocity (m/s) at low stress showing an exponential relationship with a correlation coefficient of 0.94. Right: Similar plot at 5000 psi showing an exponential relationship with less correlation coefficient 0.8.

4.4.7.3 Relationship between stress dependencies of permeability and ultrasonic velocity

The presence of microfractures appears to have a control on the stress dependencies of both gas permeability and velocity. So it might be expected that the gas permeability and P-wave velocity are correlated at high net stress at which microfractures are assumed to be closed. Plots of permeability against velocity measured at a low net stress (Figure 4-34 – left) and at a high net stress of 5000 psi (Figure 4-34 – right) both show no correlation, which could indicate different effects of the features of the microfractures on the permeability and velocity. The plot of normalized permeability (Figure 4-11) shows greater reductions in the permeabilities of all samples at the net stress range between 500 and 5000 psi, compared with normalized P-wave velocities at the stress range 1000 to 5000 psi (Figure 4-21) showing less stress dependency of velocity. This could be explained by the dependency of permeability on the square of the mean width of the connected portion of microcracks (Equation 4-8). Velocity, on the other hand is controlled by the density and orientation of microcracks that are not required to be connected, which is the case

for permeability (Smith et al., 2010; Mavko, 2009). This is consistent with the study of Coyner (1984) reporting that closure of cracks at grain contacts in Berea sandstone under pressure has great effects on velocity with minimum effect on permeability indicating no correlation can be made to predict bulk permeability from acoustic data under stress.

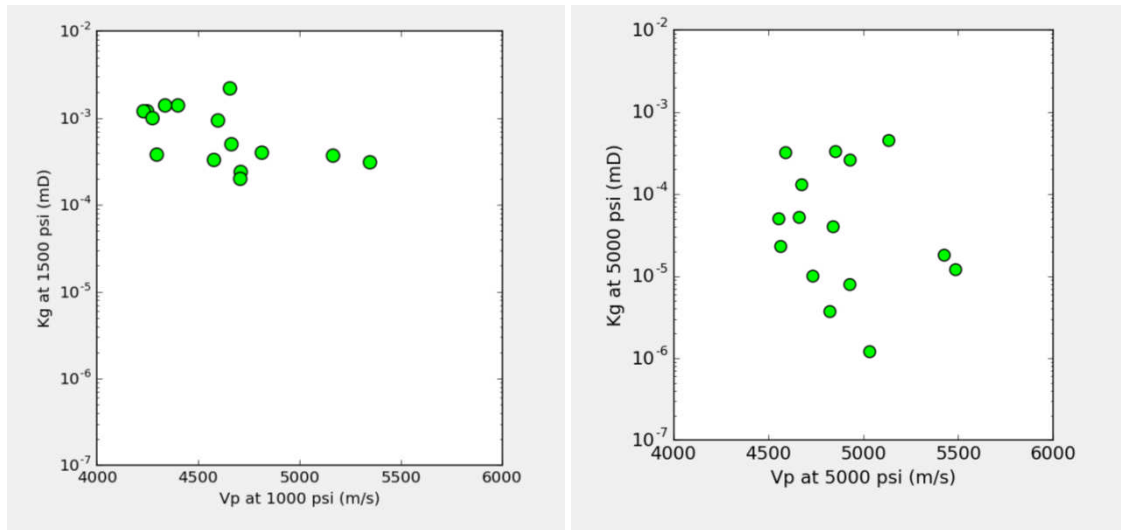


Figure 4-34: Plots of gas permeability k_g (mD) against P-wave velocity (m/s) at low net stress (left) and at in-situ stress of 5000 psi (right) for group-A samples. Both plots show no clear correlation.

4.4.8 Implications of gas slippage and stress dependency of permeability on production strategies

Stress dependency of permeability is controlled by microfractures formed by core damage, which might not be present in the subsurface. Permeability at reservoir condition won't be very sensitive to the change in stress as they are in measurements conducted in the laboratory at low confining pressure. This is consistent with the results from the drawdown experiments indicating that there is not a significant reduction in permeability of all samples from the reservoir stress (i.e. 5000 psi) to prior to abandonment condition (Figure 4-14); hence no significant presence of the induced microcracks. Therefore, applying a restricted flow rate practice might not be greatly helpful to retain permeability in tight gas sandstone reservoirs.

Moreover, the initial gas reservoir pressure decreases during production, which increases the effect of the gas slippage that could enhance the apparent permeability. The slight enhancement in the gas permeability is noticed toward the end of the drawdown tests for several samples with pore pressure of approximately 2700-3000

psi (Figure 4-12), which could be caused by gas slippage. The gas flow in tight reservoirs is dominated by the effects of net stress and gas slippage rather than ambient permeability (Swanson, 1981). So it would be more efficient to evaluate the permeability of tight rocks under reservoir conditions rather than low stresses.

4.5 Conclusions

The petrophysical properties (permeability, ultrasonic velocity and electrical properties) of tight gas sandstones showed to be stress dependent particularly at low stresses in the range of 500 to 3000 psi. The stress correction for porosity resulted in an average of 10% and less than 5% reduction at 1500 psi and 5000 psi respectively. The stress dependencies of all the properties maybe caused by microcracks which were observed in SEM images. These microfractures probably formed from the rapid change in the stress state of the rock during coring and drilling; such microfractures might not be present in the subsurface.

The stress dependency varied from one property to another. It was shown that gas permeability was the most stress-sensitive property compared to the formation resistivity factor and the ultrasonic velocity. The reason for this is that permeability is dependent on the square of the fracture width whereas electrical resistivity and velocity are not. Yet, permeability and electrical properties require connectivity of the microcracks whereas the velocity rather depends on the concentration of the microcracks. The direction of the microfractures appeared to play a role in the stress dependencies of all these properties. The stress dependency of every property is controlled by different aspects of the microfractures, and so the properties showed different stress dependencies with no correlation between their stress dependencies. Moreover, diagenesis could alter the pore geometries of the tight samples, which could result in different stress dependencies of their petrophysical properties. Samples having similar permeability measurements at ambient condition showed different stress dependencies with diverse permeability readings at reservoir conditions, and vice versa. The stress dependency of a property varied even between samples that were taken from the same reservoir and only inches apart due to diagenesis.

Volume of gas in place was estimated by calculating the water saturation in the reservoir based on the porosity and electrical properties of the rock. So it is vital to

determine the relationship between porosity and the cementation exponent, m , under stress for tight reservoirs rather than under ambient condition or using conventional formulas. Using constant values for m to estimate the formation resistivity factor of tight formations with microfractures would to be inaccurate. Calculations showed that slight errors in the value of the cementation exponent could result in large uncertainties in calculating water saturation especially in tight formations where the error is larger at lower porosity. The results of the analyses samples disagreed with the commonly used Shell formula stating that the exponent m increases as the porosity decreases. The disagreement is caused by the presence of the microfractures that act as conduits for the electrical current flow. Therefore, if the microcracks do not exist in the subsurface then the analyse may agree with the Shell formula.

The stress dependencies of the properties are greater at low net stress, which require stress corrections. So, it is recommended to measure the properties at *in-situ* condition to avoid incorrect estimations of the fluid saturation and the fluid flow. Drawdown experiments showed that the permeability is not so stress dependent at *in-situ* conditions as microfractures would not be as abundant in the subsurface as in the laboratory. So restricted rate practices might not be worthwhile to retain the permeability in tight sandstone reservoirs. In addition, gas slippage would be important at this stage and can enhance the apparent permeability during production. Thus, it is important to evaluate and quantify the stress sensitivity of permeability at reservoir condition to evaluate the gas flow rates in tight sandstone reservoirs.

5 Effective Stress Law for Permeability of Tight Gas Sandstones

5.1 Introduction

In hydrocarbon reservoirs, the rock is under an effective stress that is controlled by the total stress and the pore pressure. The total stress is composed of vertical lithostatic pressure in addition to tectonic forces. The lithostatic stress is exerted by the overburden layers and transmitted through grain-to-grain contacts, and it can be calculated with Equation 5-1 assuming pressure is the same in all directions. The reservoir fluid pressure would be described in a similar manner if the fluid is continuously connected through pathways from the surface to a certain depth (Equation 5-2) (Tiab and Donaldson, 2012). The confining stress is opposed by the reservoir fluid pressure, and thus a net stress is often defined as the difference between the confining stress and the reservoir pressure (Figure 5-1). Physical properties of the porous rock such as permeability, porosity and volumetric strain are all affected by changes in the stress and the pore pressure. However, every property responds differently to the change in the net stress. So it is important to evaluate every reservoir property under an effective net stress (Li et al., 2014).

Equation 5-1

$$\sigma_{vertical} = d_{rock} g h$$

Equation 5-2

$$P_p = d_{fluid} g h$$

where:

$\sigma_{vertical}$ = confining stress

P_p = pore pressure

d_{rock} = density of the rock

d_{fluid} = density of the fluid

g = gravity acceleration (9.8 m/s²)

h = the depth at which pressure is measured

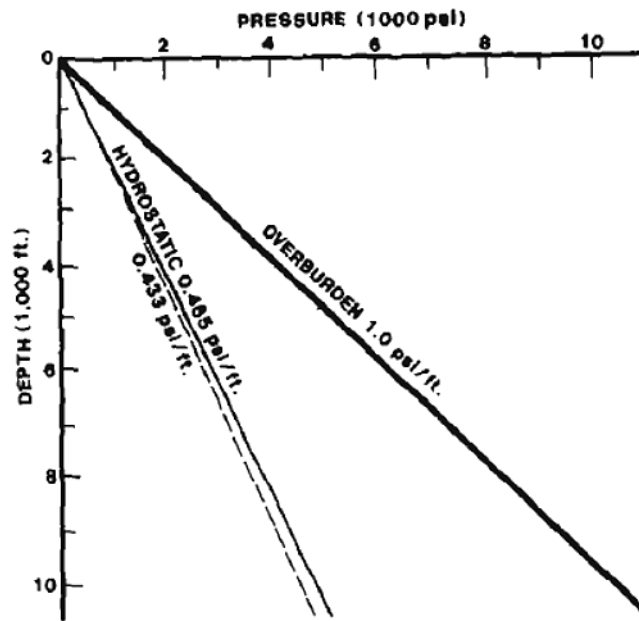


Figure 5-1: Schematic showing lithostatic pressure and fluid pressure that is often in between the lithostatic pressure and hydrostatic pressure (from Tiab and Donaldson, 2012).

Assuming that the effects of confining stress and the pore pressure on permeability are equal is not necessarily satisfied for permeability (Li et al., 2014). It is important to analyse the stress sensitivity of reservoir permeability to the changes in both the confining stress and the pore pressure specifically in tight formations that are known to be stress-dependent. To provide further insight into the effective stress law for permeability of tight gas sandstones, a series of permeability measurements under differing confining and pore pressures have been conducted.

The concept of the effective stress law for permeability is not new; however, reported values of the effective stress coefficients in the literature vary significantly (less than 0.5 and up to 7). The reported coefficients vary from one formation to another, and they are affected by several factors such as lithology, microstructure and heterogeneity. More importantly they vary depending on the properties. For example, the coefficients for volume change are different than the ones for permeability. Thus, it is also important not to use coefficients determined for conventional less stress-dependent reservoirs into the modelling of unconventional rocks. Determining the effective stress law for permeability enables the prediction of permeability under any combination of total stress and pore pressure (Robin, 1973), which improves the

modelling of fluid flow in tight reservoirs by quantifying the stress sensitivity of permeability during production.

5.1.1 Background

The concept of effective stress law was introduced by Terzaghi (1925) who investigated the effect of stress on soils, and showed that the strength of a fully saturated soil under a uniaxial stress is controlled by the difference between the confining stress and the fluid pressure. Terzaghi (1925) developed the net stress law for soil deformation, which became known as the simple effective stress law (Equation 5-3).

Equation 5-3

$$P_{eff} = P_{con} - P_p$$

where:

P_{con} = confining pressure

P_{eff} = effective pressure

Biot (1941) reviewed the strain of soil under different net stresses, and he introduced a new modulus, H , which accounts for the bulk volume strain due to change in the pore pressure with a constant external stress. Biot developed a coefficient, α , which is the ratio between the pore volume strain and the bulk volume strain for soils with the lower and upper limits being the porosity and 1 respectively. To evaluate the volumetric strain deformation due to effective stress, the simple effective stress law was modified by including the Biot coefficient into the simple law (Equation 5-4), where the coefficient α is a constant that can be calculated for an isotropic porous rock using Equation 5-5 (Nur and Byerlee, 1971).

Equation 5-4

$$\Delta\sigma' = \Delta\sigma - \alpha \Delta P_p$$

where:

$\Delta\sigma'$ = change in effective stress (psi)

$\Delta\sigma$ = change in confining stress (psi)

ΔP_p = change in pore pressure (psi)

α = Biot effective stress coefficient

Equation 5-5

$$\alpha = 1 - \frac{K_b}{K_s}$$

where:

K_b = elastic bulk modulus of the rock (psi)

K_s = elastic bulk modulus of the solids forming the rock (psi)

Brace (1972) reviewed the effect of both confining stress and fluid pressure on different properties of porous rocks such as fluid permeability and mechanical and electrical properties, and he discussed how the shape and geometry of the pores affect such properties in the porous rock. Biot coefficient is the effective stress coefficient for volume change, and every property has a different effective stress coefficient (Berryman, 1992). Consequently, it would be misleading to compare values of coefficients obtained for different properties (Bernabe, 1986). Permeability of tight rocks is dominated by the relaxation of microcracks that might not exist *in-situ* (Warpinski and Teufel, 1992). It would be easier to determine the effective stress law for conventional sandstones unlike the tight samples. Loading and unloading the sample, which is often referred to as stress cycling, minimizes the effect of such artificial microcracks (McKernan et al., 2014).

An effective stress coefficient for permeability, χ , which affect the pore pressure, was introduced into the simple "Terzaghi" stress law (Equation 5-6). This coefficient accounts for the pressure sensitivity of the rock permeability, and quantifies the relative importance of both confining stress and pore pressure into one parameter "effective stress" (Heller et al., 2014). The advantage of using one parameter, which is the effective stress σ' , for analysing the effect of the change in stress on permeability is easier than using two independent parameters, confining pressure and pore pressure (Ghabezloo et al., 2009).

Equation 5-6

$$\sigma' = \sigma - \chi P_p$$

where:

χ = effective stress coefficient for permeability

It has been argued that no effective stress law for permeability is applicable to all reservoirs, and thus many experiments were undertaken to determine the effective stress law for permeability since then (Zoback and Byerlee, 1975; Walls and Nur, 1979; Bernabe, 1986; Warpinski and Teufel, 1992; Kwon et al., 2001; Al-Wardy and Zimmerman, 2004; Li et al., 2009; Heller et al., 2014). Several studies reported effective stress coefficients for permeability of sandstones to be less than unity. David and Darot (1989) reported values for the coefficient between 0.6 and 0.75 for Fontainebleau sandstone with 6% porosity and permeability of less than 2 mD. Keaney et al. (2004) experimentally determined an average value for the effective stress coefficient of 0.75 for Tennessee sandstones having porosity in the range of 5.1 to 8.1% and permeability in the range of less than 0.3 to over 3 mD. Li et al. (2009) also reported an effective stress coefficient less than unity for samples taken from E-bei tight sandstone reservoir in China. Qiao et al. (2012) examined Nikanassin tight sandstones with permeability in the range of 0.002 to 0.01 mD and reported average effective stress coefficients of about 0.7 and 0.17 for samples perpendicular and parallel to bedding respectively. Heller et al. (2014) conducted permeability measurements on six shale samples, and reported values less than 1 for all the samples.

On the other hand, Zoback and Byerlee (1975) reported effective stress coefficients for permeability higher than unity. Walls and Nur (1979) also examined the permeability of sandstones with different clay contents under ranges of effective stress, stating that effective stress coefficient for permeability can be as high as 7 for samples with 20% clay. They used distilled water as the pore fluid in their experiments. A more recent study by Al-Wardy and Zimmerman (2004) examining the permeability under effective stress for sandstone samples with clay reported coefficients higher than unity as well. Water was used as the pore fluid for their measurements.

Loading and unloading the sample is performed by increasing the load on the sample by applying a certain net stress and leaving the sample for a certain period of time, followed by decreasing the load by reducing the net stress and leaving the sample at such net stress for some time. Coyner (1984) tested the permeability of Berea sandstone under a range of simple effective stresses with a highly saline water (50,000 ppm NaCl). He compared his permeability measurements with earlier measurements performed by Zoback and Byerlee (1975) and Walls and Nur (1979), arguing that the reported large effect of pore pressure on permeability was diminished after the third cycle of varying the combination of the confining and pore pressures. This observation suggested that it is important to consider the loading-unloading cycles prior to performing permeability measurements under stress.

This chapter discusses the techniques and methods used to conduct the gas permeability measurements under a range of net stresses (1000 to 4000 psi) with different combinations of confining stresses (3000 to 8000 psi) and pore pressures (2000 to 4000 psi) with a 1000 psi step increment in each pressure. Effective stress law is determined for every sample by fitting the permeability measurements into a best fit model to estimate the effective stress coefficient. The determined model is then used to calculate permeability at higher effective stresses to assess the implication of the model for gas production in tight sandstones. Biot's coefficients are calculated from ultrasonic velocity and bulk moduli of the rocks and the minerals, and they are presented here to be compared with the determined effective stress coefficients for permeability.

5.2 Methodology

5.2.1 Samples

Group B that is a suite of five tight sandstone samples (TS5-2, TS5-5, TS7-1, TS7-4 and TS7-5) were used to assess the effective stress law for permeability. Description of the samples and the process of preparing the samples, which includes cleaning and drying are presented in Sections 2.2 and 2.3 respectively.

5.2.2 Quantitative X-ray diffraction

The samples were analysed using the QXRD technique, which is described in Section 2.7, to determine the quantitative mineralogy, which was then used to

calculate the samples moduli based on literature information of the elastic moduli of the individual minerals forming the rock samples.

5.2.3 Porosity and density measurement

Details of the techniques used for the bulk density and porosity measurements are discussed in Sections 2.4 2.5 respectively.

5.2.4 Gas pulse decay permeameter

5.2.4.1 Loading and unloading cycles

Prior to conducting the measurements to obtain the effective stress law, loading and unloading cycles were performed on the samples. Loading-unloading cycles were conducted also to analyse the reproducibility of the measurements. Permeability was measured at every net stress point during the loading and unloading cycles. After placing the core sample into the high-pressure PDP, the loading process began by applying confining stress up to 10000 psi. The confining stress was increased gradually with pore pressure increase ensuring no pressure difference more than 7000 psi, estimated to be the net stress of the reservoir from which the samples were taken, imparted between confining and pore pressure to minimize the risk of damaging the core sample. The sample was left at approximately 10000 psi confining and 8000 psi pore pressure for more than 12 hours (overnight). Loading process was performed by keeping the confining stress fixed at 10000 psi and reducing the pore pressure in 1000 psi step leaving the sample for approximately 2 hour soaking time between each pore pressure change. The cycle ended at a net stress of 7000 psi that is 3000 psi pore pressure (Table 5-1).

Confining Stress (psi)	Pore Pressure (psi)	Net Stress (psi)	Permeability (mD)	Soaking Time (hours)
Loading Cycle				
10000	8000	2000	0.032	16
10000	7000	3000	0.019	2
10000	6000	4000	0.010	2
10000	5000	5000	0.0064	2
10000	4000	6000	0.0049	2
10000	3000	7000	0.0045	2
Unloading Cycle				
10000	3000	7000	0.0036	13
10000	4000	6000	0.0036	2
10000	5000	5000	0.0045	2
10000	6000	4000	0.0069	2
10000	7000	3000	0.012	2
10000	8000	2000	0.023	2

Table 5-1: An example of loading and unloading cycles performed for sample TS7-4 with permeability (mD) measured at each net stress (psi).

Unloading cycle was performed by reversing the process of the loading cycle that is starting with 3000 psi pore pressure with a fixed 10000 confining stress. The pore pressure was increased in steps of 1000 psi up to the starting point of the loading cycle (Table 5-1). An example of permeability measurements plotted against the net stress during both cycles are shown in Figure 5-2.

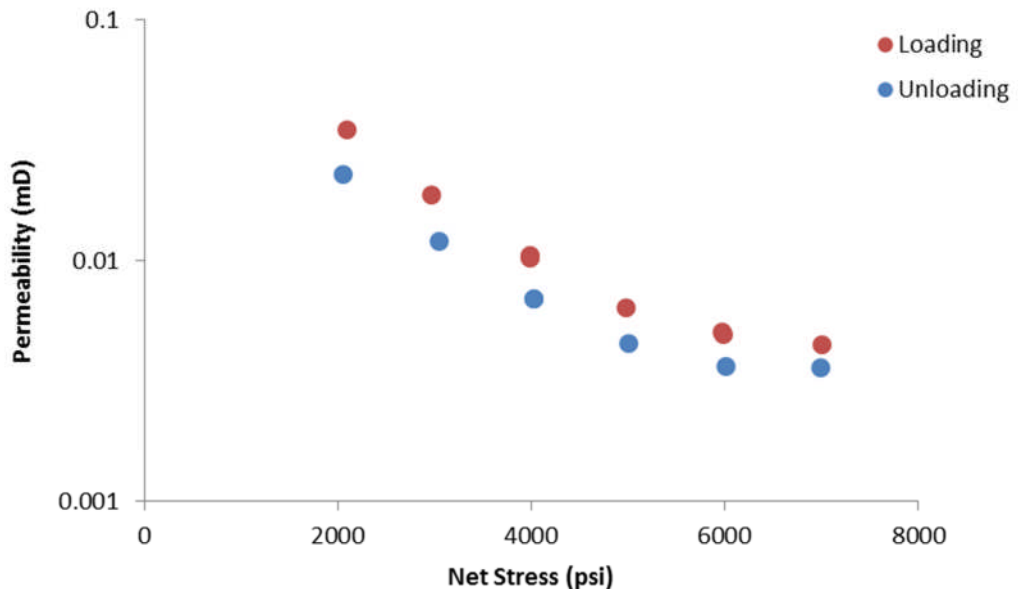


Figure 5-2: An example of helium permeability measurements (mD) with 10% uncertainty against net stress (psi) during loading and unloading cycles performed prior to conducting the effective stress law measurements for sample TS7-4.

Permeability was determined under different combinations of confining and pore pressures to independently test the effects of each pressure on the permeability, and to determine the effective stress coefficients for permeability (Heller and Zoback, 2013). The high pressure PDP technique was used to measure the permeability under a range of pore pressures (2000, 3000 and 4000 psi) with confining pressures varying at each fixed pore pressure in the range of 3000 to 8000 psi with 1000-psi increment. The permeability measurements were taken at three fixed pore pressures starting at 2000 psi with four confining pressure steps starting at 3000 psi and then with 1000 psi increment in the confining. The procedure was repeated at fixed pore pressures of 3000 and 4000 psi with four 1000-psi confining pressure increments at each fixed pore pressure. Figure 5-3 shows the steps of changing the confining pressure and the pore pressure during the measurements. The whole set of measurements took 2 to 3 days to complete. Total of 12 measurements were performed at different combinations of confining stress and pore pressure for each sample (Table 5-2). Confining and pore pressures were both constantly monitored and the confining pressure was kept always higher than the pore pressure with a minimum of 1000 psi difference.

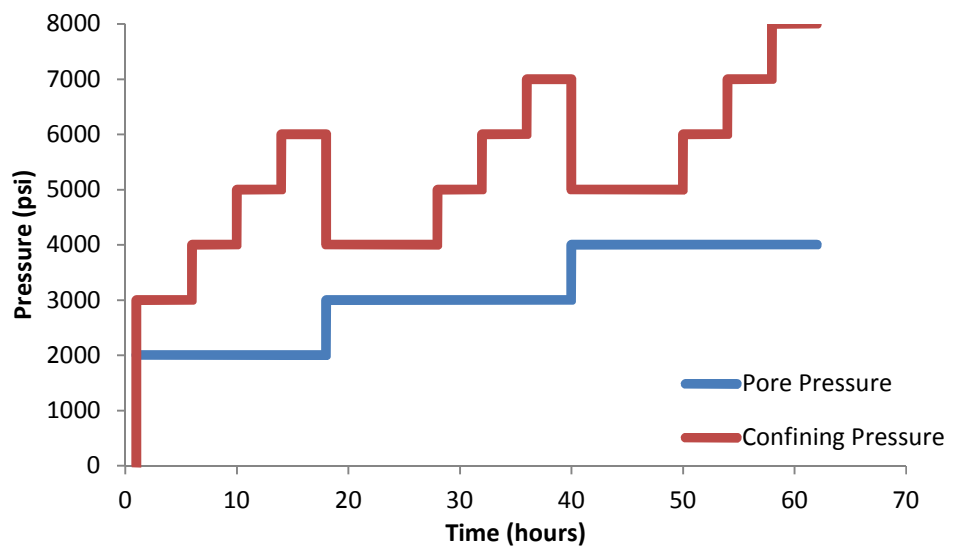


Figure 5-3: Changing the confining pressure and pore pressure in steps during permeability measurements with several hours equilibrium after each confining or pore pressure change. The whole set of measurements takes 2 to 3 days.

# of Measurements	Pore Pressure (psi)	Confining Stress (psi)
1	2000	3000
2		4000
3		5000
4		6000
5	3000	4000
6		5000
7		6000
8		7000
9	4000	5000
10		6000
11		7000
12		8000

Table 5-2: Total of 12 points at which gas permeability was measured under different combinations of pore pressures and confining stresses for each sample.

5.2.5 Biot coefficients from elastic properties

Ultrasonic velocity was measured at 1000 and 5000 psi for the samples using the acoustic system in the laboratory described in Section 2.9. The elastic bulk modulus, K_b , without pore fluid was calculated from the measured bulk density and ultrasonic velocities (shear and compressional) of each sample using Equation 5-7. The elastic moduli of the solids forming the rock, K_s , were calculated using the Voigt upper bound as the sum of the volume fraction of each mineral multiplied by the mineral bulk modulus (Equation 5-8) (Brace, 1965). The volume fractions of the minerals were obtained from the QXRD data and the elastic modulus of each mineral was obtained from Table 5-3. Biot coefficient was then calculated using Equation 5-5 for all the samples. Clay to quartz stiffness ratio was estimated as the ratio of the calculated total clay bulk modulus to the calculated quartz bulk modulus.

Equation 5-7

$$K_b = d_b(3 V_p^2 - \frac{4}{3} V_s^2)$$

where:

K_b = elastic bulk modulus (psi)

d_b = bulk density g/cm^3

V_p = compressional velocity (m/s)

V_s = shear velocity (m/s)

Equation 5-8

$$K_s = \sum_{i=1}^x f E_m$$

where:

K_s = elastic bulk modulus of the solids forming the rock (psi)

x = number of minerals

f = volume fraction of the mineral

E_m = elastic modulus of the mineral

Mineral	Rock Physics Handbook
	K (GPa)
Quartz	39
Albite	75.6
Microcline	37.5
Calcite	76.7
Dolomite	94.8
Mica	52.2
Illite-smectite	35.7
Kaolinite	46
Chlorite	165
Siderite	123.7
Anhydrite	56.1

Table 5-3: Elastic modulus of minerals used to calculate the composite bulk modulus of the minerals forming the rock (from Mavko et al., 2009).

5.3 Results:

The sandstone samples have fine grains, which are moderately to well sorted. General results of routine porosity, gas and brine permeability measurements are presented in Table 3-1.

5.3.1 Quantitative XRD

Minerals in percentages determined from the quantitative x-ray diffraction are presented in Table 3-2. The samples consist mainly of quartz with an average of 75%, and total clay of approximately 10-15 % and 5-8% dolomite.

5.3.2 Porosity with bulk density and ultrasonic velocity

The measured helium porosity was in the range of 6.5 to 11.5%. Table 5-4 presents the measured porosity in percentage with measured bulk density in g/cm^3 . Ultrasonic

velocity measurements that are P-waves and S-waves under 1000 and 5000 psi confining stress are also shown in Table 5-4. Ultrasonic velocity was not measured for TS5-5 as the sample was broken.

	Porosity % at ambient	Bulk Density g/cm ³	V _p (m/s) @ 1000 psi	V _p (m/s) @ 5000 psi	V _s (m/s) @ 1000 psi	V _s (m/s) @ 5000 psi
TS 5-2	6.5	2.54	3272	4506	2221	2933
*TS 5-5	11.3	2.38	-	-	-	-
TS 7-1	6.4	2.45	4379	5108	2835	3276
TS 7-4	11.5	2.35	4120	4688	2754	3046
TS 7-5	8.3	2.37	3748	4411	2546	2884

Table 5-4: Measured porosity and bulk density at ambient condition with ultrasonic velocity V_p and V_s (m/s) measured at 1000 and 5000 psi confining stress for group-B samples. *TS 5-5 was broken prior to measuring the ultrasonic velocity. See caption of Figure 3-5 for porosity uncertainties in plotted values.

5.3.3 Gas permeability under stress

All samples experienced different rate of permeability reduction resulting from the increase of the effective stress despite the combination of the confining and pore pressures. Table 5-5 presents the permeability measurements under a fixed pore pressure of 2000 psi and a confining stress of 3000 and 6000 psi giving simple net stresses of 1000 to 4000 psi. The reduction in permeability was significant when the confining stress was increased with a fixed pore pressure (Figure 5-4). However, permeability increased slightly when the pore pressure was increased at a constant confining pressure showing less sensitivity to the change in the pore pressure (Figure 5-5).

Sample	kg mD @ 1000 psi Net Stress	kg mD @ 4000 psi Net Stress
TS5-2	0.012	0.0030
TS5-5	0.028	0.016
TS7-1	0.0018	0.00097
TS7-4	0.010	0.0061
TS7-5	0.0018	0.0012

Table 5-5: Permeability measurements (10% uncertainty) under a fixed pore pressure of 2000 psi and increasing confining stress 3000 to 6000 psi (that is 1000 to 4000 psi simple net stress) for group-B samples.

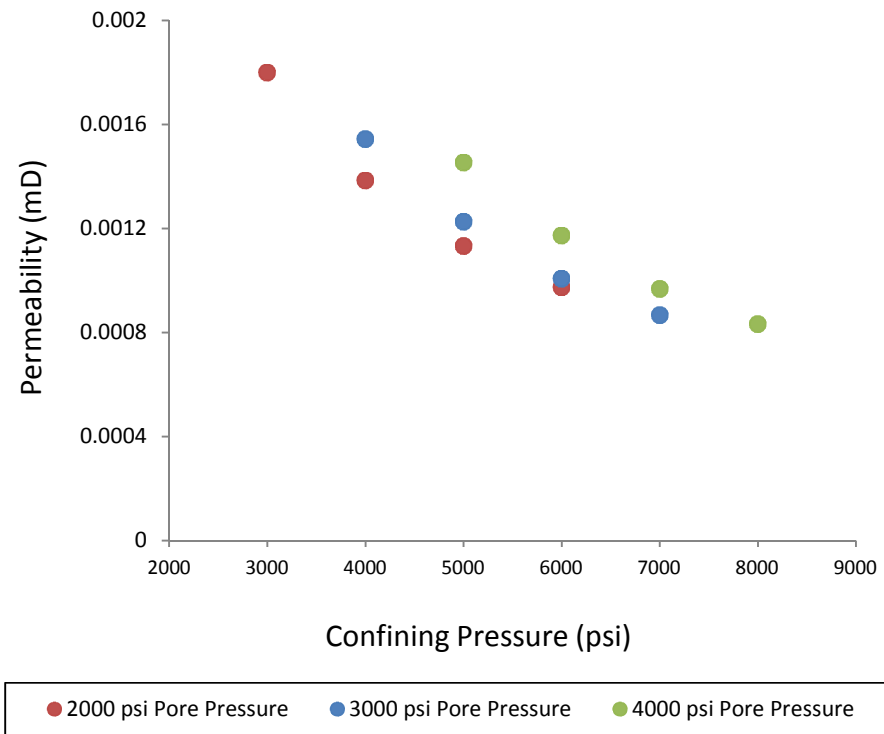


Figure 5-4: Helium permeability reduction ($\pm 10\%$ uncertainty) with increasing confining stress and different constant pore pressures for sample TS7-1.

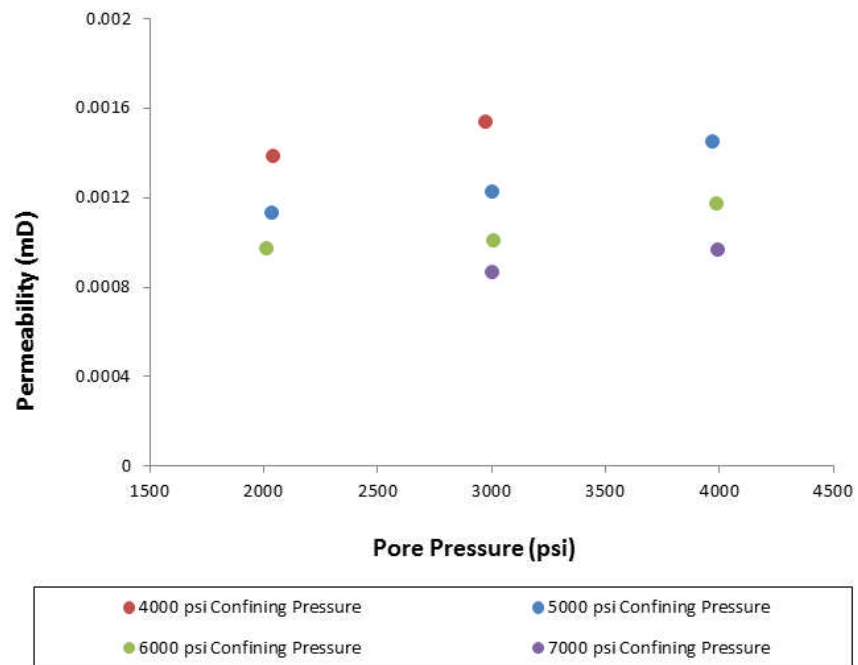


Figure 5-5: Helium permeability increases ($\pm 10\%$ uncertainty) due to the increase in pore pressure with different constant confining stresses for sample TS7-1.

Permeability measurements was plotted as a function of the simple effective stress (Figure 5-6), and as a function of the modified effective stress law with different effective-stress coefficients (Figure 5-7). The coefficient for each sample was determined from the best fit trend of the power function with the least data points dispersion (Zoback and Byrelee, 1975).

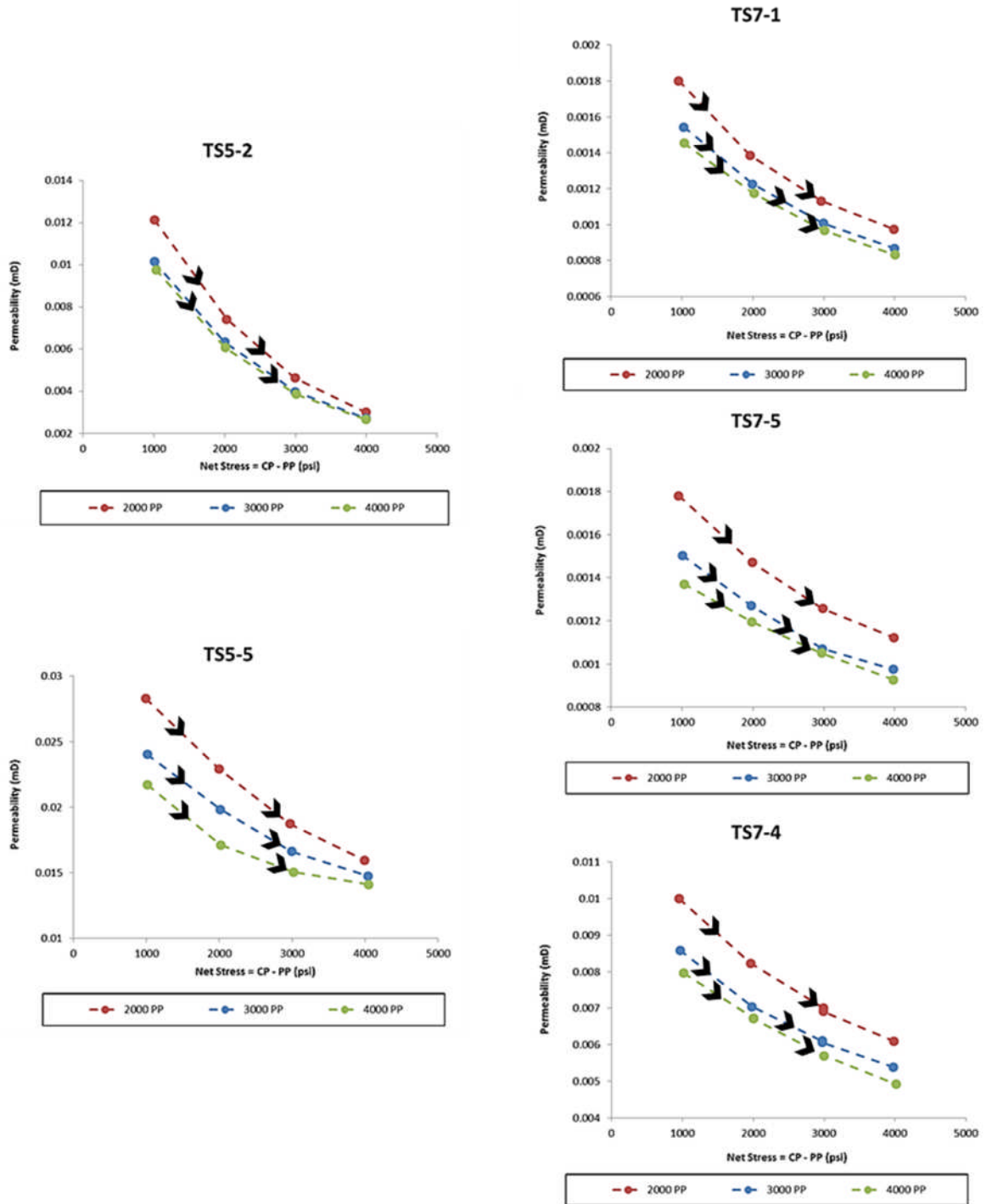


Figure 5-6: Measured helium permeability (mD) with $\pm 10\%$ uncertainty plotted against the simple effective stress that is $C_P - P_P$ (psi) for the five samples in group B. Black arrows indicate the direction of the pressure increase.

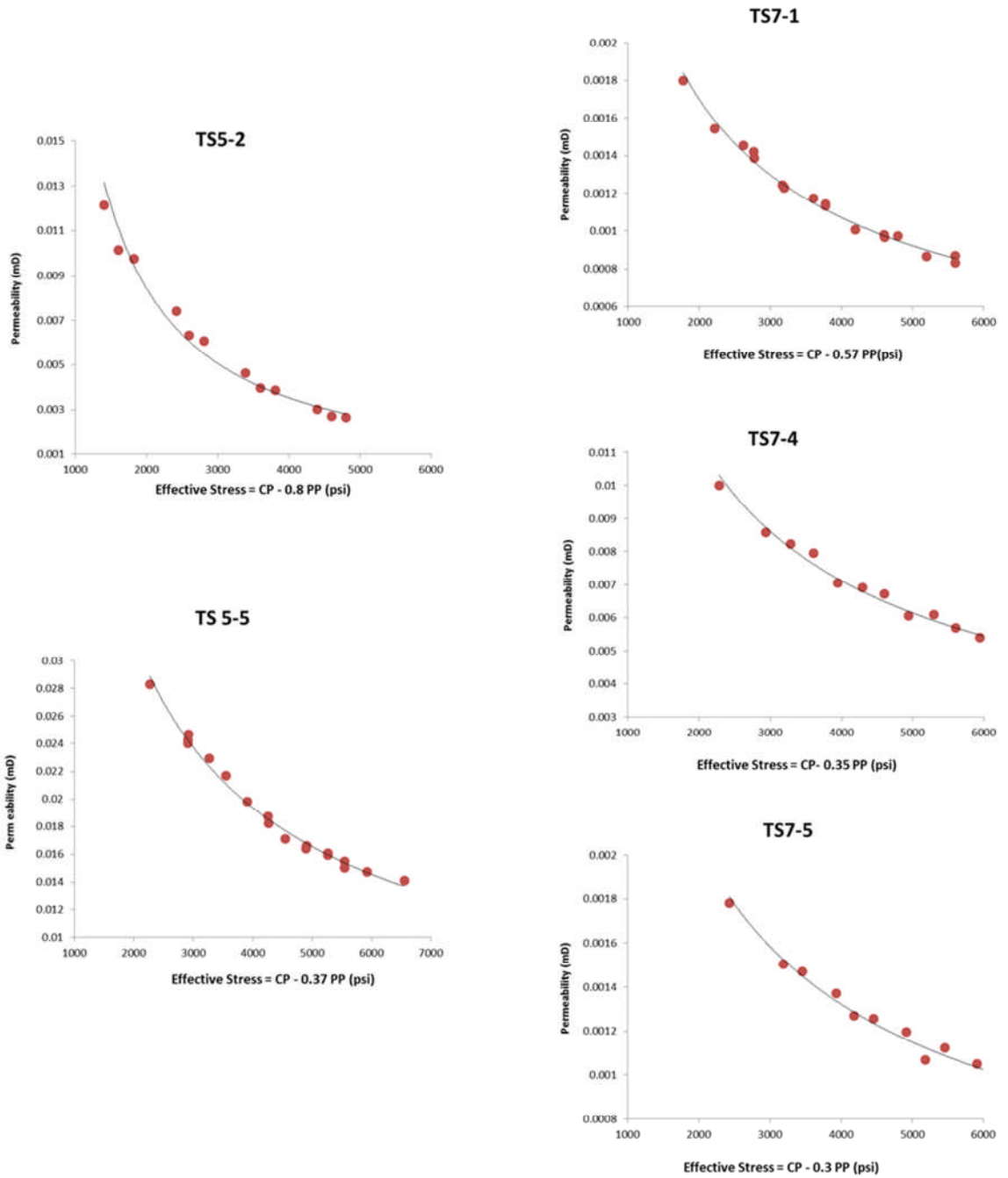


Figure 5-7: Best fitting of permeability (mD) vs modified effective stress (psi) with best effective-stress coefficient for permeability ($C_p - \chi P_p$) for the five samples in group B.

An example of finding the best fit graphically for one of the samples (TS5-2) is shown in Figure 5-8 with different coefficients (0.2, 0.4, 0.6, 0.8 and 1 that is referred to as Terzaghi) used to determine the best correlation coefficient. The coefficient $\chi = 0.8$ showed the best fit with a correlation coefficient of 0.98 for this sample.

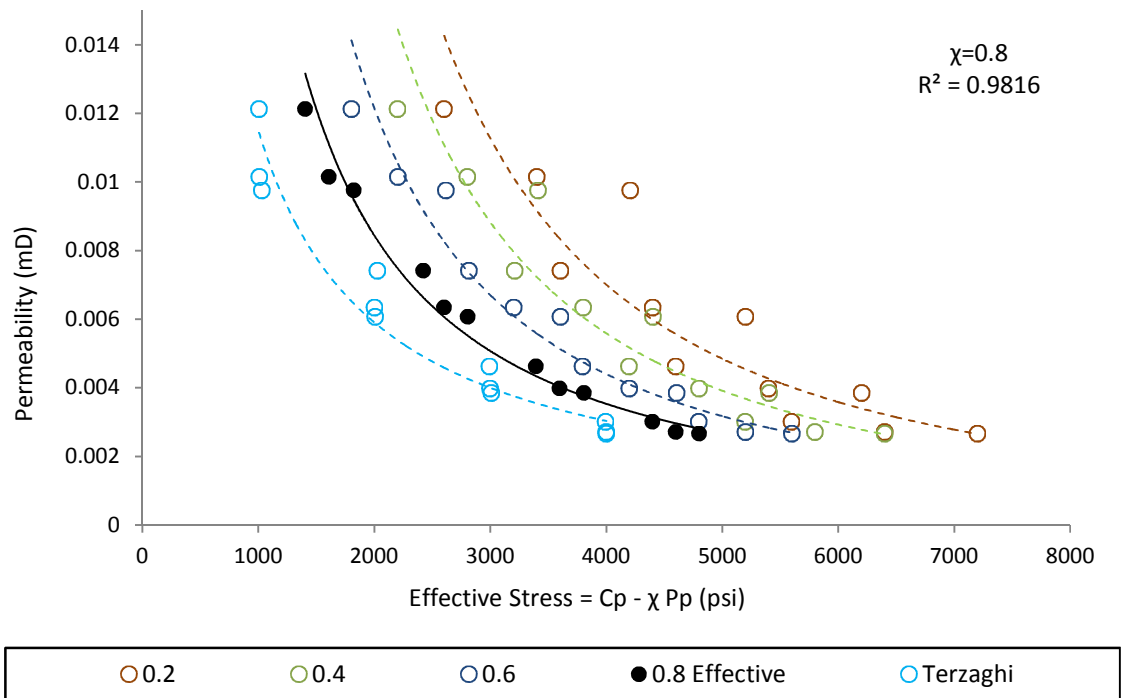


Figure 5-8: Helium permeability (mD) ($\pm 10\%$ uncertainty) of TS5-2 plotted against effective stress in power function with different coefficients (0.2, 0.4, 0.6, 0.8, and 1). $\chi = 0.8$ showed the best fit.

The determined coefficients χ for the samples were in the range of 0.3 to 0.8 with least square correlation coefficients of 0.98-0.99 (Table 5-6). The results indicate that the permeability for all the samples were more sensitive to the change in the confining stress than the change in the pore pressure. Sample TS5-5 and TS7-4 have similar measured porosity and gas permeability at low stress, which are 11.3% and 11.5% for porosity and 0.13 and 0.11 mD for permeability, respectively. Even though the two samples were taken from different tight gas sandstone reservoirs, both samples showed best fit power law models with similar effective stress coefficients χ of approximately 0.4 (Table 5-6).

Sample	kg (mD) at 500 psi	Effective Stress Coefficient χ	R^2
TS5-2	0.08	0.8	0.98
TS5-5	0.13	0.37	0.99
TS7-1	0.02	0.57	0.98
TS7-4	0.11	0.35	0.98
TS7-5	0.02	0.3	0.98

Table 5-6: Values of the determined effective stress coefficients for permeability χ of group-B samples with the correlation coefficients of the power law models.

After the best effective stress model was determined, permeability was calculated from the determined power law under higher *in-situ* net stress for implication in tight sandstone reservoir production. Calculated permeability using the power law was compared with permeability measured under similar stress condition (Figure 5-9). A good correlation was shown between the permeability calculated from the model and the permeability measured at *in-situ* stress (Table 5-7).

	Fixed Confining Stress 10,000 psi			
Sample	7000 psi Pore Pressure	6000 psi Pore Pressure	5000 psi Pore Pressure	4000 psi Pore Pressure
TS5-2	0.0065	0.0030	0.0017	0.0012
TS5-5	0.0423	0.0222	0.0143	0.0114
TS7-1	0.0028	0.0013	0.0008	0.0006
TS7-4	0.0120	0.0069	0.0045	0.0036
TS7-5	0.0022	0.0013	0.0008	0.0007

Table 5-7: Measured helium permeability in (mD) with $\pm 10\%$ uncertainty for all the samples in group-B under a fixed confining stress of 10,000 psi and varying pore pressure 7000-4000 psi.

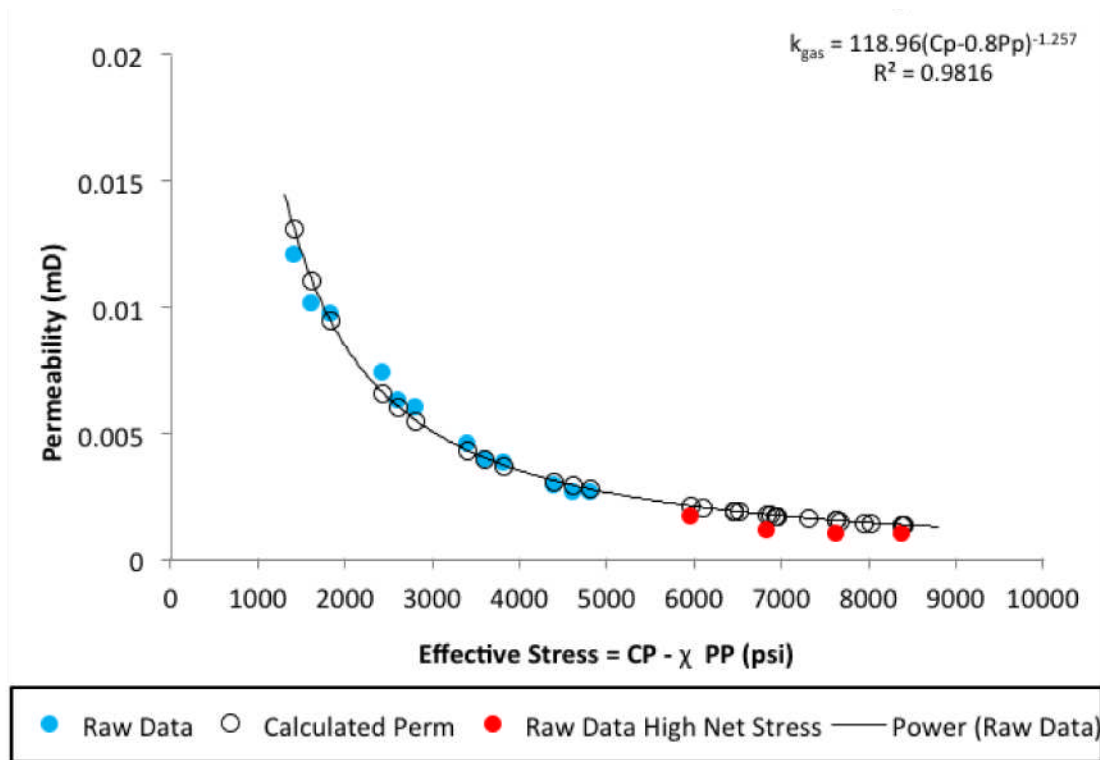


Figure 5-9: Calculated permeability from the power law model (black circles) with helium permeability measured under low net stresses (blue) and higher in-situ net stresses (red) for sample TS5-2 with ±10% uncertainty.

5.3.4 Elastic properties and Biot’s coefficients

The dry bulk modulus K_b that was calculated from the measured density and ultrasonic velocities, and the calculated bulk modulus K_s for the minerals forming the samples are presented in Table 5-8. Biot coefficients calculated from the determined K_b and K_s are also shown in Table 5-8. The estimated clay to quartz stiffness ratio for the samples were in the range of 1:2 to 1:7 with an average of 1:4 (Figure 5-9).

Sample	Dry Bulk Modulus K_b @1000 psi	Dry Bulk Modulus K_b @5000 psi	Total Minerals Bulk Modulus K_s	Biot α Coefficient @1000 psi	Biot α Coefficient @5000 psi
TS5-2	10.5	22.5	46.3	0.8	0.5
TS5-5	-	-	43.9	-	-
TS7-1	20.7	28.9	47.3	0.6	0.4
TS7-4	16.1	22.9	43.5	0.6	0.5
TS7-5	12.8	19.8	44.7	0.7	0.6

Table 5-8: Dry bulk modulus K_b at 1000 and 5000 psi calculated from density and velocity data, and calculated minerals bulk modulus K_s . Biot coefficients determined for the group-B samples at 1000 and 5000 psi from the calculated K_b and K_s .

Sample	Quartz Bulk Modulus (GPa)	Total Clay Bulk Modulus (GPa)	Clay : Quartz Stiffness Ratio
TS5-2	29.4	6.1	1:5
TS5-5	30.9	7.1	2:9
TS7-1	24.6	12.3	1:2
TS7-4	31.6	5.9	1:5
TS7-5	29.8	4.0	1:7

Table 5-9: Bulk modulus (GPa) for quartz and the total clay present in each sample and the clay to quartz stiffness ratio for the samples in group B.

5.4 Discussion

The experiments conducted to analyse the effective stress law for permeability of tight gas sandstone samples indicated that the permeability generally decreased with the increase of the net stress. Yet, the effect of increasing the confining stress is more significant than the effect of increasing the pore pressure. It would be incorrect to simply apply the Terzaghi net stress law (1925) to analyse the permeability of the tight samples under net stress. This simple law was applied for soil strength studies, and thus it might not even be correct for strength analysis because it has not taken into account the effective stress coefficient. Moreover, this simple stress law is not necessarily applicable to other rock petrophysical properties i.e. permeability (Li et al., 2014), whether it was correct or not.

5.4.1 Comparison with previous studies

The results show that gas permeabilities of the analysed samples are more sensitive to the changes in confining stress than the changes in the pore pressure. This is indicated by all the determined coefficients having values less than unity (Figure 5-7). The determined values for the samples were compared with coefficients reported from previous studies. Several studies reported that coefficient χ to be less than or nearly equal to one for sandstone reservoirs (Keaney et al., 2004; Li et al., 2009, 2014; Qiao et al., 2012) as indicated in Figure 5-10. The determined coefficients for the analysed samples agree with the coefficients reported from literature for 36 samples. The coefficients are plotted against their permeability determined at different net stresses.

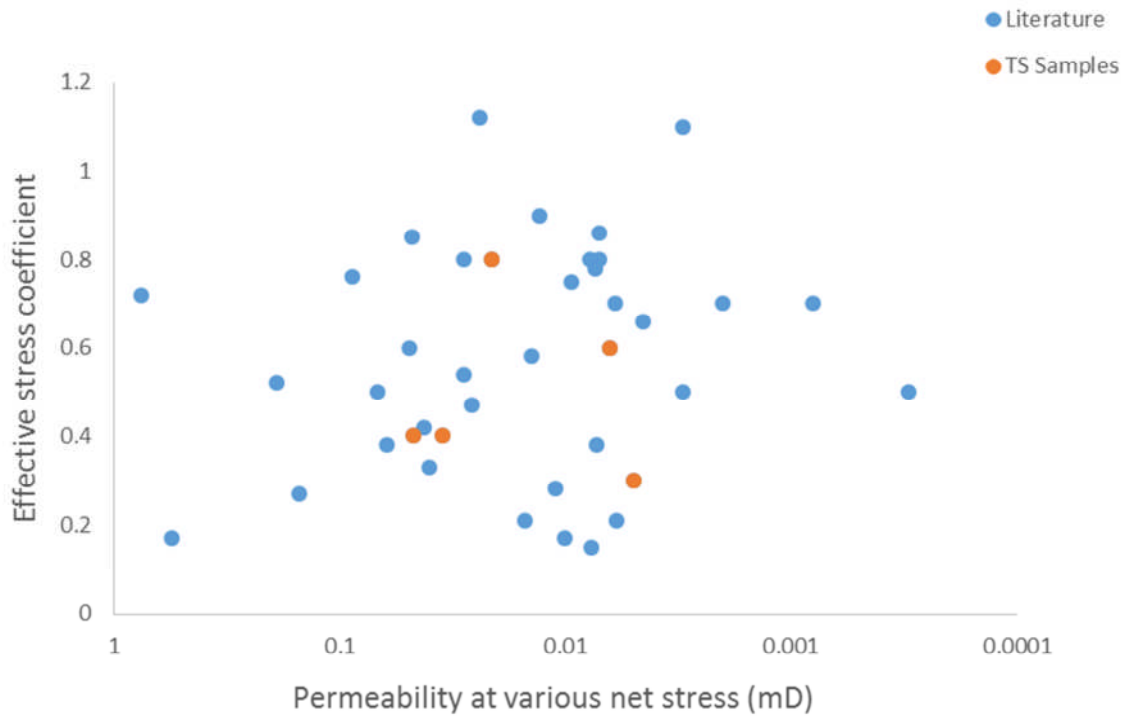


Figure 5-10: Effective stress coefficients reported from literature against their permeability measured (with 10% experimental error) at different net stresses (blue) (Keaney et al., 2004; Li et al., 2009; Qiao et al., 2012; Li et al., 2014) with coefficients determined for the TS samples in group B (orange).

In contrast, several studies reported coefficients that contradict with the results. Zoback and Byerlee (1975) reported effective stress coefficients for permeability higher than unity when examined the permeability of Berea sandstone as a function of effective stress. They concluded that the effect of the pore pressure on permeability was four times higher than the effect of the confining stress. They left the sample for 15 minutes after changing the pore pressure. Walls and Nur (1979) also examined the permeability of sandstones with different clay contents under ranges of effective stress, stating that effective stress coefficient for permeability can be as high as 7 for samples with 20% clay. They used distilled water as the pore fluid in their experiments; they also did not leave much time for equilibration between pressure steps. A recent study by Al-Wardy and Zimmerman (2004) showed effective stress coefficients greater than 2 when examined the permeability of clay-rich sandstones using 5% NaCl brine as the pore fluid. It was reported that samples were left for only few minutes to equilibrate. This might not be sufficient time for the clay-rich sandstone samples to reach equilibrium.

5.4.2 Models for effective stress coefficient

5.4.2.1 Clay shell model

Zoback and Byerlee (1975) proposed a microstructural model for sand with clay “clay shell model”. This model states that high compressible clay is uniformly lining the pore wall, which is surrounded by the stiffer quartz framework (Figure 5-11 - left). Hence, if both confining stress and pore pressure were increased by the same amount, the pore pressure effect will be higher as it expands the flow path by compressing the clay further. This results in more sensitivity of permeability to the change in pore pressure, which led to effective-stress coefficients of 3 to 4. However, clay has to be completely impermeable meaning no fluid can penetrate the micropores of the clay in order for an increase in pore pressure to result in its compaction against the pore walls. SEM image of sample TS5-5 shows the pore space at the center of the clay particles surrounded by stiffer quartz grains (Figure 5-12). Fluid in the pore would penetrate the micropores and micro fluid-paths present in the clay rather than compacting and pressing the clay particles against the pore walls, which contradicts with the model. Thus, the results of the analysed samples do not agree with the model. Li et al. (2009) suggested the presence of organic matter, as an example, saturating the micropores of the clay and preventing the fluid of penetrating into the micropores for the clay to be totally compressed by the fluid in order to have coefficients higher than 1.

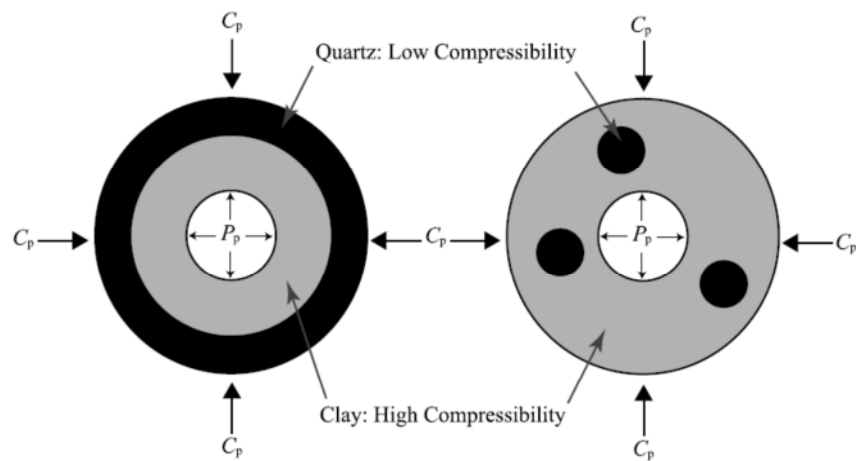


Figure 5-11: Left: Simplified pore model developed by Zoback and Byerlee (1975) for $\chi > 1$ with low compressible quartz frame (black) and high compressible clay (grey) lining the pore walls shown in white. Right: Model proposed by Kwon et al (2001) for $\chi < 1$ with low compressible quartz shown in black and more compressible clay as connected matrix in grey. C_p is confining pressure (from Heller et al., 2014).

On the other hand, experiments by Kwon et al. (2001) showed that the coefficients for permeability measured for the Wilcox shale were less than or equal to 1. They proposed a model in which the compressible clays form a connected matrix surrounding the pore with some stiffer quartz particles within the matrix (Figure 5-11 - right). The results agree with the coefficients reported by Kwon et al. (2001); however, their model assumes the clay to be so compressible and compliant with no fluid penetrate into the micropores of the clay as well. Thus their model better describes shale rather than tight sandstones.

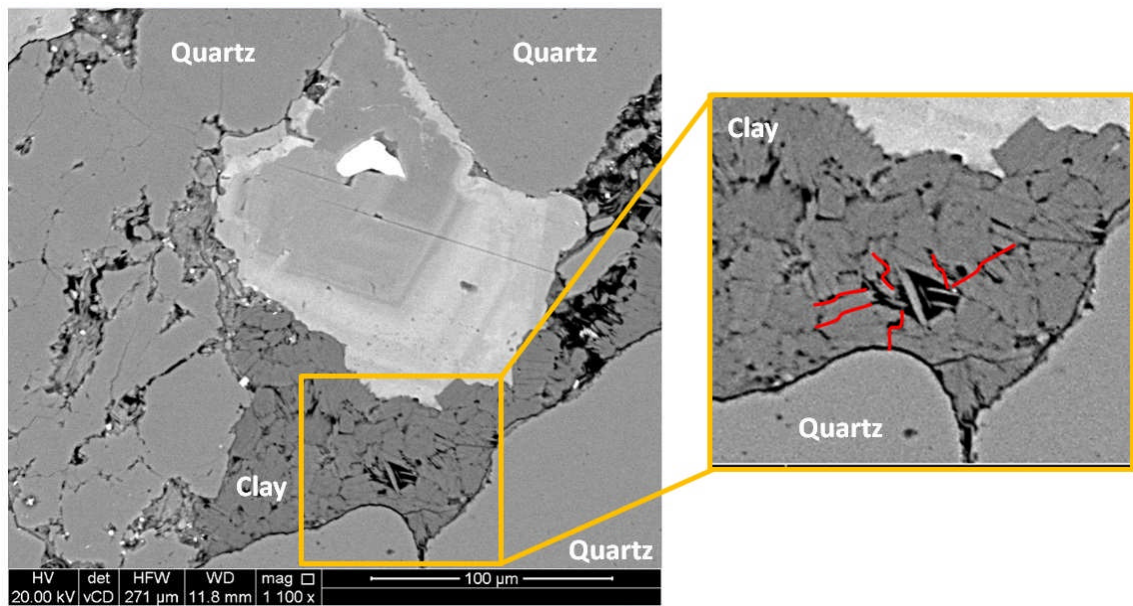


Figure 5-12: SEM image showing the clay surrounded by stiffer quartz grains with pore space at the center of the clay (black) with micropores and micro fluid paths (red) through which the gas penetrate the clay in sample TS5-5.

5.4.2.2 Clay particle model

Al-Wardy and Zimmerman (2004) developed a “clay particle” model to support their results. The clay in this model is present in the pore space as particles that are connected tangentially to the pore wall, which is surrounded by the quartz framework (Figure 5-13). The increase in confining stress will act on the outer stiffer framework with no effect on the clay in the pore space. Moreover, increasing the pore pressure would cause a uniform hydrostatic compression on the clay particle, which results in expanding the pore wall radially in a similar way as a clay-free situation. This indicates the clay particle will contract uniformly irrespective of the shape of the particle, which requires the clay to be so compliant with no micropores. SEM image for sample TS7-1 shows clay particles filling the pore spaces and tangentially attached to the pore wall (Figure 5-14). Gas flow through the sample will flow around the clay particles and penetrate their micropores as the pore pressure increases rather than simply compressing the clay as proposed.

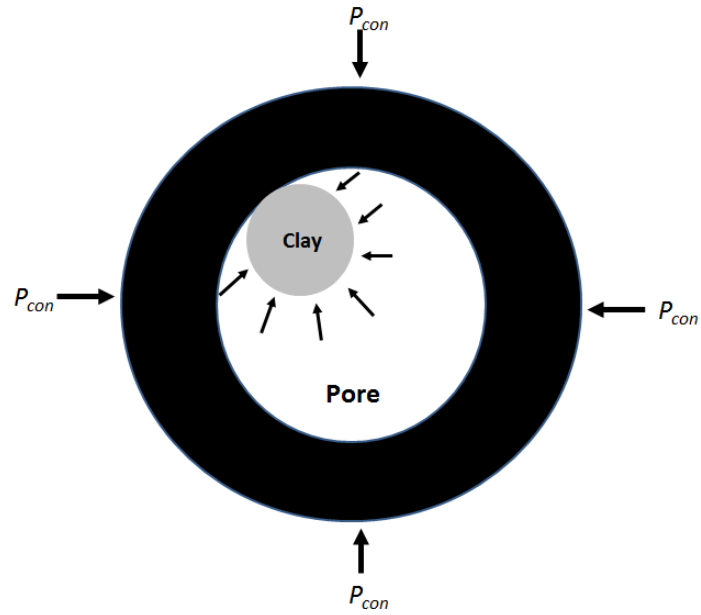


Figure 5-13: Clay particle model showing the clay tangentially connected to the pore wall that is surrounded by the stiffer quartz (from Al-Wardy and Zimmerman, 2004).

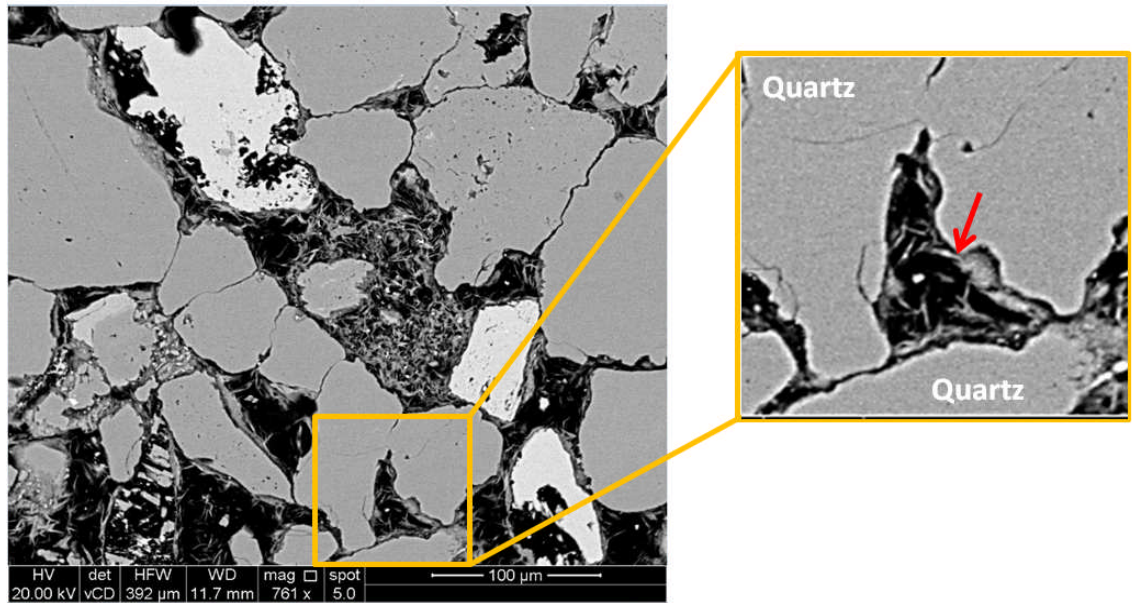


Figure 5-14: SEM image showing the clay (red) with micropores (black) surrounded by stiffer quartz grains. Micropores of the clay particles (black) through which the gas penetrates the clay in sample TS7-1.

Moreover, significantly high compressibility ratio for clay assemblages with at least a stiffness ratio for clay to quartz of 20:1 is required to explain the model. They supported their results with earlier studies reporting clay to quartz stiffness ratio of 25:1 (Mavko et al., 1998; Farber et al., 2001). However, many studies in the literature

reported bulk modulus for clay larger than 6 GPa. Berge and Berryman (1995) derived theoretically bulk modulus in the range of 10-12 GPa for clay. Coyner (1984) also noted that clay particles have the same rigidity as the silicate crystals. Prasad et al. (2002) measured Young's modulus for dickite which has a similar structure and mineralogy as kaolinite to be 6.2 GPa. Vanorio et al. (2003) presented the measurements of the bulk modulus for solid clay to be between 6 and 12 GPa. Other studies reported even higher bulk modulus for clay reaching 50 GPa (Katahara, 1996; Wang et al., 2001). The stiffness ratio for clay to quartz then will fall between 1:3 and 1:6 with measured bulk modulus for clay (6 to 12 GPa) and using 37 GPa as the modulus for quartz (Mavko et al., 1998). The bulk moduli of the quartz and total clay were calculated based on the volume fraction of quartz and the clay present in each sample, which was determined from QXRD data (Table 3-2) using Equation 5-8. The low determined clay to quartz stiffness ratio for the samples (Table 5-9) are in agreement with the studies indicating low compressibility of the clay, which contradicts with the high clay-quartz stiffness ratio required to validate the model of Al-Wardy and Zimmerman (2004). This low stiffness ratio range supports the lower than unity coefficients determined for the tight samples. The analysed samples are composed mainly of quartz with approximately 10-15% clay. Yet, none of the abovementioned models describes the samples.

5.4.3 Biot coefficient and the elastic static and dynamic moduli

Biot coefficients were determined to be compared with the effective stress coefficients for permeability. The Biot coefficients determined from the dynamic bulk moduli calculated from the density and the compressional and shear velocities (Equation 5-7). Static elastic moduli were not measured for the samples; however, it has been reported that discrepancy will exist between measured static elastic moduli and the dynamic moduli calculated from the density and velocity data. Therefore, an empirical correlation between the static and dynamic bulk moduli in dry tight gas sandstone from the Travis Peak formation reported by Jizba (1992) is used to estimate the differences for the samples (Equation 5-9). The increase in confining stress decreases the discrepancy between the static and dynamic moduli of the samples, which is another indication of the effect of microfractures that closes at higher net stress (Figure 5-15). Simmons and Brace (1965) suggested that the disagreement between the static and dynamic moduli at low stress is caused by fractures in the rock, and the

relationship between the moduli improves at high stresses. The impact of fractures on the relationship between the dynamic and static moduli has been reported by Olsen and Fabricius (2006) showing higher differences in their fractured chalk samples (Figure 5-16). Permeability of a rock sample would be more affected by the change of the confining stress given that the bulk modulus of the sample is less than the modulus of the solid forming the rock (Kwon et al., 2001). In other words, Biot coefficients calculated for the samples at 1000 and 5000 psi stresses were all positive values, which confirm that the determined moduli of the samples were all less than the moduli of the solid forming the rocks. This agrees with the determined χ values; all less than unity.

Equation 5-9

$$K_{stat} = a + bK_{dyn}$$

where:

K_{stat} = static bulk modulus directly measured (GPa)

K_{dyn} = dynamic bulk modulus calculated from velocity and density (GPa)

a and b are fitting parameters

Values used for a and b are 0.98 and 0.49 respectively at approximately 1000 psi confining stress, and 1.85 and 0.822 for the confining stress of approximately 5000 psi (Jizba, 1992) to construct the plot in Figure 5-15.

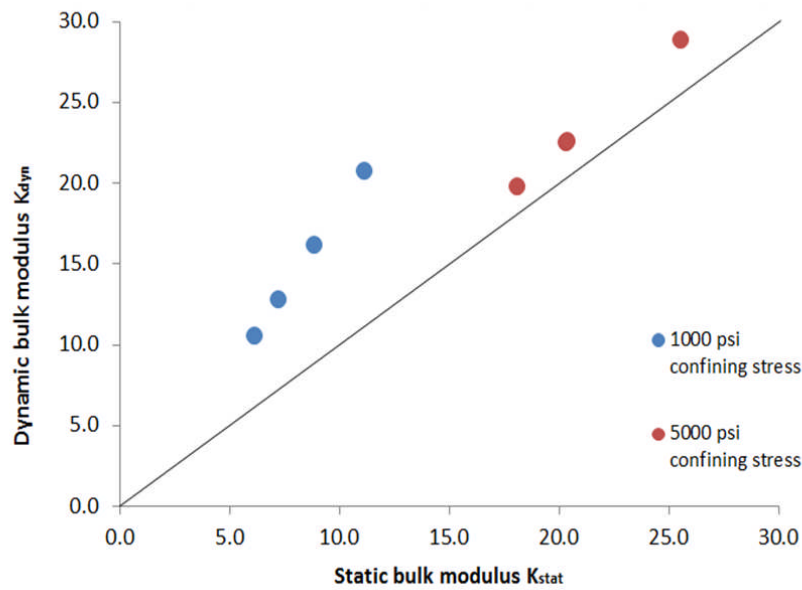


Figure 5-15: Plot of the dynamic bulk modulus K_{dyn} calculated from density and velocity at 1000 and 5000 psi ($\pm 5\%$ uncertainty) against static bulk modulus K_{stat} estimated using a correlation from tight sandstone in the Travis Peak formation for group-B samples with 1:1 line (black) (from Jizba, 1992).

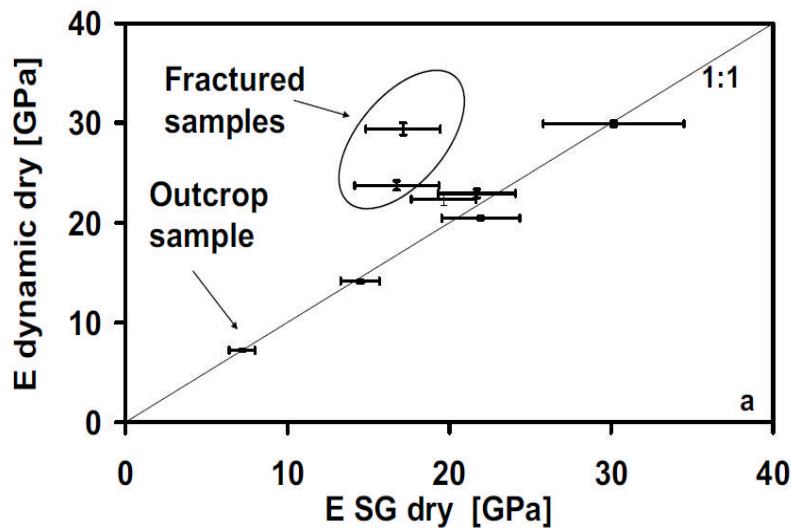


Figure 5-16: Plot showing the difference between the dynamic dry modulus against the static dry modulus of North Sea chalk with higher differences in the fractured samples (from Oslen and Fabricius, 2006).

5.4.4 Impact of equilibration time

Not leaving the samples soak long enough to equilibrate after changing the pressure and that is prior to measuring permeability produces erroneous measurements by overestimating the permeability; this leads to incorrect estimated coefficients.

According to the report of Al-Wardy and Zimmerman (2004), the samples were left only for a few minutes to equilibrate at each pressure. Zoback and Byerlee (1975) also left the Berea sandstone samples only 15 minutes to reach equilibrium after changing the pore pressure. Such equilibration time would be insufficient for the analysed low permeability clay-rich samples using the pulse-decay permeameter technique. Permeability of tight samples measured under a certain net stress shows higher value when left for only a few minutes compared to permeability measured at the same net stress but left for longer time (two hours) to equilibrate. Permeability measurements plotted against different periods of soaking time with 10% error bars is presented in Chapter 4 (Figure 4-16). Table 5-10 shows the relative error in percentage for the measured gas permeability at different net stresses with various equilibration times; the lower the permeability the longer the required equilibration time. Waiting for only five minutes for equilibration produced approximately 15% error in measured permeability compared to permeability measured after 2 hours for sample TS7-1, which has the lowest permeability in this suite of samples (Table 3-1). This is in agreement with the procedures followed by Kwon et al. (2001) who determined the coefficients for permeability for the Wilcox shale. They allowed 2-3 hours for the pore pressure to equilibrate each time the pressure was changed. The fluid pressure measured by the PDP system may not equal the actual pore pressure in the sample at first specifically after changing the pressure and significant times would be required for tight samples (Kwon et al., 2001).

	Net Stress (psi)	kg (mD)	Equilibration Time (min)	Relative Error (%)
TS5-2	5500	0.00205	5	11.8
	5500	0.00187	65	2.3
	5500	0.00186	120	1.6
	5500	0.00183	1275	0.0
TS5-5	1000	0.0247	30	2.8
	1000	0.0243	60	1.0
	1000	0.0240	120	0.0
TS7-1	4000	0.00149	5	14.6
	4000	0.00146	40	11.7
	4000	0.00137	65	4.8
	4000	0.00130	120	0.0
TS7-4	4000	0.0105	5	2.8
	4000	0.0104	30	1.5
	4000	0.0103	120	0.0
TS7-5	3000	0.00363	5	4.0
	3000	0.00356	30	2.1
	3000	0.00349	120	0

Table 5-10: Equilibration times with relative error in (%) for gas permeability k_g (mD) measured at different net stresses (psi) for the five samples in group B.

5.4.5 Impact of microfractures

The presence of microfractures makes low permeability sandstones more stress sensitive. The increase in confining stress closes most of the microcracks, where the pore pressure supports the opening of such cracks by opposing to the confining stress. The required pressure to reduce the opening of such low aspect ratio is low when the stress is normal to the walls of the openings. A complete closure of a pore with aspect ratio of a one-tenth in a porous sandstone composed of quartz grains would require a significant amount of pressure, and the more nearly spherical the pore the higher the pressure required (Walsh, 1965). Thus, the thinner the cracks, the less the confining stress is required to close them and the higher the pore pressure is required to keep them open. Figure 5-17 shows the importance of the increase in confining stress in reducing the openings of the microcracks. SEM image of sample TS7-5 (Figure 3-18) shows the abundance of microcracks, which are several microns to sub-microns in width and tens to hundreds of microns in length. The confining stress effect, simulated by the radial pressure applied at the core sample during testing, is higher than that of pore pressure opposing to keep the microcracks open, which is consistent with the effective stress coefficients lower than one. According to Bernabe (1986) the coefficient χ is a function of the aspect ratio, ϵ , of the microfractures with rough

surfaces where χ should decrease as ε increases due to confining stress increase. Increasing the confining stress closes parts of the microfractures by contacts of asperities resulting in an array of disconnected smaller fractures with high aspect ratios, which in turn reduces permeability; hence a higher effect of confining stress. SEM images of the samples show the presence of low aspect ratio microfractures having rough walls, which is consistent with the observation of Bernabe (1986).

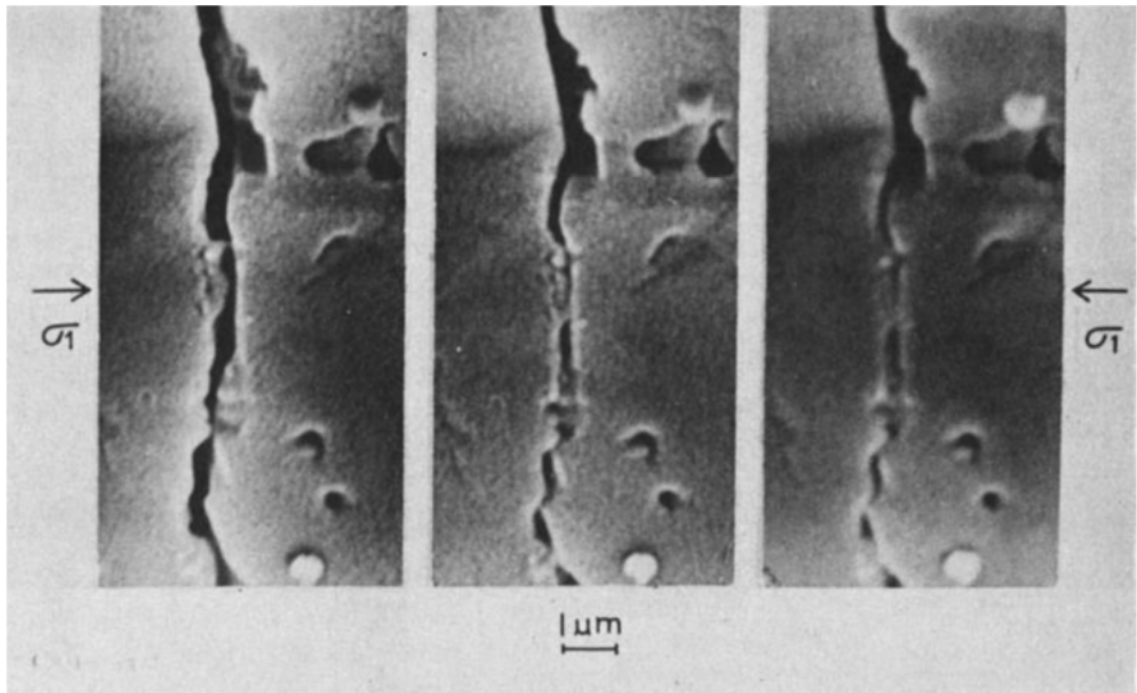


Figure 5-17: Increase in stress in the axial horizontal direction normal to the crack surfaces illustrates the closure of the crack with first image from left shows atmospheric pressure and the second and third show the closure of the opening as the stress increases to 1500 psi and 4500 psi respectively (from Batzle et al., 1980).

5.4.6 Implications for gas production

The permeabilities of the tight samples prove to be less sensitive to the decrease in the pore pressure than the change in the confining stress. Thus, it is invalid to use the simple net stress law to predict the permeability reduction during production. The analysed samples were taken from tight reservoirs at depth of approximately 15000 feet and the overburden lithostatic stress was calculated with general pressure gradient of 1 psi/ft to be 15000 psi. Using this as the confining stress for the tight reservoir with pore pressure of 10,000 and reducing to 1000 psi, permeability is plotted as a function of net stress using Terzaghi net stress and the determined effective stress model for comparison (Figure 5-18). Based on the determined effective

stress law, pore pressure decreases in tight gas sandstone resulting from production will have less effect on the permeability. Thus, applying restricted flow rate practice may not be as practical as it is to preserve the permeability that is less sensitive to the decrease in the reservoir pore pressure.

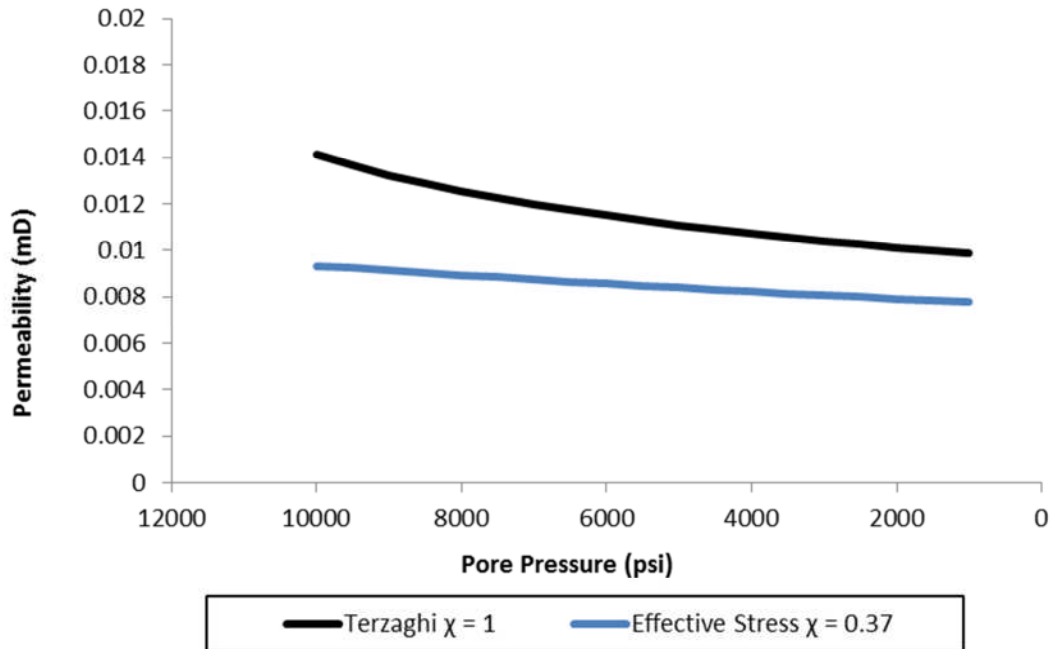


Figure 5-18: Comparison of pore pressure drop effect on permeability (with 10% uncertainty) due to production in a tight gas sandstone reservoir using Terzaghi net stress ($\chi = 1$) (black) and determined effective stress law ($\chi < 1$) (blue) for sample TS5-2.

Measuring permeability of tight rocks at *in-situ* condition that requires high pore pressure would be impossible using the steady state technique. Gas permeability was measured at higher effective stress similar to reservoir condition utilizing the maximum confining stress of 10,000 psi achieved with the high-pressure PDP equipment in the laboratory. The effective stress law determined for the samples were tested against the measured gas permeability under high net stress to cross check and validate the model. Estimated permeability from the determined power law as a function of net stress was correlated with the measured permeability at similar stress. A good correlation is shown in Figure 5-9 considering the 5-10% experimental error margin in measuring gas permeability (Li et al., 2009), which validate the determined effective stress law for the samples.

Measuring the permeability under several combinations of confining stresses and pore pressures is costly as well as time consuming. A model with random three measurements was tested to find a cost-effective way to reduce the number of measurements needed to determine the model for permeability prediction under any net stress. A minimum of 12 measurements (referred to as points hereafter) were conducted to achieve the best-fit power law model for each sample (Table 5-2). A random 3-points model with different effective stresses were examined against the determined 12-points model. After examining different combinations of several three points and comparing against the original 12-points model, a model named 1-2-3 showed the best correlation with the original 12-points model (Figure 5-19). The 1-2-3 refers to the 1st point of the 4 measurements under fixed pore pressure of 2000 psi with confining stress of 3000 psi. The second point is the point of the fixed 3000 psi pore pressure with 5000 psi confining stress, and the 3rd point is from the last 4 measurements performed under the 4000 psi pore pressure and the 7000 psi confining stress (Table 5-2).

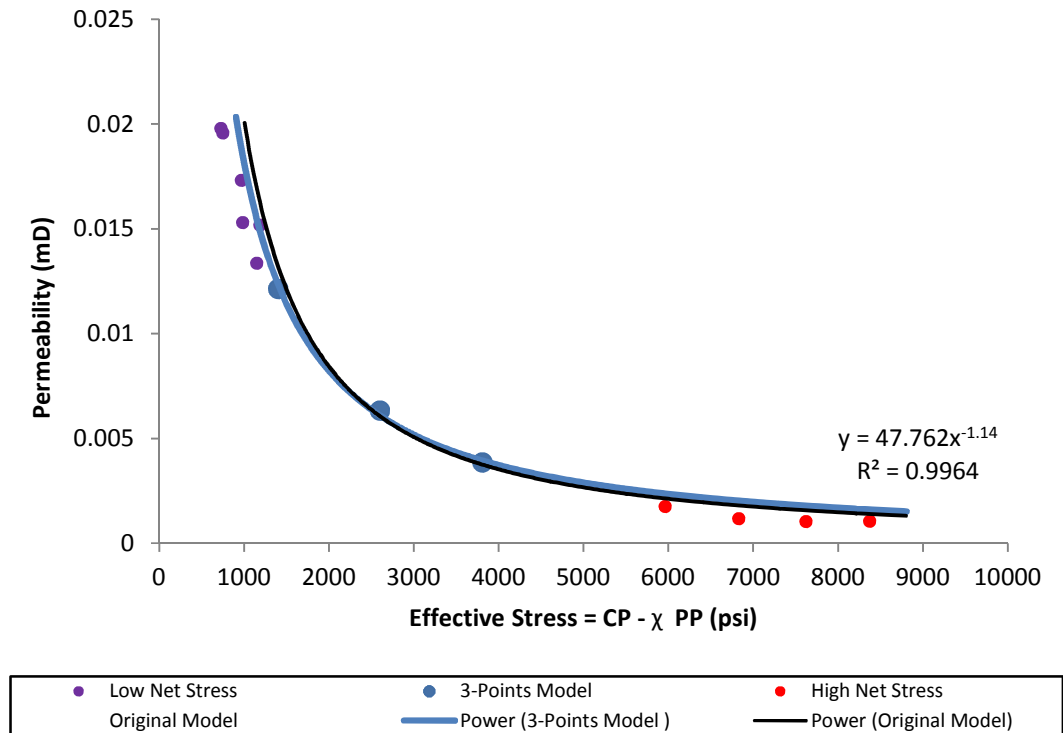


Figure 5-19: 3-Points model (blue curve) using only 3 permeability measurements (blue points) in comparison with the original 12-points model (black curve). 3-points model also correlate well with permeability measurements under low effective stress (purple points) and higher effective stress (red points).

5.4.7 Gas slippage effect

Measuring permeability under a range of effective stress using helium gas as the pore fluid would require a correction for the gas slippage effect if measured under low pore pressure. However, dealing with tight sandstone samples that are highly sensitive to the alteration in the effective stress that is changing any of the confining stress or the pore pressure, makes it practically difficult to distinguish between the effect of gas slippage and the effect of the stress dependency (Warpinski and Teufel, 1992). They indicated that Klinkenberg correction could be neglected when measuring gas permeability with pore pressure of 1000 psi or more as the compressed gas behaves more like a liquid. They reported an error of 8% when ignoring the Klinkenberg corrections at 1000 psi pore pressure, which was within the standard experimental error for their tests. To assess whether it is safe to neglect the gas slippage effects on the measurements, absolute permeability was determined under a fixed confining stress with varying pore pressures following the Klinkenberg method (Section 2.6.2).

An example of the Klinkenberg corrected permeability estimated for sample TS7-5 under 6000 psi confining stress with varying pore pressures of 2000, 3000 and 4000 psi is shown in Figure 5-20. The determined corrected permeability was approximately 0.0012 mD, which is within the range of the permeability measured (0.00112, 0.00107 and 0.0012 mD) under the different pore pressures (2000, 3000 and 4000 psi) respectively. The relative gas slippage effect is approximately 6, 10, and 0% respectively, and this is within the experimental relative error on permeability measurements. The study by Li et al. (2009) also reported less than 1% error in ignoring the Klinkenberg corrections when measuring the stress dependence of permeability under a range of effective stress for some tight sandstones samples. This value is far lower than experimental relative error on permeability measurement which is within 5 to 10% (Li et al., 2009). Thus, corrections for the gas-slippage effect in the examined samples were neglected as the lowest pore pressure used was 2000 psi that is sufficient to overcome the effect of the gas slippage.

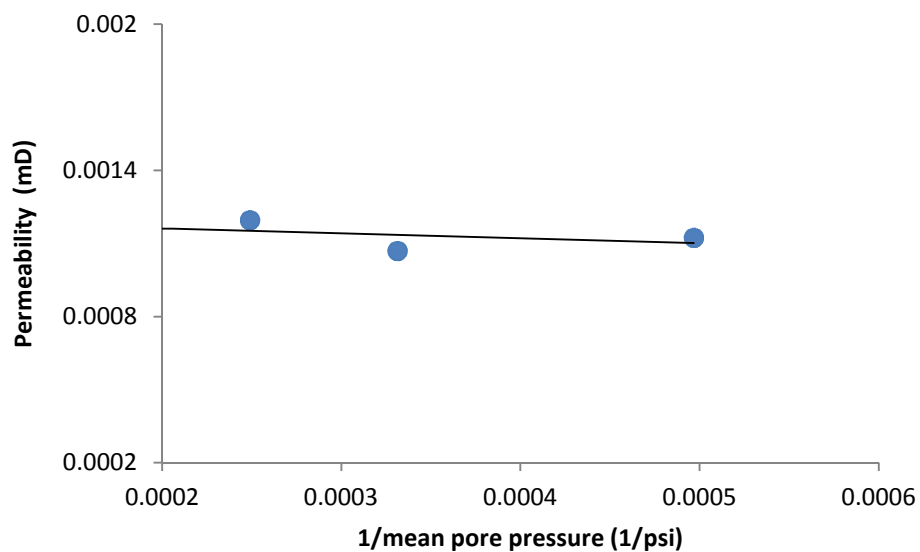


Figure 5-20: Klinkenberg corrected permeability (10% experimental error) plot for sample TS7-5 under confining stress of 6000 psi and reciprocals of pore pressures of 2000, 3000 and 4000 psi.

5.5 Conclusions

Effective stress law for permeability was determined for several samples taken from two tight gas sandstone reservoirs. All the samples showed that permeability as a

function of effective stress is following an empirically determined power law relationship with effective stress coefficients less than unity ($0.3 < \chi < 0.8$). Increasing the pore pressure generally results in permeability increase while the increase in confining stress reduced the permeability. Yet, the coefficients being lower than unity showed that permeability was more sensitive to the change in confining stress more than the pore pressure.

The analysed sandstone samples contained 10-15% clay. Yet, they did not correlate with studies reporting that sandstone samples with 10-20% clay tend to have effective stress coefficients higher than unity. Having lower than unity coefficients despite the presence of clay in the analysed samples proves that clay is not as compliant as proposed by earlier studies. On the other hand, the estimated clay to quartz stiffness ratio was between 1:2 and 1:7 for the samples, which supported the lower than unity coefficients.

Biot coefficients were calculated for the samples, and the dry dynamic bulk moduli of the rocks calculated from measured density and velocity were all less than the moduli of the solids forming the rocks. These coefficients agree with the values of χ that are lower than unity as indicated by Kwon et al. (2001). The difference between the calculated dynamic bulk moduli and static moduli estimated from a correlation from Travis Peak formation decreases with increasing the confining stress, which is another indication of the effect of microfractures that close at a higher net stress.

Equilibration "soaking" time is critical prior to the permeability measurements conducted using pulse-decay permeameter particularly for the low permeability samples. Unlike previous studies, which reported a few minutes to 15 minutes soaking time, the analysed samples were left for approximately two hours, which was the minimum time required to obtain reasonably constant measurements within less than 10% error. Not leaving the samples long enough prior to permeability measurements would result in incorrect estimations of the effective stress coefficients.

The gas flow in tight samples is affected by microcracks and low aspect ratios pores, which were observed in the SEM images of the samples. An increase in the confining stress closes most of the microcracks and thin pores having low aspect ratios, where the pore pressure supports the opening of such pores by opposing to the confining

stress. This made low permeability sandstones more sensitive to the change in the confining stress than the change in the pore pressure leading to lower than 1 effective stress coefficients.

Gas slippage is the phenomenon that needs to be corrected for when using gas as the pore fluid. However, the gas slippage effect could be neglected when using pore pressure higher than 1000 psi. A minimum of 2000 psi pore pressure was used for the samples to minimize the effect of the slippage factor and to obtain results within the experimental relative error of the permeability measurements.

Determining the effective stress law for permeability is important to evaluate independently the effect of the changes in both the confining stress and the pore pressure on the permeability of the reservoir rock during production. The less than unity coefficients determined for the tight samples indicate that the reduction in the reservoir pore pressure will reduce the permeability of the tight reservoir to a lesser extent. In comparison, the reduction in reservoir permeability would be greater if the Terzaghi stress law for permeability was used. Thus, applying restricted flow rate practices may not be as practical as it is to preserve the permeability that is less sensitive to the decrease in the reservoir pressure.

Permeability measurements were performed under a minimum of 12-points of several combinations of the confining and the pore pressures to determine the effective stress law. The law for permeability determined using the best fit technique indicated power law models for all the samples. Permeability at *in-situ* condition was estimated using the determined law and the results showed a good correlation with measured permeability at low net stresses and at *in-situ* stress. Conducting measurements at 12 points are costly and time consuming. So, a quicker and a cost-effective 3-points model was presented and tested to be a reliable way to determine the effective stress law using only 3 different combinations of confining and pore pressures.

6 Effects of Stress and Equilibration Time on Capillary Pressure Measurements and Permeability Predictions from MICP Models for Tight Gas Sandstones

6.1 Introduction

The term capillary pressure refers to the phase pressure difference between wetting and non-wetting fluids. However, within this definition it is used in two distinct ways within the petroleum industry. The first is the pressure difference that will exist between the wetting and non-wetting phases within a petroleum reservoir as a result of buoyancy forces. The second is the pressure difference between the wetting and non-wetting phase that is required to pass through a pore throat. The former can be calculated from subsurface pressure data as will be described below. The latter concept when applied to a rock with a heterogeneous pore-size distribution is generally presented as a relationship between the pressure difference between the wetting and non-wetting phases and the saturation of those phases within the rock. The two concepts are linked in that in theory it is possible to measure the relationship between capillary pressure and phase saturation of a rock sample and then use that data to predict the phase saturation within the reservoir based upon an estimate of the phase pressure difference at any position within the reservoir. Estimates of saturation are important for estimating the OGIP as well as production rates. These two different concepts surrounding capillary pressure will be discussed in more detail below. In the meantime, the main point to get over is that capillary pressure data can be very useful information that can reduce risks associated with the exploration, appraisal and production of petroleum reservoirs.

Measuring the relationship between capillary pressure and phase saturation for unconventional reservoirs can be more difficult than it is for conventional reservoirs as low permeability rocks take longer to reach capillary equilibrium. It is also the case that several commonly used experimental methods used to determine the relationship between capillary pressure and phase saturation are undertaken at low confining pressures. The use of low confining pressures is clearly worrying given the fact that

most other petrophysical properties have been shown to be very sensitive to the stress conditions under which they have been measured.

The basic aim of this chapter is to improve our understanding and measurement of capillary pressure data within tight gas sandstone reservoirs. The chapter begins by providing a more in-depth review of the meaning, use and measurement of capillary pressure data in petroleum reservoirs. In particular, it describes how capillary pressure varies within gas reservoirs and then describes and critically appraises the techniques that are commonly used for measuring the relationship between capillary pressure and phase saturation in core samples. The chapter then goes on to describe a series of experiments that have been conducted to improve our understanding of the capillary pressure measurements. These experiments concentrate on two particular aspects. First, they assess the time required to undertake capillary pressure experiments. Secondly, they assess the impact of stress on capillary pressure measurements. It is very difficult to determine the accuracy of capillary pressure measurements. In addition, an attempt has been made to assess the accuracy of measurements by evaluating their consistency with other data. In particular, the chapter assesses the consistency of capillary pressure and permeability data using well established theoretical and empirical relationships between these data types.

6.1.1 Reservoir scale capillary pressure

Low permeability, water-wet reservoirs that have small pores and pore throats tend to hold greater amount of water due to the capillary forces compared with porous and permeable reservoirs. The fraction of the water filling the pore spaces, which cannot be displaced by the hydrocarbons, is referred to as the irreducible water saturation (Schowalter, 1979). It is not an easy task to define the irreducible water saturation for rocks with micro-Darcy permeability (Byrnes, 2005). Tight reservoirs require higher hydrocarbon columns above the free water level to overcome the capillary forces, and to displace the initial water in the reservoir. Free water level, *FWL*, is defined as the level where the buoyant force (that is the result of differences in densities of water and hydrocarbons) is zero (Schowalter, 1979), and it can be indicated by the zero pressure on the capillary pressure curve obtained from a rock sample (Figure 6-1). For example, a tight sandstone reservoir with permeability of 0.001 mD would require a hydrocarbon column of approximately 50 m to begin to displace water from the pore

spaces (Byrnes, 2005). This can be illustrated on a geological structure where water tends to rise much higher above the free water level in tight sandstones with higher capillary forces in comparison with more porous and permeable or fractured reservoirs (Figure 6-1). Displacing hydrocarbon by a water drive during production is an example of imbibition (Mavko et al., 2009), where capillary forces contribute at both micro level (distribution of fluids in the pore spaces) and macro level (water flowing into high hydrocarbons saturation regions due to differences in capillary forces at the flooding front surface) (Pickell et al., 1966).

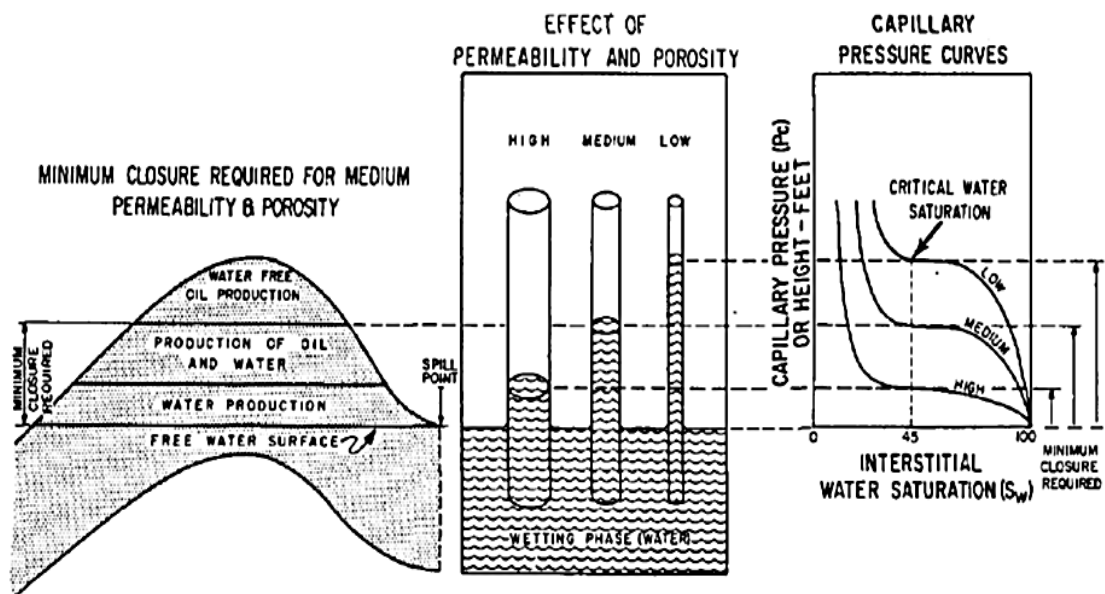


Figure 6-1: Geological structure with a minimum hydrocarbon height above free water level of rocks with different properties (from Arps, 1964).

6.1.2 Sample scale capillary pressure

Capillary pressure data can be obtained from a rock sample through several experimental methods, namely porous plate, *PP*, centrifuge, vapour sorption, and high-pressure mercury injection capillary pressure, MICP. The first three techniques use reservoir-like fluids that are brine as the wetting phase with oil or gas as the non-wetting phase. These techniques describe the capillary pressure behaviours more accurately than the mercury injection method assuming air to be the wetting phase, where in fact mercury and air are both non-wetting fluids (Newsham et al., 2004). Drainage and imbibition curves can be obtained by porous plate method, but such method is limited with the maximum capillary pressure required especially for tight sandstones (Dernaika, 2010). On the other hand, vapour sorption can be utilised to

obtain the high capillary pressure that is up to approximately 10,000 psi. Vapour sorption covers both desorption, VD , and adsorption, which are utilised to perform drainage and imbibition measurements respectively. One of the key problems for obtaining capillary pressure data for tight sandstones through porous plate and vapour sorption is that they require long equilibration times. Porous plate and vapour sorption methods have the advantage that NMR scan of the sample can be obtained after any capillary pressure measurement unlike MICP method where there is no access to the sample during or after the measurements due to mercury contamination.

In contrast, MICP is a faster, easier and cheaper method to obtain capillary pressure data (Newsham et al., 2004), which is often used as an alternative to obtain capillary pressure data. MICP curves can also be used in analysing the size and geometry of both pores and pore throats (Wardlaw and Taylor, 1976) in addition to estimating permeability (Pittman, 1992). However, the traditional MICP data is acquired at ambient conditions and thus it might result in inaccurate analyses of tight sandstones whose properties have been shown to be stress dependent. MICP data is based on Washburn (1921) formula that assumes the rock comprised of cylindrical capillaries controlling the permeability, which is not the case in tight rocks. Moreover, mercury has a high surface tension, which could also alter the microstructures of the samples by pushing and deforming the clay content.

6.1.3 Capillary pressure

A typical capillary pressure curve obtained by MICP would have an entry pressure, P_e , a displacement pressure, P_d , and a threshold pressure, P_t . All these form the initial part of the capillary pressure curve (Figure 6-2) and (Figure 6-3). The entry pressure is defined as the pressure at which the mercury conforms to the irregularities of the sample surface, and begins to enter the sample pore system (Jennings, 1987), and it is an indicative of the largest pore size (Robinson, 1966). This pressure is dependent on the sample size and its surface irregularities, which makes it difficult to determine (Pittman, 1992). It is not as important as the displacement pressure, which represents the largest pore throats of the sample. Schowalter (1979) recognized the importance of determining the displacement pressure in evaluating the seal rock. He measured the electrical conductivity during mercury injection process, and found that the

displacement pressure was in the range between 4.5 and 17%, and so the pressure at 10% mercury saturation was defined as the displacement pressure. Jennings (1987) estimated the displacement pressure by extending the slope of the plateau of the capillary pressure curve to intersect with the 0% mercury saturation as shown with the dashed line in Figure 6-2. Katz and Thompson (1986, 1987) defined the threshold pressure as the pressure at which the injected mercury forms a connected pathway through the sample. Katz and Thompson (1987) indicated that the threshold pressure occurs at the inflection point on the mercury injection plot (Figure 6-3).

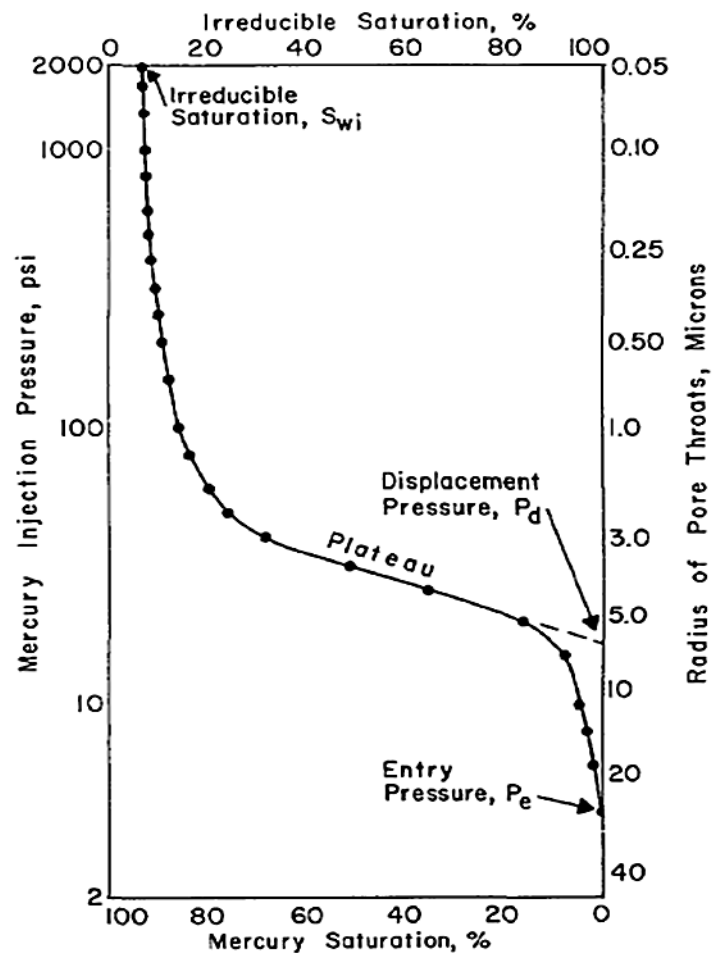


Figure 6-2: Mercury injection capillary pressure curve in a semi-log graph showing the difference between the entry pressure (P_e) and the displacement pressure (P_d) (from Jennings, 1987).

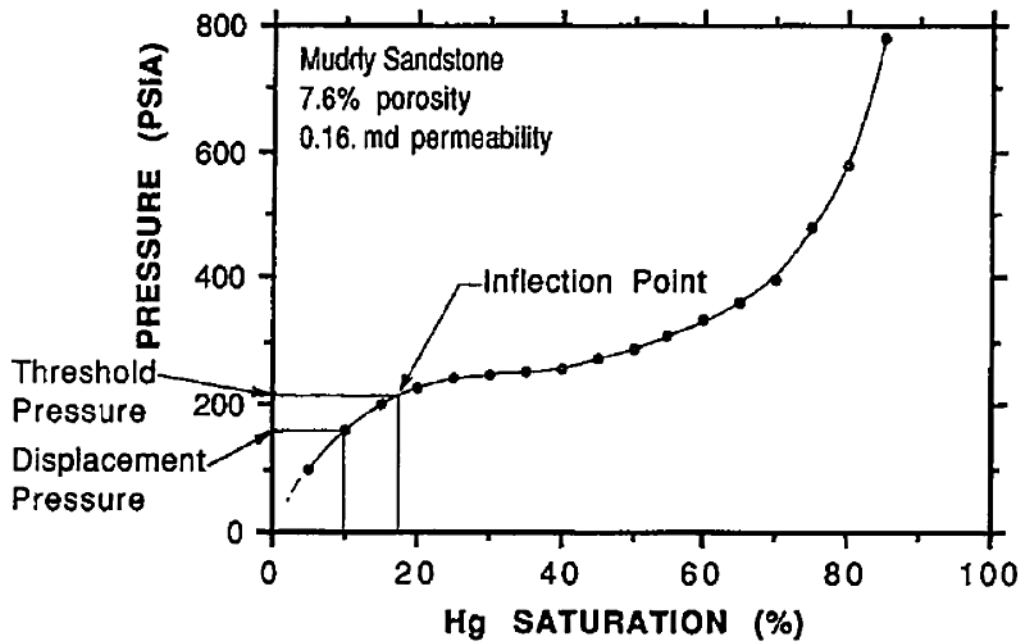


Figure 6-3: Mercury injection capillary pressure curve showing the displacement pressure at 10% mercury saturation as defined by Schowalter (1979), and the threshold pressure at the inflection point as defined by Katz and Thomson (1987) (from Pittman, 1992).

All the pressures of the capillary pressure curve represent different pore throat sizes at various capillary pressures. Katz and Thompson (1986, 1987) defined three major lengths that control the fluid flow and the electrical conductivity through the porous rocks, namely the characteristic length, L_c , the maximum hydraulic length, L_{Hmax} , and the maximum electrical conductance length, L_{Emax} . They defined L_c as the pore throat diameter representing the threshold pressure while L_{Hmax} and L_{Emax} as the effective pore throat diameters corresponding to the maximum hydraulic conductance and electrical conductance respectively. They suggested that a certain pore throat diameter that is not large enough to allow fluid to flow could be significant in conducting electricity. Comisky et al. (2007) presented the different pore throat sizes of a tight gas sandstone sample using different methods based on the relationship between the P_c and the Hg-saturation (Figure 6-4).

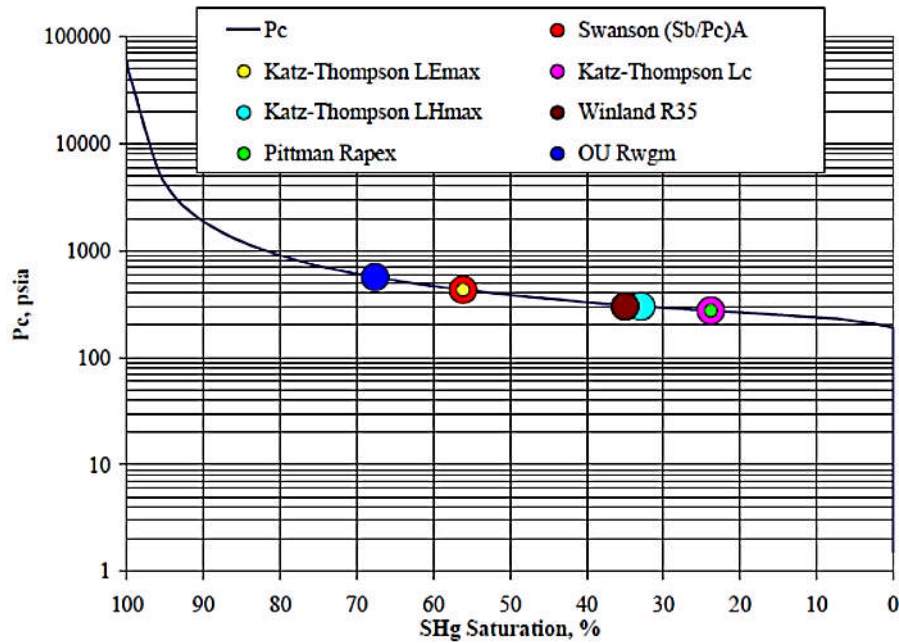


Figure 6-4: Different pore throat sizes of a tight gas sandstone sample defined by the relationship between P_c and Hg-saturation using various methods (from Comisky et al., 2007).

MICP data requires some corrections that might affect the capillary pressure data, namely a conformance and a blank corrections. Conformance correction is referred to as low-pressure end point as it appears prior to the threshold pressure where the high-pressure end point refers to the blank correction (Newsham et al., 2004). Blank correction is the result of the apparatus compressibility at very high pressure (Newsham et al., 2004). Cutting core plugs results in roughness of the outer surface of the samples due to the presence of micro pores on the surface, which must be filled with mercury prior to the pore network of the rock. This volume of mercury filling the outer irregular surface is artefact affecting the permeability estimation from MICP that is very sensitive to any change of mercury volume (Clerke, 2003). Such artefact requires the conformance correction, regularly named closure correction.

6.1.4 MICP and permeability prediction models

Washburn (1921) was the first to suggest using mercury injection to determine the pore throat size distribution in a porous media (Equation 1-13). Purcell (1949) developed an empirical model to calculate the permeability of a porous medium from the pore size distribution derived from the mercury injection capillary pressure data. His model was based on a graphical integral of mercury saturation curve versus the

reciprocal capillary pressure squared, (Equation 6-1). He considered that the rock comprised of bundles of capillaries where the flow along the capillaries depends on the diameter of the capillaries. Purcell (1949) used an empirical lithology factor $f = 0.216$ to account for the rock tortuosity for the rock samples. A new study by Comisky et al. (2007) suggested using a reduced value of $f = 0.15$ to improve the fitting for samples with low permeability.

Equation 6-1

$$k = 14254 f \phi \int_0^{100} \frac{d(S_{Hg})}{P_c^2}$$

Where:

k = permeability (mD)

f = Purcell lithology factor (0.216)

ϕ = fractional porosity

P_c = capillary pressure (psi)

S_{Hg} = mercury saturation (%)

Thomeer (1960) plotted the mercury injection capillary pressure data on log-log plot and observed that data could be represented by a hyperbola. He related empirically the hyperbolic function to air permeability based on the location and shape of the capillary pressure curve. Such curve can be defined by three parameters, the extrapolated displacement pressure, P_d , the fractional bulk volume occupied by mercury at infinite pressure, $Vb_{p\infty}$, and a pore geometrical factor, G , which is related to the degree of sorting and interconnection of the pores (Figure 6-5). Thomeer hyperbolas with different pore geometrical factors show that the larger the number the poorer the sorting of the rock, and the smaller the number the better the quality (Figure 6-6). The displacement pressure is a function of the pore throat size. So the higher the displacement pressure, the smaller the pore size is and the lower the permeability. Thus, the shape of the MICP curves can indicate the heterogeneity and the pore size distribution of the sample as presented by Thomeer (1960). A more homogenous sample with better permeability would have a flat plateau as discussed by Schowalter (1979) (Figure 6-7 – left), which is not the case with the tight heterogeneous samples that are more similar to the curve in Figure 6-7 (right).

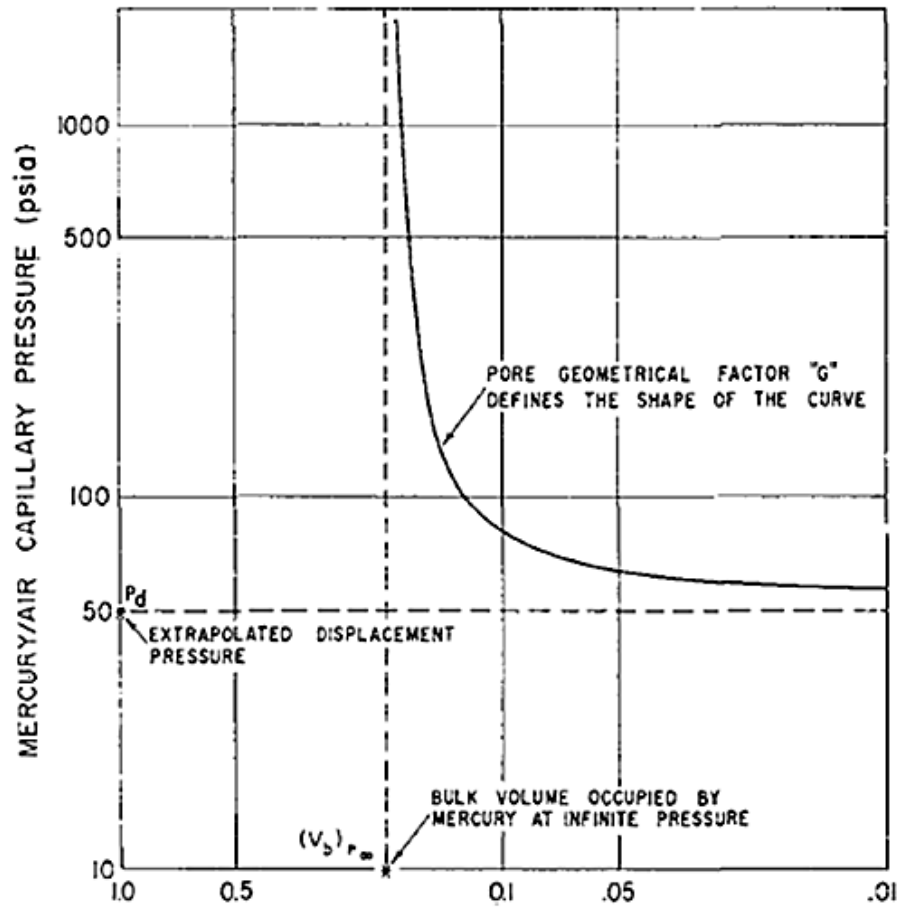


Figure 6-5: Thomeer parameters (extrapolated displacement pressure, bulk volume occupied by mercury at infinite pressure and the pore geometrical factor) defining the shape of the hyperbola representing the mercury injection capillary pressure curve (from Thomeer, 1960).

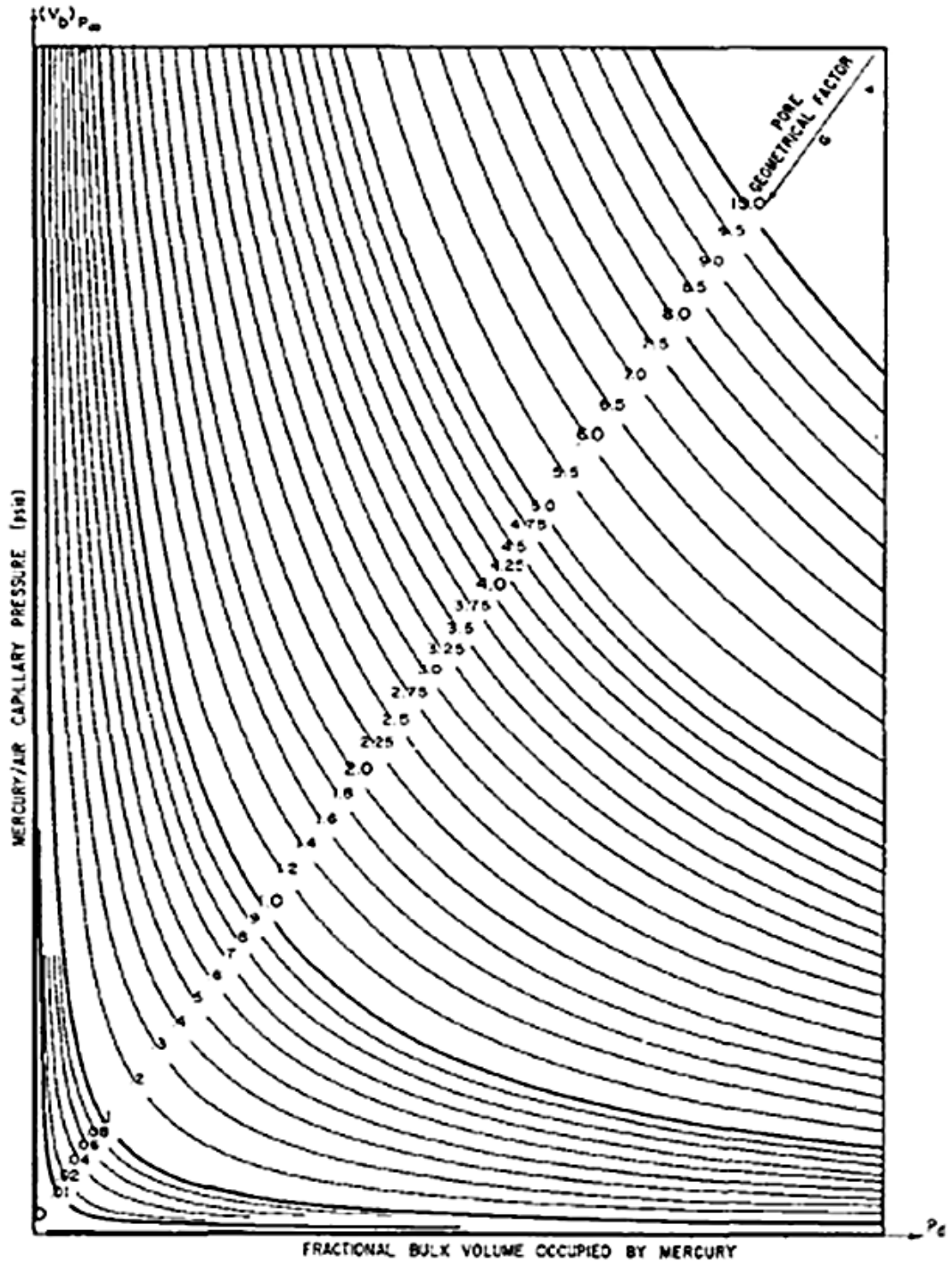


Figure 6-6: Thomeer hyperbola showing different pore geometrical factors (G) (from Thomeer, 1960).

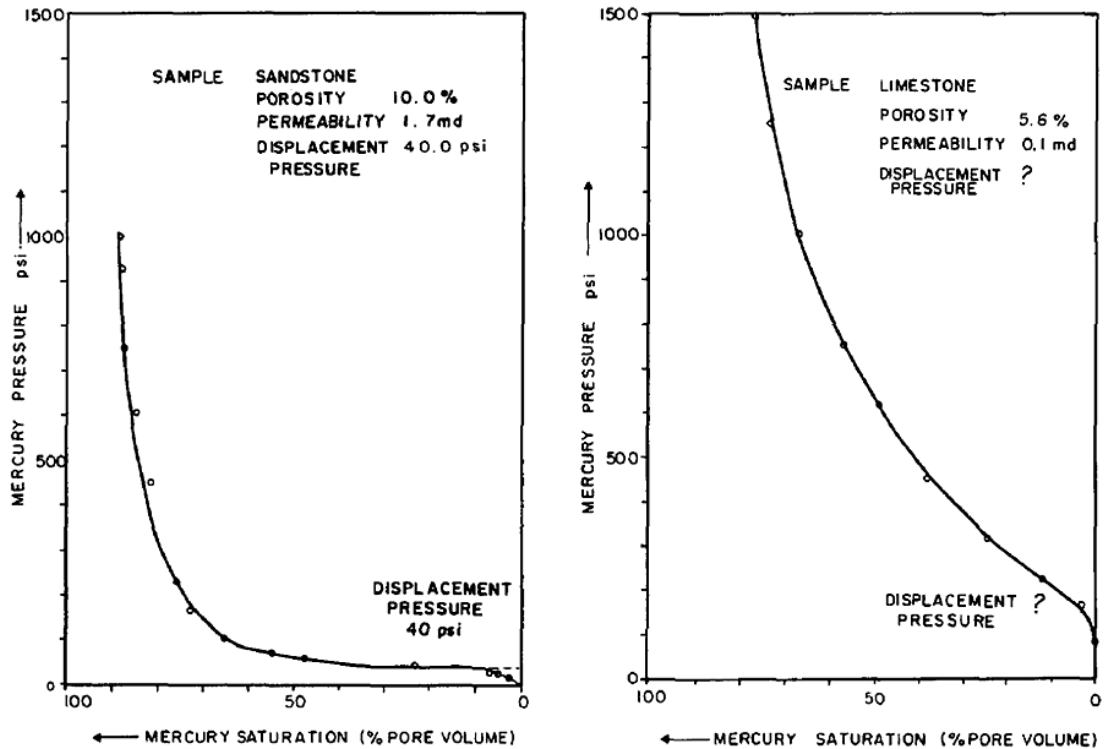


Figure 6-7: MICP curve with plateau for a porous permeable sample (left) in comparison with a less porous less permeable sample with no plateau (right) (from Schowalter, 1979).

Swanson (1981) expressed empirically the relationship between air permeability and the hyperbola of the mercury injection capillary pressure curve in log-log plot (Equation 6-2). According to Swanson (1981), the apex of such hyperbolic log-log curve corresponds to the minimum capillary pressure at which the pore sizes are effectively interconnected (Figure 6-8).

Equation 6-2

$$k_{air} = 339 \left(\frac{S_{Hg}}{P_c} \right)_{apex}^{1.691}$$

where:

k_{air} = air permeability (mD)

S_{Hg} = bulk volume mercury saturation (%)

P_c = capillary pressure (psi) corresponding to the apex of the hyperbolic log-log mercury injection plot

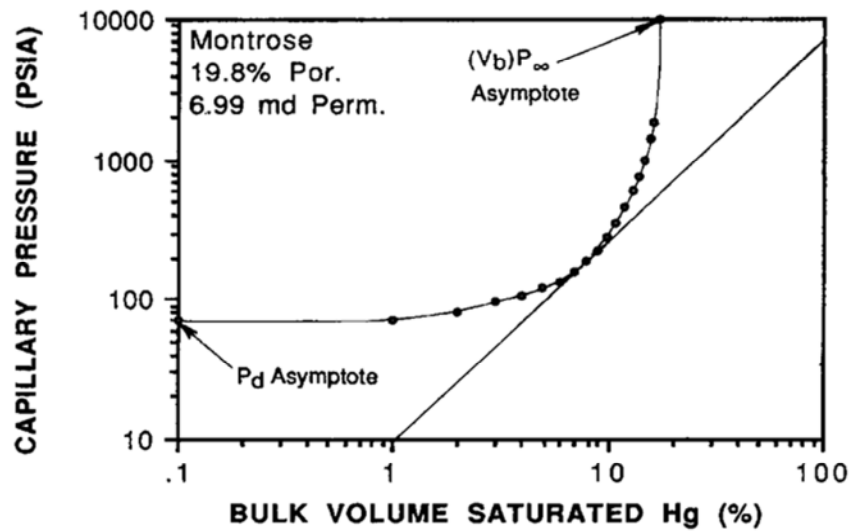


Figure 6-8: Log-log plot of capillary pressure against Hg saturation following Thomeer's method (1960) with a 45° tangent line to determine the apex Swanson (1981) (from Pittman, 1992).

Katz and Thompson (1986, 1987) introduced a model based on percolation theory for the relationship between the pore size derived from mercury injection and air permeability with no fitting parameters (Equation 6-3). The conductivity ratio could be determined by measuring the rock and formation water conductivity. They also presented a formula to derive the conductivity ratio from the length scales (Equation 6-4) where $S_{L_{Emax}}$ is the fraction of the connected pore space that are filled with mercury at the maximum electrical conductance.

Equation 6-3

$$k = \frac{1}{226} L_c^2 \left(\frac{C}{C_o} \right)$$

Equation 6-4

$$\left(\frac{C}{C_o} \right) = \left(\frac{L_{Emax}}{L_c} \right) \Phi S_{L_{Emax}}$$

Where:

k = air permeability (mD)

L_c = pore size diameter (μm) at threshold pressure

C/C_o = formation conductivity factor that is ratio of rock conductivity to formation water conductivity

H. D. Winland, while working for Amoco Production Company, developed an empirical relationship between porosity, air permeability and the pore throat radius at 35% mercury saturation, r_{35} , for 82 sandstone and carbonate samples (Kolodzie, 1980). Winland proposed several regressions ran at different percentiles with the 35th percentile showing the best correlation. The relationship was published by Kolodzie (1980) (Equation 6-5).

Equation 6-5

$$\log r_{35} = 0.732 + 0.588 \log k_{air} - 0.864 \log \phi$$

where:

r_{35} = pore aperture radius corresponding to a mercury saturation of 35%

k_{air} = air permeability (mD)

ϕ = porosity (%)

Pittman (1992) introduced a series of equations from multi-regression analyses of mercury injection data with porosity and air permeability for sandstone samples. His analyse was an extension of Winland's work, and he proposed several equations at different mercury saturations with the best R-squared at the 25th percentile of Hg saturation (Equation 6-6). Rezaee et al. (2006) followed the same process and conducted regression analysis for a set of 144 carbonate samples, and they suggested the best permeability prediction could be acquired from the 50th percentile, r_{50} , that is the pore throat radii corresponding to 50% mercury saturation. Unlike normal sandstones, r_{10} was recommended as the best permeability predictor from MICP data for tight gas sandstones samples with dominant pore throat radii in the range of 0.1 and 1 μm (Rezaee et al., 2011).

Equation 6-6

$$\log k_{air} = -1.221 + 1.415 \log \phi + 1.512 \log r_{25}$$

6.2 Methodology

The relationship between phase saturation and capillary pressure was determined for the third suite of tight samples using a wide range of techniques that are described in Section 2.15. These methods fall into two broad groups – air-brine measurements and mercury injection capillary pressure (MICP) tests. Description of the samples is

presented in Section 2.2, and the samples preparation is described in details in Section 2.3. Permeability estimated from different MICP models were correlated with gas permeability measured at ambient condition and at stress equivalent to the threshold pressures of the samples to analyse the impact of stress on samples prior to mercury entering the pore system. To further assess the stress dependency of the mercury injection capillary pressure, capillary pressure curves and pore size distributions acquired from both MICP and stressed MICP were also compared.

6.2.1 Air-brine capillary pressure tests

Air-brine capillary pressure data was obtained using the porous plate and the vapour desorption in the humidity chamber techniques which are described in Sections 2.15.1.1 and 2.15.1.2 respectively.

6.2.2 Mercury injection capillary pressure

The two tests used for mercury injection capillary pressure are referred to as MICP and PUCS respectively, which are described in Sections 2.15.2 and 2.15.2.2.

6.2.3 Estimating permeability from MICP measurements

Permeability, k_{air} , was estimated for the samples using several MICP models that are Equation 6-1 (Purcell, 1949), Winland expression that is Equation 6-5 (Kolodzie, 1980); (Thomeer, 1980) and Equation 6-2 (Swanson, 1981). The estimated permeabilities from these models were correlated with gas permeabilities measured at different stresses for all samples. Method of measuring gas permeability is described in Section 2.6.

6.2.4 Nuclear magnetic resonance measurements

Samples were scanned with NMR to obtain the water saturation after each capillary pressure using *PP* and *VD* methods. Description of the technique and the procedures followed to obtain NMR is described in Section 2.14.

6.3 Results

6.3.1 Porous plate and vapour desorption

6.3.1.1 Capillary pressure drainage curves from porous plate and vapour desorption

Capillary pressure measurements obtained from porous plate that is limited to 130 psi were combined with vapour desorption measurements that start at 1660 psi.

Figure 6-9 shows the water saturations plotted against the capillary pressure from *PP* (lower part in the graph) and from *VD* (upper part of the graph) in a semi-log plot. The water drainage process appeared to be continuous between the upper pressure limit of the porous plate and the lower pressure limit of the vapour desorption as shown in the plot. Samples showed a wide range of water drainage at 130 psi where water saturation decreased from fully saturated that is at ambient pressure to a range of approximately 77% to less than 35% water saturation. The increase in capillary pressure in the *VD* chamber resulted in further reduction in water saturations. Total reduction in S_w ranged from less than 50% for sample with gas permeability around 0.002 mD up to less than 10% water saturation for samples with gas permeability of around 0.1 mD.

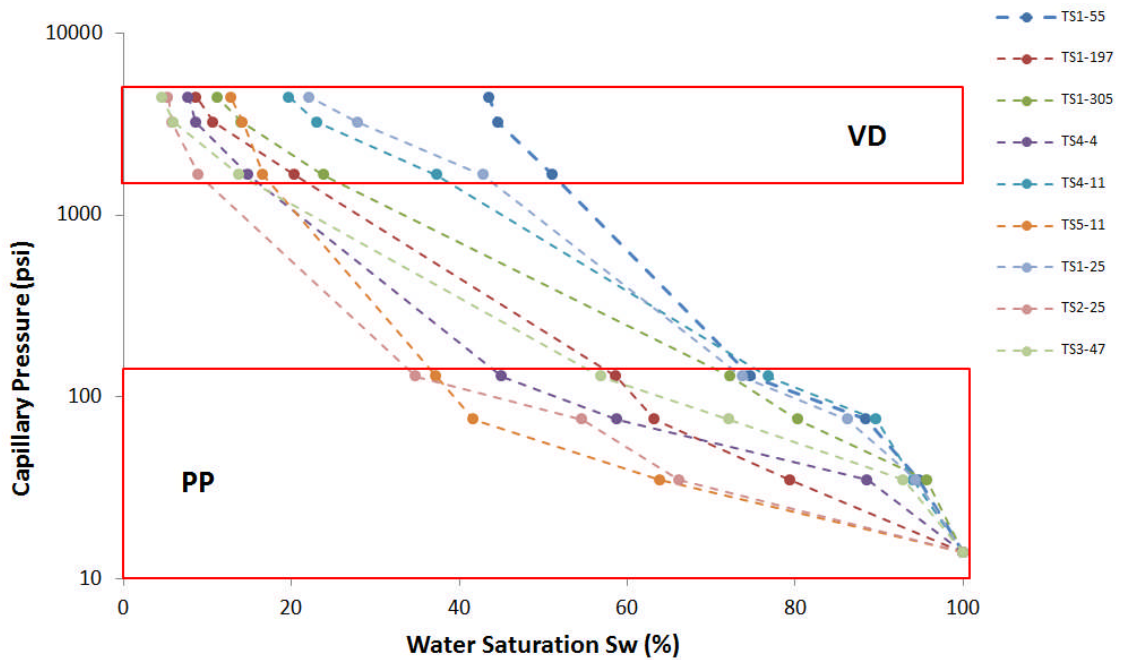


Figure 6-9: Capillary pressure (psi) against water saturation percentage data combined from porous plate *PP* (the lower part) and vapour desorption *VD* (the upper part) for the nine samples in group C.

6.3.1.2 Water saturation vs. equilibration time in porous plate

Capillary pressure data obtained from porous plate for all samples are shown in Table 6-1. Water saturations of all samples were between 64 and 96% after 17 days equilibration time at 35 psi. More water was drained as the pressure was increased to 75 psi, where the water saturations ranged between 42 and 90% after 17 days. Further water was drained at the next higher pressure of 130 psi. Saturations at this pressure

were in the range of 35 and 77% after 19 days. Water drainage appeared to be the highest for samples with the highest permeability, which are samples TS5-11 and TS2-25 as shown in Figure 6-9.

Sample	Pc = 35 psi	Pc = 75 psi	Pc = 130 psi
	Equilibration Time = 17 days	Equilibration Time = 17 days	Equilibration Time = 19 days
	Sw (%)	Sw (%)	Sw (%)
TS1-55	94.8	88.4	74.7
TS1-197	79.3	63.3	58.7
TS1-305	95.6	80.3	72.3
TS4-4	88.6	58.8	45.1
TS4-11	94.0	89.7	76.8
TS5-11	63.9	41.7	37.3
TS1-25	94.4	86.2	73.7
TS2-25	66.2	54.6	34.9
TS3-47	92.9	72.1	56.8

Table 6-1: Water saturation (%) and equilibration time (days) for the group-C samples at the three different pressures 35, 75 and 130 psi used in the porous plate method.

6.3.1.3 Water saturation vs. equilibration time in vapour desorption

Water saturations were monitored by weighing the samples constantly to ensure maximum drainage is achieved at each capillary pressure. Water saturations at every pressure (1660, 3236 and 4443 psi) in the vapour desorption chamber were plotted against the equilibration time in days to show the change in the water drainage. All the samples took up to approximately 40 to 50 days at 1660 psi until they showed nearly constant water saturations indicating no more water was drained (Figure 6-10). Samples were left for another month to maximise the drainage process at this pressure and before placed at the next higher capillary pressure of 3236 psi. The reduction in the water saturation at 3236 psi varied between the samples at the first month where several samples displayed obvious further saturation reductions while others showed minimum water drainage (Figure 6-11). Sample TS5-11 and TS2-25 showed water saturations nearly similar to their saturations from the previous capillary pressure. Samples were left for another 60 days for optimum water drainage even though there was no more obvious drop in the weights of the samples and hence no more change in water saturations.

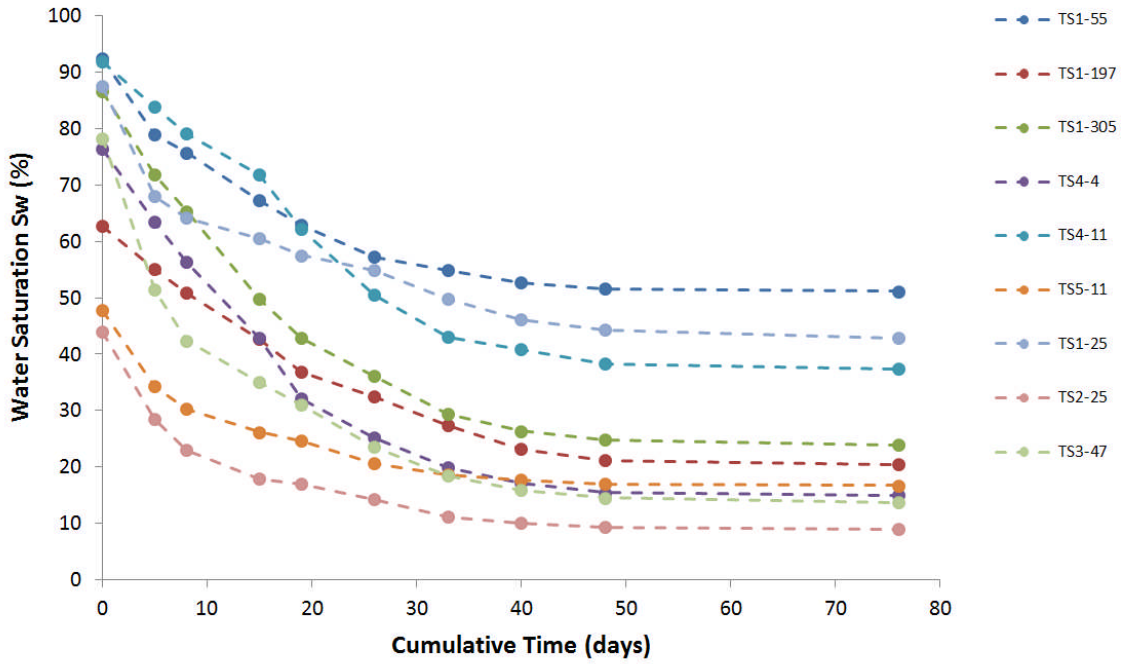


Figure 6-10: Water saturation S_w (%) against cumulative equilibration time (days) at 1660 psi capillary pressure in the vapour desorption chamber for group-C samples.

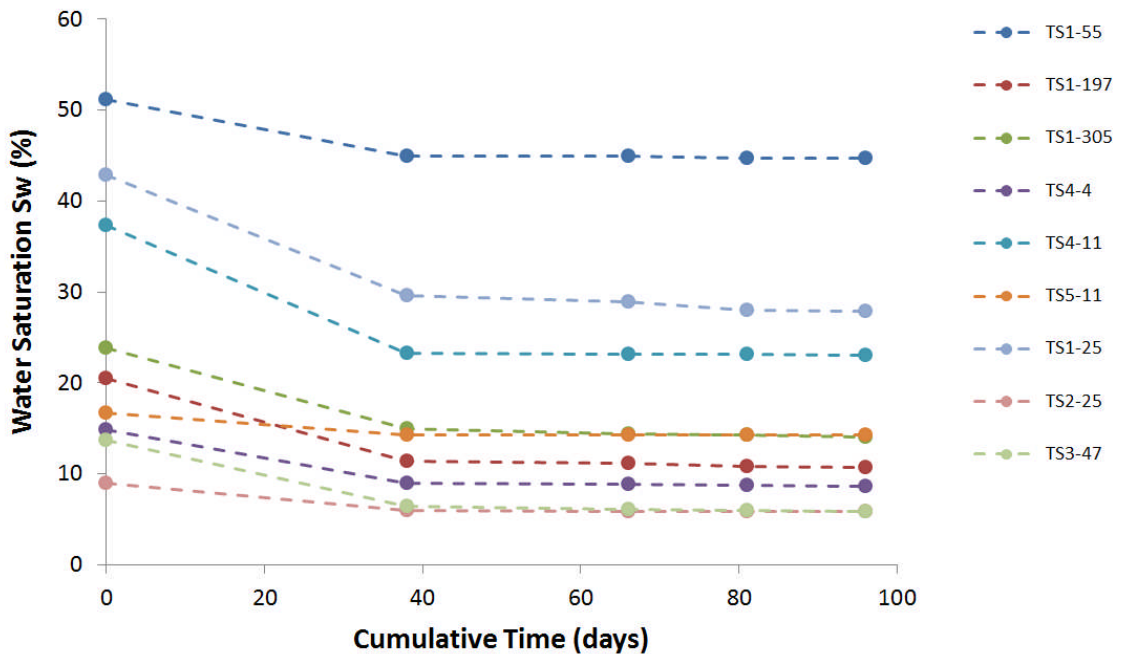


Figure 6-11: Water saturation S_w (%) against cumulative equilibration time (days) at 3236 psi capillary pressure in the vapour desorption chamber for group-C samples.

Samples were then placed into the VD chamber with the next higher pressure of 4443 psi. Several samples showed a slight further decrease in water saturation within the

first two months at this capillary pressure (Figure 6-12). Samples TS1-305, TS4-11 and TS1-25 showed greater reductions in the water saturation compared to the remaining samples some of which appeared to be at constant saturations from the previous pressure. Samples were left for approximately eight more months to maximise the drainage and ensure equilibrium was reached. Yet, no obvious reduction in S_w was noticed in all samples after this long period. A plot of the water saturation against the cumulative square root of time in days to show the entire equilibration time for the three capillary pressures used in the vapour desorption chamber is shown in Figure 6-13. All samples appeared to have constant water saturations over the entire range of the capillary pressures after approximately 250 days.

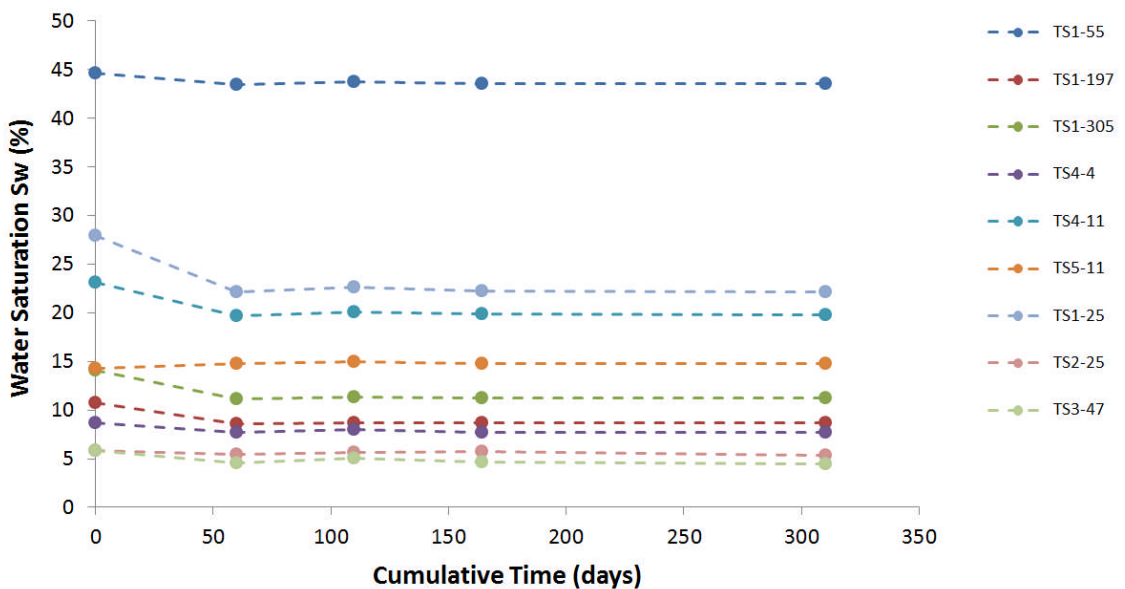


Figure 6-12: Water saturation S_w (%) against cumulative equilibration time (days) at 4443 psi capillary pressure in the vapour desorption chamber for group-C samples.

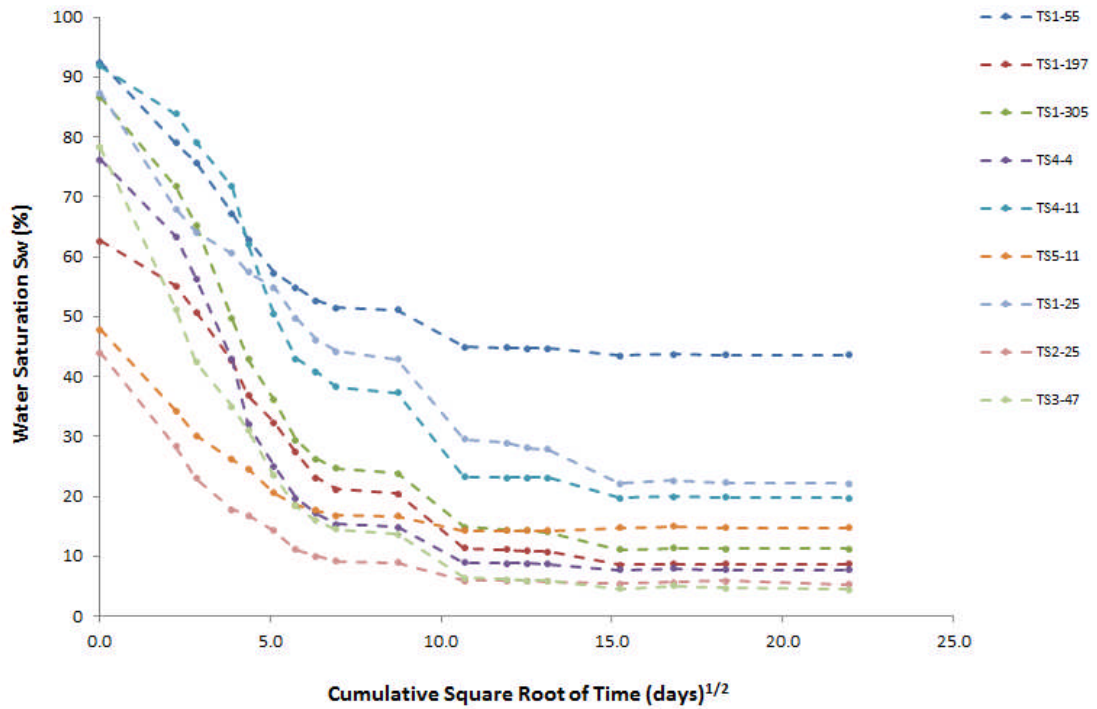


Figure 6-13: Water saturation S_w (%) against cumulative square root of equilibration time $(\text{days})^{1/2}$ for all the capillary pressures 1660, 3236 and 4443 psi in the vapour desorption chamber for group-C samples.

6.3.2 NMR

The normalized and cumulative NMR signals show the relaxation time T_2 distribution of one of the samples at different capillary pressures using *PP* and *VD* (Figure 6-14) and (Figure 6-15), respectively. The peak of the T_2 distribution shown in Figure 6-14 at 100% water saturation is about 8 ms. The peak of the normalized T_2 signal was shifted to the left after each capillary pressure increment indicating that water was drained from the larger pores with remaining water trapped only in smaller pores. The peak of T_2 is 1 ms after the drainage process at capillary pressure of 3236 psi, which corresponded to smaller pore size holding the remaining water.

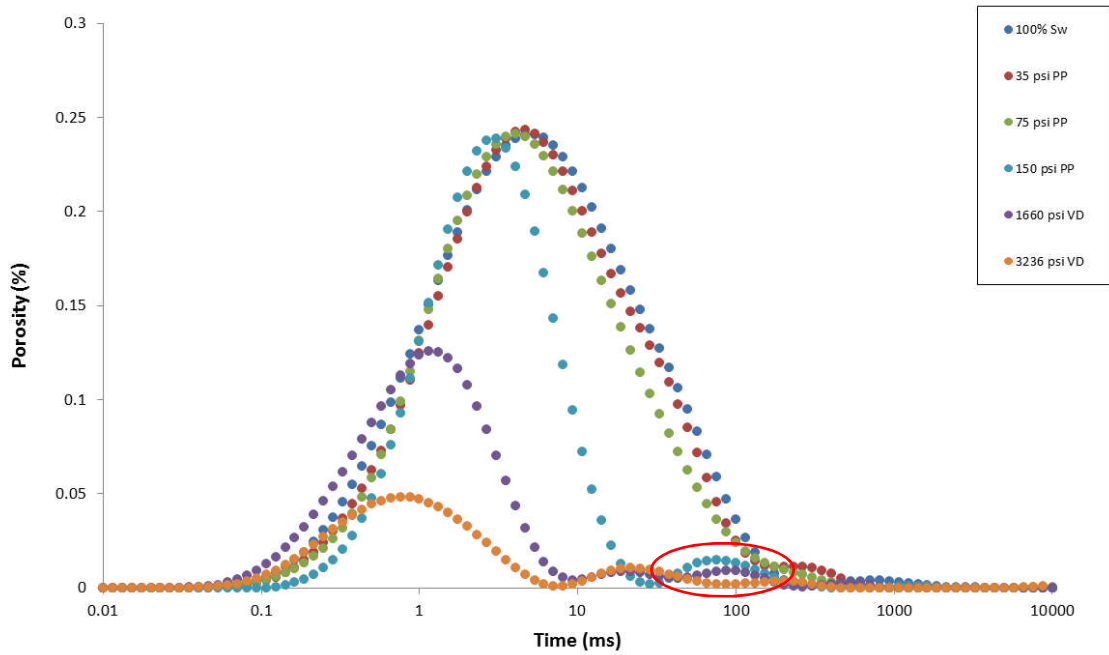


Figure 6-14: NMR normalized signal for sample TS4-11 showing different T_2 time in ms with different water saturations at different capillary pressures using PP and VD. Water trap in large pores after drainage process at high capillary pressures (red).

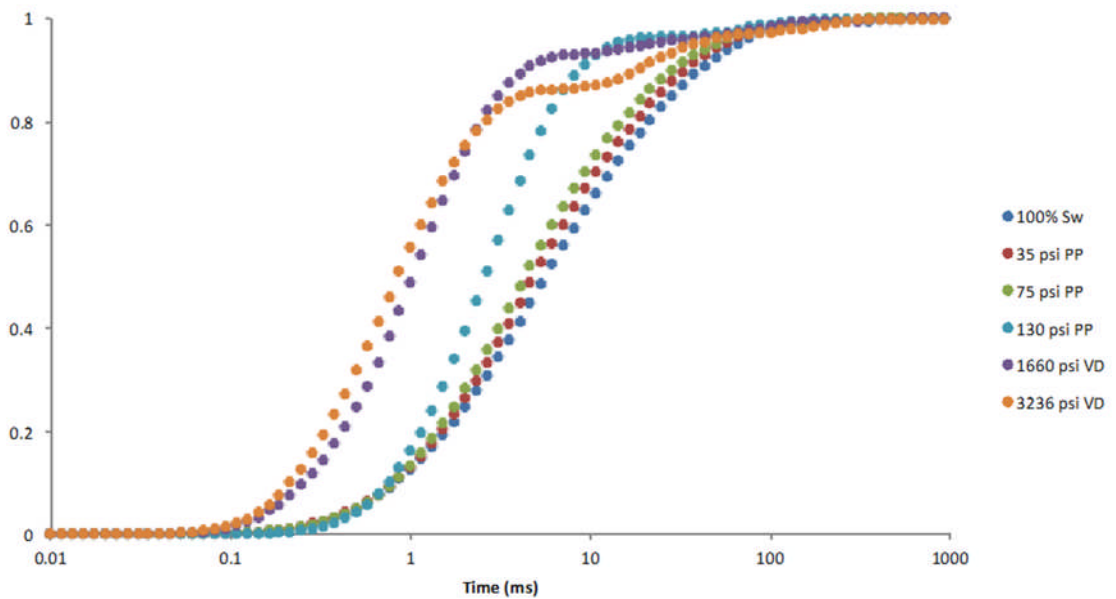


Figure 6-15: NMR cumulative signal for sample TS4-11 with different water saturations at different capillary pressures using PP and VD (lower value of T_2 indicates less water in the sample).

6.3.3 Mercury injection capillary pressure

Displacement and threshold pressures obtained from Hg-injection for the samples are presented in Table 6-2. The pore size distribution results showed that the samples

have peak pore throat radii in the range of 0.1 to 0.6 μm with a mean value of 0.15 μm (Figure 6-16). The pressure required to obtain 5% mercury saturation, S_{Hg} , was in the range of 50 to 220 psi with a mean of 130 psi (Figure 6-17). The MICP curves for the samples confirm their low permeabilities. The threshold pressure is a function of the pore throat size; so the higher the displacement pressure the lower the permeability. The shape of the curves for all samples also indicate their heterogeneity and the wide range of the pore size distribution, which would have high pore geometrical factors as shown in Figure 6-6. A more homogenous sample with better permeability would have a flat plateau as discussed by Schowalter (1979) (Figure 6-7 – left), which is not the case with the tight heterogeneous samples that are more similar to the curve in Figure 6-7 (right).

Sample	Displacement Pressure (psi)	Threshold Pressure (psi)
TS1-55	100	145
TS1-197	100	200
TS1-305	100	200
TS4-4	100	200
TS4-11	100	200
TS5-11	65	100
TS1-25	33	75
TS2-25	47	75
TS3-47	57	145

Table 6-2: Displacement and threshold pressures (psi) obtained from the mercury injection technique for group-C samples.

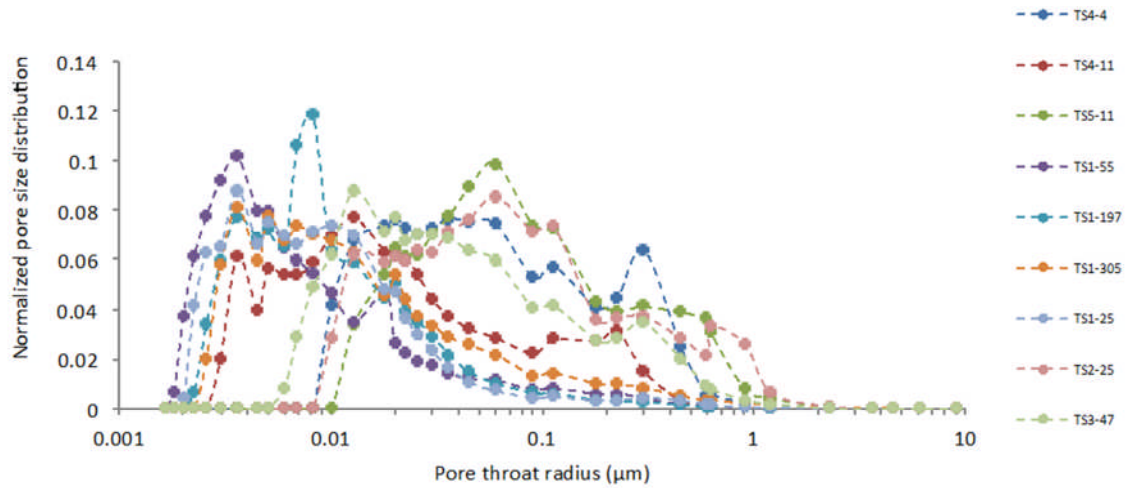


Figure 6-16: Normalized pore throat size distribution showing the pore throat radius in μm for group-C samples.

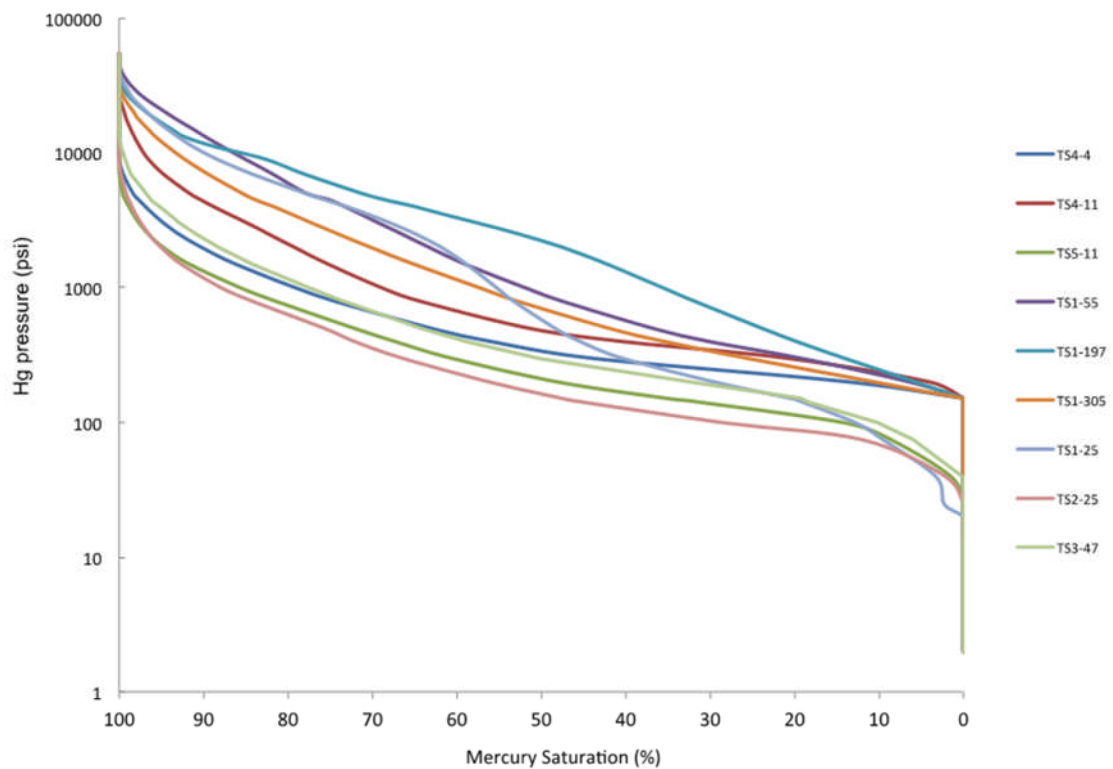


Figure 6-17: Mercury injection capillary pressure curves showing mercury saturation (%) versus capillary pressure (psi) for group-C samples.

6.3.4 Mercury injection capillary pressure under stress

Mercury saturation in fraction was plotted against the pressure in psi for sample TS2-4, which is one of the samples that were used in the stress dependency analyses (Figure 6-18). The mercury saturation obtained from the stressed MICP (PUCS) showed

to be lower than the saturation obtained from the standard MICP at a given pressure. A plot of the pore size distribution for the same sample is shown in Figure 6-19. The pore throat diameter distribution obtained from the standard MICP was in the range of 0.003 and 1 μm . the pore size distribution curve obtained from PUCS under confining stress of 7900 psi showed to be shifted to the lower pore size scale (less than 0.003 to 0.09 μm) indicating reduction in the pore size distribution due to the applied confining stress on the sample.

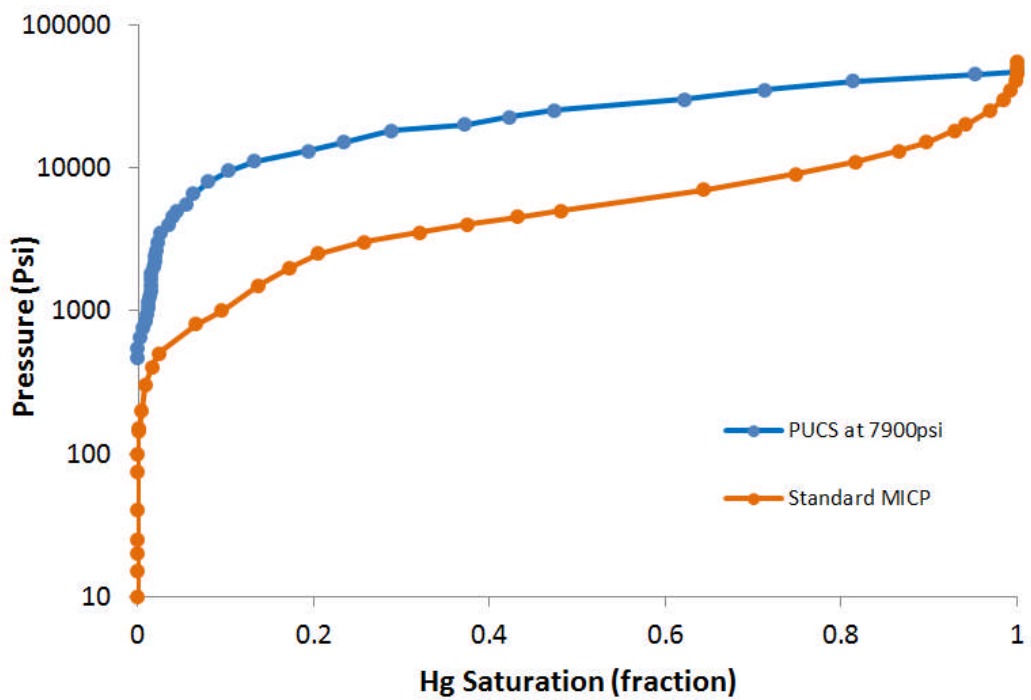


Figure 6-18: Capillary pressure curves showing mercury saturation (fraction) versus capillary pressure (psi) obtained using PUCS under stress in comparison with the standard MICP for sample TS2-4 .

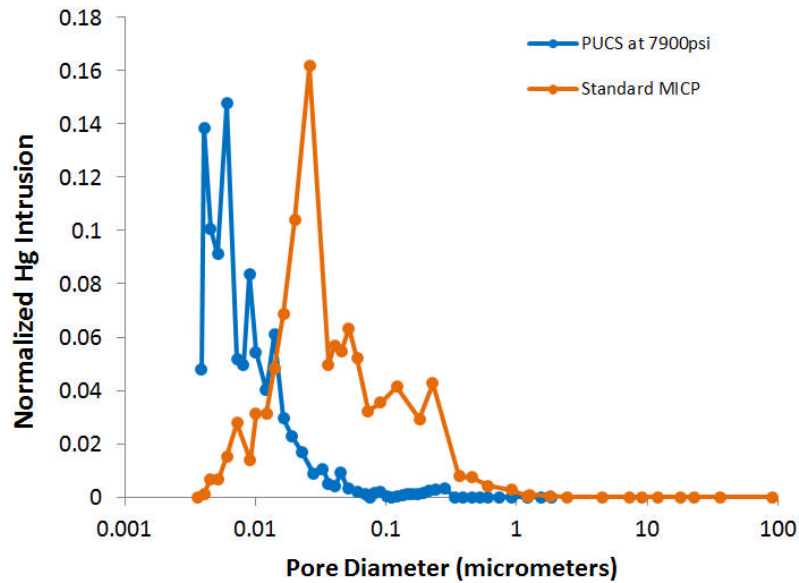


Figure 6-19: Pore diameter (μm) distribution obtained from PUCS under confining stress compared with distribution obtained from the standard MICP for sample TS2-4.

6.3.5 Permeability predicted from models using standard MICP

Estimated permeabilities using the different MICP models were plotted against measured gas permeability at 500 psi for comparison (Figure 6-20 and Figure 6-21) with clear trend but not 1:1. The first suite of samples (the suite with the lowest permeability that was used for stress dependency analysis in Chapter 4) was used here to better demonstrate the comparison between modelled permeability and measured permeability. The scatter gets slightly better for higher measured permeability (>0.001 md) and more scattered at lower permeability. Winland model showed the best correlation with measured permeability, and the most scattered correlation was Thomeer model deviating away from the 1:1 line. The comparison indicated that such models could underestimate the permeability especially for the tight sandstones.

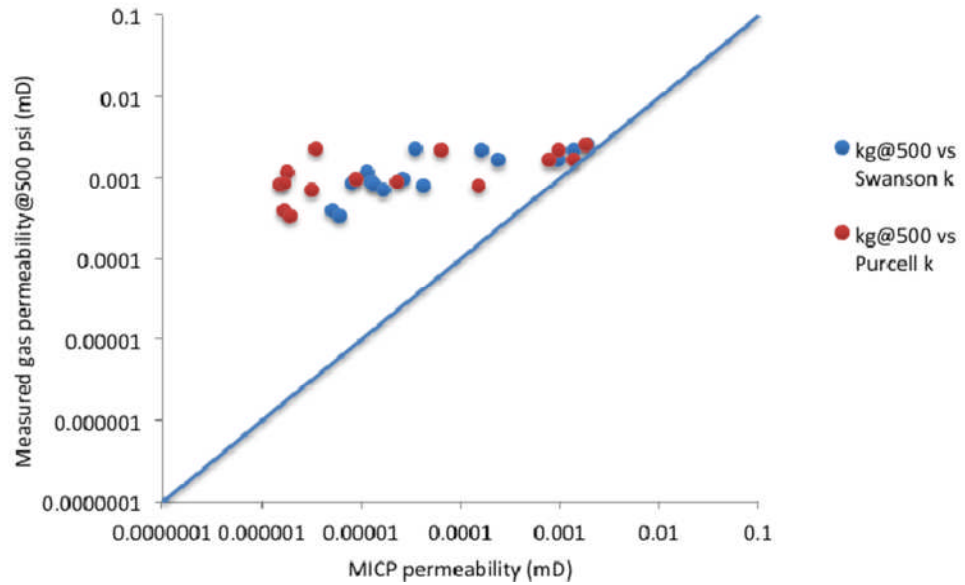


Figure 6-20: Measured gas permeability at 500 psi ($\pm 10\%$ uncertainty) against estimated permeability from MICP using Purcell and Swanson models for group-A samples.

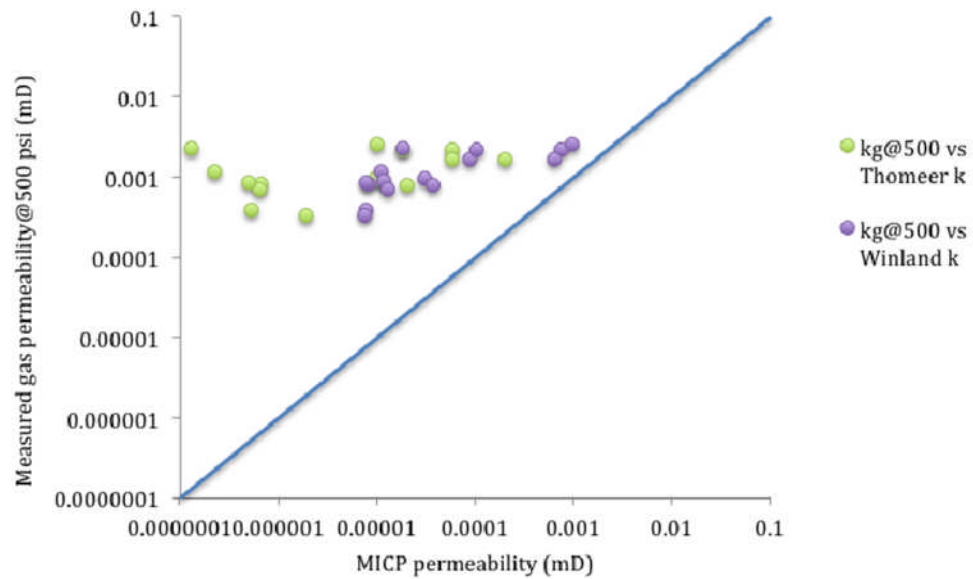


Figure 6-21: Measured gas permeability at 500 psi ($\pm 10\%$ uncertainty) against estimated permeability from MICP using Winland and Thomeer models for group-A samples.

6.3.6 Comparison of mercury injection capillary pressure to porous plate and vapour desorption composite capillary pressure

Capillary pressure data obtained from mercury injection was first converted to air-brine system at laboratory condition using Equation 2-15. The converted MICP data was compared with capillary pressure obtained using the porous plate and the vapour desorption methods.

6.3.6.1 Porous plate capillary pressure against MICP converted to air-brine system

Water saturations determined from porous plate (capillary pressure 35, 75 and 130 psi) are generally consistent with saturations estimated from the equivalent MICP converted to air-brine. Water saturations determined from *PP* at the lowest pressure of 35 psi show the best correlation with the converted MICP data (Figure 6-22). In comparison, the water saturations determined from *PP* at 75 and 130 psi show the same trend as the 35 psi but with slightly more scatter when correlated with water saturations estimated from the converted MICP at equivalent pressures (Figure 6-23) and (Figure 6-24) respectively.

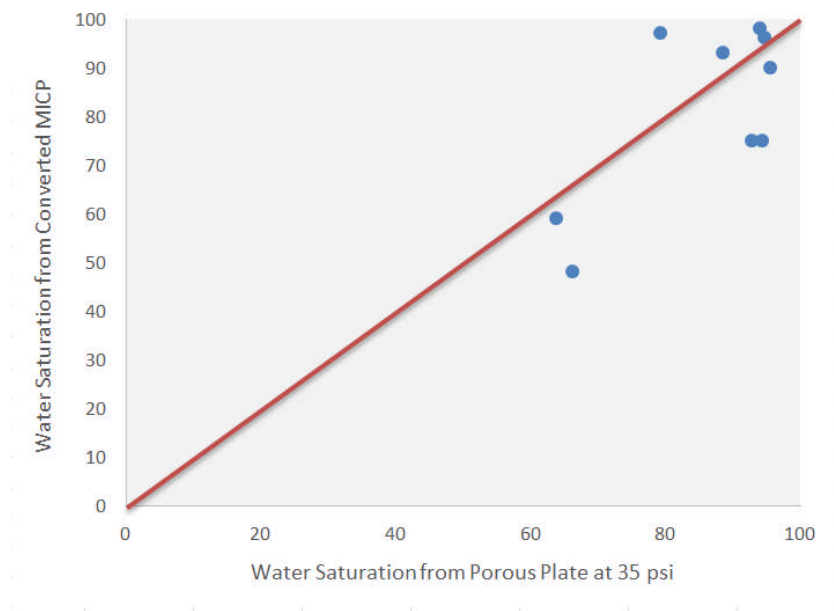


Figure 6-22: Comparison of water saturations determined from porous plate (PP) at 35 psi against the water saturations determined from the converted MICP at equivalent capillary pressure for group-C samples with 1:1 correlation (red line). All within ± 1 to 5% uncertainties.

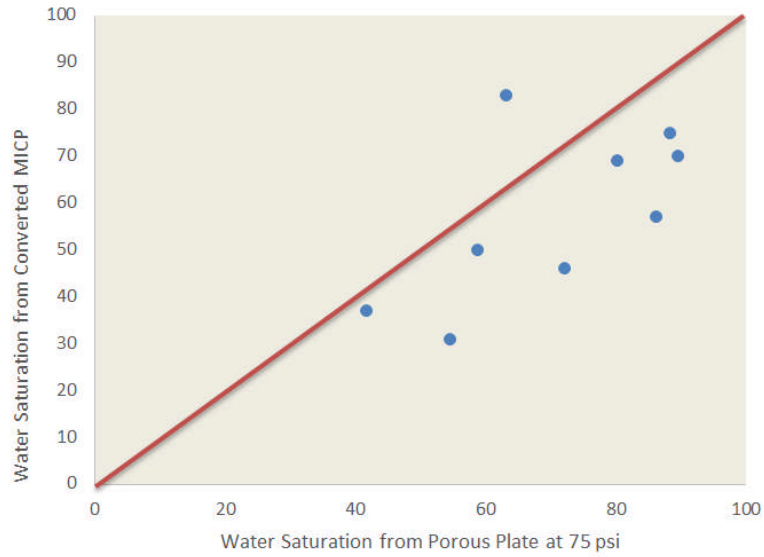


Figure 6-23: Comparison of water saturations determined from porous plate (PP) at 75 psi against the water saturations determined from the converted MICP at equivalent capillary pressure for group-C samples with 1:1 correlation (red line). All within ± 1 to 5% uncertainties.

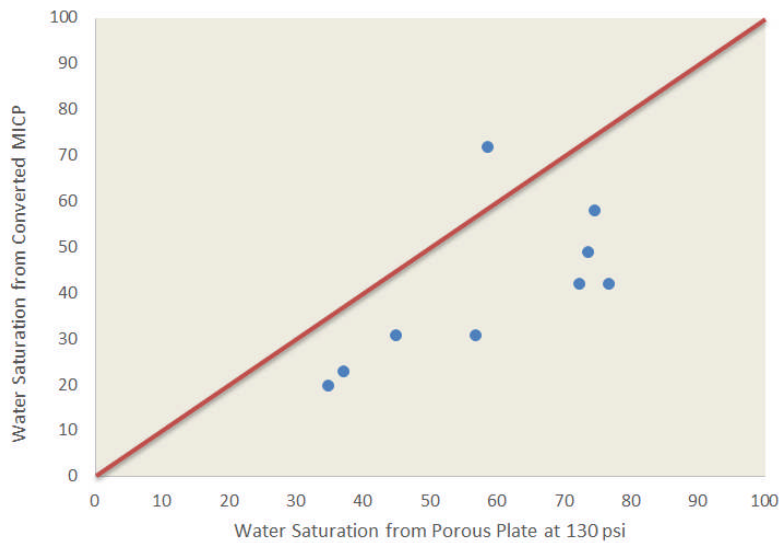


Figure 6-24: Comparison of water saturations determined from porous plate (PP) at 130 psi against the water saturations determined from the converted MICP at equivalent capillary pressure for group-C samples with 1:1 correlation (red line). All within ± 1 to 5% uncertainties.

6.3.6.2 Vapour desorption capillary pressure compared to MICP converted to air-brine system

Water saturations determined from the vapour desorption at higher capillary pressures (1660, 3236 and 4443 psi) show to be generally higher than saturations

estimated from the MICP converted to air-brine at equivalent pressures. The water saturations determined from the converted MICP show to be lower than the saturations obtained from *VD* at 1660 psi (Figure 6-25) and even lower compared to saturations from *VD* at 3236 psi (Figure 6-26). The differences between saturations obtained from the converted MICP appear to be greater at higher capillary pressure. Figure 6-27 shows the significant differences between water saturations from the converted MICP and the water saturations obtained from *VD* at 4443 psi.

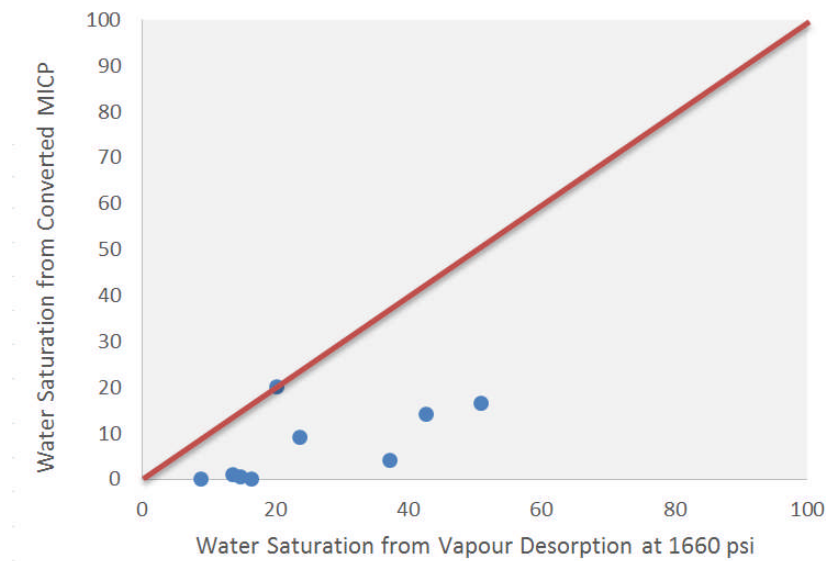


Figure 6-25: Comparison of water saturations determined from vapour desorption (VD) at 1660 psi against the water saturations determined from the converted MICP at equivalent capillary pressure for group-C samples with 1:1 correlation (red line). All within ± 1 to 5% uncertainties.

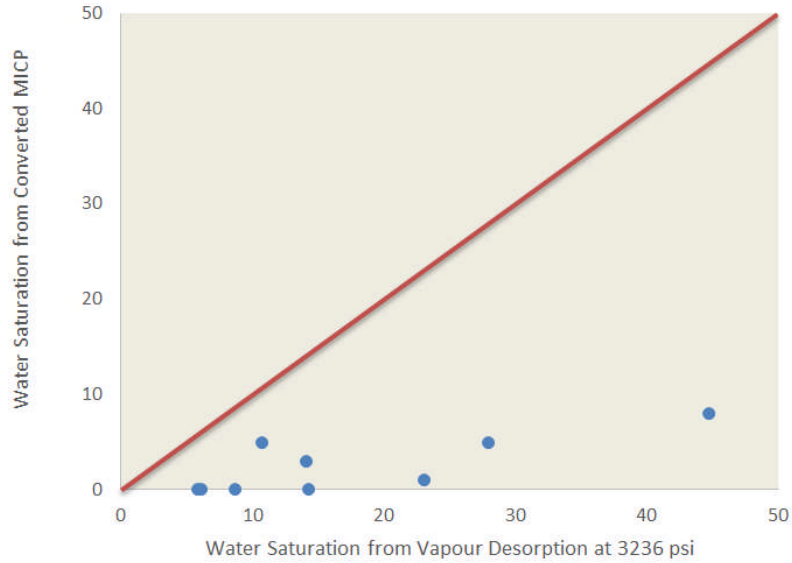


Figure 6-26: Comparison of water saturations determined from vapour desorption (VD) at 3236 psi against the water saturations determined from the converted MICP at equivalent capillary pressure for group-C samples with 1:1 correlation (red line). All within ± 1 to 5% uncertainties.

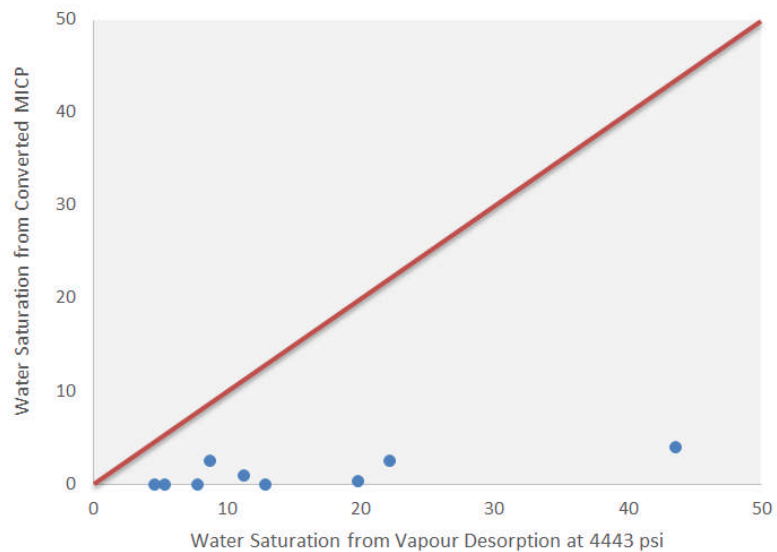


Figure 6-27: Comparison of water saturations determined from vapour desorption (VD) at 4443 psi against the water saturations determined from the converted MICP at equivalent capillary pressure for group-C samples with 1:1 correlation (red line). All within ± 1 to 5% uncertainties.

6.3.6.3 Composite porous plate-vapour desorption capillary pressure compared to MICP converted to air-brine system

The converted MICP data was compared with the combined data acquired by porous plate and vapour desorption because the MICP covers the whole water saturation

range acquired by the *PP* and *VD* methods. The converted MICP curve and the combined *PP-VD* curve show the same general trend for all the samples. Yet, MICP data shows lower water saturations compared to the combined *PP-VD* at a given capillary pressure as shown in the top plots of Figure 6-28, Figure 6-29 and Figure 6-30. The separation between the two curves, which is the difference in water saturations from the converted MICP and from the *PP-VD* data, varied between the samples at each pressure. The difference in water saturation at the low capillary pressure region is shown more clearly in the semi-log plots presented in the bottom plots (Figure 6-28), (Figure 6-29) and (Figure 6-30). The discrepancies between the saturations obtained from *VD* and converted saturation from MICP was greater compared to the differences between the saturations determined from *PP* and converted data from MICP. The discrepancies are consistent with the study by Newsham et al. (2004) reporting differences between the capillary pressure measurements of tight gas sandstones conducted using air-brine methods (*PP*, *VD* and centrifuge) with MICP converted to air-brine system.

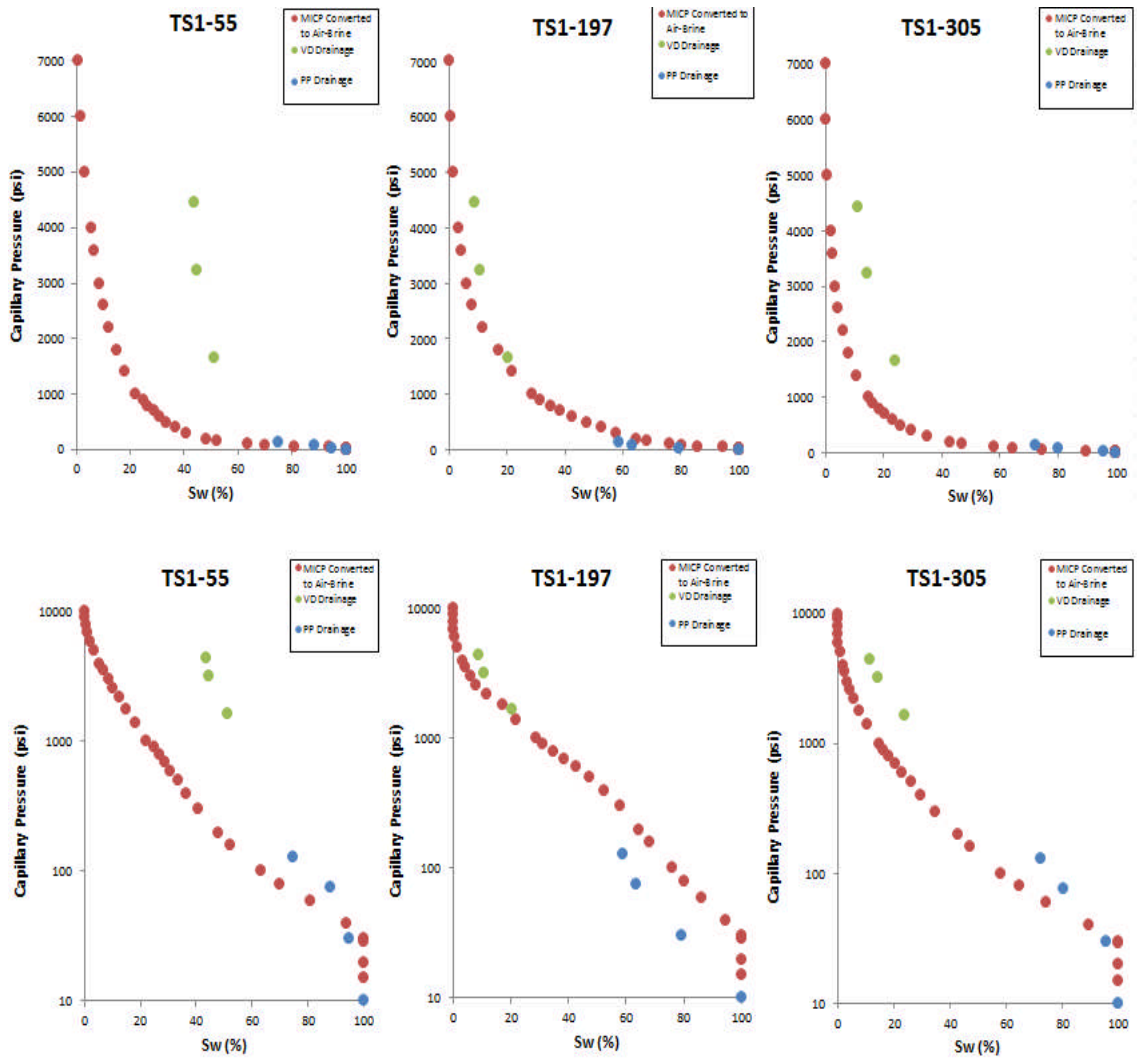


Figure 6-28: Top: Capillary pressure (psi) plotted against water saturation S_w (%) obtained from MICP and converted to air-brine system (red) in comparison with capillary pressure determined from the combined porous plate PP (blue) and vapour desorption VD (green). Bottom: Same capillary pressure curves in semi-log plots for samples TS1-55, TS1-197 and TS1-305.

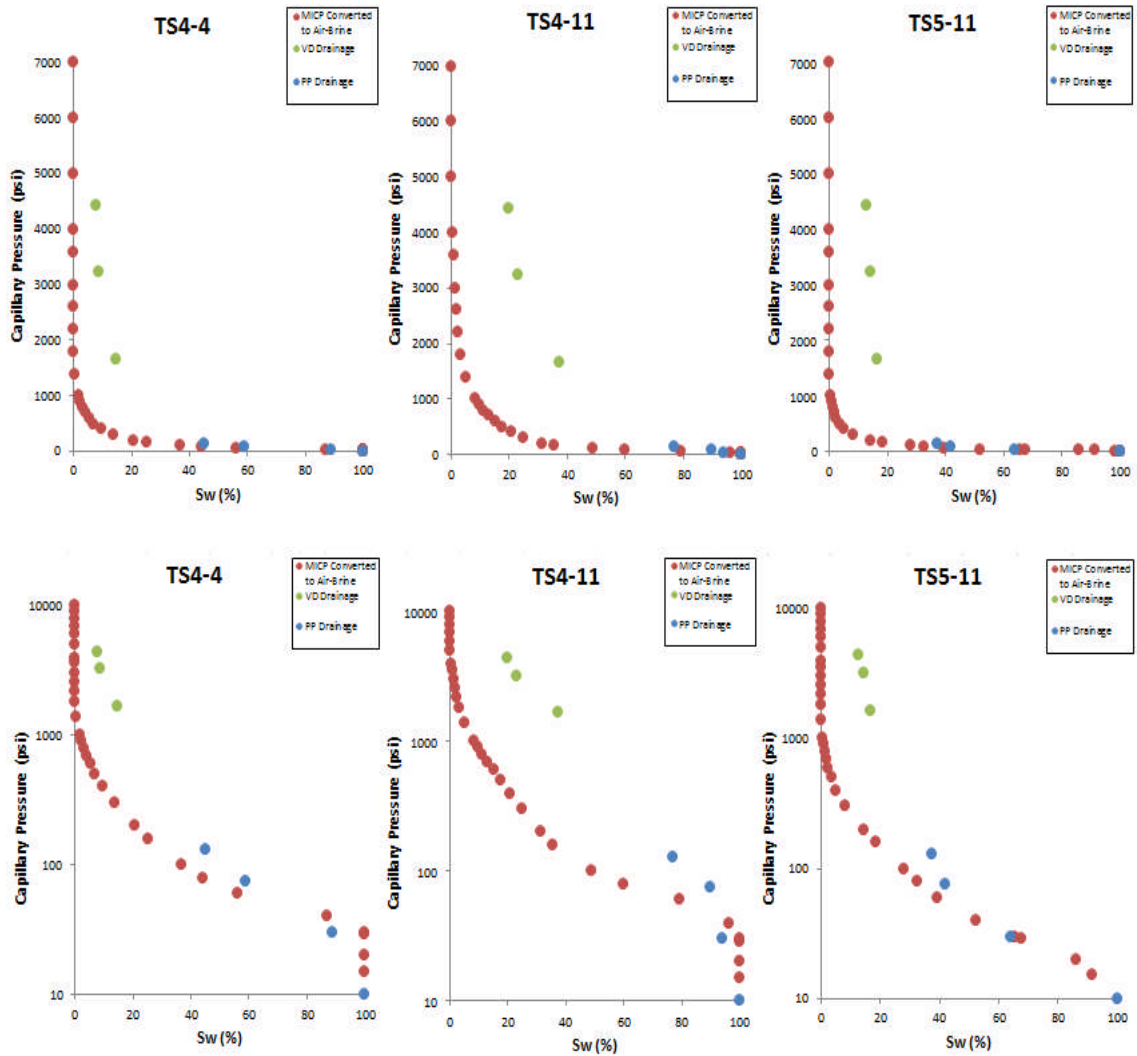


Figure 6-29: Top: Capillary pressure (psi) plotted against water saturation S_w (%) obtained from MICP and converted to air-brine system (red) in comparison with capillary pressure determined from the combined porous plate PP (blue) and vapour desorption VD (green). Bottom: Same capillary pressure curves in semi-log plots for samples TS4-4, TS4-11 and TS5-11.

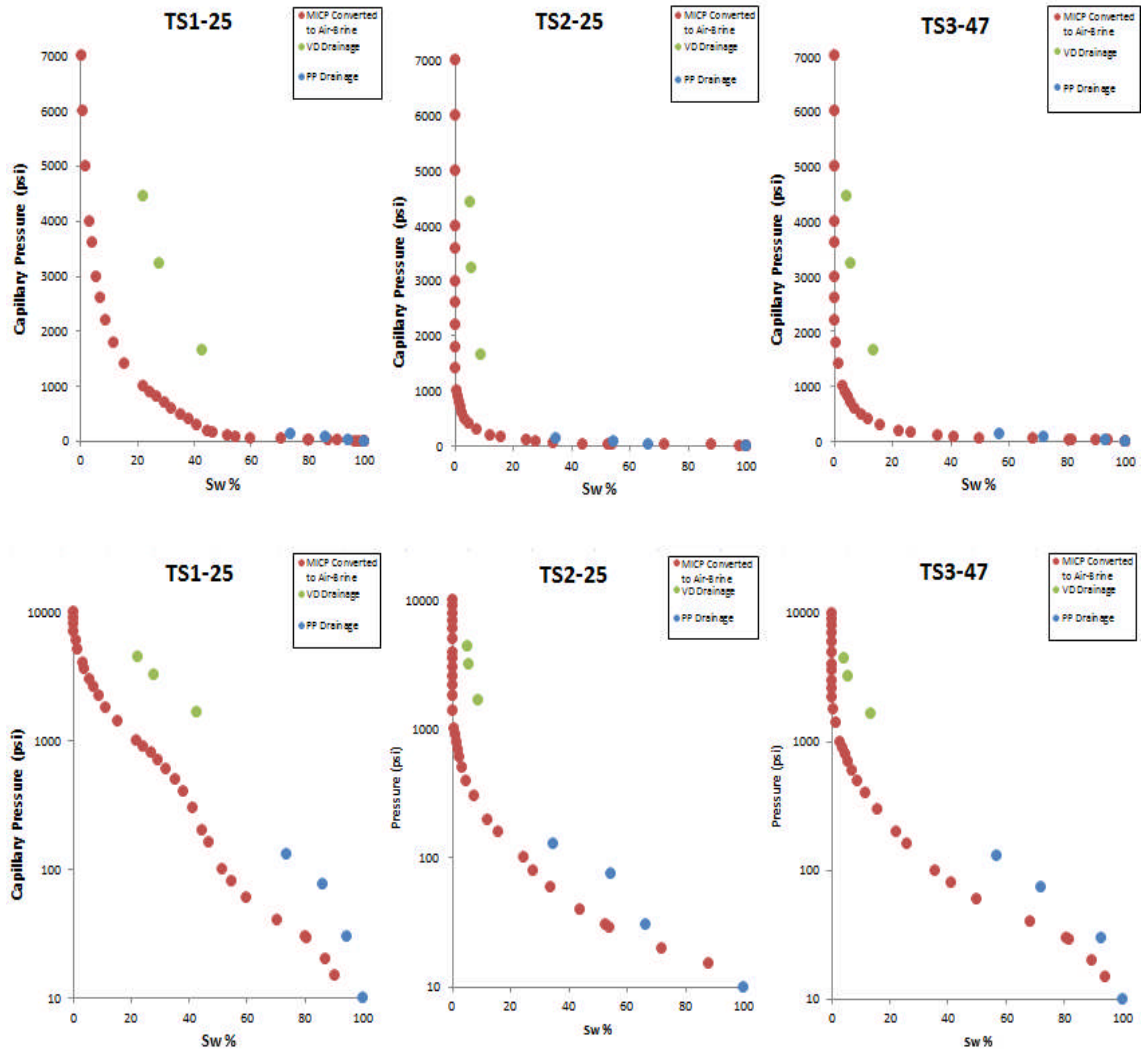


Figure 6-30: Top: Capillary pressure (psi) plotted against water saturation Sw (%) obtained from MICP and converted to air-brine system (red) in comparison with capillary pressure determined from the combined porous plate PP (blue) and vapour desorption VD (green). Bottom: Same capillary pressure curves in semi-log plots for samples TS1-25, TS2-25 and TS3-47.

6.4 Discussion

6.4.1 Causes for the discrepancies between capillary pressure obtained from air-brine system and from mercury injection

6.4.1.1 Equilibration time for air-brine system capillary pressure

All the samples exhibit high displacement pressures due to their μm -scale pore throats. Obtaining capillary pressure data using porous plate and vapour desorption methods for such low permeability samples is time consuming especially at low water saturations. It took days to weeks for the samples to reach equilibrium using the porous plate as indicated in Table 6-1. The samples took up to several months to

equilibrate with the higher capillary pressure using the vapour desorption method (Figure 6-13). Such equilibrium could be an apparent one, and there might be still some brine being displaced by gas and it is a matter of waiting longer periods of time. This apparent equilibrium might explain the higher water saturation obtained by VD than the estimated saturation from the converted MICP for an equivalent capillary pressure.

6.4.1.2 Irreducible water saturation

The concept of irreducible water saturation is unclear in the literature. The term “irreducible” is often referred to the saturation of the water in a rock, which cannot be reduced any further at a certain capillary pressure. The high drainage pressure reduces the wetting saturation further and causes the discontinuity of the wetting phase as illustrated in Figure 6-31. This means water is immobile and hence it has zero relative permeability at this pressure.

The result of the ultra-low irreducible water saturation, shown in Figure 6-28 and Figure 6-29 to reach zero, is estimated from the converted MICP might not exist in the subsurface. The results of the analysed samples would require approximately 800 m of gas column height above the free water level to be achieved, which is very rare to encounter in reservoirs. For example, if the reservoir thickness for the analysed samples is about 100 m, then water saturation in the range between 30 and 60% would not be displaced by the gas, which means this trapped water under this condition is considered irreducible at this condition. Thus, the thicker the reservoir the higher the capillary pressure is, that is more gas displacing water resulting in lower irreducible water saturation. However, exceptional cases of completely removing the water in the reservoir could be achieved by vaporising the water at extremely high pressures and temperatures exceeding 10,000 psi and 175°C respectively as reported by Newsham and Rushing (2002).

The saturation obtained from MICP basically depends on the pressure applied to inject the mercury. So the higher the capillary pressure applied the higher the mercury saturation is, hence the lower the wetting phase saturation that is water saturation when MICP is converted to air-brine system. Dullien et al. (1986) tested the continuity of the irreducible wetting phase in Berea sandstone, and they concluded that the

saturation of the irreducible wetting phase is purely dependant on the applied capillary pressure. They argued that the reported irreducible water saturation of 27.5% at pressure 4.5 times the threshold pressure could be significantly reduced by simply increasing the capillary pressure. They reached 10% irreducible water saturation by increasing capillary pressure to 30 times the threshold pressure, claiming that there is no apparent limit of the irreducible water saturation. This agrees with the very low irreducible water saturation estimated from the converted MICP at high pressure compared with the saturations directly determined from *VD* measurements.

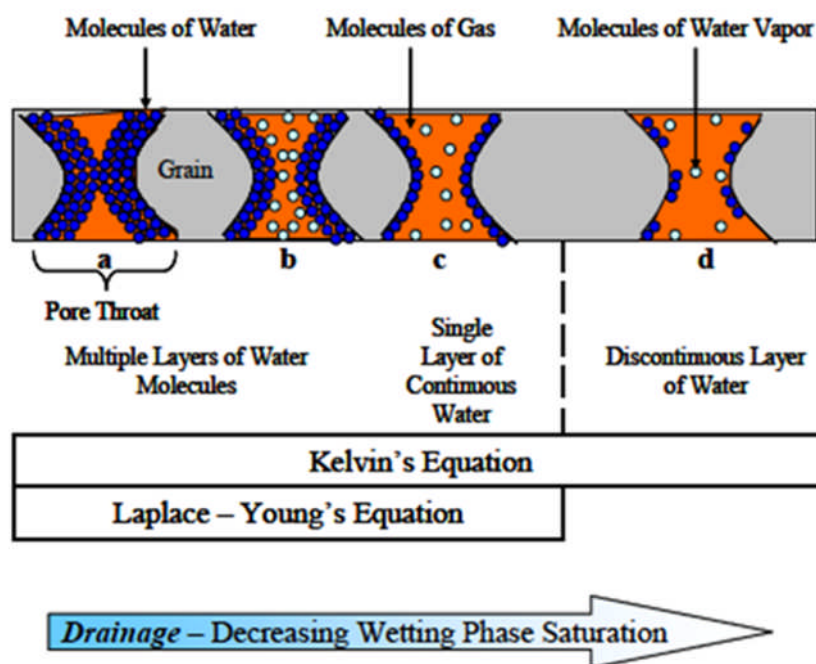


Figure 6-31: Schematic diagram showing the increase of the non-wetting phase saturation as a result of drainage process causes the discontinuity of the irreducible wetting phase (from Newsham et al., 2003).

6.4.1.3 Impact of mercury injection on microstructures

Obtaining capillary pressure data using mercury injection requires forcing mercury into the pore system of the sample. The high surface tension of the air-mercury system that is approximately (480 dyns/cm) compared to the low surface tension of the air-water system (70 dyns/cm) means that larger pressure is required to force mercury into the pore throats of the rock particularly tight samples. For instance, samples TS1-55 and TS4-11 both have porosity of 8% and 7% respectively, and gas permeability measured at 500 psi of 0.013 and 0.011 mD respectively. Yet, sample TS1-55 shows greater

difference between water saturations obtained from the *VD* at 4443 psi and saturation estimated from the converted MICP at the same pressure (Figure 6-28) and (Figure 6-29). Moreover, injecting mercury at high pressure that is 4443 psi pushes or deforms the delicate clay in the sample, which results in lower estimated water saturation. Mineralogy analyses of the samples show that sample TS1-55 contains delicate grain coating illite clay while no illite is present in sample TS4-11 (Table 3-2). This is consistent with the results of Greder et al. (1997) indicating that MICP data agreed with the porous plate capillary pressure measurements for sandstones with little or no clay, and the discrepancies increase as the amount of clay increases. Destruction of delicate clays in the sample results in lower water saturation particularly at high pressure regions (Newsham et al., 2003).

6.4.1.4 Conversion of mercury injection data to air-brine system

The acquired mercury injection data was converted to air-brine system using the simplified expression (Equation 2-15). This equation is based on the Washburn (1921) formula, which assumes parallel cylindrical capillaries. The fluid flow in the analysed samples is controlled by thin cracks that are observed in SEM images and micro-pores that are confirmed from the pore size distributions obtained from MICP. Uncertainties would exist in converting MICP data to air-brine system when using the contact angle assumed for the parallel cylindrical capillaries for the samples, which might result in lower than the real water saturation particularly at the high pressure region. This is consistent with the argument by Melrose (1990) that uncertainty from scaling MICP data to air-brine system could be significant for slit-type pores. The uncertainty is due to the dominant pore walls converging instead of being parallel as assumed for the MICP calculations and so using the conversion factor ($\cos\theta$) would be inappropriate (Melrose, 1990). Thus, irreducible water saturation determined from vapour desorption would be more accurate than estimated from the MICP.

Moreover, calculation of the wetting phase saturation from MICP could be overestimated especially in the high pressure region as indicated by the MICP converted to air-brine data (Figure 6-30). The overestimation of the wetting phase saturation is due to the absence of the wetting phase films coating the grains (Melrose, 1987; 1990). MICP is based on the assumption that air is the wetting phase and no water is wetting the grains surface, which is not the case with the reservoir rocks. This

assumption would be inaccurate for sandstones composed of grains that were compacted and had been through diagenetic processes. The roughness of the grain surfaces and the presence of clay in the tight samples form capillary grooves and micro-channels that hold a thin film of wetting fluid and could extend through the porous rock as shown in SEM image of sample TS4-4 (Figure 6-32 – right). These samples have rough connected pore surfaces unlike a smooth surface of a glass bead having disconnected craters that would not hold much of the wetting fluid (Figure 6-32 – left). Capillary pressure data obtained from porous plate and vapour desorption is considered to be more representative of the reservoir conditions than the data obtained from MICP because the *PP* and *VD* data is generated with reservoir-like fluids (Newsham et al., 2004).

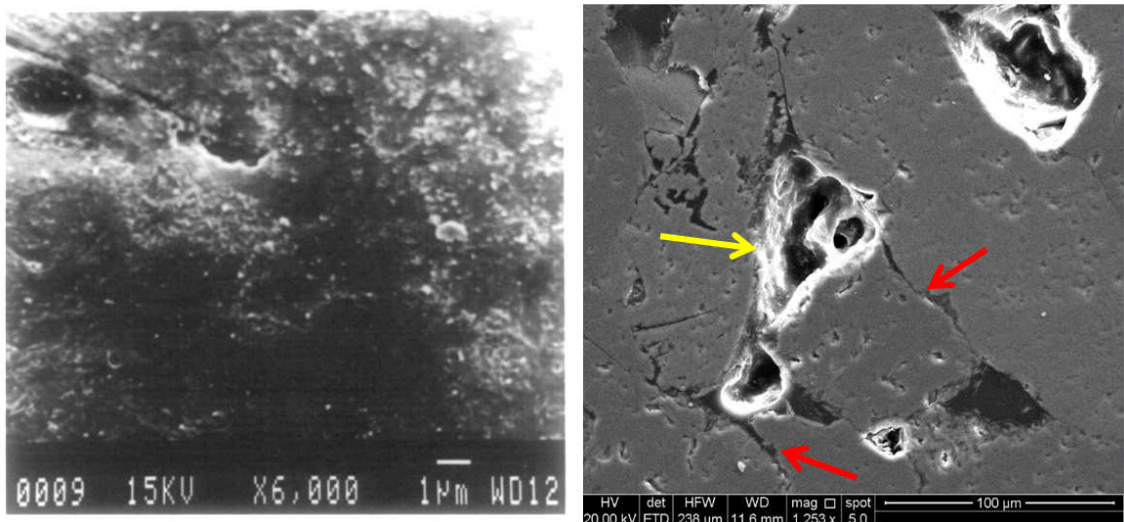


Figure 6-32: Left: Smooth surface of a glass bead with disconnected craters (from Dullien et al., 1986). Right: Roughness of pore surface (yellow) and presence of connected micro-channels (red) through the sample TS4-4.

6.4.2 Nuclear magnetic resonance analyses

Analyses of the NMR scans at different drainage capillary pressures show the water saturation is reduced further after increasing the capillary pressure. The plot of NMR showing the amount of water remaining in the pore space confirms that even large pores could have thin films of water coating the irregular grain surfaces after the water has been drained at high capillary pressure (Figure 6-14). The results could be modelled with the triangular pore model presented by Grattoni et al. (2003) showing water at several drainage stages. As shown in Figure 6-33, (A) represents a fully

saturated pore, and (B) and (C) demonstrate the remaining water at different pressures where it can be trapped in the corners of the model corresponding to crevices and irregularities of the grain surfaces. So increasing the capillary pressure drains water from large pores, but water would always remain in such crevices.

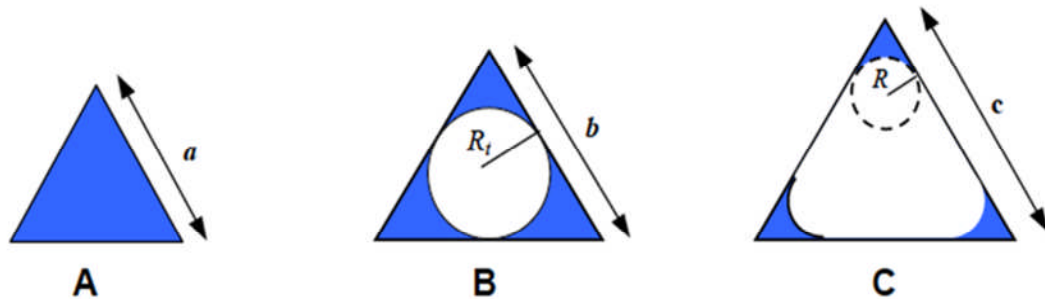


Figure 6-33: Schematic diagram of the triangular pore model at fully saturated stage (A) and at threshold capillary pressure (B) and high capillary pressure (C) (from Grattoni et al., 2003).

6.4.3 Impact of stress on mercury injection capillary pressure

Petrophysical properties, such as permeability, ultrasonic velocity and electrical resistivity, of tight gas sandstones have been shown to be stress dependent and sensitive to changes in the net stress as discussed in Chapters 4 and 5. Confining stress is also expected to affect the capillary pressure measurements. Capillary pressure data acquired using different techniques are considered to be conducted at ambient condition. Samples put in the vapour desorption chamber go under capillary suction forces that could affect the stress state of the samples especially under higher capillary pressure while porous plate was conducted at ambient condition. In contrast, it is argued that standard MICP is conducted at no confining pressure, but Hg-injection pressure can have a great effect on stressing the sample before reaching the threshold pressure. In fact, the sample would be under a hydrostatic stress as the sample would be initially stressed by the mercury until it enters the pore space (i.e. the threshold pressure) (Brown, 2015). The sample would have zero pore pressure since it was placed into a vacuum prior to the Hg-injection process. Threshold pressure depends on the pore throat size distribution and the tighter samples have higher threshold pressures. Thus, predicting permeability from MICP models for tight samples would underestimate the permeability as shown in Figure 6-20 and Figure 6-21 when correlated with permeability measured at 500 psi. The plots indicate that permeability

determined from the MICP models should correspond to permeability measured at a confining stress corresponding to the threshold pressure of each sample. Furthermore, a plot of measured gas permeability at 500 psi and at the threshold pressure of each sample against permeability predicted from MICP using Swanson model is shown in Figure 6-34. The correlation between the measured permeability at threshold pressures and MICP predicted permeability is better than the one between measured permeability at 500 psi and the MICP estimated permeability. This is in agreement with the study by Brown (2015) illustrating that permeability estimated from MICP of tight sandstones would be similar to permeability measured at stress equivalent to the threshold pressure.

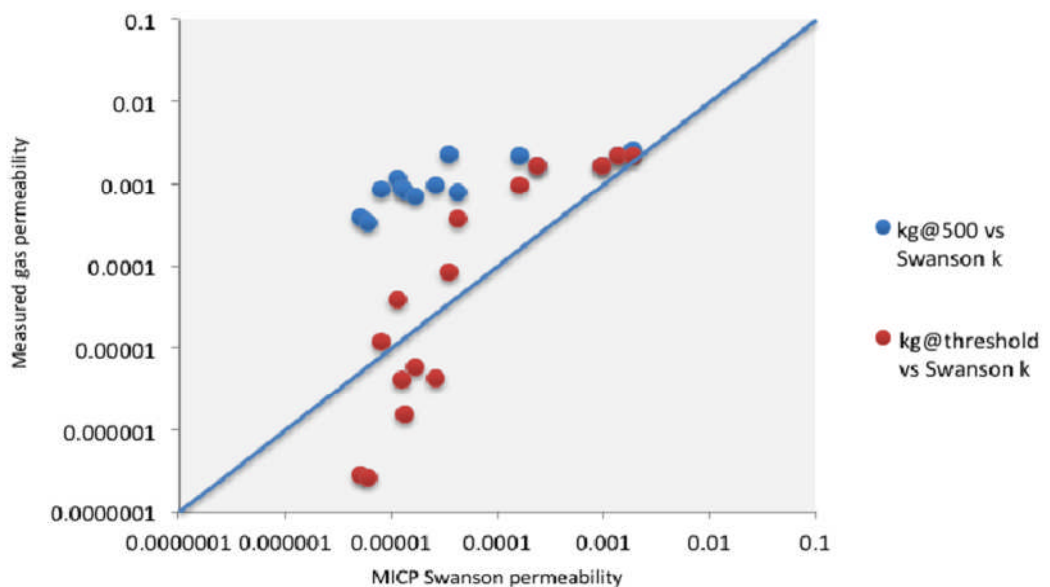


Figure 6-34: Comparison of gas permeability measured at 500 psi ($\pm 10\%$ uncertainty) and permeability at threshold pressure ($\pm 10\%$ uncertainty) of each sample in group A plotted against permeability estimated from MICP using Swanson model.

6.4.1 Permeability predicted from stressed MICP data

In an attempt to further evaluate the effect of stress on MICP analysis, Hg-injection under stress was conducted for a few samples using PUCS in the Wolfson laboratory. The results showed great discrepancies compared with data obtained from the standard non-stressed MICP equipment. The presence of microfractures due to stress relaxation caused by drilling and coring, which might not be as abundant as in the subsurface (Farquhar, 1993), could affect the capillary pressure measurements as they affect other petrophysical properties (e.g. permeability). Stressed MICP would be more

representative of the reservoir condition than data obtained from standard one as the applied confining stress might close any artificial microfracture leading to a better reservoir modelling with more pragmatic data. Pore throat size distributions derived from standard MICP and PUCS (Figure 6-19) indicate the reduction in the pore size distribution, which is consistent with the idea of closing the microfractures. The higher entry pressure observed from the capillary pressure curve obtained from PUCS would indicate a lower estimated permeability (Figure 6-18), which would be consistent with the permeability measured at higher net stress. This is in agreement with the study reported by (Guise et al., 2017) showing permeabilities estimated from standard MICP and PUCS for a set of tight sandstone samples using Katz and Thompson model (1986, 1987). They correlated estimated permeabilities from both (MICP and PUCS) with permeability measured at a net stress of 5000 psi. The permeability estimated from PUCS showed a better correlation with the measured permeability than permeability estimated from standard MICP (Figure 6-35). The former showed a correlation coefficient of 0.79 while the later showed a correlation coefficient of 0.66.

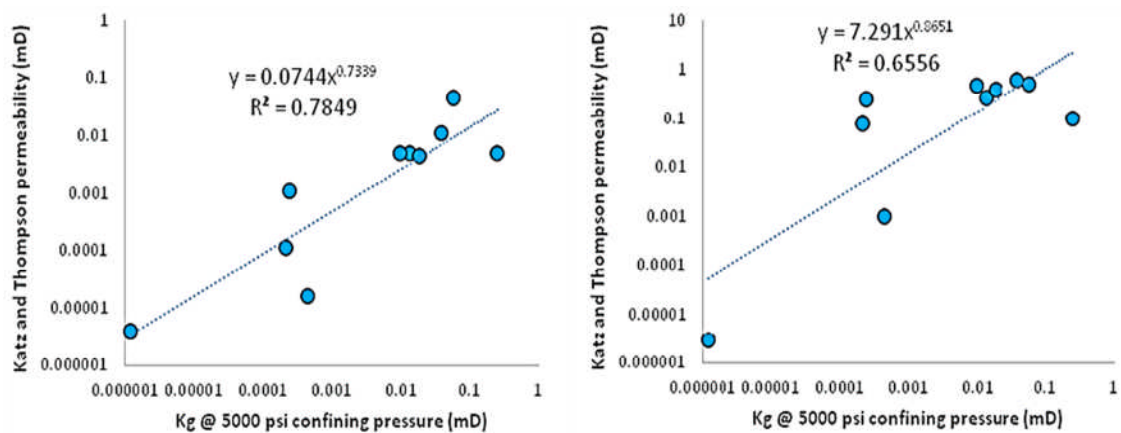


Figure 6-35: Permeability measured at 5000 psi stress plotted against predicted permeability using Katz and Thomson model from stressed MICP (left) and standard MICP (right).

6.4.2 Implications for water saturations estimation

MICP technique offers a quicker way that takes only hours compared to *PP* and *VD* that take weeks and even months to obtain capillary pressure data for tight sandstones. However, porous plate and vapour desorption are better used with samples containing delicate clays for optimum results. Injecting mercury at high pressures may alter the microstructures of the samples particularly sensitive clay particles, which results in

lower estimated water saturation especially at high capillary pressure region. MICP is better used with sandstones with no or little clay to estimate the water distribution in the reservoir as the impact of mercury injection in clay is higher in ultra-low permeability samples. Hence, the higher the clay content present in the sample, the more optimistic the MICP becomes in estimating the water saturation (Shafer and Neasham, 2000).

In addition, MICP models should be used with care to predict permeability for tight rock samples. Estimated permeability from MICP data is often referred to as k_{air} that is assumed to be equivalent to gas permeability measured at ambient condition, which would be valid with conventional reservoir samples. On the contrary, permeability estimated from mercury injection measurements for tight samples should be considered as permeability that is measured at stress equivalent to the entry pressure of the individual sample. Conducting capillary pressure under stress for the samples that are sensitive to stress would therefore optimize the estimation of permeability as well as the fluid distribution in the tight sandstone reservoirs.

6.5 Conclusions

Water saturations obtained from porous plate showed to be in reasonable correlation with water saturations determined from the MICP converted to air-brine systems at equivalent pressures. In contrast, the water saturations determined from the vapour desorption showed differences, generally higher water saturations, than the saturations determined from the converted MICP at a given pressure. The differences in water saturations from *VD* and the converted MICP at equivalent pressure were even greater at higher capillary pressures.

Water saturations at high capillary pressures were obtained using the vapour desorption technique due to the limited capillary pressure (i.e. 130 psi) of the porous plate method. Measurements of capillary pressure for the samples using the porous plate technique were consistent with the capillary pressure obtained by the vapour desorption technique. The saturations at the maximum pressure used in the porous plate (i.e. 130 psi) showed to be continuous to the saturations at the minimum pressure used in the vapour desorption chamber that is 1660 psi.

Porous plate and vapour desorption techniques showed to be time consuming especially for ultra-low permeability samples requiring weeks or even months of equilibration periods. Although the MICP technique uses air and mercury fluids that are both non-wetting phases, it is a fast, cheap and easy method to obtain capillary pressure data. Capillary pressure data acquired by porous plate and vapour desorption were combined due to their different limits of pressures. The combined capillary curve, *PP-VD*, was compared with capillary data obtained from MICP and converted to air-brine system. Converted MICP data showed discrepancies in water saturations with capillary pressure acquired using *PP* and *VD*.

Such discrepancies could be related to the equilibration time used for the porous plate and vapour desorption methods. Mercury injection at high pressures into tight samples deforms the delicate clay present in the samples and could result in ultra-low water saturation. Too low wetting phase saturation estimated by MICP could also be the result of the absence of the contributions of the wetting phase especially in the high-pressure region. The high mercury injection pressure causes discontinuity of the residual wetting fluid saturation, which resulted in underestimating the wetting fluid saturation. Analysis of the NMR scans at different drainage capillary pressures confirmed that even drained large pores could have thin film of water coating the irregular surfaces.

There might be some sources of errors that might affect the capillary pressure measurements, such as compressibility of the system and the scaling of the contact angle. It has been reported that oil and gas industry lacks the standards to correct for system compressibility. The scaling with different values for the contact angles and the interfacial tension required for Washburn (1921) formula could be another source of error in estimating the irreducible water saturation especially for tight sandstones and at high pressures.

Capillary pressure data obtained from Hg-injection needs to be reviewed carefully when estimating permeability from MICP models especially for tight sandstones. Samples with ultra-low permeability showed to have high threshold entry pressures due to their small pore throats. Such pressure could reduce or completely close microfractures resulting in fewer pathways for the mercury to permeate the sample.

Permeability determined from different MICP models showed better correlation with gas permeability measured at stress equivalent to the threshold pressures in comparison with permeability measurements at ambient condition. Thus, it is critical to consider permeability estimated from those MICP models as permeability under stress, equivalent to the threshold pressure, rather than ambient permeability, which in turn would improve the simulation of fluid flow in tight reservoirs.

MICP under stress was conducted using PUCS that is a unique equipment built to examine the effect of stress on MICP data. Peak of pore throat size distribution acquired from stressed MICP was about one order of magnitude less than peak acquired from standard MICP. In addition, permeability measured under stress showed a better correlation with permeability estimated from stressed MICP data using Katz and Thomson (1986, 1987) model compared to the permeability predicted from the standard MICP using the same model. Capillary pressure measured under stress should be considered especially when characterising tight sandstone reservoirs, as such data are likely to be more representative of the reservoir conditions than unstressed measurements. This in turn provides more accurate data that would optimise the exploration, appraisal and development operations in unconventional reservoirs.

7 Conclusions and recommendations

The aim of this project has been to analyse the effect of net stress on petrophysical properties particularly permeability as well as the effect of equilibration time on the petrophysical measurements of tight gas sandstones. This chapter presents the conclusions of this project considering the aim and objectives presented in the introduction chapter. It is divided into three parts. The first part is a comprehensive conclusion of the whole project. The second and third parts are an overall summary of the implications and recommendations for further work respectively.

7.1 Conclusions

7.1.1 Controls on porosity and permeability

Porosity and permeability of the samples of all groups (A, B and C) showed a general trend of decreasing permeability as porosity decreased with an exponential relationship and a correlation coefficient of 0.64 (Figure 3-5). Factors that affect the porosity and permeability of the samples in all groups were analysed to examine the impact of each factor on the properties and whether relationship between factors and porosity-permeability existed. The analyses indicated the following correlations:

- Measured brine permeability was lower than gas permeability measured at the same net stress of 1500 psi for all samples, and the difference was greater for samples with lower permeability. A power law relationship (Equation 3-3) existed with a correlation coefficient of 0.91 (Figure 3-7) between brine and gas permeabilities for all samples even they were taken from different formations. This determined relationship could be used to estimate the impact of water on permeability.
- Grain size and sorting did not show much of control on the porosity and permeability of the tight sandstones. Neither grain size nor grain sorting showed any correlation when plotted against the porosity-permeability cross plot (Figure 3-55) and (Figure 3-56). This is probably caused by the extensive diagenetic processes the samples had been through. Mercury injection data (Figure 3-57) and (Figure 3-58) and SEM images (Figure 3-13 (Figure 3-14)

showed different degrees of heterogeneity of the pore system, which might be related to the different grain size and sorting.

- The presence of microfractures affects mainly the permeability by improving and connecting the fluid path ways with minimum contributions to the pore volume. Several samples have similar measured gas permeabilities at ambient condition but different porosities. Analyses of SEM images of the low porosity samples showed the presence of microfractures (Figure 3-12), (Figure 3-13) and (Figure 3-18), which could be the cause of the permeability enhancement.
- Increasing the confining pressure decreased both porosity and permeability (Figure 3-6). The reduction in permeability resulted from increasing confining pressure was more significant than reduction in calculated stress-corrected porosity especially at low stress conditions (Figure 3-59).
- The properties of the samples have shown to be affected by the clay type and distribution. The presence of clay generally reduced the porosity and permeability of the samples. Illite clay coating the grains and bridging the pores showed greater reduction on the permeability compared to other clay types at a given porosity (Figure 3-60).

7.1.2 Stress dependency of petrophysical properties

The stress dependencies of permeability, ultrasonic velocity and electrical properties were investigated by analysing the measurements of the properties under a wide range of net stresses for group A tight sandstone samples. Drawdown experiments were conducted for the same group of samples to analyse the permeability response to the effects of stress change at reservoir condition and the gas slippage. The results of the measurements indicated the following:

- Permeability, ultrasonic velocity and electrical properties are all stress-dependent, meaning they were all affected by the change in the net stress. Yet, the stress dependency varied from one property to another, which is consistent with the theory that the stress dependencies of the properties are controlled by the different aspects of the microfractures. Gas permeability showed to be the most stress-dependent property (Figure 4-12) compared with electrical resistivity (Figure 4-25) ultrasonic velocity (Figure 4-21). The reason for this is that permeability is controlled by the square of the crack width. No correlation

was found between the stress sensitivity of gas permeability and either electrical properties or velocity (Figure 4-34) because the fluid and current flow properties are all dependent on the orientation of the microfractures. No correlation was identified between the stress dependency of electrical properties and velocity as velocity is mainly controlled by the density of the microfractures where current flow is affected by the connectivity of the microfractures.

- The stress dependency of a single property i.e. permeability varied within the samples even for samples taken from the same reservoir and only inches apart (Figure 4-11), which could be caused by the diagenetic processes. Stress dependency of permeability showed to be higher below net stress of 3000 psi at which most of microfractures tend to close partially or completely (Figure 4-11). Drawdown experiments also showed less reduction in the permeability measured between stress range of 5000 and 7000 psi (Figure 4-12), which is another indication of the closure of microfractures. Thus, microfractures seen in SEM images could be artificial and may not be as abundant in the subsurface as in the laboratory.
- Unlike the commonly used Shell formula that states the cementation exponent increases as the porosity decreases, the group A samples analysed during this study experienced a decrease in cementation exponent as the porosity decreases (Figure 4-28). This may also be due to the presence of the microfractures that act as conduits for the electrical current flow (Figure 4-29). Moreover, discrepancies between measured FRF and calculated FRF using constant values of m indicated the heterogeneity of the samples (Figure 4-30). It is crucial to determine the exponent m for each tight rock to estimate the gas in place. Using constant values for m or using values from conventional reservoirs resulted in inaccurate calculations of the amount of gas in place (Table 4-8) and (Table 4-9).

7.1.3 Effective stress law for permeability

The effective stress law for permeability was determined by conducting gas permeability measurements under different combinations of confining and pore pressures for a set of tight sandstone samples that is group B samples. Determining

the effective stress law for permeability quantified the stress sensitivity of permeability to the changes in both the confining pressure and the pore pressure, which enabled the prediction of permeability at any net stress. The results of the determined effective stress law for the samples were:

- The increase in confining stress reduced the permeability while increasing the pore pressure resulted in an increase in the permeability (Figure 5-4) and (Figure 5-5). Plotting the permeability as a function of effective stress followed an empirical power law with effective stress coefficients less than unity indicating the permeabilities of the samples are more sensitive to the change in the confining pressure than the change in the pore pressure (Figure 5-7). The law was determined from 12 different combinations of confining stresses and pore pressures for each sample in group B (Table 5-2). The model correlated well with permeabilities measured at low stresses and reservoir conditions (Figure 5-9). An effective model of only 3-point combinations was proposed that showed a good correlation with the measured permeabilities (Figure 5-19), which could be a quicker way to estimate the effective stress law.
- The elastic bulk moduli of the selected samples were calculated from the measured ultrasonic velocities and bulk densities (Table 5-8). The elastic bulk moduli of the total solids forming the rock samples were calculated from the volume of fraction of each mineral determined from QXRD and elastic modulus of each mineral from the literature. The estimated clay to quartz stiffness ratios estimated from the calculated elastic properties of the samples were between 1:2 and 1:7 (Table 5-9). The Biot coefficients determined for the samples were in agreement with the determined effective stress coefficients for permeability indicating more effect of the confining stress on permeability than the pore pressure (Table 5-8).
- Equilibration time prior to conducting permeability measurements is critical to reduce errors in determining the effective stress law for tight samples. The analysed samples required a minimum of two hours soaking time after changing the stress to obtain reasonable constant permeability measurements. Leaving the samples for only minutes to equilibrate showed errors greater than 10% for some samples (Table 5-10).

7.1.4 Effect of stress and equilibration time on capillary pressure measurement

The impact of equilibration time on capillary pressure measurements was analysed by obtaining capillary pressure data using porous plate and vapour desorption methods and compare the results with mercury injection capillary pressure for group C samples. The impact of stress on mercury injection capillary pressure measurements was analysed by correlating the permeability estimated from MICP and permeability measured at different net stresses. Capillary pressure using mercury injection under confining stress was obtained and compared with results from the measurements conducted using the standard MICP. The analyses showed the following key results:

- Capillary pressure data obtained using porous plate required two to three weeks of equilibration time for each drainage pressure step of 35, 75 and 130 psi (Table 6-1). Vapour desorption method was used for higher capillary pressure due to the upper limit of the PP. Samples took even longer equilibration time in the VD; they took from one to two months at 1660 (Figure 6-10) and at 3236 psi (Figure 6-11), and up to three months for the higher pressure (4443 psi) (Figure 6-12). The samples were scanned with NMR to monitor the water saturation after each capillary pressure. NMR results showed that small amount of water remained in the large pores after they were drained at high capillary pressures (Figure 6-14), which is an indication of the thin layer of irreducible water coating the irregular grain surfaces.
- MICP was converted to air-brine system for the samples and the converted data was compared with the capillary pressure obtained using porous plate and vapour desorption methods. The water saturations determined from the porous plate showed good correlations in general with the best correlation at pressure of 35 psi (Figure 6-22). Saturations determined from vapour desorption showed higher water saturations than ones estimated from the converted MICP with no clear relationship (Figure 6-25), (Figure 6-26) and (Figure 6-27).
- Discrepancies existed between capillary pressure data obtained from PP-VD and from the converted MICP (Figure 6-28), (Figure 6-29) and (Figure 6-30). The long equilibration time required for the tight samples to acquire capillary

pressure data using air-brine system might be of the reasons causing the differences. Injecting mercury at high pressure pushing and deforming the delicate clay present in the samples would be another factor resulting in ultra-low water saturations. In addition, the conversion from MICP to air-brine assumes cylindrical capillaries that are uncommon in the analysed samples, which would be another source for the discrepancies.

- Permeabilities of the samples were estimated using different MICP models. The estimated permeabilities were correlated with permeabilities measured at ambient condition (Figure 6-20) and (Figure 6-21) but showed better correlations with permeabilities measured at stresses equivalent to the threshold pressures of the samples (Figure 6-34). MICP under stress showed smaller pore size distribution (Figure 6-19) and higher entry pressure (Figure 6-18) indicating lower permeability compared to the data acquired from the standard MICP.

7.2 Implications

The gas permeabilities of the tight sandstone samples show to be less stress dependent at reservoir pressure compared to the stress dependency at lower net stress (i.e. less than 3000 psi) (Figure 4-11). The drawdown experiments indicate low stress dependency of permeability at initial reservoir net stress to prior to abandonment condition (Figure 4-12), which also confirm the less stress dependent of permeability at reservoir condition. These results indicate that operating the gas wells at restricted flow rates might not necessarily help to retain permeability during production in tight gas sandstone reservoirs.

The effective stress law determined for the permeability for group-B samples (Figure 5-7) indicate that permeability is less sensitive to the changes in the pore pressure than the confining stress. The results are in agreement with the analysis of the stress dependency of permeability, and therefore applying restricted flow rate practices may not be useful to preserve the fluid flow during production.

7.3 Recommendations for further work

The stress dependency of permeability required a large number of permeability measurements under a wide range of net stresses. It would be recommended to

measure the permeability at higher stresses close to the reservoir and minimize or even avoid measurements at ambient condition since the stress dependency of the permeability showed to be minimal at reservoir condition. Moreover, the microfractures present in the samples that contributed in the stress dependencies of the petrophysical properties were observed only in the SEM images, hence at ambient condition. Such microfractures might not be natural, thus it is recommended to measure petrophysical properties at higher stress to minimise the impact of artificial microfractures on the properties.

Further petrophysical data can be acquired from borehole wireline logs, which covers larger scale of measurements compared with petrophysical measurements conducted on core samples and thin sections. Integration of wireline logs in addition to well testing with petrophysical core analyses would also be recommended for optimum hydrocarbon in place estimates and reservoir modelling.

This work has focused on the stress dependency of different petrophysical properties with the emphasis on the permeability sensitivity to the changes in the confining stress and pore pressure of tight gas sandstone reservoirs. Yet the workflow of the analysis of the stress dependency of the different petrophysical properties and the effective stress law modelling could be conducted for tight carbonate reservoirs.

References

- Al-Wardy, W. and R. W. Zimmerman (2004). "Effective stress law for the permeability of clay-rich sandstones." *Journal of Geophysical Research-Solid Earth* 109(B4).
- Archie, G. E. (1942). "The electrical resistivity log as an aid in determining some reservoir characteristics." *Transactions of the American Institute of Mining and Metallurgical Engineers* 146: 54-61.
- Arps, J. J. (1964). Engineering concepts useful in oil finding. *AAPG Bulletin*, 48(2), 157-165.
- Baptist, O. C., & Sweeney, S. A. (1954). The effect of clays on the permeability of reservoir sands to waters of different saline contents. *US Bureau of Mines, Clays and Clay Minerals-CLAYS CLAY MINER*, 3(1), 505-515.
- Batzle, M. L., Simmons, G., & Siegfried, R. W. (1980). Microcrack closure in rocks under stress: direct observation. *Journal of Geophysical Research: Solid Earth*, 85(B12), 7072-7090.
- Berge, PA, & Berryman, JG. (1995). Realizability of negative pore compressibility in poroelastic composites. *Journal of applied mechanics*, 62(4), 1053-1062.
- Berryman, J. G. (1992). Effective Stress for Transport-Properties of Inhomogeneous Porous Rock. *Journal of Geophysical Research-Solid Earth*, 97(B12), 17409-17424. doi: Doi 10.1029/92jb01593.
- Biot, M. A. (1941). General theory of three-dimensional consolidation. *Journal of Applied Physics*, 12(2), 155-164. doi: Doi 10.1063/1.1712886.
- Bjorlykke, K. (2015). *Petroleum Geoscience: From Sedimentary Environments to Rock Physics* (2nd ed.). Springer.
- Brace, W. F. (1965). Some New Measurements of Linear Compressibility of Rocks. *Journal of Geophysical Research*, 70(2), 391-&. doi: Doi 10.1029/Jz070i002p00391.
- Brace, W. F. (1972). Pore pressure in geophysics. *Flow and fracture of rocks*, 265-273.
- Brace, W. F., Walsh, J. B., & Frangos, W. T. (1968). Permeability of Granite under High Pressure. *Journal of Geophysical Research*, 73(6), 2225-&. doi: Doi 10.1029/Jb073i006p02225.
- Brace, W., Walsh, J. B., & Frangos, W. T. (1968). Permeability of granite under high pressure. *Journal of Geophysical research*, 73(6), 2225-2236.
- Brower, K. R., & Morrow, N. R. (1985). Fluid flow in cracks as related to low-permeability gas sands. *Society of Petroleum Engineers Journal*, 25(02), 191-201.
- Brown, A. A. (2015). Interpreting permeability from mercury injection capillary pressure data. *AAPG Annual Convention and Exhibition, Denver*.
- Byrnes, A. (2005). "Permeability, Capillary Pressure, and Relative Permeability Properties in Low-Permeability Reservoirs and the Influence of Thin, High-Permeability Bed on Production." *The Rocky Mountain Association of Geologists*: 69-108.
- Byrnes, A. Cluff, R. and Webb, J. 2009. Analysis of Critical Permeability, Capillary Pressure, and Electrical Properties for Mesaverde Tight Gas Sandstone from Western U.S. Basins. Final Scientific/Technical Report.
- Cade, C. A., Evans, I. J., & Bryant, S. L. (1994). Analysis of permeability controls: a new approach. *Clay Minerals*, 29(4), 491-502.
- Calhoun Jr, J. C., Lewis Jr, M., & Newman, R. C. (1949). Experiments on the capillary properties of porous solids. *Journal of Petroleum Technology*, 1(07), 189-196.

- Cao, Z., Liu, G., Zhan, H., Li, C., You, Y., Yang, C., & Jiang, H. (2016). Pore structure characterization of Chang-7 tight sandstone using MICP combined with N2GA techniques and its geological control factors. *Scientific reports*, 6, 36919.
- Castle, J. W., & Byrnes, A. P. (2005). Petrophysics of Lower Silurian sandstones and integration with the tectonic-stratigraphic framework, Appalachian basin, United States. *AAPG bulletin*, 89(1), 41-60.
- Clarkson, C. R., M. Nobakht, D. Kaviani and T. Ertekin (2012). "Production Analysis of Tight-Gas and Shale-Gas Reservoirs Using the Dynamic-Slippage Concept." *Spe Journal* 17(1): 230-242.
- Clerke, E. A. (2003). Beyond porosity-permeability relationships—determining pore network parameters for the Ghawar Arab-D using the Thomeer method. *Geofrontier (Dhahran, Saudi Arabia)*, 1(3), 12-17.
- Clerke, E. A. (2009). Permeability, relative permeability, microscopic displacement efficiency and pore geometry of M_1 bimodal pore systems in Arab-D limestone. *SPE Journal*, 14(03), 524-531.
- Cluff, R. M., Byrnes, A. P., Whittaker, S., & Krygowski, D. (2008, July). Evidence for a variable Archie porosity exponent “m” and impact on saturation calculations for Mesaverde tight gas sandstones: Piceance, Uinta, Green River, Wind River, and Powder River basins. In *Proceedings of the AAPG Rocky Mountain Section Meeting*. Denver, Colorado (Vol. 10).
- Coates, G. R., Xiao, L., & Prammer, M. G. (1999). *NMR logging: principles and applications*. Gulf Professional Publishing.
- Comisky, J. T., Newsham, K., Rushing, J. A., & Blasingame, T. A. (2007). A comparative study of capillary-pressure-based empirical models for estimating absolute permeability in tight gas sands. *SPE Annual Technical Conference and Exhibition*. Society of Petroleum Engineers.
- Coyner, K. B. (1984). Effects of stress, pore pressure, and pore fluids on bulk strain, velocity, and permeability in rocks (Doctoral dissertation, Massachusetts Institute of Technology).
- David, C., & Darot, M. (1989). Permeability and Conductivity of Sandstones. *Rock at Great Depth*, Vol 1, 203-209.
- Davies, J. P. and D. K. Davies (2001). "Stress-dependent permeability: Characterization and modeling." *Spe Journal* 6(2): 224-235.
- Davies, J. P. and S. A. Holditch (1998). *Stress Dependent Permeability in Low Permeability Gas Reservoirs: Travis Peak Formation, East Texas*, Society of Petroleum Engineers.
- Dernaika, M. (2010). Combined Capillary Pressure and Resistivity Index Measurements in Tight Gas Sands Using Vapor Desorption Method. In *SPE Deep Gas Conference and Exhibition*. Society of Petroleum Engineers.
- Dobrynin, V. M. (1962). Effect of overburden pressure on some properties of sandstones. *Society of Petroleum Engineers Journal*, 2(04), 360-366.
- Dong, J. J., J. Y. Hsu, W. J. Wu, T. Shimamoto, J. H. Hung, E. C. Yeh, Y. H. Wu and H. Sone (2010). "Stress-dependence of the permeability and porosity of sandstone and shale from TCDP Hole-A." *International Journal of Rock Mechanics and Mining Sciences* 47(7): 1141-1157.
- Dong, Z., Holditch, S., McVay, D., & Ayers, W. B. (2012). Global unconventional gas resource assessment. *SPE Economics & Management*, 4(04), 222-234.
- Dong, Z., Holditch, S. A., & Lee, W. J. (2015). Resource Estimation for Shale Gas Reservoirs. *Fundamentals of Gas Shale Reservoirs*, 301-323.
- Dullien, F. A. L., Lai, F. S., & Macdonald, I. F. (1986). Hydraulic continuity of residual wetting phase in porous media. *Journal of colloid and interface science*, 109(1), 201-218.

- Annual Energy Outlook 2016 Early Release: Annotated Summary of Two Cases. (2016). Retrieved from [https://www.eia.gov/outlooks/aeo/er/pdf/0383er\(2016\).pdf](https://www.eia.gov/outlooks/aeo/er/pdf/0383er(2016).pdf).
- Ertekin, T., G. A. King and F. C. Schwerer (1986). "Dynamic Gas Slippage: A Unique Dual-Mechanism Approach to the Flow of Gas in Tight Formations."
- Ertekin, T., G. A. King and F. C. Schwerer (1986). "Dynamic Gas Slippage: A Unique Dual-Mechanism Approach to the Flow of Gas in Tight Formations."
- Farber, DL, Bonner, BP, Balooch, M, Viani, B, & Siekhaus, W. (2001). Observations of a Water Induced Transition from Brittle to Viscoelastic Behavior in Nanocrystalline Swelling Clay. Paper presented at the AGU Fall Meeting Abstracts.
- Farquhar, R. A., Smart, B. G. D., Todd, A. C., Tompkins, D. E., & Tweedie, A. J. (1993, January). Stress sensitivity of low-permeability sandstones from the Rotliegendes sandstone. In SPE Annual Technical Conference and Exhibition. Society of Petroleum Engineers.
- Farquhar, R. A., SMART, B., Crawford, B. R., Todd, A. C., & Tweedie, J. A. (1993). Mechanical properties analysis: the key to understanding petrophysical properties stress sensitivity. In 1993 SCA Conference Paper.
- Fatt, I. (1958). "Pore Volume Compressibilities of Sandstone Reservoir Rocks." Transactions of the American Institute of Mining and Metallurgical Engineers 213(12): 362-364.
- Fatt, I. (1958). Pore structure in sandstones by compressible sphere-pack models. AAPG Bulletin, 42(8), 1914-1923.
- Fatt, I. and D. H. Davis (1952). "Reduction in Permeability with Overburden Pressure." Transactions of the American Institute of Mining and Metallurgical Engineers 195: 329-329.
- Georgi, D. T., & Chen, S. (2007). What Does NMR Really Contribute To Formation Evaluation?. Offshore Mediterranean Conference and Exhibition. Offshore Mediterranean Conference.
- Ghabezloo, S., Sulem, J., Guédon, S., & Martineau, F. (2009). Effective stress law for the permeability of a limestone. International Journal of Rock Mechanics and Mining Sciences, 46(2), 297-306. doi: <http://dx.doi.org/10.1016/j.ijrmms.2008.05.006>.
- Glover, P. W. "Introduction to petrophysics and formation evaluation." Petrophysics MSc (2016). University of Leeds.
- Graton, L. C., & Fraser, H. J. (1935). Systematic packing of spheres: with particular relation to porosity and permeability. The Journal of Geology, 43(8, Part 1), 785-909.
- Greder, H. N., Gallato, V., Cordelier, P., Laran, D., Munoz, V., & d'Abriègeon, O. (1997). Forty Comparisons of Mercury Injection Data with Oil/Water Capillary Pressure Measurements by the Porous Plate Technique. Society of Core Analysis, SCA, 9710.
- Guise, P., Grattoni, C., Allshorn, S., Fisher, Q. J., Schiffer, A. (2017). Stress Sensitivity of Mercury Injection Measurements. In International Symposium of the Society of Core Analysts, Vienna, Austria.
- Guyod, H. (1952). Electrical well logging fundamentals. Well Instrument Developing Co., Houston, TX.
- Heid, J. G., McMahon, J. J., Nielsen, R. F. and Yuster, S. T. (1950). Study of the Permeability of Rocks to Homogeneous Fluids, American Petroleum Institute. Drilling and Production Practice, New York, New York.
- Heller, R., and Zoback, M. (2013). Laboratory Measurements of Matrix Permeability and Slippage Enhanced Permeability in Gas Shales. In Unconventional Resources Technology Conference (pp. 1706-1715). Society of Exploration Geophysicists, American Association of Petroleum Geologists, Society of Petroleum Engineers.

- Heller, R., Vermylen, J., & Zoback, M. (2014). Experimental investigation of matrix permeability of gas shales. *Aapg Bulletin*, 98(5), 975-995. doi: 10.1306/09231313023.
- Herrick, D. C., & Kennedy, W. D. (1993, January). Electrical efficiency: A pore geometric model for the electrical properties of rocks. In *SPWLA 34th Annual Logging Symposium*. Society of Petrophysicists and Well-Log Analysts.
- Holditch, S. A. (2006). Tight gas sands. *Journal of Petroleum Technology*, 58(06), 86-93.
- Holditch, S. A. (2013). Unconventional oil and gas resource development—Let's do it right. *Journal of Unconventional Oil and Gas Resources*, 1, 2-8.
- Hubbert, M. K. (1953). Entrapment of petroleum under hydrodynamic conditions. *AAPG Bulletin*, 37(8), 1954-2026.
- Javadpour, F. (2009). "Nanopores and Apparent Permeability of Gas Flow in Mudrocks (Shales and Siltstone)." *Journal of Canadian Petroleum Technology* 48(8): 16-21.
- Jennings, J. B. (1987). Capillary pressure techniques: application to exploration and development geology. *AAPG Bulletin*, 71(10), 1196-1209.
- Jizba, D. L. (1992). Mechanical and acoustical properties of sandstones and shales. PhD thesis, Stanford University.
- Jones, C., J. M. Somerville, B. G. D. Smart, O. Kirstetter, S. A. Hamilton and K. P. Edlmann (2001). "Permeability prediction using stress sensitive petrophysical properties." *Petroleum Geoscience* 7(2): 211-219.
- Jones, F. O. and W. W. Owens (1980). "A Laboratory Study of Low-Permeability Gas Sands." *Journal of Petroleum Technology* 32(9): 1631-1640.
- Jones, S. C. (1972). A rapid accurate unsteady-state Klinkenberg permeameter. *Society of Petroleum Engineers Journal*, 12(05), 383-397.
- Jones, Stanley C. (1972). A rapid accurate unsteady-state Klinkenberg permeameter. *Society of Petroleum Engineers Journal*, 12(05), 383-397.
- Katahara, Keith W. (1996). Clay mineral elastic properties. Paper presented at the 1996 SEG Annual Meeting.
- Katz, A. J. and Thompson, A. H., (1986). Quantitative prediction of permeability in porous rock: *Physical Review B*, v. 34, 8179–8181.
- Katz, A. J. and Thompson, A. H., (1987). Prediction of rock electrical conductivity from mercury injection measurements: *Journal of Geophysical Research*, v. 92, 599–607.
- Kennedy, Martin. (2015). *Practical Petrophysics* (Vol. 62): Elsevier.
- Kilmer, N. H., N. R. Morrow and J. K. Pitman (1987). Pressure sensitivity of low permeability sandstones. *Journal of Petroleum Science and Engineering* 1(1): 65-81.
- Klinkenberg, L. J. (1941). *The Permeability Of Porous Media To Liquids And Gases*, American Petroleum Institute.
- Kolodzie Jr, S. (1980). Analysis of pore throat size and use of the Waxman-Smiths equation to determine OOIP in Spindle Field, Colorado. *SPE Annual Technical Conference and Exhibition*. Society of Petroleum Engineers.
- Kwon, O., Kronenberg, A. K., Gangi, A. F., & Johnson, B. (2001). Permeability of Wilcox shale and its effective pressure law. *Journal of Geophysical Research-Solid Earth*, 106(B9), 19339-19353. doi: Doi 10.1029/2001jb000273.
- Law, B. E. (2002). Basin-centered gas systems. *AAPG bulletin*, 86(11), 1891-1919.

- Law, B. E., & Curtis, J. B. (2002). Introduction to unconventional petroleum systems. AAPG bulletin, 86(11), 1851-1852.
- Lever, Andrew, & Dawe, Richard A. (1987). Clay migration and entrapment in synthetic porous media. *Marine and petroleum geology*, 4(2), 112-118.
- Li, M., Xiao, W. L., Bernabe, Y., & Zhao, J. Z. (2014). Nonlinear effective pressure law for permeability. *Journal of Geophysical Research-Solid Earth*, 119(1), 302-318. doi: 10.1002/2013jb010485.
- Li, M., Y. Bernabe, W. I. Xiao, Z. Y. Chen and Z. Q. Liu (2009). "Effective pressure law for permeability of E-bei sandstones." *Journal of Geophysical Research-Solid Earth* 114.
- Longeron, D. G., M. J. Argaud and J. P. Feraud (1989). "Effect of Overburden Pressure and the Nature and Microscopic Distribution of Fluids on Electrical Properties of Rock Samples." 4(02).
- Luffel, D. L., W. E. Howard and E. R. Hunt (1991). "Travis Peak Core Permeability and Porosity Relationships at Reservoir Stress."
- Ma, Y. Z., & Holditch, S. (2015). Unconventional resources from exploration to production. In *Unconventional Oil and Gas Resources Handbook: Evaluation and Development* (pp.3-52). Gulf Professional Publishing.
- Maron, S. H. and Prutton, C. F. *Principles of Physical Chemistry. Third Edition of Fundamental Principles of Physical Chemistry*, 1958. p 101-102.
- Mavko, G., Mukerji, T., & Dvorkin, J. (2009). *The rock physics handbook: Tools for seismic analysis of porous media*. Cambridge university press.
- Mavko, G. (2009). Parameters that Influence Seismic Velocity. *Conceptual Overview of Rock and Fluid Factors that Impact Seismic Velocity and Impedance*.
- McKernan, R. E., Rutter, E. H., Mecklenburgh, J., Taylor, K. G., & Covey-Crump, S. J. (2014). Influence of effective pressure on mudstone matrix permeability: implications for shale gas production. *SPE/EAGE European Unconventional Resources Conference and Exhibition*. Society of Petroleum Engineers.
- McLatchie, A. S., Hemstock, R. A., & Young, J. W. (1958). The effective compressibility of reservoir rock and its effects on permeability. *Journal of Petroleum Technology*, 10(06), 49-51.
- McPhee, C., Reed, J., & Zubizarreta, I. (2015). *Core Analysis: A Best Practice Guide* (Vol. 64). Elsevier.
- Melrose, J. C. (1987). Use of Water Vapor Desorption Data in the Determination of Capillary Pressures. In *SPE International Symposium on Oilfield Chemistry*. Society of Petroleum Engineers.
- Melrose, J. C. (1990). Valid Capillary Pressure Data at Low Wetting-Phase Saturations (includes associated papers 21480 and 21618). *SPE Reservoir Engineering*, 5(01), 95-99.
- Naik, G. C. (2005). *Tight Gas Reservoirs - An Unconventional Natural Energy Source for the Future*.
- Neasham, J. W. (1977). The morphology of dispersed clay in sandstone reservoirs and its effect on sandstone shaliness, pore space and fluid flow properties. In *SPE Annual Fall Technical Conference and Exhibition*. Society of Petroleum Engineers.
- Nelson, P. H. (2009). Pore-throat sizes in sandstones, tight sandstones, and shales. AAPG bulletin, 93(3), 329-340.
- Neustaedter, R. H., (1968). Log evaluation of deep Ellenburger gas zones: paper SPE 2071, *Deep Drilling and Development Symposium-Delaware basin, Monahans, TX, March 28*.

- Newsham, K. E., Rushing, J. A., Chaouche, A., & Bennion, D. B. (2002). Laboratory and field observations of an apparent sub capillary-equilibrium water saturation distribution in a tight gas sand reservoir. paper SPE, 75710, 5-8.
- Newsham, K. E., Rushing, J. A., & Lasswell, P. M. (2003). Use of vapor desorption data to characterize high capillary pressures in a basin-centered gas accumulation with ultra-low connate water saturations. In SPE Annual Technical Conference and Exhibition. Society of Petroleum Engineers.
- Newsham, K. E., Rushing, J. A., Lasswell, P. M., Cox, J. C., & Blasingame, T. A. (2004). A comparative study of laboratory techniques for measuring capillary pressures in tight gas sands. SPE Annual Technical Conference and Exhibition. Society of Petroleum Engineers.
- Nichols, G. (2009). Sedimentology and stratigraphy. John Wiley & Sons. (2nd ed., p.88).
- Nur, A., & Byerlee, J. D. (1971). Exact Effective Stress Law for Elastic Deformation of Rock with Fluids. *Journal of Geophysical Research*, 76(26), 6414-&. doi: Doi 10.1029/Jb076i026p06414.
- Olsen, C., & Fabricius, I. L. (2006). Static and dynamic Young's modulus of North Sea chalk. In SEG Technical Program Expanded Abstracts 2006 (pp. 1918-1922). Society of Exploration Geophysicists.
- Ostensen, R. W. (1983). Microcrack permeability in tight gas sandstone. *Society of Petroleum Engineers Journal*, 23(06), 919-927.
- Pettijohn, F. J., Potter, P. E., & Siever, R. (1987). *Sand and Sandstone*.—553 pp.
- Pickell, J. J., Swanson, B. F., & Hickman, W. B. (1966). Application of air-mercury and oil-air capillary pressure data in the study of pore structure and fluid distribution. *Society of Petroleum Engineers Journal*, 6(01), 55-61.
- Pittman, E. D. (1992). Relationship of porosity and permeability to various parameters derived from mercury injection-capillary pressure curves for sandstones. *AAPG bulletin*, 76(2), 191-198.
- Prasad, Manika, Kopycinska, Malgorzata, Rabe, Ute, & Arnold, Walter. (2002). Measurement of Young's modulus of clay minerals using atomic force acoustic microscopy. *Geophysical Research Letters*, 29(8).
- Purcell, W. R. (1949). Capillary Pressures - Their Measurement Using Mercury and the Calculation of Permeability Therefrom. *Transactions of the American Institute of Mining and Metallurgical Engineers* 186(2): 39-48.
- Qiao, LP, Wong, RCK, Aguilera, Roberto, & Kantzas, Apostolos. (2012). Determination of Biot's Effective-Stress Coefficient for Permeability of Nikanassin Sandstone. *Journal of Canadian Petroleum Technology*, 51(03).
- Revil, A., Grauls, D., & Brévar, O. (2002). Mechanical compaction of sand/clay mixtures. *Journal of Geophysical Research: Solid Earth*, 107(B11).
- Rezaee, M. R., Jafari, A., & Kazemzadeh, E. (2006). Relationships between permeability, porosity and pore throat size in carbonate rocks using regression analysis and neural networks. *Journal of Geophysics and Engineering*, 3(4), 370.
- Rezaee, R., Saeedi, A., & Clennell, B. (2012). Tight gas sands permeability estimation from mercury injection capillary pressure and nuclear magnetic resonance data. *Journal of Petroleum Science and Engineering*, 88, 92-99.
- Robin, P. Y. F. (1973). Note on Effective Pressure. *Journal of Geophysical Research*, 78(14), 2434-2437. doi: Doi 10.1029/Jb078i014p02434.
- Recommended practices for core analysis. (1998). Washington, D. C.

Rushing, J. A., K. E. Newsham, P. M. Lasswell, J. C. Cox and T. A. Blasingame (2004). *Klinkenberg-Corrected Permeability Measurements in Tight Gas Sands: Steady-State Versus Unsteady-State Techniques*, Society of Petroleum Engineers.

Saner, S., M. Amabeoku and M. Kissami (1996). "Formation resistivity response to loading and unloading confining pressure." *Journal of Petroleum Science and Engineering* 16(1-3): 169-179.

Schmitt, M., Fernandes, C. P., Wolf, F. G., da Cunha Neto, J. A. B., Rahner, C. P., & dos Santos, V. S. S. (2015). Characterization of Brazilian tight gas sandstones relating permeability and Angstrom-to-micron-scale pore structures. *Journal of Natural Gas Science and Engineering*, 27, 785-807.

Schowalter, T. T. (1979). Mechanics of secondary hydrocarbon migration and entrapment. *AAPG bulletin*, 63(5), 723-760.

Shafer, J., & Neasham, J. (2000). Mercury porosimetry protocol for rapid determination of petrophysical and reservoir quality properties. In *International Symposium of the Society of Core Analysts, SCA* (Vol. 2021, p. 12).

Shanley, K. W., Cluff, R. M., & Robinson, J. W. (2004). Factors controlling prolific gas production from low-permeability sandstone reservoirs: Implications for resource assessment, prospect development, and risk analysis. *AAPG bulletin*, 88(8), 1083-1121.

Simmons, G., & Brace, W. F. (1965). Comparison of static and dynamic measurements of compressibility of rocks. *Journal of Geophysical Research*, 70(22), 5649-5656.

Smith, T., Sondergeld, C., & Tinni, A. O. (2010). Microstructural controls on electric and acoustic properties in tight gas sandstones; some empirical data and observations. *The Leading Edge*, 29(12), 1470-1474.

Sneider, R. M., Sneider, J. S., Bolger, G. W., & Neasham, J. W. (1997). *AAPG Memoir 67: Seals, Traps, and the Petroleum System*. Chapter 1: Comparison of Seal Capacity Determinations: Conventional Cores vs. Cuttings.

Spencer, C. W. (1989). "Review of Characteristics of Low-Permeability Gas-Reservoirs in Western United-States." *Aapg Bulletin-American Association of Petroleum Geologists* 73(5): 613-629.

Spencer, C. W. (1989). Review of characteristics of low-permeability gas reservoirs in western United States. *AAPG bulletin*, 73(5), 613-629.

Swanson, B. F. (1979). Visualizing pores and nonwetting phase in porous rock. *Journal of Petroleum Technology*, 31(01), 10-18.

Swanson, B. F. (1981). A simple correlation between permeabilities and mercury capillary pressures: *Journal of Petroleum Technology*, Dec., 2488-2504.

Terzaghi, K. (1925). *Principles of Soil Mechanics*. *Engineering News-Record*, 95, 987-990.

Thomas, R. D. and D. C. Ward (1972). "EFFECT OF OVERBURDEN PRESSURE AND WATER SATURATION ON GAS PERMEABILITY OF TIGHT SANDSTONE CORES." *Journal of Petroleum Technology* 24(NFEB): 120-&.

Thomeer, J. H. (1960). Introduction of a pore geometrical factor defined by the capillary pressure curve. *Journal Petroleum Technology*, Mar., 73-77.

Thomson, W. (1871). LX. On the equilibrium of vapour at a curved surface of liquid. *The London, Edinburgh, and Dublin Philosophical Magazine and Journal of Science*, 42(282), 448-452.

Tiab, D. and E. C. Donaldson (2012). *Petrophysics: theory and practice of measuring reservoir rock and fluid transport properties*, Gulf professional publishing.

- Tyrolougou, P., Dudeney, A. W. L., & Grattoni, C. A. (2005). Evolution of porosity in geotechnical composites. *Magnetic resonance imaging*, 23(6), 765-768.
- Vairogs, J., C. L. Hearn, D. W. Dareing and V. W. Rhoades (1971). "Effect of Rock Stress on Gas Production from Low-Permeability Reservoirs." *Journal of Petroleum Technology* 23(Sep): 1161-&.
- Vanorio, T., Prasad, M., & Nur, A. (2003). Elastic properties of dry clay mineral aggregates, suspensions and sandstones. *Geophysical Journal International*, 155(1), 319-326. doi: DOI 10.1046/j.1365-246X.2003.02046.
- Walls, J. D., & Nur, A. (1979). Pore pressure and confining pressure dependance of permeability in sandstones—7th Formation Evaluation Symp. Proc., Canada. Well Logging Society, Calgary.
- Walsh, J. B. (1965). The effect of cracks on the compressibility of rock. *Journal of Geophysical Research*, 70(2), 381-389.
- Wang, Zhijing, Wang, Hui, & Cates, Michael E. (2001). Effective elastic properties of solid clays. *Geophysics*, 66(2), 428-440.
- Wardlaw, N. C., & Taylor, R. P. (1976). Mercury capillary pressure curves and the interpretation of pore structure and capillary behaviour in reservoir rocks. *Bulletin of Canadian Petroleum Geology*, 24(2), 225-262.
- Warpinski, N. R., & Teufel, L. W. (1992). Determination of the Effective-Stress Law for Permeability and Deformation in Low-Permeability Rocks. SPE. doi: 10.2118/20572-PA.
- Washburn, E. W. (1921). "Note on a method of determining the distribution of pore sizes in a porous material." *Proceedings of the National Academy of Sciences of the United States of America* 7: 115-116.
- Watfa, M., & Nurmi, R. (1987, January). Calculation of saturation, secondary porosity and producibility in complex Middle East carbonate reservoirs. In SPWLA 28th Annual Logging Symposium. Society of Petrophysicists and Well-Log Analysts.
- Wentworth, C. K. (1922). A scale of grade and class terms for clastic sediments. *The Journal of Geology*, 30(5), 377-392.
- Wilson, M. D. (1982). Origins of clays controlling permeability in tight gas sands. *Journal of Petroleum Technology*, 34(12), 2-871.
- Wyble, D. O. (1958). Effect of applied pressure on the conductivity, porosity and permeability of sandstones. *Journal of Petroleum Technology*, 10(11), 57-59.
- Zoback, M. D., & Byerlee, J. D. (1975). Permeability and Effective Stress. *Aapg Bulletin-American Association of Petroleum Geologists*, 59(1), 154-158.